INFORMATION TO USERS

This manuscript has been reproduced from the microfilm master. UMI films the text directly from the original or copy submitted. Thus, some thesis and dissertation copies are in typewriter face, while others may be from any type of computer printer.

The quality of this reproduction is dependent upon the quality of the copy submitted. Broken or indistinct print, colored or poor quality illustrations and photographs, print bleedthrough, substandard margins, and improper alignment can adversely affect reproduction.

In the unlikely event that the author did not send UMI a complete manuscript and there are missing pages, these will be noted. Also, if unauthorized copyright material had to be removed, a note will indicate the deletion.

Oversize materials (e.g., maps, drawings, charts) are reproduced by sectioning the original, beginning at the upper left-hand corner and continuing from left to right in equal sections with small overlaps.

Photographs included in the original manuscript have been reproduced xerographically in this copy. Higher quality 6" x 9" black and white photographic prints are available for any photographs or illustrations appearing in this copy for an additional charge. Contact UMI directly to order.

UMI®

.

Lithium-ion Battery Reactions
at Elevated Temperatures

by

Dean Delehanty MacNeil

B.Sc., University of New Brunswick, Fredericton, NB, Canada, 1997

Submitted in partial fulfillment of the requirements for the degree of

Doctor of Philosophy

in the Department of Chemistry

at

Dalhousie University

Halifax, Nova Scotia, Canada

September 2001.

Canada

DALHOUSIE UNIVERSITY

FACULTY OF GRADUATE STUDIES

The undersigned hereby certify that they have read and recommend to the Faculty of Graduate Studies for acceptance a thesis entitled "Lithium-ion Battery Reactions at Elevated Temperatures" by Dean D. MacNeil in partial fulfillment of the requirements for the degree of Doctor of Philosophy.

Dated: August 29, 2001

External Examiner:

Research Supervisor:

Examining Committee:
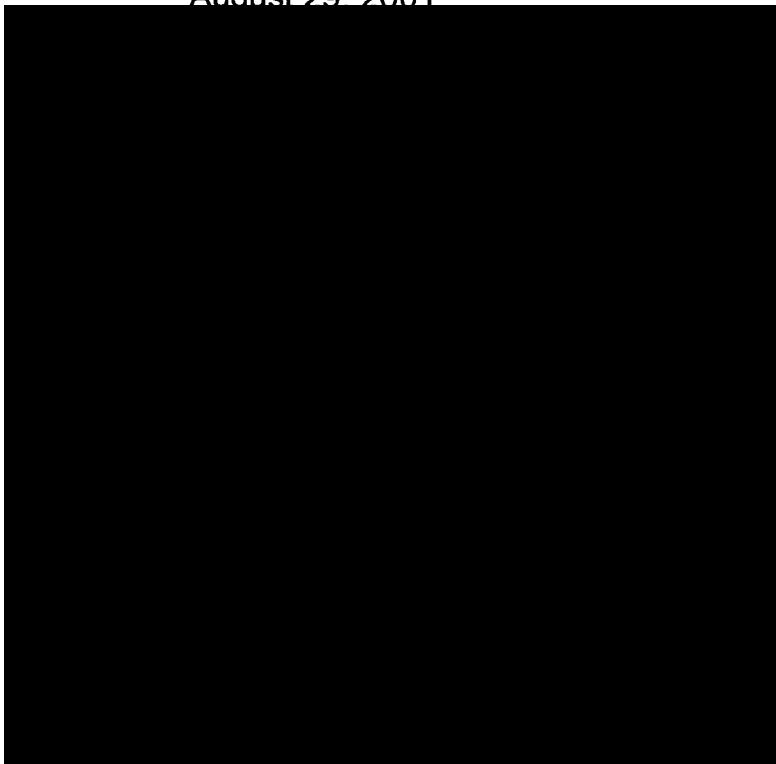
DALHOUSIE UNIVERSITY

DATE: September 13, 2001
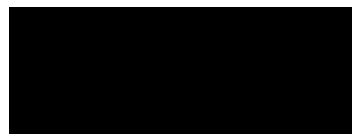
AUTHOR: Dean Delehanty MacNeil

TITLE: Lithium-ion Battery Reactions at Elevated Temperatures

DEPARTMENT OR SCHOOL: Chemistry

DEGREE: PhD   CONVOCATION: October   YEAR: 2001

Permission is herewith granted to Dalhousie University to circulate and to have copied for non-commercial purposes, at its discretion, the above title upon the request of individuals or institutions.

███████████████

Signature of Author

The author reserves other publication rights, and neither the thesis nor extensive extracts from it may be printed or otherwise reproduced without the author's written permission.

The author attests that permission has been obtained for the use of any copyrighted material appearing in the thesis (other than the brief excerpts requiring only proper acknowledgement in scholarly writing), and that all such use is clearly acknowledged.

iii

Table of Contents

List of Figures

List of Tables

Abstract

In this thesis, the behaviour of charged lithium-ion battery electrodes upon exposure to elevated temperatures has been examined using a combination of Accelerating Rate Calorimetry (ARC) and Differential Scanning Calorimetry (DSC). The bulk of this thesis is concerned with developing a reaction mechanism for the cathode, $LiCoO_2$. The charged electrode ($Li_{0.5}CoO_2$) releases oxygen and forms $LiCoO_2$ and Co_3O_4 when temperature is raised. In the presence of an organic solvent, the electrode gets further reduced to CoO and the solvent combusts. When the temperature is increased even further in the presence of excess solvent full reduction to cobalt metal occurs. In electrolyte solutions of $LiPF_6$, the HF produced as a side reaction, promotes the polymerization of the solvent at elevated temperatures. The product of polymerization deposits on the surface of the electrode particles and slows the release of oxygen from the structure; thus a more thermally stable electrode is obtained.

The reaction of $Li_{0.5}CoO_2$ at elevated temperatures in various solutions was found to follow Avrami-Erofeev reaction kinetics for the decomposition of solids. The reaction kinetics were then used, in combination with kinetics derived in the literature for the anode, to develop a full thermal model for the exposure of lithium-ion batteries to elevated temperatures. This model can be used to predict the outcome of various thermal events for any cell geometry.

At the anode, ARC studies were used to show that the reaction processes for six different carbon materials were similar. However, the rates of these reactions were strongly dependent on the surface area of the graphitized samples.

In addition to $LiCoO_2$, other possible cathode materials for lithium-ion cells were studied and their thermal reactivity was compared. The results of this thesis are of importance to commercial electrode developers trying to safely increase the size of their electrodes for applications such as electric vehicles.

List of Abbreviations and Symbols

A – cross sectional area

Ah – ampere-hour

ARC – accelerating rate calorimetry

a – lattice constant

B – cell height or thickness

BET – Brunauer-Emmett-Teller

BETI - $LiN(SO_2CF_2CF_3)_2$

C_c – operational capacity of carbon $(mAhg^{-1})$

C_{co} – operational capacity of $LiCoO_2$ $(mAhg^{-1})$

C_{tot} – total heat capacity (JK^{-1})

c – concentration $(molml^{-1})$

c_c – specific heat of cylindrical material

c_i – specific heat of component i $(Jg^{-1}K^{-1})$

c_p – specific heat capacity $(Jg^{-1}K^{-1})$

c_{pc} – specific heat of cell $(JK^{-1}g^{-1})$

c_{ps} – specific heat of sample $(JK^{-1}g^{-1})$

c_{tot} – total specific heat $(JK^{-1}g^{-1})$

c- lattice constant

DC – direct current

DEC – diethyl carbonate $(C_5H_{10}O_3)$

DME – dimethoxy ethane $(C_4H_{10}O_2)$

DMC – dimethyl carbonate $(C_3H_6O_3)$

DSC – differential scanning calorimetry

DTBP – di-t-butyl peroxide

d – separation of the planes of atoms in a crystal

E_1 – activation energy of reaction 1

E_2 – activation energy of reaction 2

E_a – activation energy (eV)

EC – ethylene carbonate ($C_3H_4O_3$)

EMC – ethyl-methyl carbonate ($C_4H_8O_3$)

EV – electric vehicles

e – electron charge

eV – electron Volt

f_c - percent active of carbon

f_{co} – percent active of $LiCoO_2$

$f(\alpha)$ – reaction model

g – mass in grams

H – total heat generated per gram (Jg^{-1})

H_1 – total heat by reaction 1 per unit mass of reactant (Jg^{-1})

H_2 – total heat by reaction 2 per unit mass of reactant (Jg^{-1})

H_{exp} – total heat generated by experiment (J)

H_{cal} – total heat calculated for experiment (J)

HQ - $LiN(SO_2CF_3)_2$

H_{tot} – total heat produced (J)

HWS – heat-wait-search

h – total heat evolved (J)

h_s – surface heat conductivity of cylindrical material ($Wcm^{-1}K^{-1}$)

I – thermal current (W)

IEC – International Electrotechnical Commission

IUPAC – International Union of Pure and Applied Chemistry

k_B – Boltzmann constant

k – thermal conductivity ($Wm^{-1}K^{-1}$)

k_T – thermal conductivity of cylindrical material

k – rate constant (min^{-1})

L – liter

L – length of cell

Li - Lithium

LIAC – lithium alkyl carbonate

LIC – lithium intercalated carbons

M - molarity

MCMB – mesocarbon microbeads

M_c – mass of carbon (g)

M_{co} – mass of $LiCoO_2$ (g)

m – unit of length (meter)

m_c – mass of cell (g)

m_{cat} – mass of cathode (g)

m_{el} – mass of electrolyte (g)

m_i – mass of component i (g)

min – unit of time (minute)

m_s – mass of sample (g)

m_{tot} – mass of reactant (g)

m, n, p – exponents to describe reaction model

N – number of data points

N – number of rings or layers (molecules – Appendix)

NMP – n-methyl pyrroldinone

n – path length difference

P – Power (Wg^{-1}) (Random Stacking probability – Chapter 8)

P – mean probability

Pa – Unit of Pressure (Pascal)

P_a – Power produced in the anode

P_i – power per unit volume produced in the ring (probability – Appendix)

p_i^K - probability

PC – propylene carbonate ($C_4H_6O_3$)

PVDF – polyvinylidene difluoride

Q – heat released by the reactant ($Jmol^{-1}$)

Q_i - Probability

q – thermal energy released (J)

q_i^K - probability of an arbitrary event

R – gas constant (8.3145 $JK^{-1}mol^{-1}$)

redox – reduction and oxidation

r_i – radius of ith ring

r_N – radius of nth ring

S – surface area (cm^2)

s – unit of time (seconds)

SEI – solid electrolyte interface

SEM – scanning electron microscopy

T – Temperature (K)

T_a – ambient temperature (K)

T_i – temperature of the ith ring

T_p – peak temperature (K)

t – time (sec)

TIG – tungsten inert gas

TGA – thermal gravimetric analysis

TMO – transition metal oxide

UHP – Ultra-High-Purity

UL – Underwriters Laboratories

UN – United Nations

V – voltage

V – volume (mL)

W – unit of power (Watt)

W – width of cell

Wh – watthour

x – unit of length

x_f – amount of lithium containing metastable species in the SEI

x_i – amount of lithium intercalated within the carbon

XPS – X-ray photoelectron spectroscopy

z – dimensionless measure of the SEI thickness

α - fractional degree of conversion

β - temperature scan rate ($Kmin^{-1}$)

χ - surface heat transfer coefficient ($Wcm^{-2}K^{-1}$)

χ^2 – goodness of fit

ΔT – change in temperature (K)

$\Delta(T_i)$ – change in temperature of the ith ring

$\Delta(T_N)$ – change in temperature of outer ring

Δx – bar length (m)

Φ - phi-factor

γ - frequency factor (min^{-1})

γ_1 – frequency factor of reaction 1 (min^{-1})

γ_2 – frequency factor of reaction 2 (min^{-1})

λ - wavelength

μ - chemical potential

ρ - density (gcm^{-3})

σ - shape factor

τ - time (s)

Acknowledgements

Do not float through life, ... make waves!!!

Chapter 1

Introduction

Transportation has played a key role in the lives of many people during the 20th century. This need for mobility has resulted in the production of millions of vehicles, such as automobiles, aeroplanes and boats. Today, many of these vehicles are propelled by the combustion of fossil fuels that must be extracted from various regions of the planet. In addition to these fossil fuels being non-renewable, recent research has shown that their combustion products (greenhouse gases) are harmful to the earth's atmosphere and ultimately cause the temperature of this planet to rise [1]. This can cause widespread environmental problems. A large amount of research has been conducted in the search for alternatives to fossil fuels. Large-scale power generating stations are using such technologies as nuclear and hydroelectric power, while local legislatures are developing laws to force the introduction of non-polluting vehicles.

In order to eliminate the widespread internal combustion engine used in vehicles today, automobile manufacturers are mainly concentrating on two technologies, fuel cells and electric (battery powered) vehicles. Both technologies offer the prospect of reduced emissions and a decreased reliance on imported petroleum and therefore have attracted great interest from environmentalist and legislators alike. Although, there are advantages and disadvantages to both technologies, this thesis is of importance to electric vehicle (EV) applications. Specifically, the results of this thesis will address the safety concerns of using lithium-ion battery technology in electric vehicle applications.

Today, lithium-ion batteries are the state of the art power source for portable consumer electronics and are currently used in most laptop computers and digital cellular phones. This is due to their large energy density, higher voltage and longer lifetimes over conventional battery systems. Currently, the total lithium-ion cell production rate is near 550 million per year [2]. Many of these cells are 18mm in diameter by 65mm in length (18650) or about the size of an index finger and deliver approximately 2 Ah of electricity.

For electric vehicle applications larger cells will be required. Currently, for a pure EV (no combustion engine), a number of 100 Ah cells are being considered to supply the necessary energy to the car [3]. These cells have not been widely introduced due to the high cost associated with these larger volume cells.

In addition to the increased cost of these larger cells, there is also a concern about the thermal stability of the components of the cell. A lithium-ion cell contains, simplistically, two active electrodes separated by a polymeric separator, surrounded by an organic electrolyte solution. The active electrodes, in the charged state, have been shown previously to partake in exothermic reactions at elevated temperatures. These exothermic reactions, in the presence of the flammable organic electrolyte and oxygen from the surrounding environment of the cell, present a dangerous situation that must be understood and controlled.

Thermal stability concerns for lithium-ion cells in electric vehicle applications is a much greater concern than in 18650 cells due to their increased size. If the components of these cells begin to react, due to the exposure to elevated temperatures from some abuse situation (e.g. short circuit), then the evolved heat from the exothermic reactions must be dissipated. Heat dissipation is not as effective when the surface area to volume ratio decreases, as would occur in 100 Ah cells as compared to 18650 cells. Some of the products of the reactions between the components of a lithium-ion cell are gases and thus during the reaction there will be an increase in pressure of the cell to such a point that an explosion may occur [4]. These reactions are not well understood and for lithium-ion cells to continue their presence in the consumer market, or for growth in new markets (EVs), an understanding of these reactions must be obtained so that they can be prevented or controlled. This thesis will further enhance the understanding of thermally induced reactions that occur between the active electrode materials and the electrolyte of the cell.

A more detailed understanding of the reaction(s) that occur within the cell as it is exposed to elevated temperatures is required. An investigation, where an individual electrode is exposed to high temperatures in the presence of electrolyte, will be beneficial to understanding these complex systems. For the anode, I confirmed the dependence of thermal stability on the surface area of graphitic electrodes, where the smaller the surface area of the graphite the more thermally stable the electrode. Most of my work has been

centred on the understanding of the reactions occurring at the cathode. I have performed a detailed kinetic analysis of the reaction of lithium cobalt oxide charged to 4.2 V in the presence of 1M lithium hexafluorophosphate ($LiPF_6$) in ethylene carbonate (EC)/ diethyl carbonate (DEC). This kinetic analysis has lead to the development of a thermal model that can predict the thermal response, of not only our test samples, but also the thermal response of a complete lithium-ion cell. In addition to the kinetic model, a reaction mechanism has been proposed for the decomposition of lithium cobalt oxide charged to 4.2 V. Alternative cathode materials are constantly being introduced and I will present some results for the thermal stability of these cathode materials. Such studies may help evaluate suitable cathode materials in terms of thermal stability.

Chapter 2 gives a brief history and an introduction to electrochemical cells. Lithium and lithium-ion batteries are then reviewed, culminating with a description of the present lithium-ion technology. This section serves as an introduction to the materials chosen for analysis in this thesis.

A variety of testing methods for the thermal stability of commercial lithium-ion batteries exists and Chapter 3 will give an overview of these methods and a review of earlier results. In addition, many researchers use other techniques in their studies of specific electrode materials and their results will also be analysed in Chapter 3. This chapter will serve as an overview to the current understanding about the thermal stability of lithium-ion electrodes and cells.

Chapter 4 describes the experimental techniques developed and used throughout this project. Each section of Chapter 4 will give a brief introduction to the theory behind the experimental technique and how it was used to aid in the goal of the thesis.

During the investigation of the thermally stability of the individual electrode materials, reaction kinetics had to be determined. Chapter 5 will present the various kinetic analysis methods available as they pertain to the experimental methods I used during the course of my work.

Much of my work has centred on understanding and modelling the reactions that occur at the cathode. Currently, the most commonly used cathode material in mass produced lithium-ion cells is $LiCoO_2$. Chapter 6 provides an analysis of the reaction mechanism that occurs when a sample of $LiCoO_2$, charged to 4.2 V, is exposed to

elevated temperature. The reaction mechanism was investigated in a stepwise fashion where the dry electrode was analysed by itself, in an organic solvent and in electrolyte solutions. Each system provided insight into the possible reaction mechanism. Chapter 7 shows the development of a kinetic model to describe the initial process that occurs when $LiCoO_2$, charged to 4.2V, is exposed to elevated temperature in the presence of EC/ propylene carbonate (PC) and in the presence of 1M $LiPF_6$ in EC/DEC.

There has been very little published work on the safety of lithium-ion battery electrodes as compared to the electrochemical analysis of new electrode materials (charge capacity, rate capability, and structure). Much of the work that does exist has involved the anode side of the battery. Chapter 8 details the results I have obtained on the thermal stability of a variety of anode materials. These results support the mechanism previously proposed for the instability of graphitic anode material.

The combination of the kinetic model for the cathode, which is described in Chapter 7, with that proposed previously for the anode has allowed the construction of a full thermal mathematical model for the exposure of charged lithium-ion batteries to elevated temperatures. Although I did not produce the mathematical model, some of the necessary data were taken from my work. The model predicts the result of exposing a lithium-ion battery to elevated temperatures and has a variety of implications for the safety of lithium-ion cells. These results will be discussed in Chapter 9.

Throughout the course of this thesis, I have analysed a number of cathode materials that have been proposed for use in lithium-ion batteries. Although I have concentrated this thesis on the study of $LiCoO_2$, Chapter 10 will serve as a brief comparison of some of the possible alternate cathode materials to $LiCoO_2$. Finally, Chapter 11 will present the conclusions of this thesis along with suggestions for future work on this project.

Chapter 2

A Brief Review of Lithium Based Batteries

2.1 General Battery History and Terminology

Batteries are devices that convert chemical energy into electrical energy via electrochemical reduction and oxidation (redox) reactions of their active materials. The basic electrochemical unit is called a cell, while a battery consists of one or more of these cells connected in series, parallel, or both, depending on the required application. Redox reactions involve the transfer of electrons, which upon insertion of the battery into a circuit allows electrical current (electrons) to pass through the circuit and do work. At the same time within the cell, charge flows in the form of ions that are transported from one electrode to the other. As the process continues, the active materials become depleted until the battery is no longer capable of supplying electrons and at this point the battery is said to be in the discharged state. Primary batteries (alkaline) partake in irreversible redox reactions and thus when fully discharged they are simply discarded or recycled. Secondary batteries (e.g. lithium-ion, lead-acid, etc.) have reversible redox reactions and, thus, by reversing the current (charging) with an external charger, the active materials can be regenerated and the battery reused. A schematic of an electrochemical cell is shown in Figure 2.1.
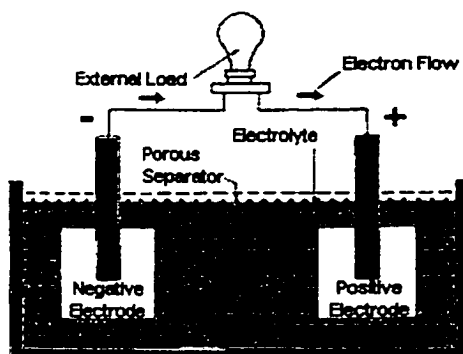
Figure 2.1 Schematic of a typical electrochemical cell during discharge.

The first battery was developed by Count Alessandro Volta in 1796 while trying to refute the "animal electricity" introduced by Luigi Galvani years earlier when Galvani fastened brass hooks between the spinal cord of a dissected frog and an iron railing causing the twitching of the frog's leg [5]. The original voltaic pile, designed by Volta, used zinc and silver disks separated by paperboard disks that had been soaked with sea water. The voltaic pile was the forefather of modern alkaline batteries. In 1860 Raymond Planté invented the lead-acid battery and since that time there has been much development in rechargeable battery systems [5].

The active materials in the electrodes determine the voltage of a battery. The total quantity of charge involved during the electrochemical reaction is expressed as the capacity of the cell and is measured in ampere-hours (Ah). The product of the quantity of charge available (Ah) and the voltage (V) of the cell gives the energy available in the cell and is measured in Watt-hours (Wh). The energy density of a cell is measured on a volume (Wh/L) basis.

2.2 Lithium Metal Batteries

Lithium metal is the lightest metal in the periodic table; this combined with its highly negative redox potential makes it an attractive negative electrode for high energy density batteries. Lithium primary cells, with lithium metal anodes, have been designed with a number of chemistries and in a variety of sizes (5 mAh - 20000 Ah) and configurations [6]. Lithium's high reactivity presents some difficulties in the operation and construction of these cells. Some of the necessities are the handling of lithium in a dry and inert atmosphere, the use of non-aqueous electrolytes and special cell design features to ensure safety. A variety of cells have been developed and these include soluble cathode cells (SO_2, $SOCl_2$), solid cathode cells (V_2O_5, MnO_2, CuO) and solid electrolyte cells.

The most widely used primary lithium cell is the lithium/ manganese dioxide (MnO_2) couple. The characteristics of Li/MnO_2 cells include high voltage operation (3V), an energy density of 230 Wh/kg or 550 Wh/L, wide operating temperature range, long shelf life and low cost [6].

Rechargeable lithium cells have been studied since the early 1970s. A schematic of a rechargeable lithium cell is shown in Figure 2.2. The operation of a rechargeable lithium cell is fairly simple. During discharge, the lithium atoms pass from a high-energy state in the negative electrode (lithium) to a low energy state in the positive electrode by transfer of the ion through the non-aqueous electrolyte and the electron through the external circuit. The opposite reaction occurs during charge and thus the efficiency of a charge/discharge cycle depends on the reversibility of the reactions at the electrodes. In order to achieve a high number of efficient charge/discharge cycles the electrode reactions need to be completely reversible. For example, a 99% cycling efficiency at an electrode is detrimental, since after 100 cycles, only 37% of the initial energy can be obtained (after 500 cycles less than 1%). By comparison, for preparative chemistry a product yield of 99% is excellent.
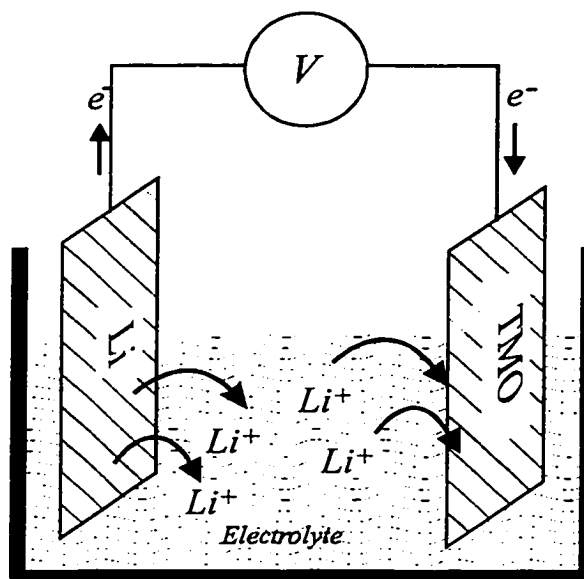
Figure 2.2 Schematic of a rechargeable lithium cell during discharge.

The positive electrode material in rechargeable lithium cells was either a transition-metal oxide or chalcogenide (MnO_2, MoO_2, and TiS_2) that was capable of reversible lithium insertion [7]. The reversibility was due to the incorporation of the lithium atom within the host structure forming a solid solution, without destruction of the lattice (intercalation), for example,

$$xLi^+ + xe^- + MoO_2 \rightleftharpoons Li_xMoO_2. \qquad (2\text{-}1)$$

The voltage of the electrochemical cell depends on the difference in the chemical potential of the lithium atoms in the two host materials,

$$V = \frac{-(\mu_{cathode} - \mu_{anode})}{e} , \qquad (2\text{-}2)$$

where $\mu_{cathode}$ and μ_{anode} are the chemical potential of lithium atoms in the cathode and anode materials respectively and e is the magnitude of the electron charge. The chemical potential of lithium metal, μ_{anode}, is constant because it is composed of a single phase, but the chemical potential of lithium within the transition metal oxide cathode varies with the lithium content of the lattice. Thus, the change in the cell potential is a direct measure of the change in chemical potential of lithium within the transition metal oxide.

Although lithium primary batteries have seen rapid commercialisation and are now used in many applications, the commercialisation of rechargeable batteries based on lithium metal, with a liquid electrolyte failed. The failure is due to the incomplete reversibility of the lithium metal electrode [8]. During charge, non-uniform current density causes lithium to plate on the electrode surface as dendrites and as the charge/discharge cycles continue there is a growth of these dendrites. This dendrite formation produces a highly porous lithium surface, which, in the presence of an organic electrolyte, presents a serious safety hazard due to the high reactivity of lithium with the organic solvent. These hazards created a concern for all lithium-based batteries and thus stringent safety tests were developed for these batteries.

Currently, there is a great deal of research in the area of lithium metal rechargeable batteries based on a solid polymer electrolyte [2, 9]. The increased strength afforded by the use of a polymer electrolyte has given rise to the popularity of this type of cell. However, more research is required on various aspects of the lithium/polymer technology, such as increased conductivity and performance at low temperature, before the widespread use of these cells will occur.

2.3 Lithium-ion Batteries

The most successful approach to overcoming the problems associated with the use of a metallic lithium electrode was the replacement of the lithium metal with a lithium

insertion electrode. Various substances have been identified, such as various types of carbon, oxides and metals (alloys). In order to replace lithium metal the chemical potential of the new anode material must be considered. To produce a large potential from the electrochemical cell (Equation 2-2) and thus a large energy density cell, the difference between the chemical potential of lithium within the electrodes must be maximised. Figure 2.3 shows the binding energy of lithium atoms in various lithium intercalation hosts. To differentiate between the two technologies, electrochemical cells using two lithium intercalation hosts are called lithium-ion (Li-ion) cells. At the positive electrode, most research concentrated on $LiCoO_2$ since it has a high lithium binding energy and good charge/discharge characteristics. Early lithium-ion cells used negative electrodes containing transition metal oxides or chalcogenides with low binding energy to lithium, such as MoO_2, MoS_2 and WO_2 [10, 11]. These Li-ion cells showed low specific charge and a low cell voltage.
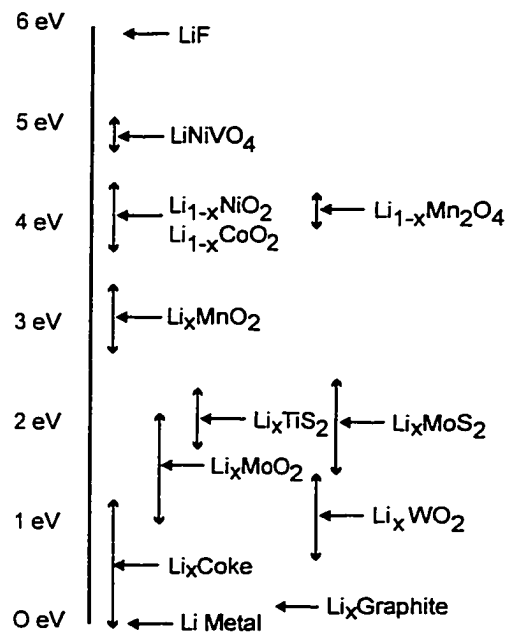
Figure 2.3 Binding energy of lithium in various lithium compounds versus lithium metal.

The success of lithium-ion batteries has been due to the replacement of the lithium metal anode with a carbonaceous material. Armand first introduced the use of carbon as an anode material in 1980 [12]. Figure 2.3 shows that carbon has a low

binding energy for lithium. The combination of a carbon negative with a high binding energy cathode ($LiCoO_2$) produces a cell having a high voltage. In addition, carbon materials show a high degree of structural tolerance for reversible intercalation giving rise to very good charge/discharge cycling characteristics [8].

2.4 Present Lithium-ion Technology

2.4.1 Anode

Today, all the major manufacturers of lithium-ion cells use a carbon material for the anode. The variety of carbons used is vast and include hard carbon (Sony, A&TB), mesocarbon microbeads (MCMB) (Panasonic, E-One/Moli Energy), natural graphite (Sanyo), and carbon fiber (A&TB). The anode material is combined with a few percent of a polymeric binder (to ensure everything sticks together) and a highly conductive carbon (to provide electrical conductivity to all the active material). The mixture is then coated (typically both sides) on a thin copper current collector (~25 μm). These current collectors act as substrates for the electrode films and carry the current to and from the electrode. Copper is chosen for the anode current collector since it is relatively cheap, conductive, easily rolled into thin films, does not form lithium alloys and it is stable at the operating voltages of the anode.

2.4.2 Electrolyte

Early attempts at using graphite as an anode material for lithium-ion batteries failed due to the high reactivity of lithium intercalated graphite towards electrolyte and the co-intercalation of solvent molecules into the graphite structure, causing exfoliation [13, 14, 15]. Due to this reactivity the first commercial battery (Sony) used poorly crystalline carbon materials (hard or soft carbons), which do not exfoliate due to pinning of adjacent layers by defects [16, 17]. The reactivity of these lithium intercalated carbons (LIC) materials with electrolyte is due to their chemical potential being very close to that

of metallic lithium (see Figure 2.3). Lithium and LIC have a large reducing power that causes the reduction of the organic electrolyte and the formation of a passivating layer of decomposed electrolyte components that has been called the solid electrolyte interphase (SEI). This interphase is ionically conductive, allowing the passage of lithium-ions, but is an electronic insulator. The SEI was first studied by Peled in 1979 and has been under continuous study since the chemistry of the SEI varies with the composition of the electrolyte and anode [18, 19, 20, 21, 22, and 23]. Since the positive electrode is the lithium source in a Li-ion cell, the lithium that is lost during the formation of the SEI is detrimental to the efficiency of the cell and has to be minimal for optimum performance.

It was not until the early 1990's, when an electrolyte solution based on ethylene carbonate (EC) was developed, that graphite could be effectively used as anode in lithium-ion cells [24, 25]. This was because the decomposition products of EC formed an effective protective coating on external graphite surfaces that permitted lithium insertion and prevented solvent co-intercalation [19, 24]. As EC is a solid at room temperature it was mixed with low viscosity solvents such as ethers (e.g., 1,2-dimethoxyethane (DME) [25, 26]) and alkyl carbonates (e.g., dimethyl carbonate (DMC) [27, 28], and diethyl carbonate (DEC) [28]) to lower the melting point and viscosity of the solvent and thus increase ionic conductivity.

Commercial manufacturers do not divulge the composition of their electrolyte solutions, but they are most likely either $LiPF_6$ or $LiBF_4$ dissolved in a variety of organic solvents, based mainly on EC. In addition, many manufacturers add various types of additives to improve cycling characteristics or other aspects such as safety [29. 30]. Manufacturers continuously modify the amount and type of additives placed in their cells and thus it is difficult to keep abreast of the current electrolyte composition of commercial cells.

2.4.3 Cathode

$LiCoO_2$ was first suggested as cathode in 1980 and has seen continued use because of favourable electrochemical properties (stability, capacity) and its ease of preparation in a high quality, ideal layered structure [31, 32]. The structure of $LiCoO_2$ is

shown in Figure 2.4. Currently, all the major Japanese manufacturers of Li-ion cells use $LiCoO_2$ as the cathode material, despite the fact that only half of the incorporated lithium can be used reversibly during cycling [33]. This is because if all the lithium is removed from $LiCoO_2$, the electrostatic repulsion between the oxygen array in the crystal lattice makes the structure unstable. In addition, the +4 oxidation state is not common for cobalt. Currently, there is much effort in finding a replacement for $LiCoO_2$ because of its cost and toxicity. Most of these replacements involve the alteration of the $LiCoO_2$ stoichiometry by substitution of more abundant (inexpensive) metal ions [34].

O
Li
Co
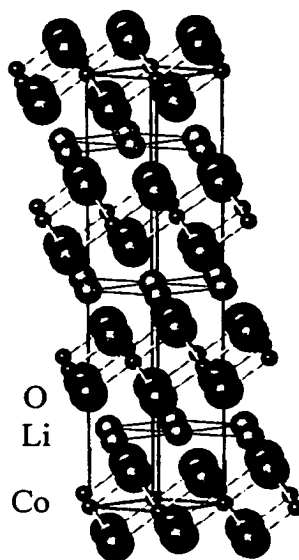
Figure 2.4 Structure of LiCoO₂.

Currently, two major manufacturers (E-one/Moli and NEC) are making a commercial Li-ion cell with a different cathode, namely $LiMn_2O_4$, but many other manufacturers have performed research in its possible use. $LiMn_2O_4$ has been chosen since it is a low cost alternative to $LiCoO_2$. Manganese is abundant in nature, and its delithiated structure (Mn_2O_4) has a higher thermal stability than $Li_{0.5}CoO_2$ [35]. The increase in thermal stability is of great importance when the size of the electrochemical cell has to be increased (EV applications). The reversible charge capacity of $LiMn_2O_4$ (120 mAh/g) is lower than that of $LiCoO_2$ (140 mAh/g) and thus replacing the cathode of a $LiCoO_2$ cell with $LiMn_2O_4$ will result in the reduction of the total capacity of the cell.

This lower cell capacity has hindered the widespread introduction of $LiMn_2O_4$ as a cathode material for commercial cells.

Similar to the preparation of the anode, the cathode material is combined with a polymeric binder and a conductive carbon and excess solvent to make a slurry. The slurry is then coated, on both sides, of a thin aluminium current collector. Aluminium is used since it is inexpensive, easily rolled into thin foils and it is stable at the operating voltages of the cathode [36].

2.4.4 Current Designs

Lithium-ion cells are most widely available in two designs: cylindrical and prismatic. In a cylindrical cell, the electrode coated current collectors are wound in a jellyroll fashion and separated by a polymeric separator containing microporous holes (see Figure 2.5) [37]. The jellyroll is inserted into a stainless steel can to which electrolyte is added. Welding a top to the can then seals it. The top of the can (header) contains the primary safety device of the cell. If a cell overheats, the generated pressure will force a safety valve to burst, disconnecting the current and allowing the release of pressure. Li-ion cylindrical cells are normally 18mm in diameter and 65mm in length, but there are many sizes available. Cylindrical cells are mainly used in portable computer applications.
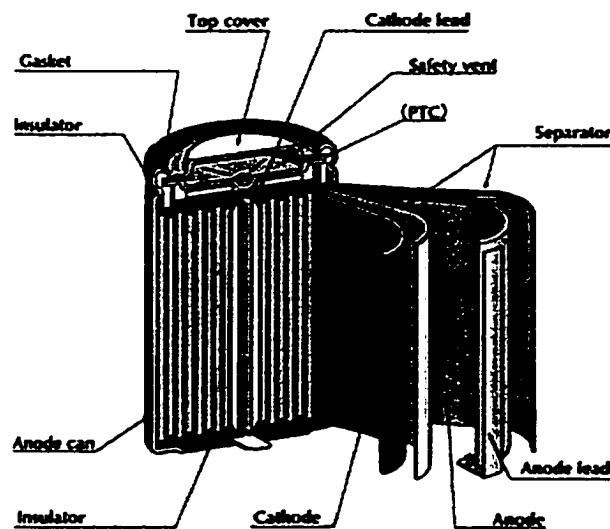
Figure 2.5 Schematic of a commercial cylindrical cell (Sony) showing jellyroll wrapping.

Currently, two major types of separators are used, namely polyethylene and polypropylene. The polymers differ in their melting temperature (130 and 150°C, respectively). When the melting point of the polymer is reached, current flow stops, by the closure of the separator holes. The lithium-ion cell can no longer operate (dead cell) due to the discontinuation of ion flow from one electrode to the other [38].

A prismatic Li-ion battery is generally fabricated in the same manner as a cylindrical cell except that the cell is flat (see Figure 2.6) [37]. These cells come in many sizes and thickness and are mainly used in cellular phone applications, where the thickness of the cell is of prime importance.
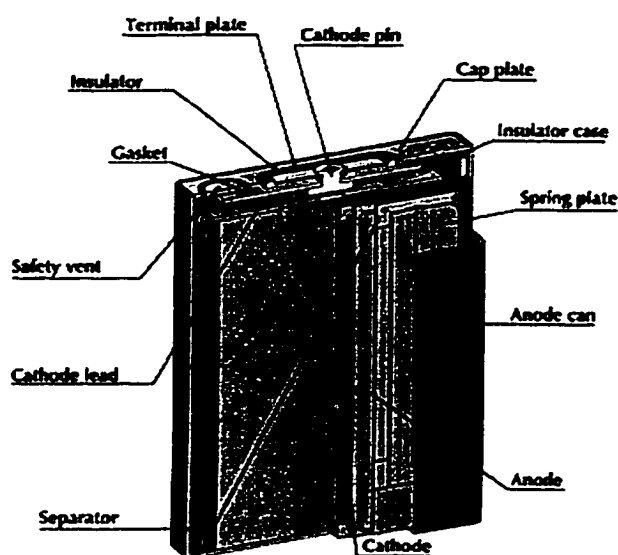
Figure 2.6 Schematic of a prismatic Li-ion battery (Sony).

Chapter 3

Thermal Analysis of Lithium-ion Batteries

3.1 Commercial Lithium-ion Cells

In order to protect consumers, strict safety guidelines have been developed for lithium metal-based batteries. Although lithium-ion batteries do not contain any lithium metal, they have been classified in the same manner as lithium metal-based batteries. In normal use, lithium-ion cells are safe; it is under abuse conditions that problems tend to arise. A variety of agencies have adopted a number of tests to simulate possible abuse scenarios. Monitoring the safety of cells is the responsibility of the cell manufacturer. The benchmark tests for the safety of lithium-ion cells have been developed by Underwriters Laboratories (UL-1642) [39], the United Nations (UN) for the transportation of dangerous goods [40], and the International Electrotechnical Commission (IEC) [41]. Other agencies have guidelines for specific applications (military, space), but these are based on the tests proposed by UL. There are a number of tests and they can be generally sorted into four groups as described in Table 3.1.

Table 3.1 Variety of safety tests for lithium batteries.

Group	Sample Tests
Electrical	Overcharge, overdischarge, external short-circuit, forced discharge
Mechanical	drop, impact, nail, crush, vibration acceleration
Thermal	flame, sandbath, oven exposure, thermal shock
Environmental	Decompression, altitude, immersion

To cell manufacturers, it is clear that some of the tests in Table 3.1 are more difficult to pass than others. Many of the mechanical and environmental group tests are "easier" to pass than tests that induce a temperature gradient (thermal group and short-circuit) [42]. Thus the thermal stability of a lithium-ion cell is a good indicator of the overall safety of the cell, since the most dangerous abuse situations lead to thermal abuse. An advantage of thermal stability tests is that they are generally quite reproducible, unlike mechanical tests [42].

Specific examples involving lithium-ion batteries in the field demonstrate the danger that thermal events present to these cells. In 1996, a battery pack consisting of two cylindrical lithium-ion cells exploded. The explosion was the result of a bus crushing the pack [43]. In 1997, a battery pack for a laptop computer burned, supposedly the result of a short-circuit within a cell [44]. There have also been numerous reports of recalls for lithium-ion cells due to the possibility of fire [44, 45]. In spite of these events, lithium-ion cells are widely used due to their many advantages (large energy density, long life) and the fact that only a few safety incidents have occurred while 1.5 billion cells have been produced.

Heat generation is the cause for many of the current safety problems associated with lithium-ion batteries. Thermal events or short-circuits are problematic since the resulting chemical reactions may cause self-heating of the cell and increase its temperature to the point of no return (thermal runaway). Imagine a closed reaction vessel (in this case a sealed electrochemical cell) in which an exothermic reaction proceeds. Initially, the temperature of the vessel is at ambient temperature but it will rise until the rate of heat generation due to the exothermic chemical reaction is equal to the rate of heat escape from the reaction vessel surface. If a thermal balance is not established the chemical reactions will increase the temperature of the reaction vessel to a point where thermal runaway occurs (extreme rise in the temperature of the vessel, see Figure 3.1). The rate of temperature change of the reaction vessel (dT/dt, °C/min) can be represented by the following equation,

$$c_p\rho(dT/dt) = Qc\gamma\exp(-E_a/RT) - \chi(S/V)(T - T_a), \qquad (3\text{-}1)$$

where c_p is the specific heat capacity of the reaction vessel and its contents ($Jg^{-1}K^{-1}$), ρ is its density of the reaction vessel (g/cc), Q is the heat released by the reactant ($Jmol^{-1}$), c is

the concentration of reactant (molcm^{-3}) and $\gamma\exp(-E_a/RT)$ is the reaction rate constant (sec^{-1}). The first term on the right hand side of Equation 3-1 describes the heat generation while the second term describes the heat dissipation from the surface, where χ is the surface heat transfer coefficient (Wcm^{-2}K^{-1}), S/V is the ratio of surface area (cm^2) to volume (ml) of the reaction vessel, and T$_a$ is the ambient temperature (K). Equation 3-1 demonstrates the importance of thermal design when considering lithium-ion batteries, especially for large-volume (EV applications) lithium-ion batteries. To avoid thermal runaway, critical values exist for capacity, cell size, operating temperature and cell chemistry. The absence of any exothermic reactions between cell components is the ideal situation for large-volume (EV) lithium-ion batteries.
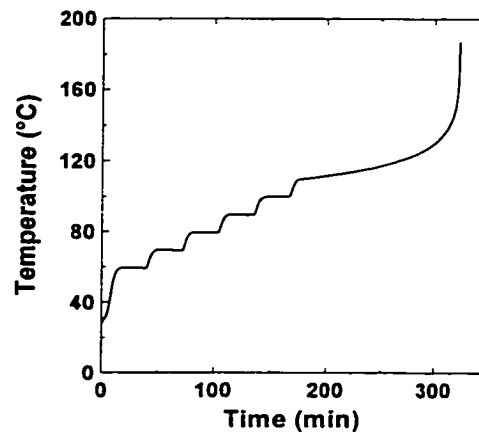
Figure 3.1 Temperature versus time profile for the thermal decomposition of di-t-butyl peroxide, showing thermal runaway at 320 min.

There is not a vast amount of information available in the literature about the thermal stability of full sized commercial lithium-ion cells and much of the information available on these commercial cells comes from cells removed from battery packs. Typically, the only information available about cells from a battery pack is their active electrode compositions, while the other components, as will be shown, play an important role on the thermal stability of cells.

Maleki et al performed an adiabatic experiment on a LiCoO$_2$/Graphite cell which showed self-heating beginning near 120°C [46]. The cell then proceeded into thermal runaway with temperatures reaching above 300°C. Adiabatic calorimetry has been used by researchers at Moli Energy (Maple Ridge, B.C.) on LiCoO$_2$/coke cells to demonstrate

that a) an electrolyte based on a $LiPF_6$ salt has better thermal stability than one based on a $LiBF_4$ salt, b) anode surface area and morphology strongly influences thermal stability, and c) the reaction rate of Li_xCoO_2 in electrolyte depends strongly on x and on temperature [35].

Researchers at NTT Telecommunications Laboratories have recently published a number of results about abuse tests on $LiMn_2O_4$/carbon and $LiCoO_2$/carbon prismatic lithium-ion cells [47]. In general terms, lithium-ion prismatic cells based on $LiMn_2O_4$ were found to be safer than those of $LiCoO_2$, which confirms results obtained by MacNeil and Dahn for cylindrical cells [48]. NTT showed tests of a variety of cells from different manufacturers and found varying results due to different reaction chemistries. Typically, the thermal stability limit (the temperature above which thermal runaway occurs) varied from 155-160°C for cells with a $LiCoO_2$ cathode, while cells using $LiMn_2O_4$ did not go into thermal runaway at 170°C. When the thermal limit was surpassed for the $LiCoO_2$ cathode cells, the cell temperature exceeded 200°C and the cell casing exploded and expelled some of its contents [47].

In an overcharge test (where the cell was charged to 10 volts in about 30 min), NTT researchers found that $LiCoO_2$ cathode prismatic cells proceeded into thermal runaway, while $LiMn_2O_4$ cathode prismatic cells did not, again confirming the increased thermal stability of $LiMn_2O_4$ cells. During a simulated short-circuit (nail penetration through cell can) no thermal runaway was detected for either type of prismatic cell. Short-circuit tests on cylindrical cells are very difficult to pass and have a wide variety of thermal responses (runaway, fire) depending on the depth, speed and length of time of nail penetration. Nail penetration tests are very important because many of the accidents reported above are the result of internal shorts. These internal shorts may be caused by manufacturing defects (impurities in the jellyroll) or the poor alignment of the separator upon assembly [47].

Cell manufacturers incorporate a variety of safety features in their cells that help control the danger these cells may pose under abuse conditions. One feature common to many larger commercial lithium-ion cells is a pressure vent (or an adapted form of it). A typical 18650 cell top (header), containing the pressure vent is shown in Figure 3.2 [49]. The pressure vent is controlled by the disk and is used to relieve the internal pressure of

the can, if it becomes excessive. An increase in cell pressure occurs when the exothermic reaction, described previously, takes place generating many gaseous products. Simplistically the pressure vent prevents the rupture of the cell since, when the vent opens (disk burst), there is a rapid expulsion of the generated gases easing the pressure inside the cell. In addition to preventing the rupture of the cell, the rapid release of gas allows for some cooling of the cell, which may help prevent thermal runaway.
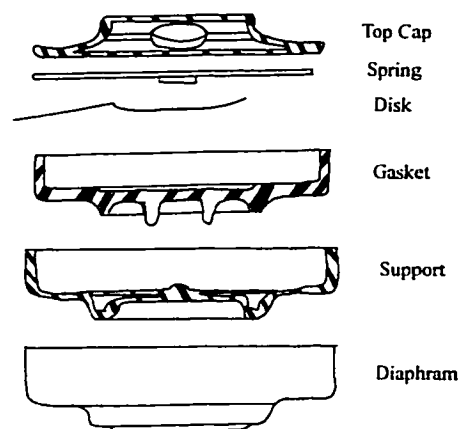
Figure 3.2 Exploded view of header for a cylindrical Li-ion cell (not to scale, adapted from [49] Texas Instruments).

In addition to the engineering aspects of cell designs, manufacturers add various materials to the components of the cell, most commonly to the electrolyte, to help suppress possible thermal events. These additives should not hinder cell performance and, thus, a trade-off is often required to obtain an acceptable additive. Most of these additives are proprietary to the manufacturers and they are constantly changing, which makes the understanding of commercial cells difficult. I will describe the use of biphenyl, for controlling overcharging, as an example of what chemical additives can do [50]. Biphenyl decomposes at high voltage producing a high vapour pressure; thus, if overcharging occurs, the pressure vent will open and the cell will be open circuited before any detrimental exothermic reactions can begin. In addition, the decomposition of biphenyl deposits polyphenylene on the cathode, which increases the cell impedance such that the cell can tolerate mechanical abuse [50]. Furthermore, the polyphenylene is electronically semiconducting and if deposited in the separator during overcharge, it will

slowly discharge the cell even after the header has ruptured, which increases the overall safety of the cell [50].

3.2 Laboratory Analysis of Lithium-ion Cells

There are inherent difficulties in testing full sized lithium-ion cells for safety. The major concern with a full cell is that the reactions occurring at each electrode can not be isolated during the experiment. Thus, the information obtained is limited to a full cell response and nothing is known as to the stability of the components of the cell themselves or the identity of the most reactive component. In addition, the production of full sized lithium-ion cells is difficult in an academic institution since the manufacturing equipment and materials are not available.

These issues have been addressed by numerous researchers who have performed experiments on individual electrodes in electrolyte to propose a possible reaction mechanism for the instability of lithium-ion cells at elevated temperatures. These researchers have used differential scanning calorimetry (DSC), thermal gravimetric analysis (TGA) and accelerating rate calorimetry (ARC) to analyse the stability of various components of a lithium-ion cell.

One of the first published works on the thermal stability of lithium-ion electrode materials was a TGA study on the stability of three cathode candidates (Li_xNiO_2, Li_xCoO_2, $Li_xMn_2O_4$) [51]. The authors demonstrated that, upon heating in an inert atmosphere, the onset temperature for oxygen release (weight loss) was in the order of $Li_xNiO_2 <$ $Li_xCoO_2 <$ $Li_xMn_2O_4$. The conclusion was that $Li_xMn_2O_4$ should be used as cathode material in lithium-ion cells to decrease the possibility of oxygen evolution. This evolved oxygen could react with the electrolyte solvent by a combustion process, evolving heat. A DSC study by Zhang et al. [52] has verified the results obtained by Dahn et al. [51]. In addition, Zhang et al. found that as the value of x decreased in Li_xNiO_2 and Li_xCoO_2, the reactivity of the material increased, but $Li_xMn_2O_4$ was less sensitive to variations in x. Work by Biensan et al. has also confirmed the above classification of stability for Li_xNiO_2, Li_xCoO_2 and $Li_xMn_2O_4$ in electrolyte [42].

Biensan et al. also showed results for Li_xCoO_2 and Li_xNiO_2 as the cell voltage increased (thus x decreased). They found increased electrode reactivity at higher voltages.

Maleki et al. gave a DSC profile for Li_xCoO_2 in electrolyte charged to 4.15 V [46]. They showed similar reactivity as presented before, but in addition to DSC measurements a simultaneous TGA scan was used. The TGA data showed the loss of mass. Any de-lithiated cathode material in the presence of electrolyte is air/moisture sensitive and thus must be sealed before analysis. The DSC analyses by Maleki et al. were made in hermetically crimped Al DSC pans, which were shown by TGA to leak. Researchers have not carefully addressed this point and I believe that most DSC data that have been presented in the literature for the reaction of electrodes with electrolyte may be affected by leaks and thus the results are questionable. To address this problem, I have developed a new DSC sample cell that assures no mass loss and this will be described in Chapter 4.

The most common use of DSC on cathode material is in the comparison of new materials to the standard $LiCoO_2$. Most of these data are presented in the forms of patents [53, 54]. Another widespread use of DSC is in its use to demonstrate improved stability when a variety of coatings or electrolyte additives are used [55].

For the anode side of the cell, most thermal investigations use differential scanning calorimetry (DSC). One of the earliest and more detailed DSC analyses of the reactions, which occur at the anode, was performed by du Pasquier et al. [56]. They proposed a reaction scheme for the anode in electrolyte; which was the decomposition of the solid electrolyte interphase (SEI) on the carbon followed by the reaction of intercalated lithium with the electrolyte. They also correlated the larger amplitude of the SEI decomposition peak to those carbons with the largest irreversible capacity. Finally, they proposed a reaction between the intercalated lithium and the polymeric binder used in the electrode fabrication process.

If the DSC data of du Pasquier et al. are examined closely, many of the profiles contain sharp endothermic peaks, which I believe are due to leaks in their sample pans. Thus, the values that were obtained for the heats of reaction could be spurious. Leaking pans may also cause misinterpretations of the processes that occur during the decompositions.

Maleki et al. inferred a similar reaction mechanism to du Pasquier et al. and again Maleki's simultaneous TGA demonstrated that the DSC pans were not sealed [46]. There are mixed reports for the classification of the second decomposition process. Zhang et al. believed that the reaction involved the binder [52]. Previous work in the Dahn Laboratory (presented below) supports the reaction scheme given by du Pasquier et al.

Accelerating rate calorimetry (ARC) was used in 1995 to demonstrate that the reaction of lithium-intercalated coke with electrolyte showed increased thermal stability when compared to the reaction of cycled metallic lithium with electrolyte [35]. The experiments also demonstrated the improved stability of a $LiPF_6$ based electrolyte, in the presence of a lithium-intercalated anode, compared to a $LiBF_4$ based electrolyte. The thermal stability of the anode was found to be dependent on the surface area and morphology of the carbon. The value of x in Li_xC_6 was not found to strongly influence the self-heating rate until metallic lithium started to electroplate on the carbon surface. On the cathode side, von Sacken et al. found that the self-heating rate of Li_xCoO_2 was dependent on the value of x and on temperature [35]. These results will be verified and expanded upon in this thesis.

Richard demonstrated the use of the ARC in an academic setting in 1998 [57]. She developed a method that could analyse a small amount (~300 mg) of air and moisture sensitive electrode material in the presence of electrolyte. Her work concentrated on lithium intercalated mesocarbon microbead (MCMB) graphite material in 1M $LiPF_6$ EC/DEC (33/67, vol/vol) electrolyte. Reaction kinetics determined from her ARC results were used to predict the outcome of other thermal events (DSC).

Typical results for the MCMB material, with various amounts of intercalated lithium (voltages), are shown in Figure 3.3. The reaction process, which occurs during the first 20 degrees (80-100 °C), was assigned to the decomposition of the metastable components of the passivating layer. The remaining section of the ARC profile was found to be due to the reaction of lithium intercalated in the carbon with the electrolyte, in addition to the decomposition of the electrolyte itself, occurring above 190°C (see Figure 3.3). Kinetic parameters were extracted from these profiles from which a mathematical model was developed to predict the self-heating profiles of lithium intercalated MCMB reacting with 1M $LiPF_6$ EC/DEC. Richard also gave a brief

introduction to the thermal stability of cathode materials and the effect of different electrolytes.
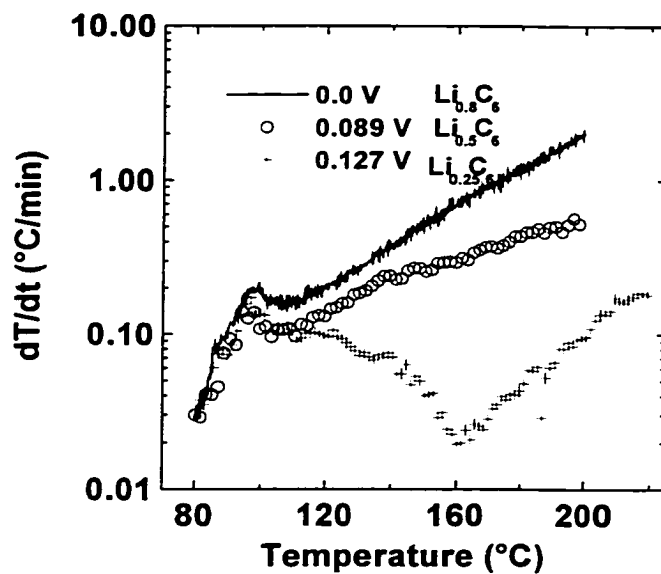
Figure 3.3 Self-heating profile of MCMB in 1M LiPF₆ EC/DEC (33/67) electrolyte, discharged to three voltages, corresponding to three different lithium concentrations. Results are from reference 57.

Chapter 4

Experimental Techniques and Thermal Analysis Methods

4.1 Electrochemical Cell Construction and Testing

4.1.1 Initial Electrochemical Investigation

Lithium metal electrochemical cells can be used to measure the voltage of a cell with respect to its capacity. This information allows one to infer information about a variety of electrochemical properties of the electrode, such as the voltage of lithium insertion/de-insertion, and phase changes that may occur in the electrode material.

A variety of stock electrode materials were analysed in this study and they are listed in Table 4.1 along with their supplier. The electrodes were prepared by combining the stock powder with 7% by mass, each, of Super S carbon black (MMM Carbon, Belgium) and polyvinylidene difluoride (PVDF) polymeric binder (10 % in n-methyl-pyrolidinone, NMP, NRC). The carbon black ensured electrical contact between all the grains in the electrode while the binder was used to ensure that the electrode holds together. n-methyl pyrrolidinone (NMP) was then added in excess to make a slurry. After mixing for ten minutes the mixture was poured onto a thin metal foil (copper – anodes, aluminium – cathodes) and a 0.28 mm (0.011") notch bar was used to spread the slurry. The electrode was then dried overnight in an oven set at 110°C to evaporate the NMP. The next day, 1.3 cm diameter electrodes were cut and weighed.

The electrochemical cells were then assembled in an argon-filled glove box, following Figure 4.1. The 2325 cell hardware (23 mm diameter, 2.5 mm thickness) had a stainless steel top and bottom casing. The desired electrode was placed in the centre of the bottom casing and 1M $LiPF_6$ in ethylene carbonate (EC)/ diethyl carbonate (DEC) (33/67, vol/vol, Mitsubishi Chemicals) was added as electrolyte. A polypropylene

separator (Celgard 2502, Celanese) was placed above the electrode after which a 125 μm thick lithium foil (FMC), previously cut to 1.3 cm diameter, was added. Finally, a stainless steel spacer and spring were added to maintain good electrical contact. The cell top, on which there is a polypropylene gasket, was then placed and the cell was crimped shut, sealing the contents from the outer environment. When the electrochemical cells were removed from the glove box, stainless steel tabs were spot welded to the outer casing and the cell connected to the charger system.

Cells were tested using a computer controlled constant-current charger system obtained from Moli Energy (1990) Ltd. The temperature of the cells was monitored and kept constant at 30.0 ± 0.1°C. The current used for the electrochemical testing of electrode characteristics was selected based on the active mass and type of material. The carbon electrodes (typically 10 mg) were tested using a 100-hour rate, which corresponds to a change of $x = 1$ in Li_xC_6 in 100 hours. The cathode samples' charging current was based on a 20-hour charge rate for $LiCoO_2$. The theoretical charge capacity of $LiCoO_2$ is 270 mAhg^{-1} and thus an 18 mg cathode sample would have a current of 0.246 mA selected for electrochemical testing.

Table 4.1. Stock electrode materials used during the course of this thesis.

Stock Electrode	Surface Area (m^2g^{-1})	Supplier
MCMB 2850 (mesocarbon microbeads)	0.8	Osaka Gas
KS-75	9.2	Timcal
SFG-75	3.5	Timcal
SFG-44	4.3	Timcal
Heat treated Carbon Fiber	0.4	BP Amoco
XP-3 Petroleum Coke	6.7	Conoco
$LiCoO_2$	0.1	Moli Energy
$LiMn_2O_4$	0.6	Chemetals
$LiNiO_2$	0.7	FMC
$LiNi_{0.7}Co_{0.2}Mg_{0.05}Ti_{0.05}O_2$	0.8	FMC
$LiNi_{0.8}Co_{0.2}O_2$	0.3	FMC
$LiFePO_4$	15.2	Dahn
$Li[Ni_{3/8}Co_{1/4}Mn_{3/8}]O_2$	5.9	Dahn

Casing Top (Negative Terminal)

Gasket

Stainless Steel Spring

Stainless Steel Spacer

Lithium Metal
Counter/Reference Electrode

Separator

Working Electrode

Casing Bottom (Positive Terminal)
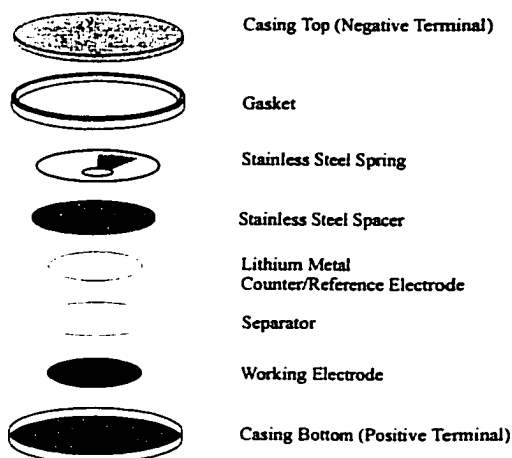
Figure 4.1 Exploded view of the hardware in a 2325 lithium coin cell.

4.1.2 Carbon Electrode Cell Construction for ARC analysis

The electrochemical cells described in Section 4.1.1 were used to determine the electrochemical properties of the various samples under study. For thermal analysis in the accelerating rate calorimeter (ARC), the sample had to generate enough heat to overcome the thermal mass of the bomb (~ 1g) and still produce a self-heating rate of 0.02°C/min. The electrode described in Section 4.1.1 was inappropriate since only approximately 10 mg of active material was analysed. This amount of sample would not generate enough heat for a detectable self-heating rate to be observed by the ARC. The fabrication and testing methods of electrochemical cells that produced enough material for useful thermal data from the ARC will be described.

The carbon electrodes were fabricated using the same preparative techniques as described in 4.1.1, except that the amount of material prepared was on the order of 10 grams and it was not coated on a copper foil. After drying the electrode slurry, the electrode powder was lightly ground in a mortar and then passed through a 300 μm sieve. Approximately 300 mg of the electrode was then placed in a stainless steel mould to which 13.8 MPa (2000 psi) was applied to produce an approximately 1 mm thick carbon pellet.

The carbon pellet was then placed in the bottom casing of a 2325 coin cell and assembled following Figure 4.2 in an argon-filled glove box. Electrolyte (1M $LiPF_6$

EC/DEC 33/67, vol/vol, Mitsubishi Chemicals) was added to the electrode pellet until it was fully wetted and then two polypropylene separators (Celgard 2502, Celanese) were placed on top of the wet pellet. Four pieces of 125 μm thick lithium foil (FMC) were added on top of a stainless steel mesh (1 mm mesh, 125 μm thick) to ensure full electrical contact with all of the lithium. The lithium foil and stainless steel mesh were previously cut to 1.3 cm in diameter. A stainless steel spacer was then added above the lithium to provide pressure to the contents of the cell. Finally, the cell top, with polypropylene gasket, was attached and the cell was crimped shut to seal it from the outside environment.
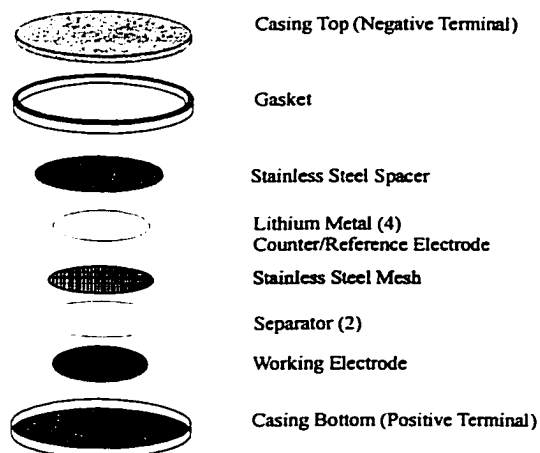
Figure 4.2 Exploded view of hardware used to prepare charged carbon electrodes for the ARC.

The electrochemical cells were fully discharged to 0 V, until the cell's voltage under open circuit was less than 50 mV after 24 hours. The cells were then transferred to an argon-filled glovebox for ARC sample preparation (described in Section 4.2.3).

4.1.3 Li-ion Cell Construction for ARC Analysis of Cathodes

In order to obtain information about cathode materials used in commercial lithium-ion batteries and to simulate conditions of true commercial batteries, lithium-ion cells were constructed. To produce these cells the lithium metal electrode of Section

4.1.2 was replaced with a lithium transition metal oxide (TMO). The stock TMO electrode was prepared in the same fashion as the stock carbon electrode.

In a lithium-ion cell, the electrodes must be balanced [58]. The balanced construction is required so that the cell operates at the highest efficiency and avoids lithium plating by ensuring that the lithium available from the cathode just fills the carbon and accounts for any irreversible capacity loss. For example, Li_xCoO_2 has the ability to deliver good cycling behaviour and operate efficiently between the lithium content range of x= 0.5 and 1. This range limits the operational capacity of $LiCoO_2$ to near 140 mAh/g, while for MCMB the working capacity is limited to near 340 mAh/g. Thus, the active masses (mass of only active material) of the two electrodes must be balanced, or,

$$M_{Co} * f_{Co} * C_{Co} = M_C * f_C * C_C, \qquad (4\text{-}1)$$

where M_x = mass of electrode x, f_x = % active material in electrode x, C_x = operational capacity of electrode x, and Co- $LiCoO_2$ or C-Carbon. Thus for a 300 mg carbon sample,

$$M_{Co} = \frac{0.300g * 0.87 * 340mAh/g}{0.87 * 140mAh/g} \approx 0.75g, \qquad (4\text{-}2)$$

is needed to make a balanced Li-ion cell.

Therefore, 0.75 g of $LiCoO_2$ was placed in a stainless steel mould to which 13.8 MPa (2000 psi) was applied to produce an electrode pellet. Both carbon and TMO pellets were then transferred to the glove box and the cell was assembled as depicted in Figure 4.3. Electrolyte (1M $LiPF_6$ EC/DEC 33/67, vol/vol, Mitsubishi Chemicals) was first added to the TMO electrode until fully wetted and then three polypropylene separators were added on top of it, to which the carbon pellet was added. The cell can's top, with gasket, was added and the can was crimped shut. When the electrochemical cells were removed from the glove box, stainless steel tabs were spot-welded to the outer casing and the cell was then connected to the charger system. Due to the increased thickness of the electrode pellets, these electrochemical cells suffered from diffusion difficulties and thus through trial and error a charge/discharge current of 1 mA was selected to avoid lithium plating, which causes dendrites to form that may lead to the short-circuit of the cell. A variety of experiments were performed with the cells on the charger system to simulate a

variety of charging characteristics. After the tests were finished, the cells were transferred to an argon-filled glove box for ARC sample preparation.

Casing Top (Negative Terminal)

Gasket

Carbon Electrode

Separator (3)

LiCoO$_2$ Electrode

Casing Bottom (Positive Terminal)
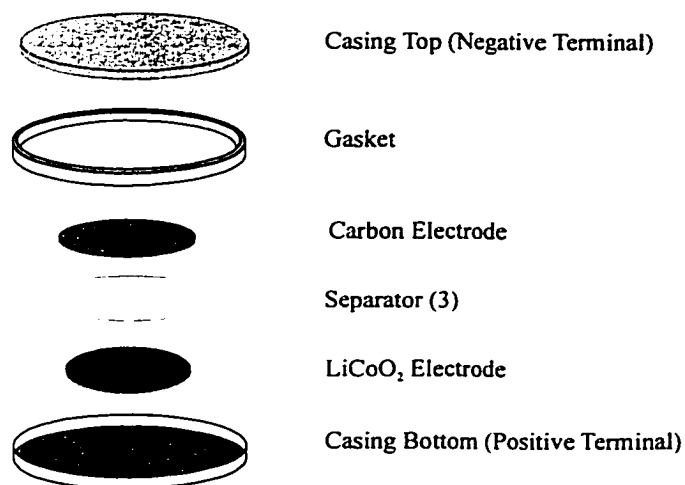
Figure 4.3 Exploded view of the construction of lithium-ion coin cells, for the production of charged cathode materials for analysis.

4.2 Accelerating Rate Calorimetry (ARC) Theory and Testing

4.2.1 Theory

Hazard evaluation is an area of study in which chemistry and engineering come together in an attempt to describe the factors causing, influencing and preventing an undesirable event. A thermal hazard is governed by the thermodynamics and chemical kinetics of the chemical reactions taking place in sample, process or storage container.

The accelerating rate calorimeter (ARC), initially developed by the Dow Chemical Company, but later commercialised by Columbia Scientific, was designed and marketed as an instrument that can investigate the kinetic aspects of the reactions as well as their heats of reaction [59, 60].

The operational principle of the ARC is simple - maintain a sample in adiabatic conditions once an exothermic reaction has been detected. A schematic of an ARC, as designed by Columbia Scientific, is shown in Figure 4.4. The sample bomb is mounted inside a nickel-plated copper jacket. The three heating-zones of the jacket; top, side, and

base, are each individually heated and monitored by Nicrosil/Nisil type N thermocouples referenced to an ice point reference. The calorimeter is enclosed in a 1" thick steel shell to provide a barrier in case of an explosion during the experiment. The shell also contains four micro-switches that must be depressed before any heat can be provided to the instrument.

Top Zone Thermocouple

Bomb Thermocouple

Top Zone Heaters

Sample Bomb

Jacket

Side Zone Heaters

Side Zone Thermocouple

Bottom Zone Thermocouple

Bottom Zone Heaters
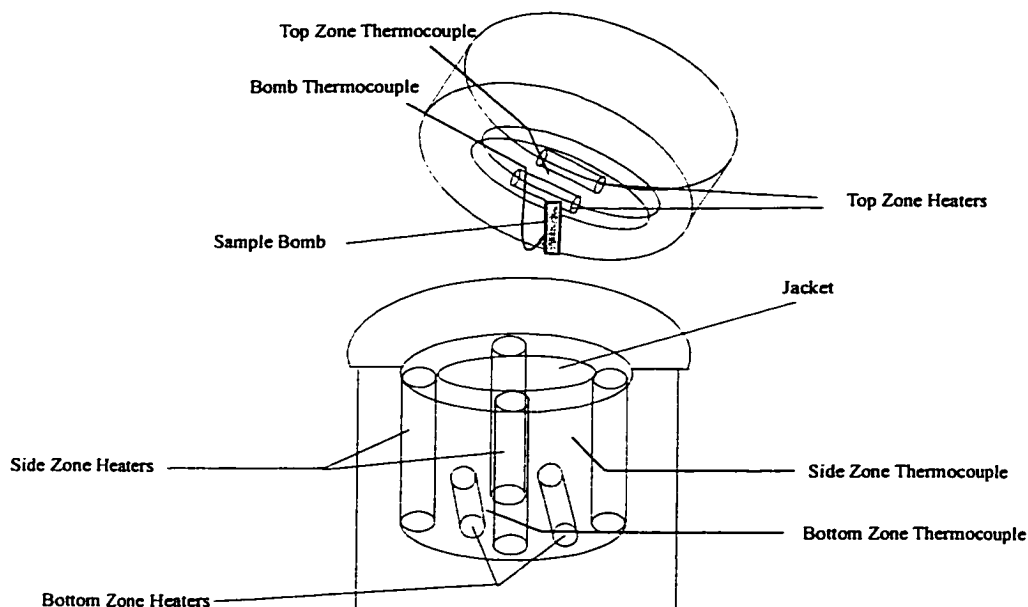
Figure 4.4 Schematic of the Accelerating Rate Calorimeter (ARC, from Columbia Scientific).

The ARC processor executes the desired measuring program and controls the heating of the copper jacket. The heating method produces a quasi-adiabatic environment. A slight drift from adiabaticity will occur when the thermocouples are slightly mismatched. Performing a calibration run corrects for this mismatch. With a calibration performed, the ARC can maintain adiabatic conditions throughout its operational range and measure the self-heating profiles of different samples.

The ARC is operated in a heat-wait-search (HWS) mode which entails heating the environment (jacket) to a desired temperature, waiting for a set time such that thermal equilibrium between the jacket and the sample can be achieved. After equilibrium, the processor then searches for a temperature increase greater than or equal to the set sensitivity (usually 0.02°C/min). If the rate is less than the sensitivity after the search

period, the ARC will proceed to the next temperature step and this HWS sequence continues until an exotherm is detected or the stop temperature is reached. If an exotherm is detected, the ARC will track it by maintaining adiabatic conditions until the completion of the exotherm.

The change in temperature, ΔT (K), of the calorimeter during analysis is proportional to the thermal energy released during the exothermic process [61]. The amount of thermal energy, q (J), released for a particular reaction is proportional to the total specific heat of the reactant(s) and bomb (sample), c_{tot} ($JK^{-1}g^{-1}$), and the mass of reactant(s) and bomb present, m_{tot} (g). These relationships combine to give

$$q = c_{tot} m_{tot} \Delta T, \qquad (4\text{-}3)$$

which governs all reactions taking place in the ARC. Equation 4-3 is identical to the total heat capacity, C_{tot} (JK^{-1}), of the sample multiplied by the change in temperature. For a multi-component mixture the total heat capacity of the mixture is equal to the sum of the individual heat capacities

$$\text{total heat capacity} = \Sigma \text{ individual heat capacities} \qquad (4\text{-}4)$$

$$C_{tot} = m_{tot} c_{tot} = \sum_i m_i c_i \qquad (4\text{-}5)$$

where m_i is the mass of component i and c_i is its specific heat. Rearranging equation 4-3 and solving for temperature and taking the derivative with respect to time gives the self-heating rate of the reaction,

$$\frac{dT}{dt} = \frac{dq}{dt} \frac{1}{c_{tot} m_{tot}}. \qquad (4\text{-}6)$$

The variation in self-heating rates with electrode materials, temperature and conditions is a very important aspect of this investigation.

4.2.2 ARC Testing Method

The sample holders (bombs) supplied with the ARC were inappropriate for the analyses performed here. The mass of the testing electrodes was such that it would have been difficult for these samples to produce enough heat to overcome the thermal mass of the provided bombs without developing larger electrode preparation procedures. In

addition, the provided sample bombs were difficult to load with a solid sample. Monique Richard developed a convenient method of measuring the self-heating of a small amount of electrode material in electrolyte [57]. Her procedure was the backbone for the method given below, but with some modifications to improve the speed and ease of analysis. The new sample holders consisted of a 39.1 mm (1.54") long stainless steel type 304 tube. The stainless steel tubing was 6.35 mm (0.250") in diameter with a 0.152 mm (0.006") wall thickness and contained a stainless steel pocket welded to its side. The ends of the sample tubes were then sealed in an argon-filled glovebox by Tungsten Inert Gas (TIG) welding within the confines of a large copper block (heat sink).

The samples to be analysed (anode and cathodes) were obtained by carefully disassembling the electrochemical cells in the glove box and the desired pellet(s) were recovered. The wet pellet was then lightly ground and transferred to the ARC sample bomb. One end of the bomb had been previously welded shut by Tungsten Inert Gas (TIG) welding. Typically, 350 mg of the wet electrode was transferred, with an equal amount of excess electrolyte added to the bomb. The bomb was then crimped closed and finally TIG welded shut. The amount of actual electrode transferred to the sample tube varied slightly from sample to sample, depending on the capability of the sample to absorb electrolyte. For example, the carbon fibre pellets are less dense and therefore contain more electrolyte than the other carbon types. For the cathode samples approximately 20% electrolyte was absorbed on the electrode before ARC analysis.

During the course of this thesis a rinsing procedure for the cathode samples was developed to remove the original electrolyte from the electrode. A portion of the wet charged electrode powder was placed into a centrifuge tube. To that tube a portion of dimethyl carbonate (DMC), a volatile organic solvent, was added and the tube was then shaken by hand. The tube was then placed in a centrifuge, within the glovebox, and spun at 10000 rpm for 5 minutes. The sample was decanted and the DMC rinsing procedure was repeated. After the second decanting, the sample was placed in the anti-chamber of the glovebox and placed under vacuum to remove the DMC solvent. After 1 hour of vacuum, the sample was returned to the glovebox where ARC samples could be prepared. These ARC samples could be run dry (as is) or they could have an amount of solvent or

electrolyte added to the ARC sample tubes, before TIG welding the samples shut and removing them from the glove box for analysis.

The ARC samples were mounted in the calorimeter by hooking the pocket of the stainless steel tube over the thermocouple (Figure 4.5). The calorimeter was then sealed and a variety of runs were performed.
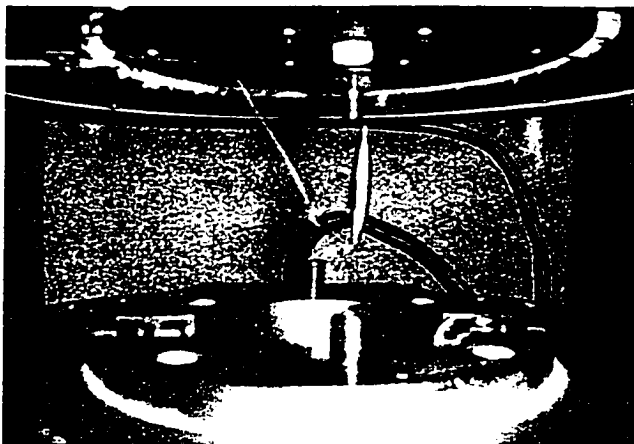
Figure 4.5 Sample mount inside the ARC.

4.3 Differential Scanning Calorimetry (DSC) Theory and Testing

4.3.1 Theory

Differential Scanning Calorimetry (DSC) is a technique in which the heat-flow rate (power) to the sample is monitored against time or temperature while the temperature of the sample is programmed [62]. This technique allows for the investigation of both endothermic (heat absorption) or exothermic (heat liberation) processes. The DSC used throughout this thesis is a heat flux DSC (model 910) from Du Pont. In a heat flux DSC, the heat flowing from or being absorbed by a sample as it is heated or cooled is compared to the heat flow into or out of a reference material that is at the same temperature as the furnace (Figure 4.6) [62]. When the steady state equilibrium is disturbed by a sample transition, a signal is generated which is proportional to the difference between the heat flow rates to the sample and to the reference sample. Many of the DSC results serve to enhance the information available from ARC measurements, to verify reaction

mechanisms, or to qualitatively compare the onset temperature and peak power of various cathode materials for lithium-ion batteries.
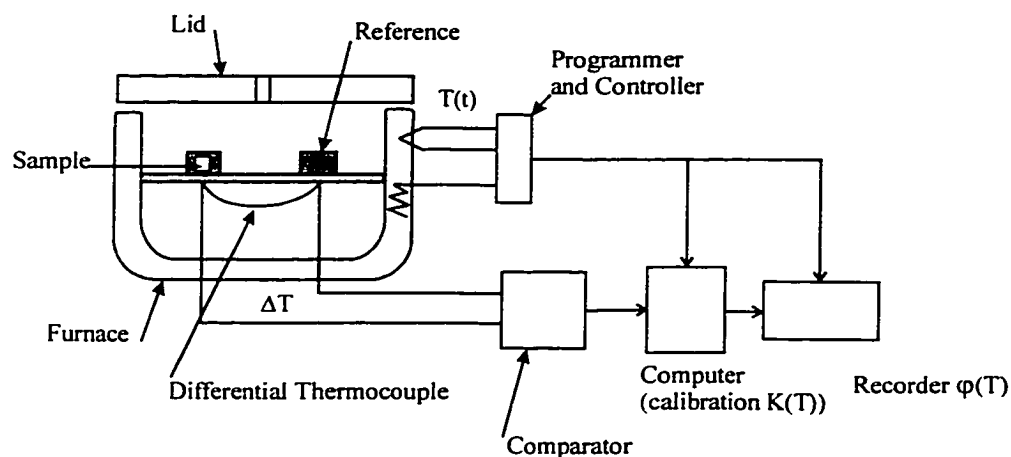
Figure 4.6 Schematic of the Differential Scanning Calorimeter (DSC).

4.3.2 DSC Testing Methods

Differential Scanning Calorimetry (DSC) testing was performed on a Du Pont 910 DSC using Ultra High Purity (UHP 99.999%) argon gas as the flow gas at a rate of approximately 1.5 cm^3s^{-1}. Many of the samples analysed during the course of this thesis were air and moisture sensitive and thus they were sealed in DSC sample pans in an argon-filled glovebox. The samples were measured on the DSC at a variety of temperature scan rates and to a variety of end point temperatures described in the pertinent figures. When the heats of reaction were calculated (area underneath DSC trace), the method of masses was used. The area underneath the DSC curve of power (W/g) versus time (s) was determined by taking the ratio of the masses of the peaks as compared to the whole graph [63].

All DSC graphs shown in this thesis do not use the convention adopted by IUPAC for the presentation of thermal data. I have decided to display these plots according to the convention in safety reports on lithium-ion battery electrodes. Thus the convention used in this thesis is that exothermic events have an upward deflection, while endothermic events have a downward deflection from the baseline and the temperature scale will be shown as degrees Celsius.

During the initial work in this thesis, DSC samples were analysed in hermetic Al DSC pans from TA Instruments (part # 900794.901 (lids) and 900793.901 (pans)), while the reference material was an empty pan. Those initial DSC experiments were very limited due to the inability to contain high pressure and thus any gaseous products (gases).

A new sample pan was developed based on the sample bombs used in ARC testing. The new DSC sample cell consists of a 3.14 mm (0.125") outer diameter stainless steel, type 304 seamless tube having a wall thickness of 0.015mm (0.006") (MicroGroup, Medway, Mass.). The stainless steel tubing was cut into 8.8 mm (0.35") long pieces, but these can be longer if desired. These new sample cells, see Figure 4.7, are inexpensive (50¢ each). The sample cells are cleaned and have one end flattened. The flattened end is then welded shut by TIG welding. The welding of the sample tube is performed with the sample contained within a large copper block as a heat sink. Figure 4.8 shows the sample within the confines of the copper block. The slot at the top of the block is just large enough to accommodate the cell within a recess with thin jaws (1 mm thick) at the top. The jaws of the block are then clamped together to ensure good contact to the heat sink (copper block) and the cell is ready to be welded. The TIG welding is performed under a flow of Ar and essentially melts the end of the tube together. Typical welding conditions were DC currents between 2 and 5 amps at voltages below 15 V, once the arc was started. Typical weld times were under 2 seconds.
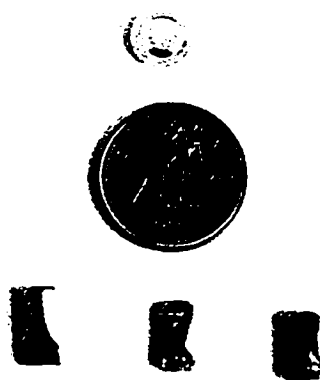
Figure 4.7 Comparison between conventional hermetic Al DSC pans and the new stainless steel welded DSC pans. A Canadian 10 cent piece showing the famous "Bluenose" is shown for size comparison.
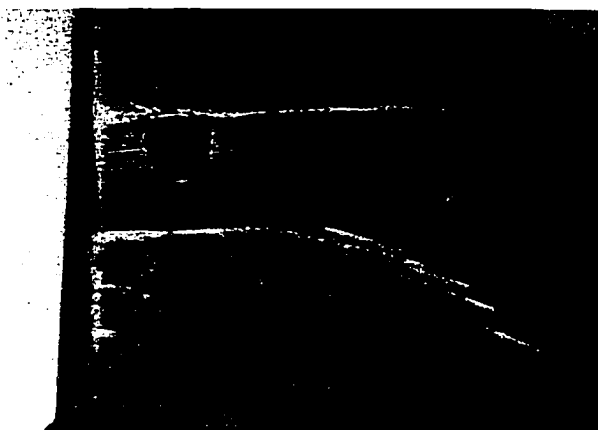
Figure 4.8 Sample pan placed in the pocket of the large copper block (heat sink) prior to welding.

With one end of the sample cell sealed, the desired sample was placed into the tube. The sample cell can contain liquid, a solid or a combination of both. When the sample had been loaded, the tube was crimped and welded shut. Concerns about the generated temperatures during the welding process led to an estimate for the amount of heat generated in a "worst-case" scenario. Let us assume that all the electrical power supplied by the welding was added as heat to the end of the sample tube that protrudes above the jaws. This assumption neglects the fact that some power will be dissipated to the atmosphere and that the welding process is not 100% efficient. Figure 4.9 gives a sketch of the heat flow during the weld operation. The welding of the sample tube was performed at a maximum of 15 V and 5 A, for a total power of 75 W, for a duration of approximately 2 s. Using a simple equation for thermal conduction through a bar of length Δx and cross-sectional area, A [64];

$$\Delta T = \frac{\Delta x}{kA} I , \qquad (4\text{-}7)$$

where k is the thermal conductivity of the bar and I is the thermal current (in watts), the temperature increase, ΔT, during welding can be calculated.

Assume a steady state condition with 75 W being input at the sample side of the jaws, and the block side of the jaws at room temperature. This is a generous estimate because the weld time was only 2 s. Using the dimensions given in Figure 4.9 and the room temperature thermal conductivity of copper ($401 \ Wm^{-1}K^{-1}$), a temperature increase

of about 35 K would be predicted for the sample in a "worst case" scenario. Thus, the sample holder will certainly remain below 60°C during welding.
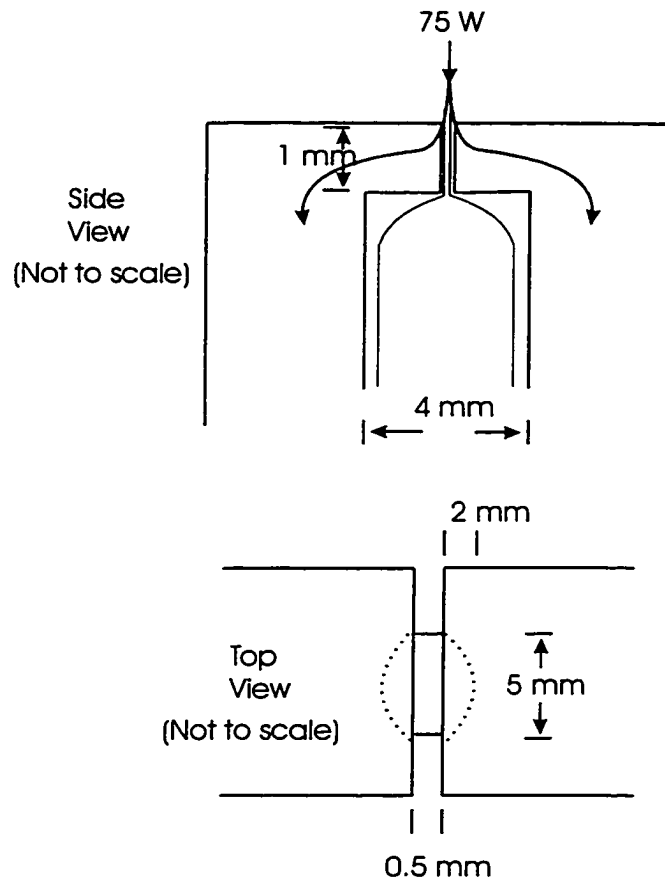
Figure 4.9 Sketch of heat sink block design showing the direction of heat flow during the welding step (not to scale).

Once sealed, the sample cell was weighed and analysed in the DSC with no special adapters or holders required. The stainless steel sample cells, shaped like a miniature pillow, sit on the same spots in the DSC head as the previous sample cells. The maximum pressure the new sample cell can contain was not calculated, but a large number of experiments on thermally unstable liquids with a mass of up to 15 mg have been performed with no explosion of the DSC sample cell. Experience with the larger ARC sample bombs has shown that cell explosions occur in the middle of the tube showing that the weld is not a point of weakness. To verify there were no leaks in the sample cell, its mass was determined before and after analysis. Only those runs showing no weight loss were used for data analysis.

The thermal conductivity of stainless steel is much lower than that of Al [65]. This lower thermal conductivity facilitates the welding of the sample cell without heating the sample, but might also cause changes in the DSC signal due to inefficient heat transfer at the programmed heating rate. Thus the application of these cells may be limited to low heating rates. To test the effect of the stainless steel pan on the response of the DSC, a typical standard for high temperature work, tin, was used. A 10 mg sample of tin (99% pure, Aldrich) was placed in an Al sample pan and then hermetically sealed. The sample was then heated at 10 °C/min to above its melting temperature, to record the shape and location of the endotherm. The experiment was then repeated, after cooling to room temperature, but at 2 °C/min. The same type of experiment was performed but in the newly designed stainless steel DSC sample cells and 13 mg of tin was used. The results of the two experiments are shown in Figure 4.10. The results for the two sample cells are practically identical and thus the lower thermal conductivity of the stainless steel does not affect the response of welded DSC at least up to 10 °C/min.
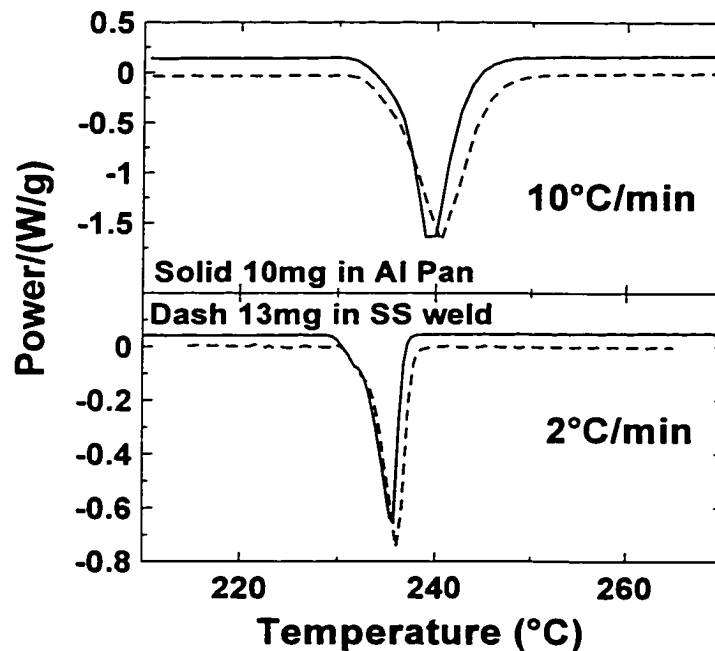
Figure 4.10 Comparison between the endothermic melting peaks of Sn measured in the welded stainless steel sample pan (dashed line) and in a conventional hermetic Al DSC pan (solid line).

These new sample pans are most useful when analysing solids or liquids that decompose or partake in reactions that produce gaseous products at high temperature, since these samples produce high pressures that are difficult to contain. To demonstrate the performance of these new sample cells, a small portion of di-t-butyl peroxide (DTBP, Aldrich) was sealed in stainless steel sample cells and analysed under a variety of heating rates. These profiles were then compared to samples of DTBP, sealed in hermetic Al DSC pans, under the same conditions. The results of these experiments are shown in Figure 4.11. All of the profiles for the samples contained within the hermetic Al DSC pans, except one, contain sharp downward (endothermic, indicating evaporation) peaks, which indicate the liberation of the generated gases from the decomposition of DTBP. Indeed the mass of the cells before and after the DSC run in Al pans had changed. The samples measured in the welded stainless steel tubes exhibit only one peak that moves in a fashion typical for non-isothermal DSC experiments at various heating rates [66]. The sample holders did not leak. Figure 4.11 demonstrates the clear advantage in using welded sample containers for DSC analysis of thermally unstable liquid specimens.
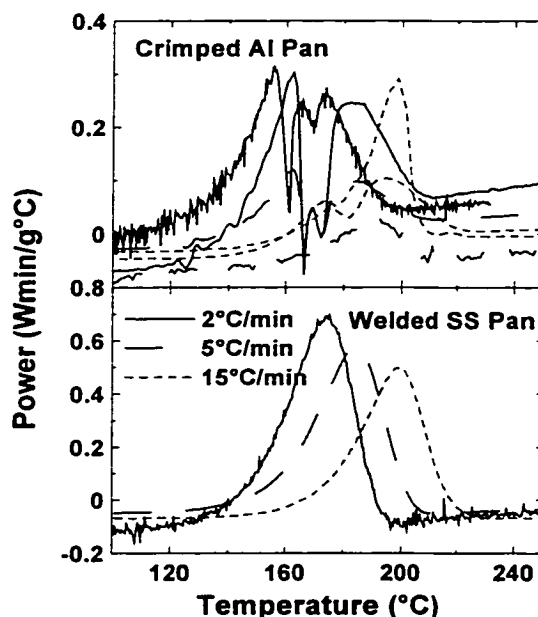
Figure 4.11 Comparison of the thermal decomposition of di-t-butyl peroxide (DTBP) measured in hermetic Al DSC pans and in welded stainless steel pans at various heating rates (2, 5, 15 °C/min). Evolved power has been divided by the heating rate to present the results clearly on the same axis.

4.4 Other Techniques

4.4.1 X-ray Diffraction

X-ray diffraction was the main technique used to explore the atomic and crystalline structure of each sample under study. It was used to compare the structure of the sample before thermal events to its structure after thermal events in order to help determine the mechanism of the reaction. X-ray diffraction was also used to fully characterise the initial samples.

In 1912, Max von Laue suggested that x-rays might be diffracted when passed through a crystal since x-rays have wavelengths similar to the distances separating atomic planes in a crystal. Consider a plane of atoms as a mirror, and that a crystal can be modelled by a stack of these atomic planes with a separation of length d (Figure 4.12). The path-length difference of the two rays shown in Figure 4.12 is,

$$AB + BC = 2d \sin \theta , \qquad (4-8)$$

where θ is the glancing angle, AB and BC are the length between point A and B and between point B and C, respectively. When the path-length is an integral multiple of wavelengths, λ, (AB + BC = nλ), the reflected waves are in phase and interfere constructively. Thus constructive interference will be observed when

$$n\lambda = 2d\sin(\theta) , \qquad (4-9)$$

is satisfied. Equation 4-9 is known as the Bragg law, where $n = 1, 2, 3...$ correspond to path-length differences of 1, 2, 3... wavelengths [61].
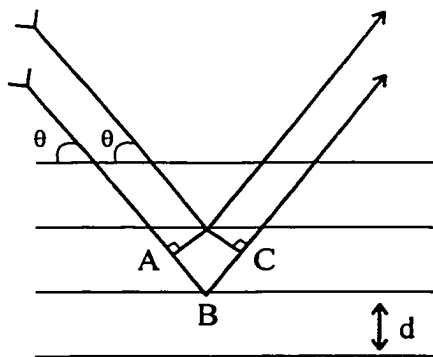
Figure 4.12. Derivation of the Bragg Law.

The x-ray diffraction measurements were made using a Siemens D5000 diffractometer equipped with a copper target x-ray tube and a diffracted beam monochromator. The cumulative intensity for a specified count time was measured for 0.05° steps. For carbon samples the region of interest was a diffraction angle between 20 and 30°, since this is where the 002 diffraction peak in graphite occurs [67].

The intercalation of lithium into graphite occurs in a variety of stages and, as more and more lithium is intercalated, the 002 diffraction peak moves to a substantially lower angle [67]. The change in peak location can be used to determine the amount of lithium consumed during the self-heating reaction [68].

Cathode samples were also analyzed by x-ray diffraction in a similar manner except that the samples were monitored between a diffraction angle of 10 and 70°. The lattice parameters of Li_xCoO_2, as a function of x are well known [69]. Both cathodes and anodes were believed to be moisture sensitive and thus had to be mounted in a specially designed sample holder (see Figure 4.13) [57]. The holder has a specially cut silicon wafer placed in a well on a stainless steel base. The silicon wafer has been cut such that no diffraction pattern arises from the wafer and thus it is a perfect zero background holder. The x-ray sample is placed on this holder and a 0.25 mm thick, 2.54 cm x 2.54 cm beryllium window (certified leak tight) is placed on top of the surrounding o-ring. An aluminum top is then screwed tightly into the base causing the beryllium window to seal the contents inside the o-ring from the environment.

Figure 4.13 X-ray diffraction sample holder for air and moisture sensitive samples.

4.4.2 Surface Area Measurements

Single-point Brunauer-Emmett-Teller (BET) surface area measurements were performed on each sample using a Micromeritics Flowsorb II 2300 surface area analyzer. The amount of gas adsorbed on the surface of the sample is a measure of its surface area. The sample was placed in a U-shaped tube, weighed and degassed at 130°C overnight and 250°C for 30 minutes prior to the test to remove any volatile impurities. The sample was in a constant flow of a helium/nitrogen gas mixture (70/30 mol %) and was immersed in liquid nitrogen for adsorption. After equilibration, the sample was quickly warmed to room temperature by placing the tube in water which resulted in desorption of the adsorbed layer from which the single-point BET measurement was taken. This measurement was obtained from the difference in the concentration of nitrogen in the gas flow, before and after the sample, as measured by thermal conductivity cells. Assuming a constant flow rate, the difference is integrated to determine the volume of nitrogen desorbed from the sample.

4.4.3 Scanning Electron Microscopy (SEM)

To obtain an understanding of the differences in the morphology in each of the carbon samples a SEM image was produced for each of the carbon samples. The images were taken on a JEOL JSM-35CF electron microscope.

Chapter 5

Reaction Kinetics

5.1 Introduction

When a reactant is converted to products by a single-step thermally induced reaction, it is common to write

$$\frac{d\alpha}{dt} = k(T) f(\alpha), \qquad (5-1)$$

where t is the time, T is the temperature and α is the fractional degree of conversion of reactants ($0 \leq \alpha \leq 1$). It is common to assume that the temperature dependence of the rate constant $k(T)$ can be separated from the reaction model, $f(\alpha)$, and that

$$k(T) = \gamma\, e^{-\frac{E_a}{k_B T}}, \qquad (5-2)$$

where E_a is the activation energy, k_B is Boltzmann's constant and γ is the frequency factor [61]. The reaction model, $f(\alpha)$, can be derived from a number of physical situations and examples are given in Table 5.1 [70]. The table contains a column for the reaction model type, a column for the differential equation describing the extent of conversion and columns used to describe exponents in a "universal" equation for the thermal decomposition of solids [70],

$$\frac{d\alpha}{dt} = k\alpha^m (1-\alpha)^n (-ln(1-\alpha))^p. \qquad (5-3)$$

The variables in Equation 5-3 can be chosen to describe most solid thermal decomposition mechanisms from simple n^{th}-order to diffusion-controlled reactions. In order to describe the reaction kinetics accurately, it is necessary to determine the "kinetic triplet", $f(\alpha)$, E_a and γ. This chapter will describe different methods used to determine the kinetic triplet with the two thermal analysis instruments (ARC and DSC) used during this

43

thesis and the method I have developed to perform a kinetic analysis on $LiCoO_2$ in the presence of 1M $LiPF_6$ EC/DEC, exposed to elevated temperatures and charged to 4.2V.

Table 5.1. Reaction models typically applied to describe the thermal decomposition of solids [57].

	Reaction Model	$\dfrac{d\alpha}{dt} =$	$k\alpha^m(1-\alpha)^n(-\ln(1-\alpha))^p$		
			m	n	p
1	One-dimensional diffusion	$k\alpha^{-1}$	-1	0	0
2		$K\alpha$	1	0	0
3	Power law	$k\alpha^{1/2}$	0.5	0	0
4	Power law	$k\alpha^{2/3}$	0.6667	0	0
5	Power law	$k\alpha^{3/4}$	0.75	0	0
6	Zero order	k	0	0	0
7	Contracting sphere	$k(1-\alpha)^{2/3}$	0	0.6667	0
8	Contracting cylinder	$k(1-\alpha)^{1/2}$	0	0.5	0
9	First order (n[th] order)	$k(1-\alpha)$	0	1	0
10	Second order (n[th] order)	$k(1-\alpha)^2$	0	2	0
11	Avrami-Erofeev	$k(1-\alpha)(-\ln(1-\alpha))^{1/2}$	0	1	0.5
12	Avrami-Erofeev	$k(1-\alpha)(-\ln(1-\alpha))^{2/3}$	0	1	0.6667
13	Avrami-Erofeev	$k(1-\alpha)(-\ln(1-\alpha))^{3/4}$	0	1	0.75
14	Autocatalytic	$k\alpha(1-\alpha)$	1	1	0
15	Two-dimensional diffusion	$k(-\ln(1-\alpha))^{-1}$	0	0	-1
16	Diffusion controlled	$k(1-(1-\alpha)^{1/3})^{-1}(1-\alpha)^{2/3}$			
17	Diffusion controlled	$k((1-\alpha)^{-1/3}-1)^{-1}$			

5.2 Differential Scanning Calorimetry (DSC)

There have been numerous procedures developed to determine reaction kinetics from differential scanning calorimeter experiments operated in the temperature scan mode [70, 71]. However, significant care must be taken to ensure that the kinetic triplet obtained from an analysis of DSC results is meaningful [72, 73]. Typically, the kinetic triplet has been determined by fitting (optimizing activation energy and frequency factor) alternative reaction models to a single or a series of differential scanning calorimeter (DSC) experiments. The kinetic triplet giving the lowest residual was then selected as representative of the reaction, even though other reaction models may have had fits of slightly higher residual with values of activation energy and frequency factor that differed by a factor of four and several orders of magnitude, respectively. For example, Vyazovkin and Wight [72] showed that fitting models to experiment can lead to a variation in E_a and $\ln(\gamma)$ of a factor of four, depending on the model chosen, with little change in the residual of the fit (see Table 3 in ref. [72]). It is clear that a reliable discrimination between the possible reaction models using non-isothermal DSC is rarely possible. Early methods for determining reaction kinetics from DSC experiments have been found to accurately reproduce the kinetic behaviour of the sample, if the reaction model of the sample is already known [74.75].

During the development of the new DSC sample holder, described in Section 4.3.2, a kinetic analysis of the thermal decomposition of di-t-butyl peroxide was performed. Di-t-butyl peroxide (DTBP) has been widely studied as a cetane improver in diesel fuels [76]. These cetane improvers are used to improve the ability of the fuel to autoignite in the combustion chamber of a diesel engine and thus the thermal decomposition of DTBP has been studied extensively [77]. A wide variety of kinetic parameters have been determined depending on the method used for analysis but all have concluded a first-order decomposition mechanism [78]. A summary of Arrhenius parameters from the literature for DTBP is given in Table 5.2. Since the mechanism of decomposition for DTBP was well known from previous classical gas phase kinetic

work, the above DSC kinetic analysis techniques were ideal to test the DTBP samples and thus the new sample holder.

Table 5.2. Summary of the Arrhenius parameters reported for di-tert-butyl peroxide.

E_a (kJ/mol)	γ, s^{-1}	Conditions	Ref
144-151		Cumene solution	78
148	1.40×10^{16}		79
163	2.80×10^{16}	Gas phase	80
154	1.30×10^{15}	DSC, mineral oil	81
158	2.30×10^{16}	ARC, mineral oil or toluene	81
122	3.20×10^{11}	DSC, 725 psi	82
158	6.47×10^{15}	Gas phase "best" literature average	83
136	7.36×10^{12}	0.1M in diesel fuel	84
148	7.39×10^{14}	Neat	76
140	5.50×10^{13}	Neat	This study

In a DSC experiment, the generated power per unit mass and time for a first-order decomposition is

$$P = H \, \gamma \, \exp(-E_a/k_B T) \, (1-\alpha), \quad\quad\quad (5\text{-}4)$$

where H is the total heat generated by the reaction per gram of reactant, and the other variables are as described above [62]. Using the results for the welded samples in Figure 4.11, a least squares fit to the three data sets (at different temperature scan rates) was performed to obtain the best-fitted Arrhenius parameters [85]. The results of this fitting to the normalized power are shown in Figure 5.1. The analysis gave an activation energy of 140 kJ/mol and a frequency factor of 5.50×10^{13} s^{-1}, which is in good agreement with the results published in the literature as listed in Table 5.2.

Differential scanning calorimeters can also be operated in an isothermal mode. The classical techniques of chemical kinetics can then be used. Here, a quasi-isothermal DSC mode was used to confirm a proposed reaction model. The isothermal experiment consisted of heating the DSC sample at a rate of 2°C/min until it reached a temperature where an exothermic process occurred. After reaching the set temperature the

calorimeter would then switch from the temperature scan mode to the isothermal mode and monitor the power required to maintain the sample at a constant temperature (isotherm).
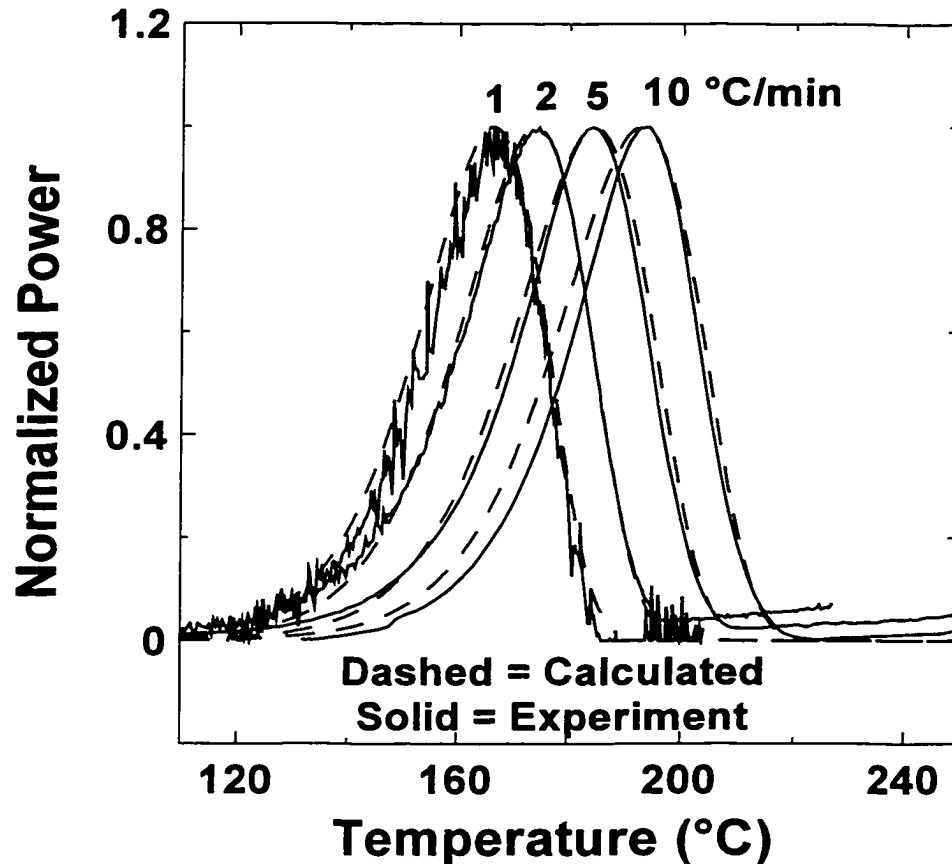
Figure 5.1. Comparison of calculation (dashed line) and experiment (solid line) for the thermal decomposition of di-t-butyl peroxide (DTBP) at the indicated heating rates (1, 2, 5, 10 °C/min).

5.3 Accelerating Rate Calorimetry (ARC)

The information available from adiabatic calorimetry, such as accelerating rate calorimetry (ARC), can be classified into two groups: a) thermodynamic information; and b) kinetic information. The ARC has been typically used as a method to determine thermodynamic parameters, such as adiabatic temperature rise and heats of reactions [59, 60].

The amount of published work on kinetic analyses with the ARC is not abundant and limited to simple one-component systems, such as DTBP [59, 60]. Most kinetic treatments of adiabatic calorimetry results assume a reaction model to calculate the kinetic parameters, and the proper parameters are chosen based on the goodness of fit between the experiment and model [62, 86].

New methods for determining reaction kinetics from the ARC have been introduced. Sempere et al. developed a method based on the change in self-heating rate with respect to the change in the thermal inertia (Φ factor, phi-factor) of the sample. The phi-factor is defined as [86],

$$\Phi = \frac{m_s c_{ps} + m_c c_{pc}}{m_s c_{ps}}, \tag{5-5}$$

where m_s and m_c are the masses of the sample and the mass of the cell respectively, while c_{pc} and c_{ps} are the specific heat of the cell and sample respectively. Although this kinetic method does not assume a particular reaction model, its ability to discern different reaction models is not very effective (see Figures 7 and 8 in ref. 85).

5.4 Discerning Reaction Mechanisms using a Combination of ARC and DSC

In order to have confidence in predicting the outcome of unexplored thermal events, an experimental method that probes the relevant reactions over a wide temperature range is needed. Furthermore, a kinetic triplet that can fit all these experimental results satisfactorily is required. The difficulty with determining the kinetic triplet using only DSC results is that the shape of DSC profiles are not strongly dependent on the choice of reaction model. In particular, a single DSC trace of a single-step reaction can be fitted quite closely for most choices of $f(\alpha)$, provided that the choice of E_a and γ is arbitrary. If several DSC experiments are available at very different sweep rates, then the kinetic triplet can be more tightly determined [72]. Selecting kinetic parameters and models from the analysis of DSC peak shapes has been reviewed elsewhere (see Baider Ceipidor et al. and references therein, [87]), but again the selection

of the most suitable kinetic triplet was often determined by the fit to experiment having the smallest sum of residuals.

The shape of accelerating rate calorimeter (ARC) profiles (self-heating rate versus temperature) is very sensitive to the choice of $f(\alpha)$. This has been discussed by Sempere et al. [86] for a limited number of functions of $f(\alpha)$ (see Figure 3 in [86]). Accelerating rate calorimetry has a number of advantages over DSC analysis, because the ARC has a detection limit of 0.02 °C/min that effectively corresponds to a sweep rate that is 50 times lower than conveniently obtainable by DSC. This lower effective sweep rate gives rise to a much larger range over which exothermic reactions can be analysed and the kinetic triplet tested. Thus, including ARC results in any kinetic analysis allows for a stringent test of any proposed reaction model.

In an ARC experiment, the self-heating rate is given by

$$\frac{dT}{dt} = \frac{h}{C_{tot}} * \frac{d\alpha}{dt} , \qquad (5\text{-}6)$$

where h is the total heat which can be evolved by the sample due to the reaction (Joules) and C_{tot} is the total heat capacity of the reactants and the sample bomb (JK^{-1}). h/C_{tot} corresponds to the temperature rise, ΔT, from the onset of the exotherm to the end of the exothermic behaviour because;

$$\int_0^\infty \frac{dT}{dt} dt = \Delta T , \text{ and} \qquad (5\text{-}7)$$

$$\int_0^\infty \frac{h}{C_{tot}} \frac{d\alpha}{dt} dt = \frac{h}{C_{tot}} \Delta\alpha = \frac{h}{C_{tot}} , \text{ and} \qquad (5\text{-}8)$$

since $\Delta\alpha = 1$ for the complete consumption of the reactant, thus,

$$\Delta T = \frac{h}{C_{tot}} . \qquad (5\text{-}9)$$

To estimate the activation energy and frequency factor of the self-heating process, the following equation was used for the initial self-heating rate (from Equations 5-6 and 5-9),

$$\frac{dT}{dt} = \Delta T k(T) f(\alpha_o) . \qquad (5\text{-}10)$$

Taking the natural logarithm of both sides, gives

$$\ln(\frac{dT}{dt}) = \ln(\gamma \Delta T f(\alpha_o)) - \frac{E_a}{k_B T}, \qquad (5\text{-}11)$$

where the substitution for the rate constant, k (Equation 5-2), has been made. Hence, a plot of the natural logarithm of the initial self-heating rate versus 1/T (an Arrhenius plot) has a slope related to the activation energy, E_a, of the process and an intercept related to the frequency factor, γ.

In a DSC experiment, the generated power is

$$P = H \, d\alpha/dt, \qquad (5\text{-}12)$$

where H is the total heat generated by the reaction per gram of reactant and α and t are as described above.

The strength of using a combination of both ARC and DSC profiles to determine a kinetic triplet can be seen by a comparison of ARC and DSC curves for various reaction models. The comparison was performed with the following restrictions. First, E_a was selected to be 1.6 eV, which was close to that of experiments on $Li_{0.5}CoO_2$, as will be shown in Chapter 7. Next, γ was selected so that the ARC simulation would produce a measurable self-heating at 140°C. Finally, α_o was selected to be 0.001 for most simulations. Table 5.3 lists the values of the parameters used for the simulations of the reaction models given in Table 5.1.

The ARC and DSC profiles for a typical zero-order reaction are shown in Figure 5.2. The start points for the ARC calculations were 140, 150, 160 and 170°C, and the DSC sweep rates were 1, 2, 5, and 15 °C/min. In a zero order reaction, the consumption of reactants does not affect the reaction rate until they are completely consumed ($\alpha = 1$), thus both DSC and ARC profiles increase until they abruptly stop. The dashed line through the start points of the ARC experiments is called the "Arrhenius line" here, since these points are used in an Arrhenius plot to determine E_a.

Table 5.3. Parameters used to calculate ARC and DSC profiles for the reaction models of Table 5.1.

Reaction Model	E_a (eV)	γ (min^{-1})	α
1	1.6	5×10^{15}	0.001
2	1.6	5×10^{18}	0.001
3	1.6	5×10^{17}	0.001
4	1.6	5×10^{17}	0.001
5	1.6	8×10^{17}	0.001
6	1.6	5×10^{16}	0.001
7	1.6	5×10^{16}	0.001
8	1.6	5×10^{16}	0.001
9	1.6	5×10^{16}	0.001
10	1.6	5×10^{16}	0.001
11	1.6	5×10^{17}	0.001
12	1.6	5×10^{17}	0.001
13	1.6	5×10^{17}	0.001
14	1.6	5×10^{18}	0.001
15	1.6	5×10^{15}	0.001
16	1.6	5×10^{15}	0.001
17	1.6	5×10^{15}	0.001
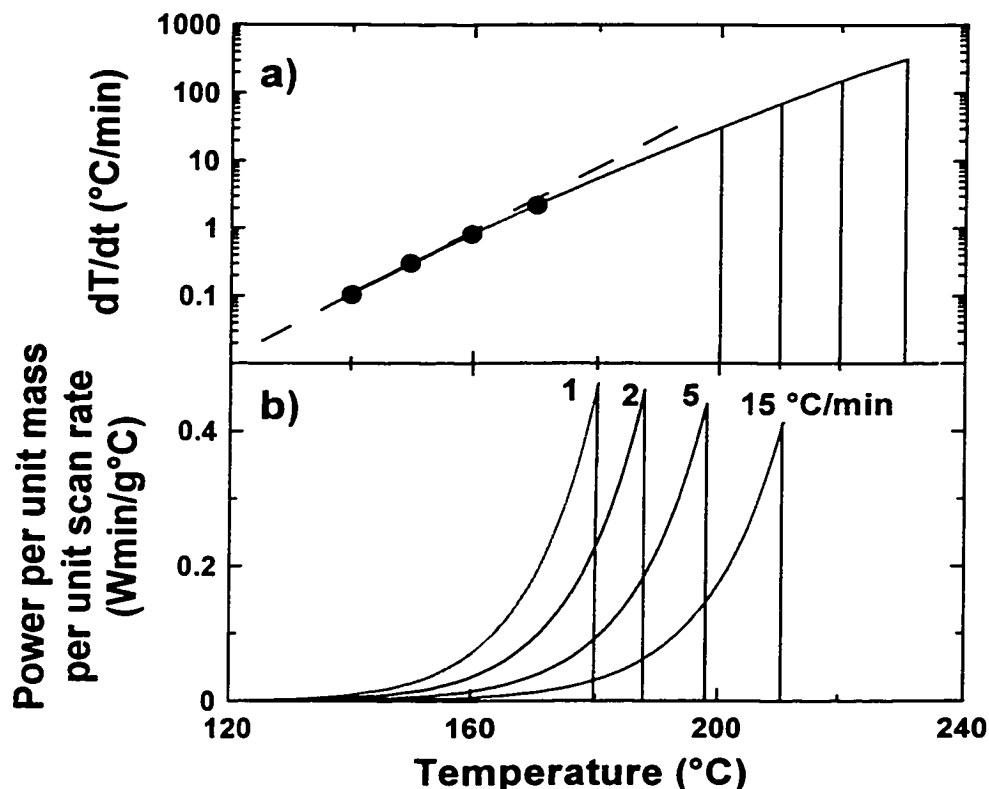
Figure 5.2. Calculated a) ARC and b) DSC profiles for zero order kinetics (model 6 in Table 5.1) using the parameters for model 6 in Table 5.3. The large circles in a) indicate the start point of the ARC calculations. A value of $h/C_{tot} = 60$ °C was used in a) and $H =$ 270 J/g in b). The scan rates in b) were 1, 2, 5 and 15 °C/min. The dashed line in a) is the "Arrhenius line" described in the text.

Figure 5.3 shows ARC and DSC profiles for a first-order reaction. The DSC curves display a bell-shaped appearance, while the ARC profile deviates to the right of the "Arrhenius line". When the order of the reaction was increased (e.g. model 10 in Table 5.1) the shapes of the DSC and ARC profiles remained approximately the same except that the DSC trace became broader (half width increases) and the ARC trace had a greater deviation from the "Arrhenius line". When the order of the reaction was decreased (model 7 in Table 5.1) the shapes of the DSC and ARC profiles remained approximately the same except that the DSC trace became narrower (half width decreases) and the ARC profile was closer to the "Arrhenius line".
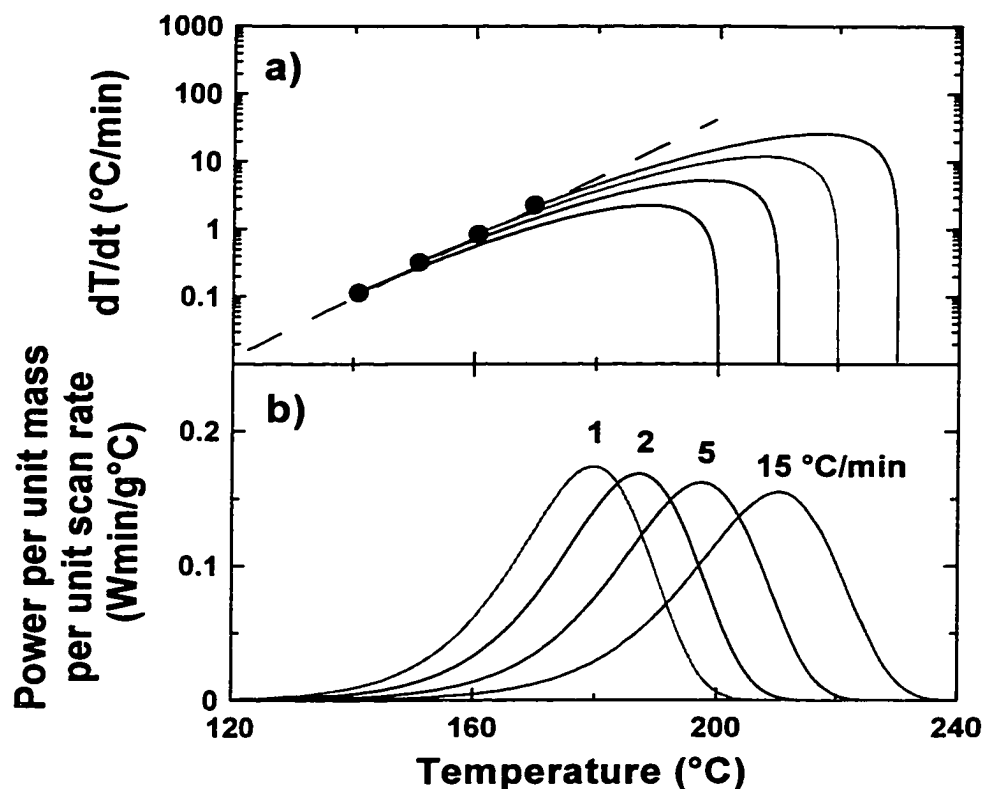
Figure 5.3. Calculated a) ARC and b) DSC profiles for first order kinetics (model 9 in Table 5.1) using the parameters for model 9 in Table 5.3. The large circles in a) indicate the start point of the ARC calculations. A value of $h/C_{tot} = 60$ °C was used in a) and $H = 270$ J/g in b). The scan rates in b) were 1, 2, 5 and 15 °C/min. The dashed line in a) is the "Arrhenius line" described in the text.

Figure 5.4 shows the typical profiles that would be obtained in a reaction governed by diffusion (model 15 in Table 5.1). These reactions have their overall rate governed by the movement of one or more reactant species to, or a product from, a reaction interface. The ARC profile is easily distinguishable from n^{th}-order reaction kinetics since it has a high initial self-heating rate that rapidly decreases followed by a region of approximately constant increasing slope. On the other hand, the DSC profile increases slowly from low temperature and then falls off fairly rapidly after the peak in the trace in a manner not so different from zero order kinetics.
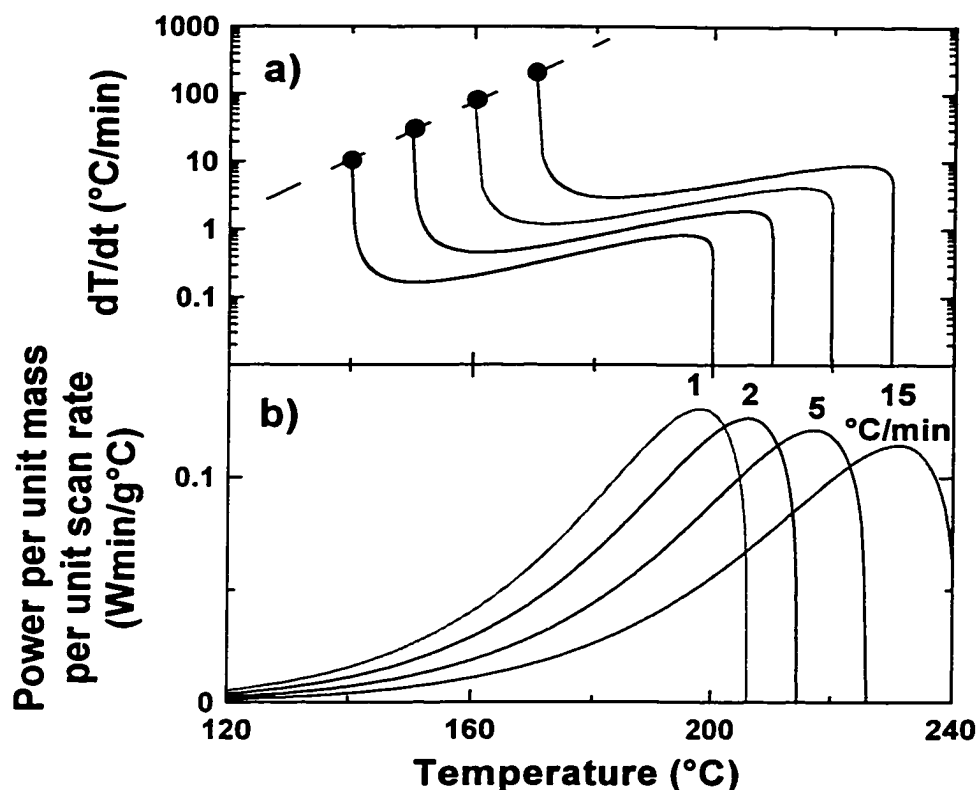
Figure 5.4. Calculated a) ARC and b) DSC profiles for diffusion-controlled kinetics (model 15 in Table 5.1) using the parameters for model 15 in Table 5.3. The large circles in a) indicate the start point of the ARC calculations. A value of h/C$_{tot}$ = 60 °C was used in a) and H = 270 J/g in b). The scan rates in b) were 1, 2, 5 and 15 °C/min. The dashed line in a) is the "Arrhenius line" described in the text.

Figure 5.5 shows the ARC and DSC profiles for a reaction governed by power law kinetics (model 4 in Table 5.1). Power law kinetics are obtained when the initial growth of nuclei is slower than the constant value that is subsequently attained [70]. The DSC profile is similar to that of a zero-order reaction as can be seen by comparing to Figure 5.2. The ARC profile is to the left (above) of the "Arrhenius line" indicating that the reaction is accelerated by the presence of product. This is seen by the rapid initial rise in self-heating rate that levels to an approximately constant upward slope, which continues until the reaction is complete. The ARC profile is easily distinguished from those previously shown.
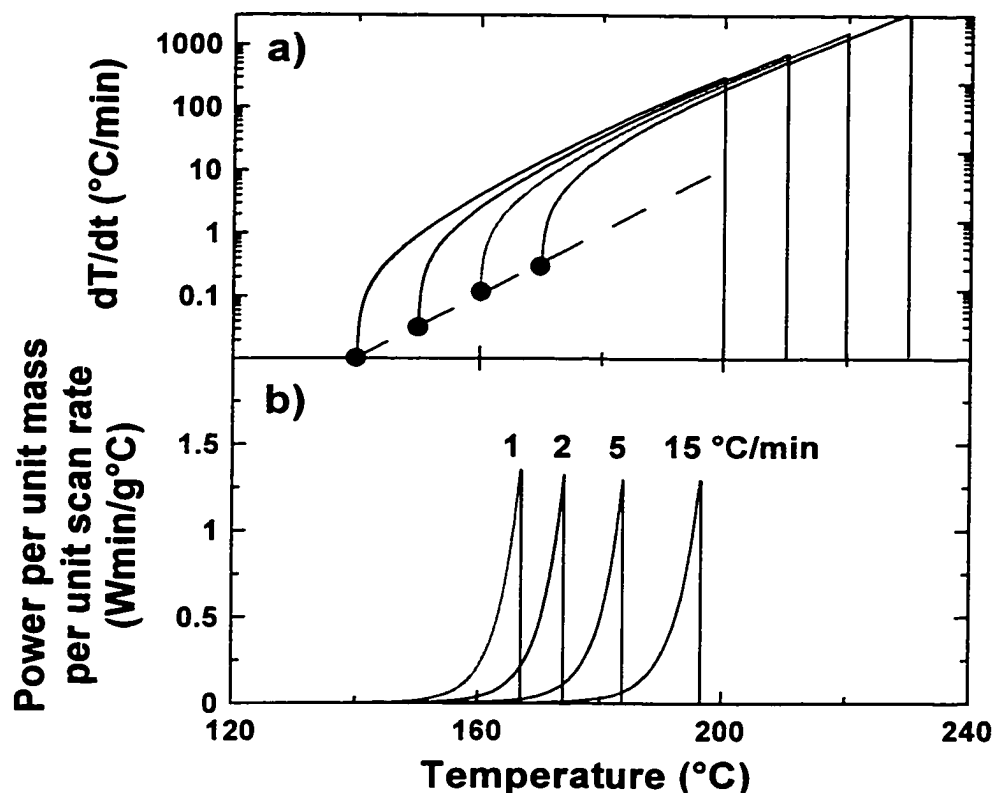
Figure 5.5. Calculated a) ARC and b) DSC profiles for power-law kinetics (model 4 in Table 5.1) using the parameters for model 3 in Table 5.3. The large circles in a) indicate the start point of the ARC calculations. A value of h/C_{tot} = 60 °C was used in a) and H = 270 J/g in b). The scan rates in b) were 1, 2, 5 and 15 °C /min. The dashed line in a) is the "Arrhenius line" described in the text.

Figure 5.6 shows the ARC and DSC profiles for an Avrami-Erofeev reaction (model 12). The Avrami-Erofeev expressions have been found to describe many solid phase decompositions, phase transformations, recrystallizations and reactions between solids [70]. The DSC profile has a peak shape similar to an nth-order reaction, except that the peak width is smaller. The ARC profile lies to the left (above) of the "Arrhenius line" with an increasing self-heating rate, but decreases smoothly when the reactant begins to run out.
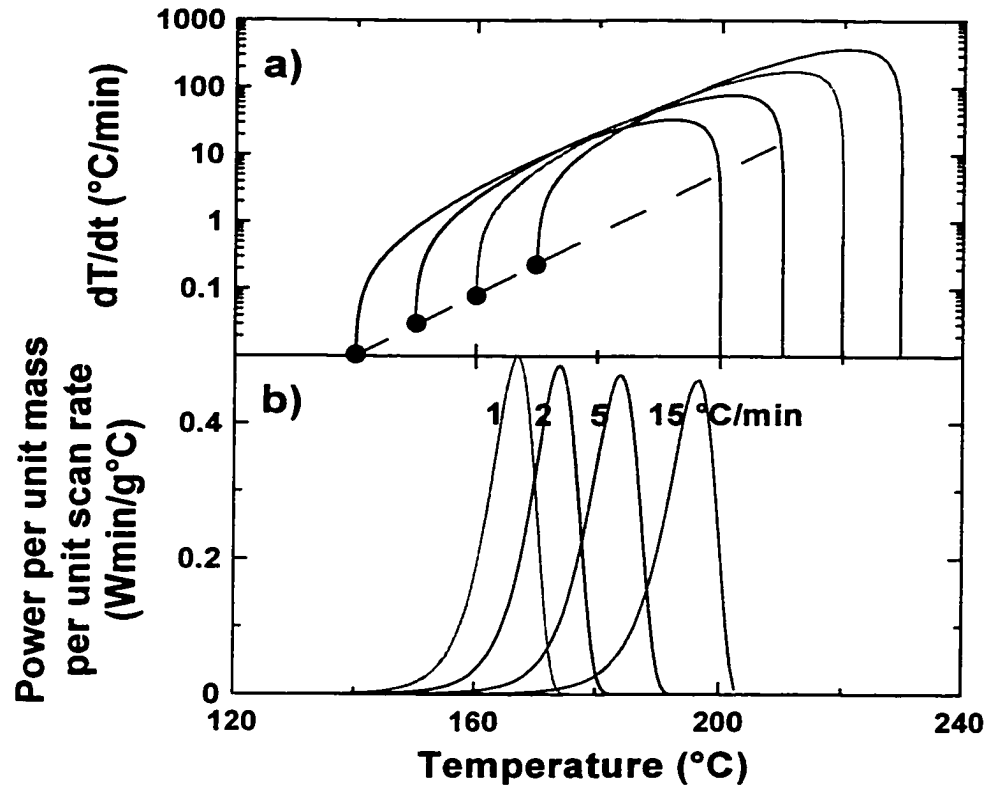
Figure 5.6. Calculated a) ARC and b) DSC profiles for Avrami-Erofeev kinetics (model 12 in Table 5.1) using the parameters for model 12 in Table 5.3. The large circles in a) indicate the start point of the ARC calculations. A value of $h/C_{tot} = 60$ °C was used in a) and $H = 270$ J/g in b). The scan rates in b) were 1, 2, 5 and 15 °C/min. The dashed line in a) is the "Arrhenius line" described in the text.

So far the value of α_o in all the simulations has been set to 0.001. Figure 5.7 shows the dependence of a typical ARC profile for an Avrami-Erofeev reaction (model 12 in Table 5.1) on the initial choice of α_o. As the value of α_o increases, the initial rise in the self-heating rate is reduced. Figure 5.8 shows the dependence of the DSC profile on α_o for the same reaction model. As α_o increases the peak width of the DSC trace increases although the effect is small for $\alpha_o < 0.02$. If α_o is treated as an adjustable parameter during modelling of reactions, then fits to ARC profiles can help to extract it.
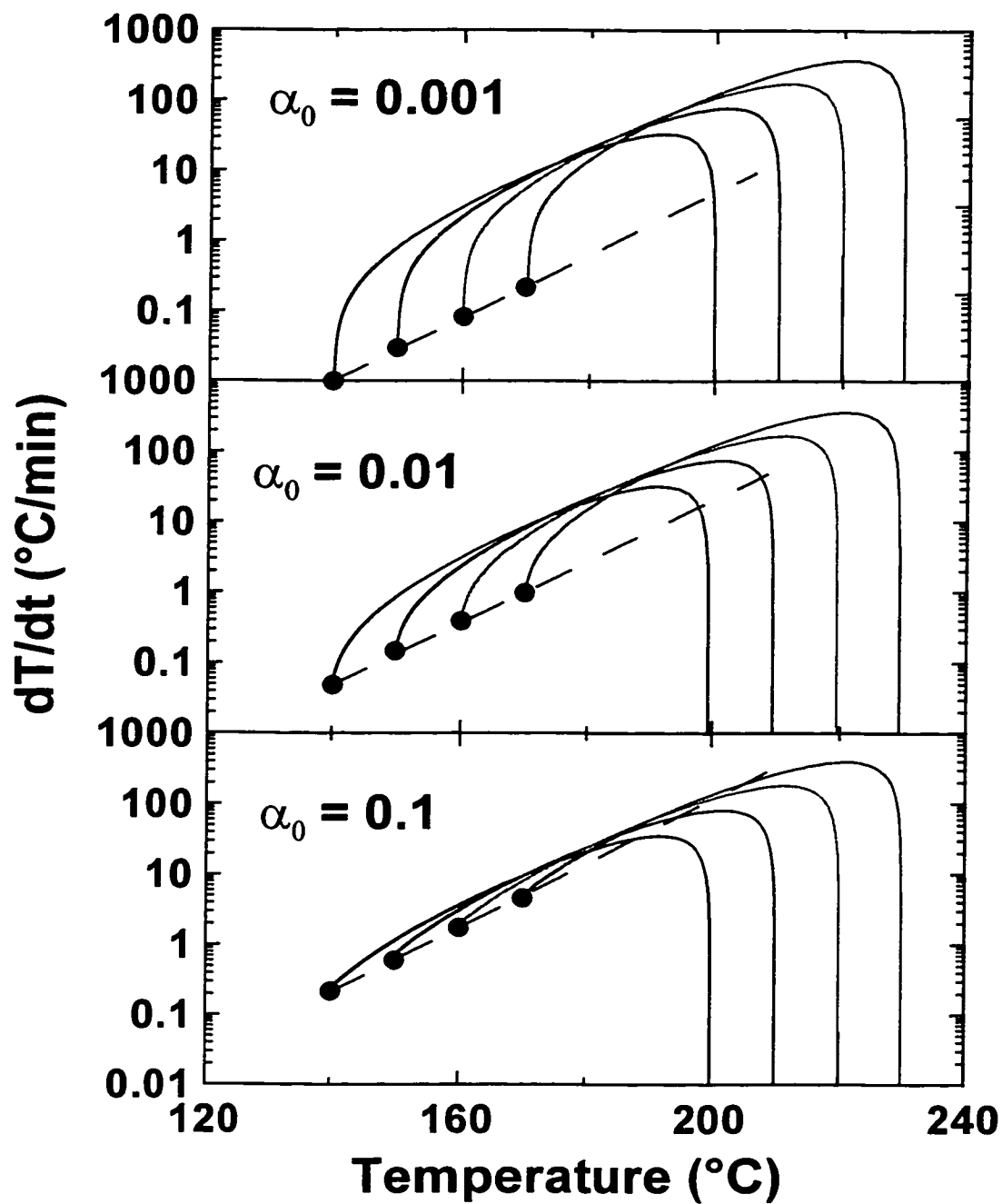
Figure 5.7. Calculated ARC profiles based on the model and parameters used in Figure 5.6, except for values of α_o as indicated.
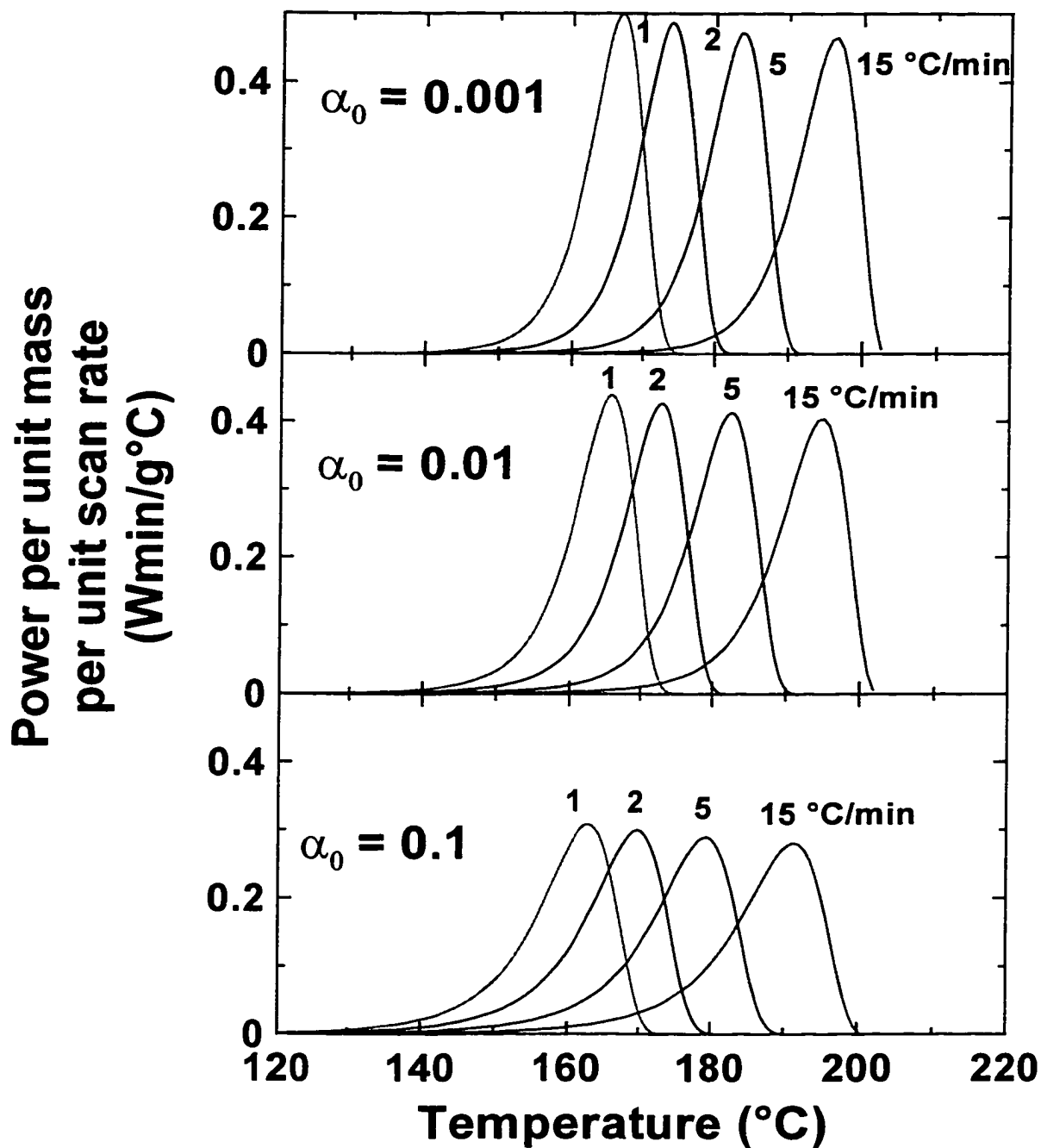
Figure 5.8. Calculated DSC profiles based on the model and parameters used in Figure 5.6, except for values of α_o as indicated.

Calculations of ARC and DSC traces for the other models in Table 5.1 are similar to one of the profiles in Figures 5.2 through 5.6. It is clear that the changes in the ARC profiles with reaction model are more profound than the changes seen in DSC. In any

event, the combination of studies by both ARC and DSC should lead to a more reliable determination of kinetic triplets.

The procedure followed here to determine the kinetic triplet required ARC experiments to be performed on a number of nominally identical samples. The first ARC experiment was used to find the temperature of the exotherm at the detection limit of the ARC and follow it to completion. Subsequent experiments on fresh samples were forced to temperatures above the initial onset of the exotherm. Provided that the heating rate of the ARC to the target (5 °C/min) was much larger than the initial self-heating rate of the sample at the target temperature, then $f(\alpha)$ in Equation 5-1 had approximately the same value for all the samples at the start of their exotherms. Since the self-heating rate dT/dt is proportional to $d\alpha/dt$ (see Equation 5-5), an Arrenhius plot of the initial self-heating rates at various temperatures can be used to determine E_a and $\gamma f(\alpha_o)$, where α_o is the initial value of α at the start of the reaction. The shape of the dT/dt versus T plots, the ARC profiles, are then used to assist in the selection of the reaction model. Once $f(\alpha)$ is determined, then one can solve for γ.

DSC results are then used to test the kinetic triplet obtained. Generally, the obtained kinetic triplet can model the DSC results approximately, without severe adjustment. However, the temperature dependence of the DSC peak position and the shape and width of the DSC peaks can be used to "fine tune" the kinetic triplet obtained from ARC. Finally, the kinetic triplet is adjusted until the best fit (lowest χ^2) is obtained to a number of DSC runs at different sweep rates and a number of ARC runs at different starting temperatures.

Since DSC results at several sweep rates and ARC profiles for a number of different start temperatures can be fit with a single kinetic triplet, confidence in the description of the reaction is high. This gives confidence in the ability to predict the outcome of other unexplored thermal events (such as thermal modelling of Li-ion cells exposed to elevated temperatures).

Chapter 6

Reaction Mechanisms for $Li_{0.5}CoO_2$

6.1 Methodology

Charged lithium-ion cells contain solid electrodes and an electrolyte composed of a multi-component solvent and a dissolved lithium salt. In addition the electrolyte may contain a number of undisclosed additives for improved cell performance. This is a very complicated reactive system and gives rise to many reaction possibilities. Step by step calorimetric studies for $Li_{0.5}CoO_2$ will be described in this chapter.

Initially, the decomposition of $Li_{0.5}CoO_2$ itself was studied. Solvent was then added to samples of $Li_{0.5}CoO_2$ and the decomposition studied anew. Finally, a series of electrolytes was tested to examine the effect of the electrolyte salt on the electrode/ solvent reactions.

A rinsing procedure that removed the original electrolyte used to prepare the $Li_{0.5}CoO_2$ electrode was described in Section 4.2.2. In order to ensure that the structure of the $Li_{0.5}CoO_2$ electrode remained intact during the rinsing procedure an x-ray diffraction pattern of the material was obtained before and after rinsing. The diffraction patterns were unchanged to the eye, and a least squares fit to the lattice constants showed little or no change had occurred (see Table 6.1). Thus the rinsing procedure did not damage the bulk structure of the material.

Similarly, the rinsing procedure did not affect the calorimetric behaviour of the samples significantly. Figure 6.1 shows the self-heating rate versus temperature for two samples. One sample contains 0.2 g $Li_{0.5}CoO_2$ (directly from the cell) plus 0.1 g electrolyte (1M $LiPF_6$ EC/DEC 33/67), and the other contains 0.2 g $Li_{0.5}CoO_2$ (rinsed and dried) plus 0.1 g of the electrolyte. The two data sets are almost identical. Thus, the rinsing procedure did not change the thermal response of the electrode and can be used to

isolate and identify some of the reactions involved in the decomposition of $Li_{0.5}CoO_2$ upon exposure to high temperatures.

Table 6.1: Lattice constants from x-ray diffraction experiments on $Li_{0.5}CoO_2$ recovered at various points during ARC experiments.

$Li_{0.5}CoO_2$	a (Å)	c (Å)	Volume (Å³)
	±0.002	±0.002	±0.008
Before DMC Wash	2.807	14.406	32.770
After DMC Wash	2.809	14.435	32.869
After 180°C	2.810	14.313	32.625
After 320°C	2.823	13.932	32.049
Fresh LiCoO₂	2.824	13.891	31.972
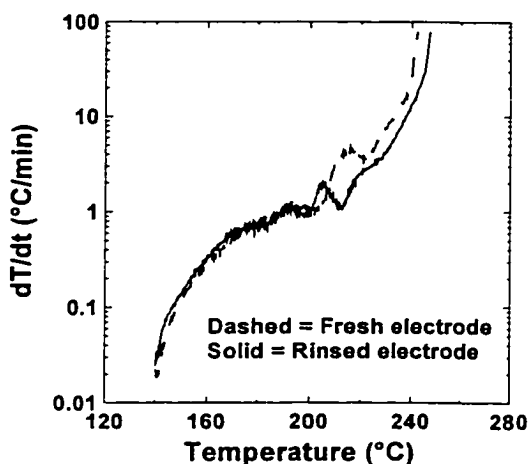
Figure 6.1. Self-heating rate versus temperature of 0.2 g of $Li_{0.5}CoO_2$ powder with 0.1 g of 1M LiPF₆ in EC/DEC electrolyte. Dashed line is the fresh electrode, solid line is the rinsed electrode.

6.2 Reaction of Dry $Li_{0.5}CoO_2$

Figure 6.2 shows the self-heating rate of the dried, charged $Li_{0.5}CoO_2$ electrode. Two distinct regions are seen. Initially, there is a small exotherm that begins at about 140°C, which continues for about 15 degrees. After tracking this first exothermic event,

the ARC continues its heat-wait-search program and discovers no sustainable exothermic events until 240°C. The second exothermic event shows a rapid rise in the self-heating rate that continues until the stop temperature of 320°C is reached. Nominally identical samples were run in the ARC to a temperature of 180°C and 320°C respectively for x-ray diffraction analysis. Similar ARC profiles to those in Figure 6.2 were obtained on ARC samples with different masses of $Li_{0.5}CoO_2$ added to the sample bomb, but are not shown for clarity.
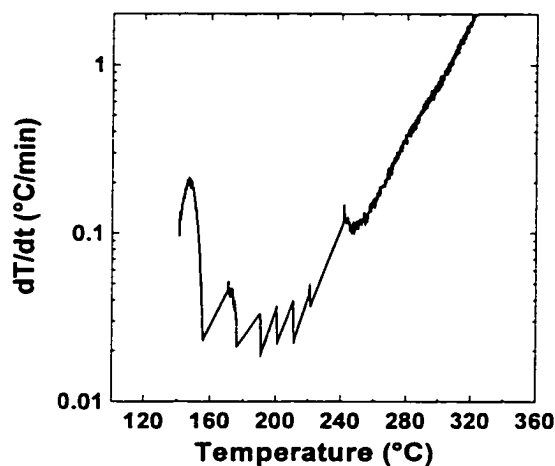
Figure 6.2. Self-heating rate versus temperature of 0.2 g of dry $Li_{0.5}CoO_2$ with no additional solvent or electrolyte added to the sample tube.

Figure 6.3a shows the x-ray diffraction pattern of $Li_{0.5}CoO_2$ after rinsing, taken with the sample holder described in Section 4.4.1. Figures 6.3b and 6.3c show the diffraction patterns of samples stopped at 180°C and 320°C respectively, while the corresponding panels in Figure 6.4 show a close up of certain regions in the diffraction profiles. There is little difference between the positions of the peaks in panel a and b of Figures 6.3 and 6.4. However, between 180°C and 320°C, the diffraction pattern shows significant changes, particularly in the splitting between the (108) and (110) peaks. In panel b, the (108) peak is near 64.5° and the (110) peak is near 66.5°. After heating to 320°C, these peaks merge into a single peak, which is coincident with a Co_3O_4 peak. The diffraction peaks of Co_3O_4 and $Li_{0.5}CoO_2$ overlap in many areas, except in the region of the Co_3O_4 (220) peak near 31.3°. This peak is clearly observed in panel c, proving that Co_3O_4 is produced.
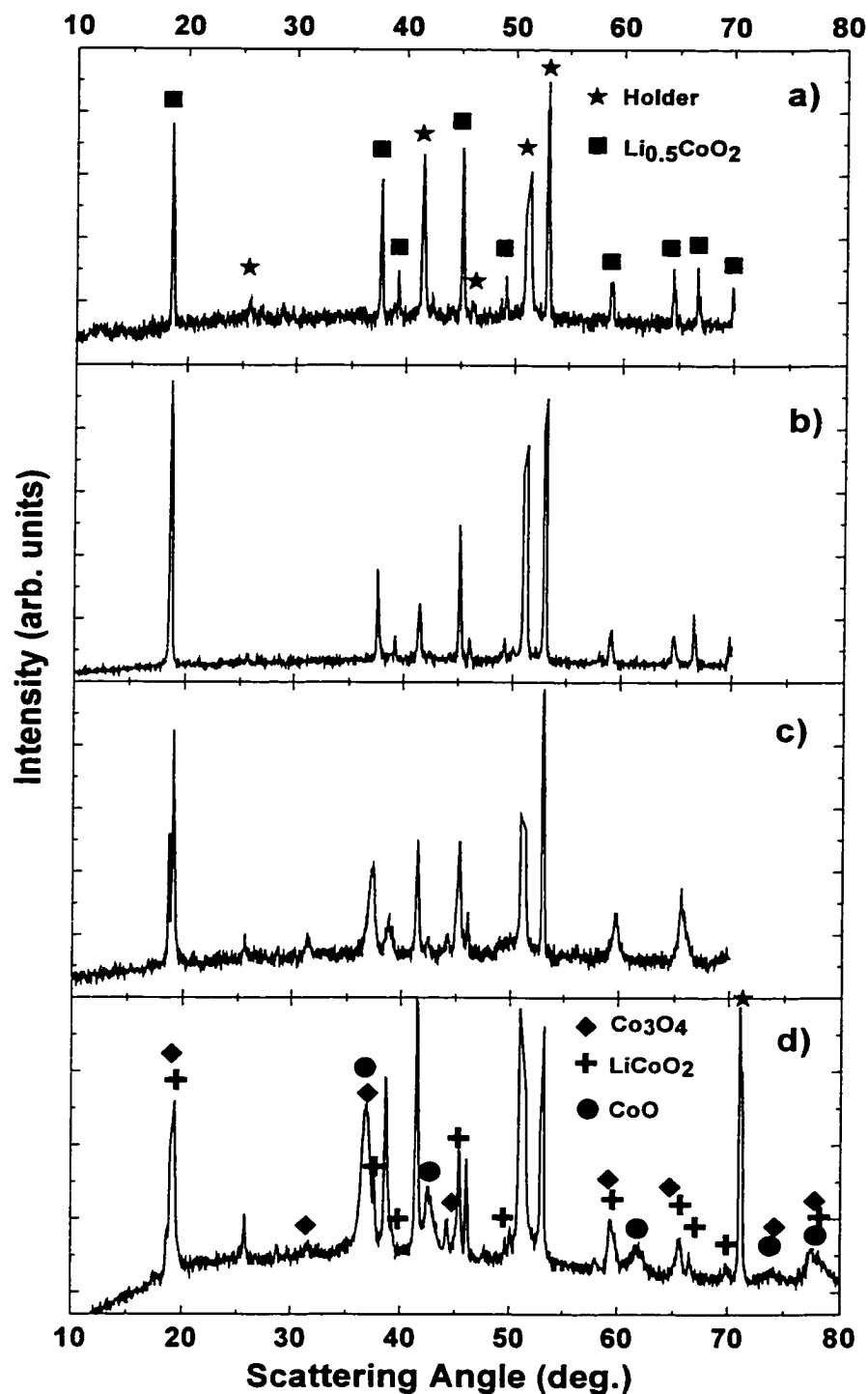
Figure 6.3. X-ray diffraction profiles of $Li_{0.5}CoO_2$ subjected to different treatments. All diffraction patterns collected in air-tight holders with Be windows. a) Fresh $Li_{0.5}CoO_2$ after DMC rinsing. b) Rinsed and dryed $Li_{0.5}CoO_2$ heated to 180°C in the ARC. c) Rinsed and dryed $Li_{0.5}CoO_2$ heated to 320°C in the ARC. d) XRD pattern of 0.1 g $Li_{0.5}CoO_2$ and 0.1 g of EC/DEC solvent heated to 275°C in the ARC.

Scattering Angle (deg.)
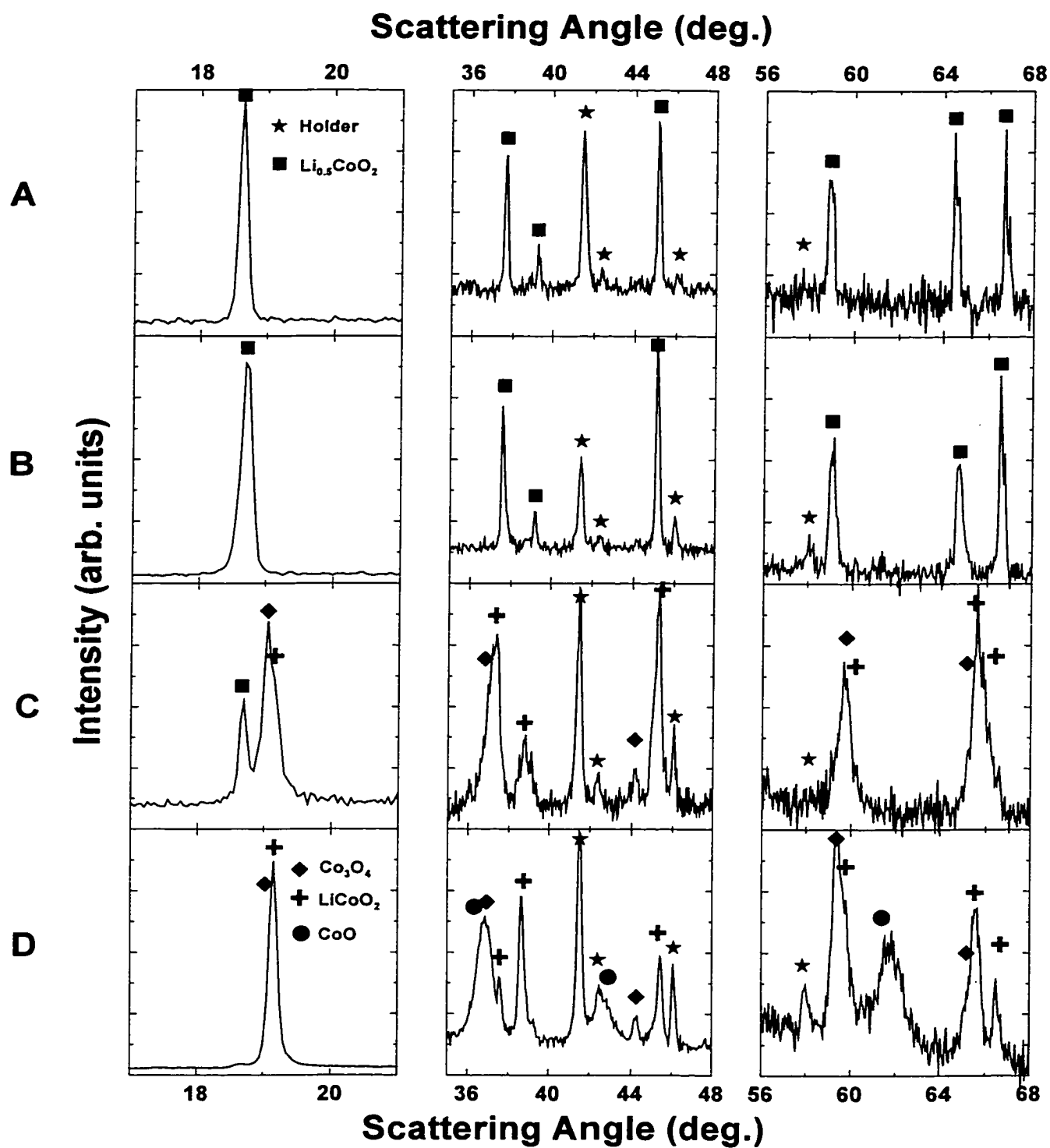
Figure 6.4. Close up of three regions in the corresponding x-ray diffraction profiles of

Figure 6.3.

An analysis of the x-ray patterns at various points in the ARC profiles is given in Table 6.1. The lattice constants measured at 180°C, where the first exothermic process had finished, are close to the lattice constants of the original washed electrode, $Li_{0.5}CoO_2$. After the termination of the ARC experiment (320°C), the lattice constants obtained were quite close to those of $LiCoO_2$. The initial thermal instability (130°C) is thus the reaction of $Li_{0.5}CoO_2$ with residual organics on the powder surface from the rinsing procedure. Because there was little solvent present very little oxygen loss from the electrode occurred and there was little change of the structure during this first thermal event. Further heating (through the exotherm beginning at 240°C) resulted in the formation of $LiCoO_2$ and Co_3O_4 with the subsequent release of oxygen. This can be visualised by the following equation,

$$Li_x CoO_2 \xrightarrow{\Delta} xLiCoO_2 + \frac{(1-x)}{3}Co_3O_4 + \frac{1-x}{3}O_2. \qquad (6\text{-}1)$$
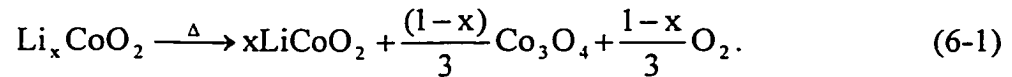
The experiment described by Figure 6.2 suggests that in the presence of residual organics, the decomposition of $Li_{0.5}CoO_2$ begins much earlier than in their absence. This is confirmed for the case of the reaction between $Li_{0.5}CoO_2$ and significant amounts of solvent (Section 6.4).

Differential scanning calorimeter (DSC) profiles of the dried $Li_{0.5}CoO_2$ electrode are shown in Figure 6.5. The DSC profiles show a small exothermic behaviour near 200°C that results in a peak. This peak corresponds to the initial self-heating in the ARC experiment. After the peak in the DSC, there is not a return to baseline, indicating other thermal events occurring. A steady growth in exothermic behaviour is seen culminating in a peak near 300°C.

The process giving rise to the steady growth in exothermic activity may not have produced enough heat for sustainable self-heating as measured by the ARC. But, ARC detection would have occurred for the event giving rise to the peak near 300°C.

The peak near 300°C corresponds to the conversion of the $Li_{0.5}CoO_2$ structure to Co_3O_4 and $LiCoO_2$ (Equation 6-1). After the last peak in the DSC profile there is not a return to baseline, which may be due to the conversion of the residual $Li_{0.5}CoO_2$ in the sample or a change in baseline due to the change in the heat capacity of the sample.
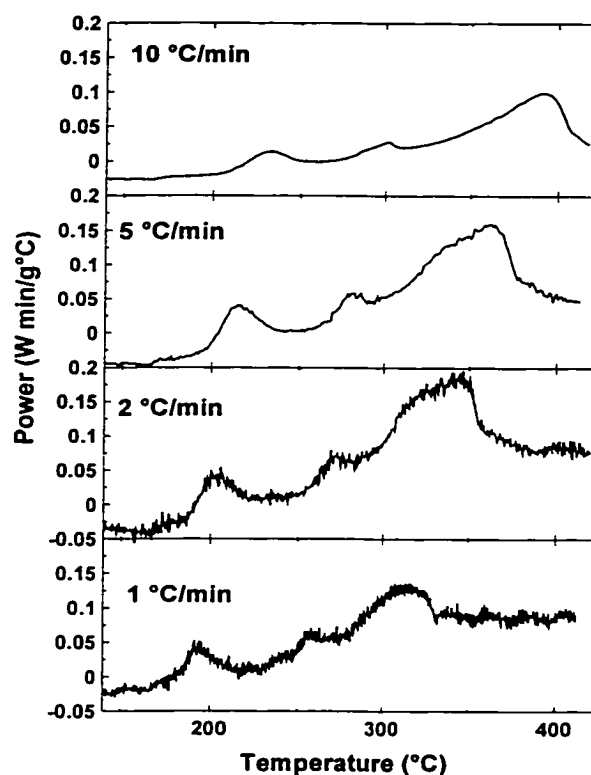
Figure 6.5. Differential Scanning Calorimetry (DSC) experiments on dry $Li_{0.5}CoO_2$, with no additional solvent or electrolyte added, at the temperature scan rates indicated.

During the cooling of the DSC sample no exothermic or endothermic activity was detected indicating that upon heating, the dry electrode partakes in irreversible reactions. An x-ray diffraction analysis of one sample (5°C/min) was performed and the results (solid line profile) along with literature peaks (vertical lines in indicated panel) are shown in Figure 6.6. The diffraction profile indicates the formation of Co_3O_4 and a small portion of $LiCoO_2$ is detectable. This confirms the results obtained and the equation derived from ARC experiments.

6.3 Summary of Dry $Li_{0.5}CoO_2$ Reaction

The dry electrode decomposes, upon heating, to Co_3O_4 and forms $LiCoO_2$.

$$Li_xCoO_2 \xrightarrow{\Delta} xLiCoO_2 + \frac{(1-x)}{3}Co_3O_4 + \frac{1-x}{3}O_2 \qquad (6\text{-}1)$$
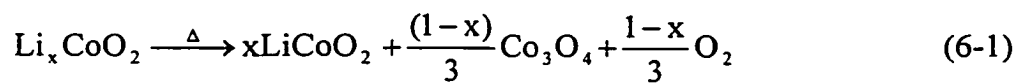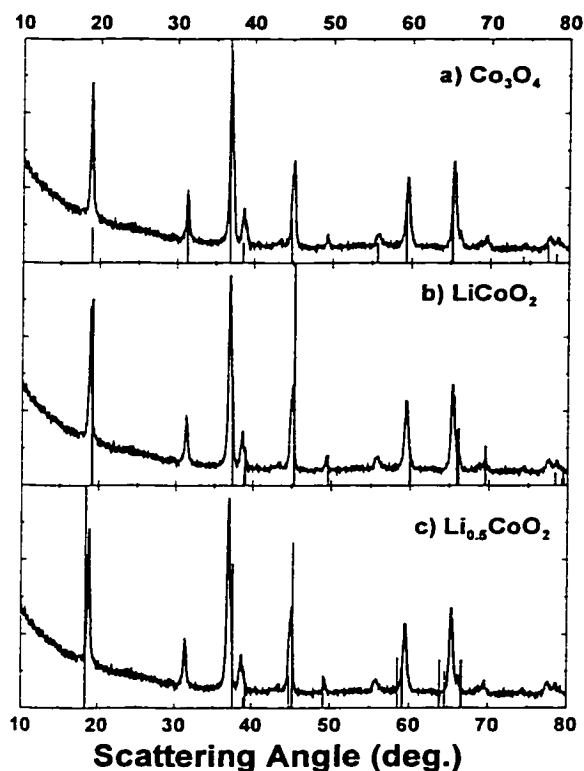
Figure 6.6. X-ray diffraction profile of the 5°C/min sample of Figure 6.5 compared to literature positions of three compounds (vertical lines in indicated panel).

6.4 Reaction of $Li_{0.5}CoO_2$ in EC/DEC (33/67) Solvent

Before examining the effect that an organic solvent may have on the decomposition of $Li_{0.5}CoO_2$, the thermal stability of the solvent itself was investigated. Figure 6.7a shows the temperature versus time profiles (from ARC) of 0.3 g of EC/DEC (33/67, vol/vol), and in Figure 6.7b 0.3 g of EC/PC (50/50, vol/vol) is shown. It is clear that no exothermic activity takes place.

Figure 6.8 shows the self-heating rate versus temperature of 0.2 g of rinsed $Li_{0.5}CoO_2$ with 0.05 g of EC/DEC (33/67) added. The dashed line in Figure 6.8 shows the self-heating rate versus temperature of the dry electrode on its own. The dry electrode ARC sample begins to self-heat at 140°C and its initial self-heating rate profile is very similar to the initial self-heating rate profile of the electrode sample with the added solvent. The sample with the added solvent begins to self-heat at 130°C and proceeds rapidly to a point where the ARC can no longer track the exotherm properly

(>20°C/min). The addition of solvent to the electrode causes the combustion of the solvent to begin at 130°C. The self-heating from the combustion reaction continues until the self-heating rate of the sample reaches the maximum self-heating rate value of the machine (set by operator).
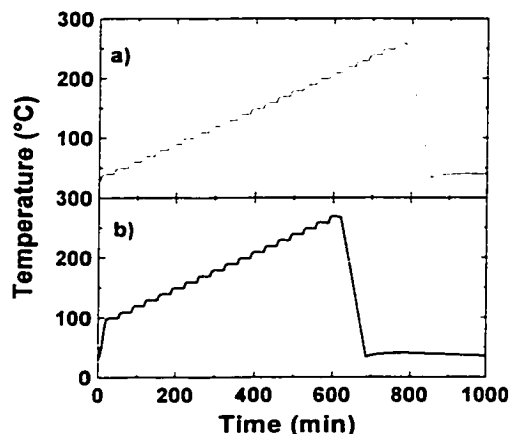
Figure 6.7. Temperature/Time ARC profiles of 0.3 g of EC/DEC (33/67, panel a) and 0.3 g of EC/PC (50/50, panel b).
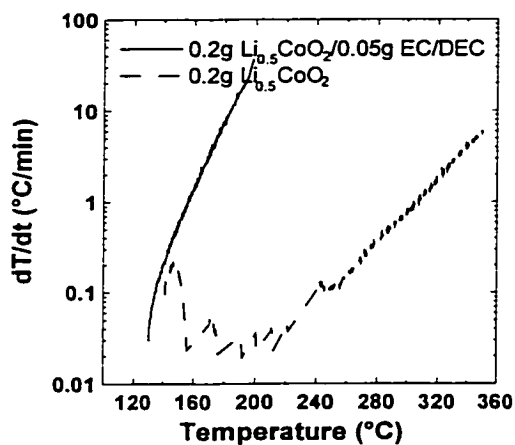
Figure 6.8. Self-heating rate versus temperature of 0.2 g of $Li_{0.5}CoO_2$ in the presence of 0.05 g of EC/DEC as the solid line, while the dashed line is that of 0.2 g of $Li_{0.5}CoO_2$ alone.

The products from the combustion of the solvent were expected to contain CO_2, H_2O and possibly other gases and/or products of incomplete combustion. At the end of the experiment in Figure 6.8 the ARC tube for the sample with solvent added was

significantly expanded due to the high pressure generated within it, suggesting combustion products.

The oxidant for the combustion reaction is believed to be $Li_{0.5}CoO_2$. Lowering the amount of oxidant placed into the ARC sample tube, from 0.2 g to 0.1 g, will decrease the total heat, h (J), produced during the combustion. This would reduce the temperature rise, ΔT (K), that will be seen in the ARC experiment and make it easier to observe the full reaction before the stop temperature is reached. The temperature rise for a single adiabatic reaction process is given by:

$$\Delta T = h/C_{tot}, \qquad (6\text{-}2)$$

where C_{tot} is the heat capacity of the entire sample (electrode material, solvent plus stainless steel ARC tube, JK^{-1}).

For our samples, the heat capacity is calculated as

$$C_{tot} = \sum_i c_i m_i = 1.0 \frac{J}{gK} m_{cat} + 0.46 \frac{J}{gK} 0.9g + 1.5 \frac{J}{gK} m_{el} = (0.414 + m_{cat} + 1.5 m_{el}) \frac{J}{K}, \qquad (6\text{-}3)$$

where m_{cat} is the mass of cathode in grams in the ARC tube, and m_{el} is the mass of electrolyte or solvent in grams in the ARC tube. A specific heat (c_i) of 1.0 J/(gK) is estimated for $LiCoO_2$ [88], 1.5 J/(gK) is the estimated specific heat of EC/DEC from the specific heats of EC [89] and DEC [90] and 0.46 J/(gK) is the specific heat of stainless steel [65]. Since h is proportional to m_{cat}, and C_{tot} depends weakly on m_{cat} for $m_{cat} \approx 0.1$ g, then ΔT can be reduced by reducing m_{cat}. In addition, since C_{tot} increases with m_{el}, ΔT can be decreased by increasing m_{el}, assuming that the reaction stops when the oxygen available from $Li_{0.5}CoO_2$ is used up.

Figure 6.9 shows self-heating rate versus temperature for 11 ARC samples consisting of 0.1 g of $Li_{0.5}CoO_2$ in 0.1, 0.2 or 0.3 g of EC/DEC solvent. In all cases, the entire reaction is complete before the stop temperature of the calorimeter is reached. Table 6.2 shows the values of ΔT obtained for each of the 11 trials as well as the calculated heat capacity, C_{tot}, of the sample using Equation 6-3. Figure 6.10 shows ΔT plotted versus $1/C_{tot}$. This graph should yield a straight line of slope h, the heat in joules produced by the reaction of 0.1 g of $Li_{0.5}CoO_2$. The slope is 50. ± 6 J or 500 ± 60 J/g. The linearity of Figure 6.10 suggests that there is excess solvent in the tube for each of the trials and that the reaction stops when the oxygen available from $Li_{0.5}CoO_2$ is used up.
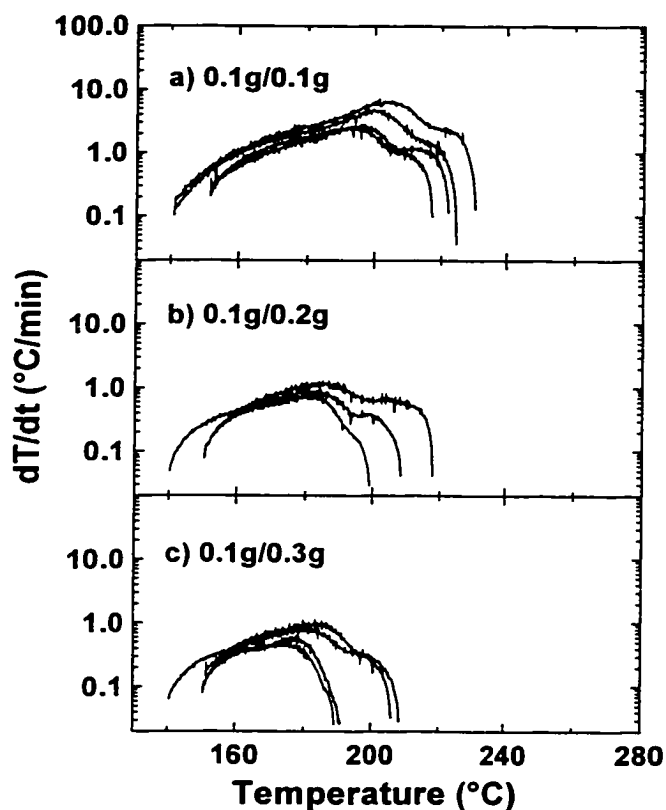
Figure 6.9. Self-heating rate versus temperature of 0.1 g of $Li_{0.5}CoO_2$ in the presence of various amounts of added solvent (EC/DEC): panel a) 0.1 g solvent; panel b) 0.2 g solvent; panel c) 0.3 g solvent.

Table 6.2. Analysis of the results in Figure 6.7.

Trial	Solvent mass (g)	$Li_{0.5}CoO_2$ mass (g)	ΔT (K)	C_{tot} (J/K)
1	0.1045	0.099	90	0.670
2	0.0992	0.100	83	0.663
3	0.1003	0.100	70	0.664
4	0.0968	0.100	70	0.659
5	0.2035	0.101	67	0.820
6	0.2013	0.101	58	0.817
7	0.2044	0.098	60	0.819
8	0.2964	0.102	50	0.961
9	0.3034	0.099	40	0.968
10	0.3037	0.100	55	0.970
11	0.2970	0.100	57	0.960
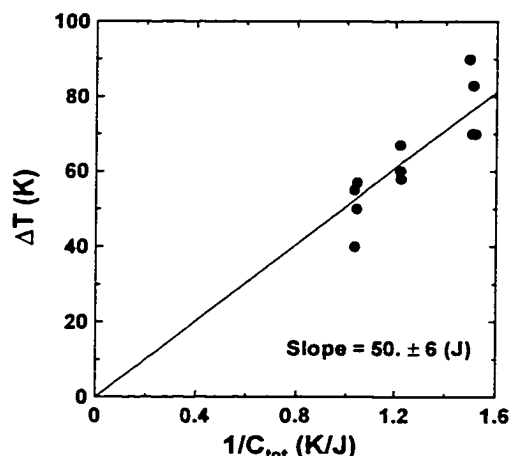
Figure 6.10. Temperature rise, ΔT versus inverse heat capacity $(1/C_{tot})$ of the samples described by the data shown in Figure 6.9. The straight line is the best fit of the equation

$$\Delta T = h/C_{tot}.$$

Panel d of Figures 6.3 and 6.4 show the x-ray diffraction profile of a 0.1 g $Li_{0.5}CoO_2$ sample after reaction with 0.1 g of EC/DEC (33/67, after trial 1 in Table 6.2). When the ARC tube used to prepare the XRD sample was opened, the sample was not completely dry, demonstrating that the reaction terminated due to consumption of available oxygen in the electrode powder, not due to a lack of available solvent. In addition to $LiCoO_2$ and Co_3O_4, the x-ray diffraction pattern showed CoO. The peaks attributed to CoO were indexed and the lattice constant was refined to be 4.25 Å. The lattice constant of $Li_xCo_{(1-x)}O$ varies from 4.26 Å to 4.18 Å as x changes from 0 to 0.2 [91]. The observed lattice constant of 4.25 Å suggests a small amount of Li may be within the phase and is consistent with x = 0.025 in $Li_xCo_{(1-x)}O$. Since the amount of Li is very small, this phase will be referred to as CoO.

It is the reducing power of the solvent that is responsible for the formation of CoO. Thus, in the presence of solvent (say EC) the reaction in Equation 6-1 proceeds to CoO, or

$$Li_{0.5}CoO_2 + 1/10\ C_3H_4O_3 \rightarrow 0.5\ LiCoO_2 + 0.5\ CoO + 3/10\ CO_2 + 2/10\ H_2O, \quad (6\text{-}4)$$
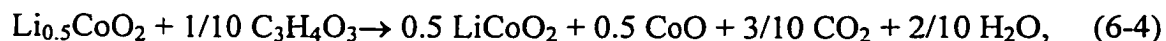
assuming full combustion of the solvent.

Assume that the heat produced by the experiments in Figure 6.9 originates from the combustion of the solvents by the oxygen released through Equations 6-1 and/or 6-4.

For simplicity, the solvents are assumed to fully combust to H_2O and CO_2. It is true that this may not be the case and that other products caused by partial oxidation may be present. However, in order to make an estimate of the heat produced, the assumption of full oxidation allows tabulated values of the heat of combustion to be used. The heat of combustion for EC is 1161.4 kJ/mol [92], while that of DEC is 2715 kJ/mol [93]. One mole of DEC $((CH_3CH_2)_2COO_2)$ requires 12 moles of O atoms to fully combust to CO_2 and water, while EC $(C_3H_4O_3)$ requires 5 moles of O atoms for full combustion. The reaction given in Equation 6-1 shows that 1 mole of $Li_{0.5}CoO_2$ can supply 1/3 mole of oxygen atoms. The reaction given in Equation 6-4 implies that 1 mole of $Li_{0.5}CoO_2$ can supply ½ mole of oxygen atoms. Therefore, since the molar mass of $Li_{0.5}CoO_2$ is 94.4 g/mole, a heat of,

$$((1/3 * 1/5 * 0.33\ (1161.4\ kJ/mol)) + (1/3 * 1/12 * 0.67\ (2715\ kJ/mole))) \div 94.4\ g/mole = 806\ J/g, \qquad (6\text{-}5)$$

or

$$((1/2 * 1/5 * 0.33\ (1161.4\ kJ/mol)) + (1/2 * 1/12 * 0.67\ (2715\ kJ/mole))) \div 94.4\ g/mole = 1209\ J/g, \qquad (6\text{-}6)$$

is expected to be generated when the oxygen available from 1 g of $Li_{0.5}CoO_2$ combusts the EC/DEC (33/67) solvent. The experimental value of 500 ± 60 J/g from the results shown in Figures 6.9 and 6.10 is of the right order of magnitude. Please note that the heats associated with the solid-solid transformations in Equations 6-1 and 6-4 are not known nor are the heat capacities of cathode or electrolyte accurately known over the temperature range involved. These could be the reasons for the discrepancy. Nevertheless, the exotherms shown in Figure 6.9 are consistent with solvent combustion until the available oxygen from the cathode electrode is used up.

Figure 6.11 shows DSC profiles of $Li_{0.5}CoO_2$ in the presence of EC/DEC (33/67, vol/vol). These DSC experiments contain a peak near 180°C. This initial peak is similar to that described in Section 6.2, but the peak in Figure 6.11 represents more heat than the corresponding peak in Figure 6.5. After the initial peak, some of the samples show the development of a shoulder, while other samples did not. The average result for the heat

of reaction for this initial peak (with shoulder) is 1160 ± 450 J/g, which supports the decomposition of the $Li_{0.5}CoO_2$ electrode to CoO, as calculated in Equation 6-5 and 6-6. There is a discrepancy between the two heats of reaction calculated by the two different experiments. The main reason for the discrepancy is that accurate values of the heat capacities for the electrode and solvent are not available in the temperature range analysed. In addition, weighing an accurate amount of electrode material for DSC analysis is difficult inside a glovebox.
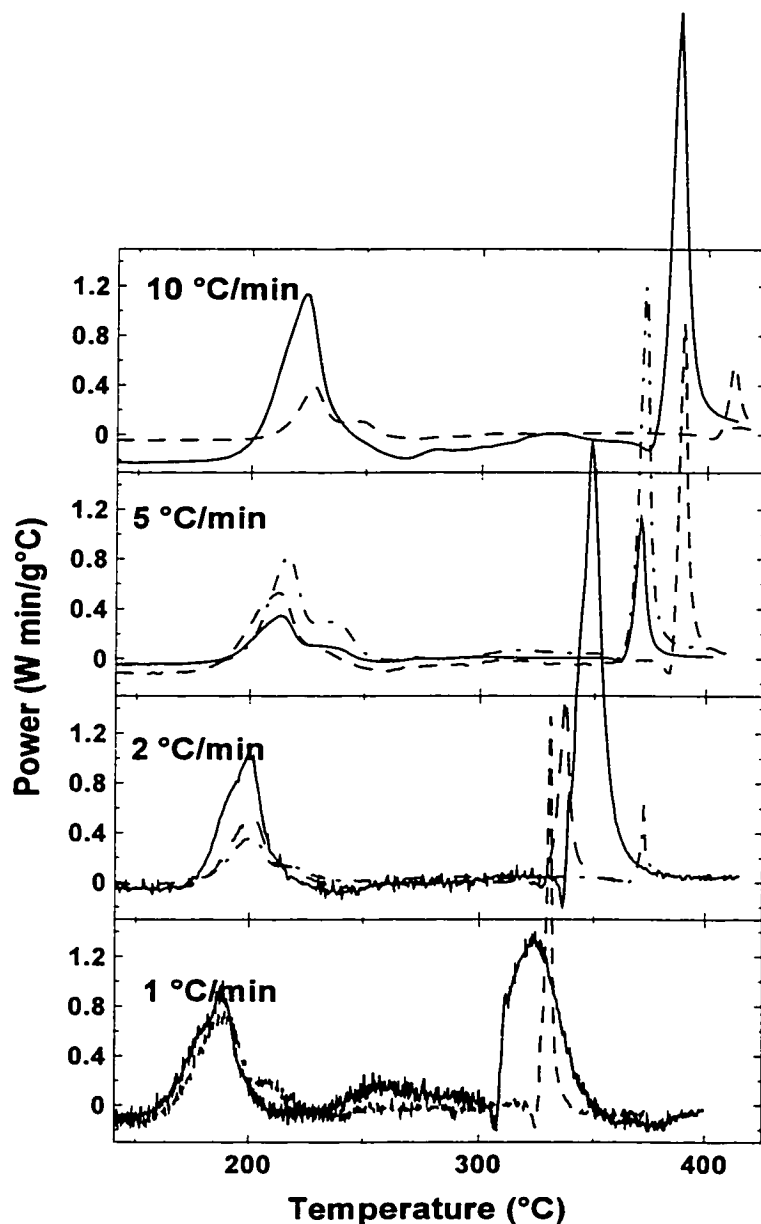
Figure 6.11. DSC profiles of $Li_{0.5}CoO_2$ in the presence of EC/DEC (33/67, vol/vol) solvent at indicated heating rate. Dashed lines are those of a duplicate sample.

Upon forcing the DSC samples of Figure 6.11 to higher temperature, no further exothermic activity occurs until after about 320°C. The exothermic activity after 300°C varies in shape, temperature and intensity for nominally the same $Li_{0.5}CoO_2$ sample whereas the initial instability is reproducible, except for the shoulder. An explanation for these anomalous behaviours is required.

The samples from Figure 6.11 typically contained between 1-7 mg of rinsed and dried $Li_{0.5}CoO_2$ and 3-6 mg of solvent. Typically, the samples that contained a larger amount of electrode material also showed more defined shoulders and variations in the high temperature reactivity. Controlling the amount of solvent added to the sample cell was difficult, but the mass of solid electrode introduced could be controlled. An experiment was proposed to determine the effect on the DSC profiles when different masses of the solid electrode are introduced into the DSC sample cell.

Figure 6.12 shows the results of DSC experiments with various amounts of $Li_{0.5}CoO_2$ and a nominally identical mass of EC/DEC (33/67) introduced (3-5 mg). TIG welding the higher mass sample cells was difficult, due to the presence of a large amount of material. In Figure 6.12 the profiles with a dashed line are from cells that leaked during analysis.

It is believed that these "leakers" were qualitatively correct and only their heats of reactions are affected. It is clear that the addition of a larger amount of the electrode causes the development of the shoulder and the diminution of the high temperature reactivity. In fact, the shoulder develops into two resolved exothermic peaks and the high temperature activity is eliminated when a larger mass of $Li_{0.5}CoO_2$ is used. The reactivity below 250°C is believed to be the reaction of $Li_{0.5}CoO_2$ to CoO, but this conversion may not consume all the available solvent and thus on forcing the sample to higher temperature there is the reaction of CoO with the solvent to form Co metal. The reduction to the metal only occurs if there is sufficient solvent remaining, thus there is a strong dependence of the high temperature reactivity on the ratio of the mass of the electrode to the mass of the solvent. The high temperature reactivity will diminish when the amount of $Li_{0.5}CoO_2$ introduced into the DSC sample is large.

Figure 6.13 shows the heat released below 250°C for each of the samples of Figure 6.12 versus the mass of $Li_{0.5}CoO_2$ used. The figure demonstrates that as the mass of $Li_{0.5}CoO_2$ increases the heat released increases linearly and thus the reactivity below 250°C does not depend on the amount of solvent present as long as it wets the electrode powder.
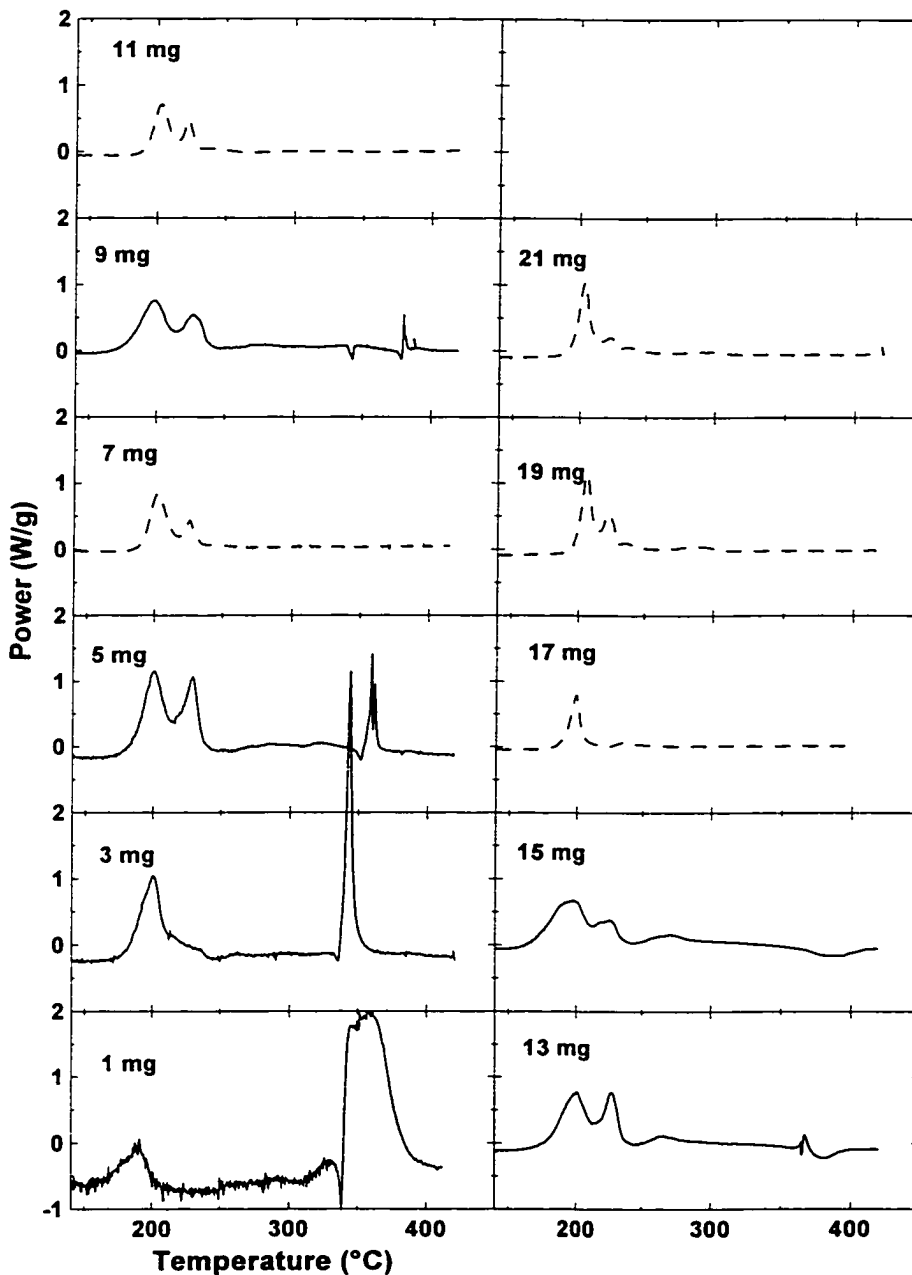
Figure 6.12. DSC profiles of $Li_{0.5}CoO_2$ at 2°C/min in EC/DEC (33/67) solvent with indicated amount of solid electrode added. Profiles with a dash line are those which leaked during analysis.
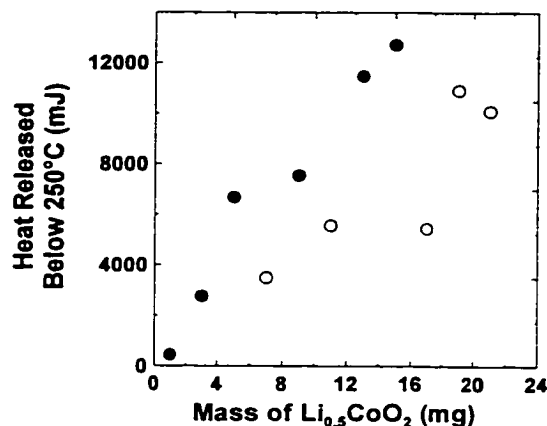
Figure 6.13. The heat released below 250°C for the samples in Figure 6.12. Solid dots are for the sealed samples, while the open dots represent the samples that leaked during analysis.

An important part of the DSC profiles of Figures 6.11 and 6.12 is absent. The cooling curves of each sample have not been presented for clarity, but Figure 6.14 shows a full DSC profile of one sample and indicates an exothermic reaction during cooling. This reaction occurs only for those samples that did not leak and thus is a reaction of one of the solid products with a gaseous product.
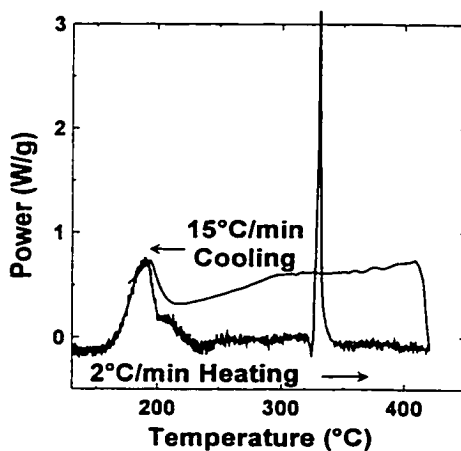
Figure 6.14. DSC profile of $Li_{0.5}CoO_2$ in the presence of EC/DEC solvent showing exothermic peak on cooling.

In order to prove the proposed reaction mechanism an x-ray analysis of some of the DSC samples in Figure 6.12 was performed. The x-ray profiles were obtained on an open air zero-background holder and are shown in Figures 6.15 through 6.21 (excluding

Figure 6.16 and 6-20). The diffraction patterns indicate an assortment of possible compounds within the sample. Each figure contains the x-ray profile of the sample in each panel of the figure. In addition each panel contains the reference positions of a particular phase that may or may not be present in the sample. The x-ray patterns were obtained from the 3, 5, 9, and 15 mg samples of Figure 6.12.
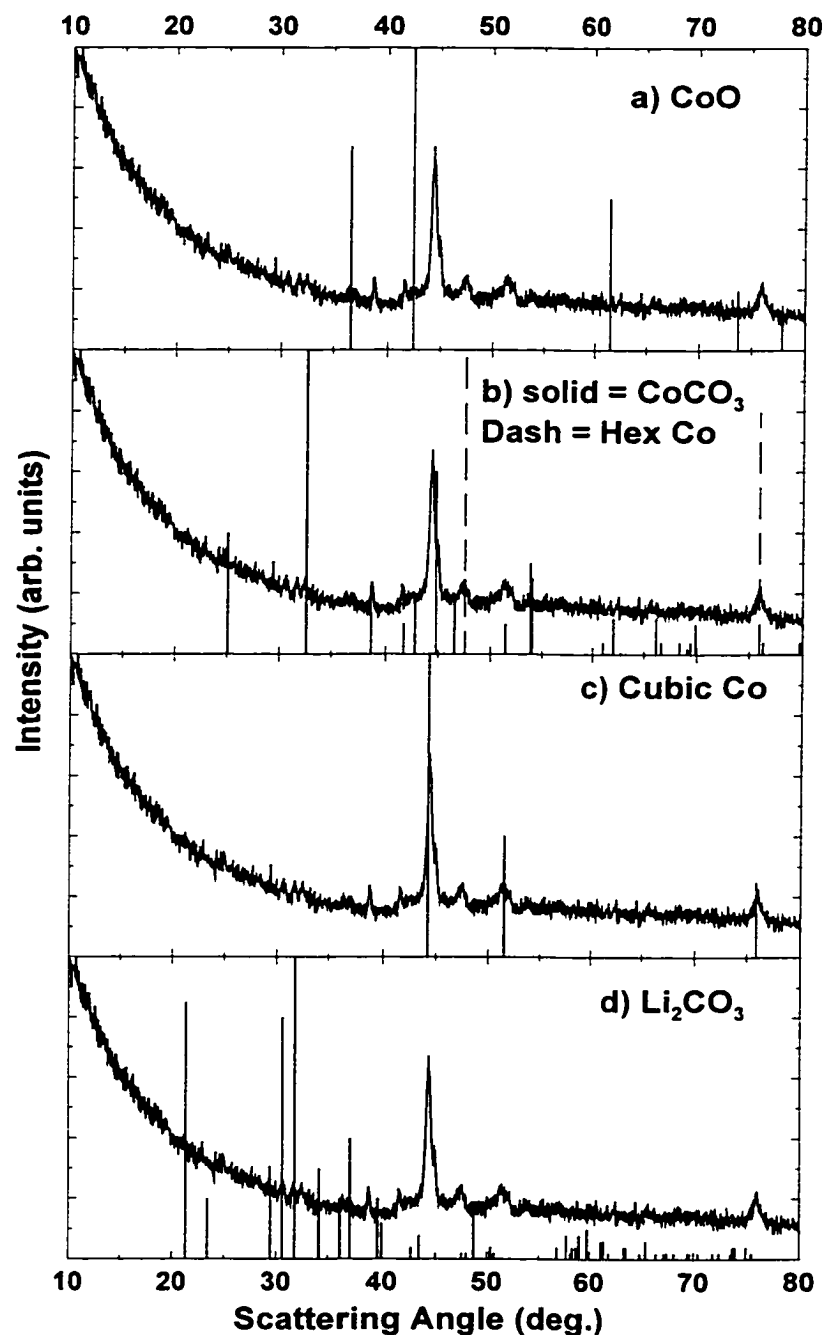
Figure 6.15. X-ray diffraction analysis of the 3 mg sample in Figure 6.12. Each panel contains the 3 mg diffraction profile and the indicated reference peaks.

Figure 6.15 shows the x-ray profile of the 3 mg sample and clearly there is a large amount of Co metal present in the sample. In addition, there is evidence for a small portions of $CoCO_3$ and Li_2CO_3. These species arose from the following equations, where the "Δ, solv" above the arrow indicates that the reaction occurs in the presence of solvent (solv) and at elevated temperatures (Δ).

$$Li_{0.5}CoO_2 \xrightarrow{\Delta} 0.5LiCoO_2 + \frac{1}{6}Co_3O_4 + \frac{1}{6}O_2, \qquad (6\text{-}7)$$

$$Co_3O_4 \xrightarrow{\Delta,\,solv} 3CoO + \frac{1}{2}O_2, \qquad (6\text{-}8)$$

$$\frac{5}{2}O_2 + C_3H_4O_3 \xrightarrow{\Delta} 3CO_2 + 2H_2O. \qquad (6\text{-}9)$$
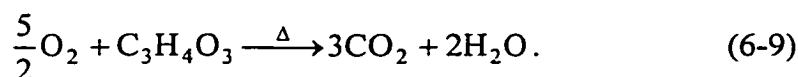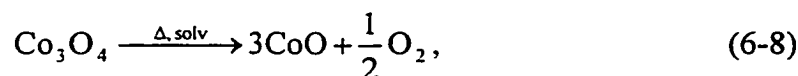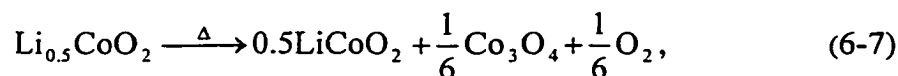
These reactions (6-7 to 6-9) occur during the initial instability between 150°C and 225°C. The high temperature reactivity produces the cobalt metal species through the following reactions,

$$CoO \xrightarrow{\Delta,\,solv} Co + \frac{1}{2}O_2 \text{ (combust more solvent)}, \qquad (6\text{-}10)$$

$$2LiCoO_2 + CO_2 \xrightarrow{\Delta,\,solv} Li_2CO_3 + 2Co + \frac{3}{2}O_2 \text{ (combust more solvent).} (6\text{-}11)$$
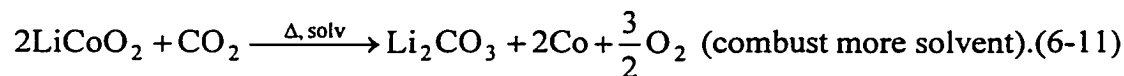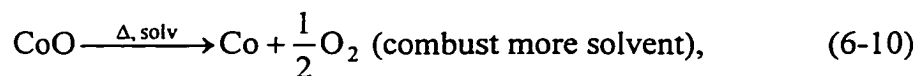
These reactions (6-10 and 6-11) occur due to the strong reducing power of the "virgin" solvent remaining in the sample tube. Full reduction of $LiCoO_2$ occurs since only a small amount of solvent is consumed during the reactions below 250°C.
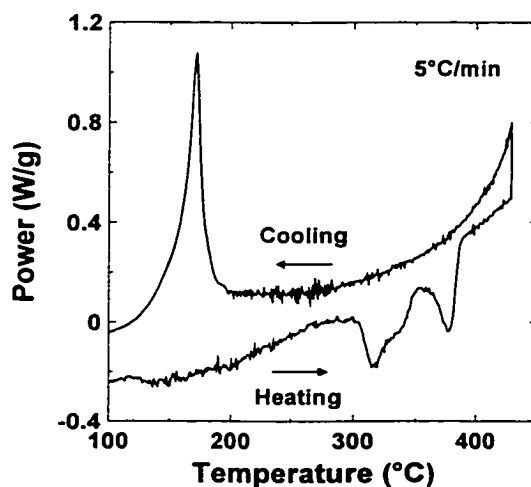
Figure 6.16. DSC of $CoCO_3$ at 5°C/min in a sealed stainless steel tube, showing decomposition on heating near 300°C and reformation on cooling near 200°C.

During cooling, cobalt carbonate is formed by the reaction of the residual CoO with CO_2, according to

$$CoO + CO_2 \longrightarrow CoCO_3. \qquad (6\text{-}12)$$

$CoCO_3$ can not be formed during heating since it decomposes to CoO and CO_2. Figure 6.16 shows a DSC of solid $CoCO_3$, where $CoCO_3$ decomposes during heating and reforms with a large exothermic peak during cooling (see Equation 6-12).

The x-ray profile of the 5 mg sample is shown in Figure 6.17, and it contains a large amount of CoO, some Co metal and $CoCO_3$, in addition to small portions of Li_2CO_3 and $LiCoO_2$. Here much more $CoCO_3$ is produced than the 3 mg sample since in the 3 mg sample only a small amount of CO_2 is produced and thus the amount of $CoCO_3$ is lower. Also, the 5 mg sample contains much more CoO than the 3 mg sample since more of the solvent is reduced between 150 and 250°C. Also, the reducing power of the remaining solvent above 350°C (production of Co, decomposition of $LiCoO_2$) is lower, but some Co is still produced while $LiCoO_2$ does not get fully reduced. Thus the equations for the products of the 5 mg sample in addition to those above could be

$$2LiCoO_2 + CO_2 \xrightarrow{\Delta} 2CoO + Li_2CO_3 + \frac{1}{2}O_2 \text{ (combust more solvent). } (6\text{-}13)$$
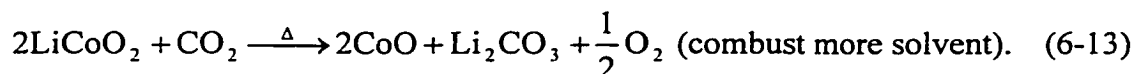
Figure 6.18 shows the x-ray profile of the 9 mg sample. An analysis of the profile indicates that the major products are Co metal and $CoCO_3$, as well as some residual CoO and a small amount of Li_2CO_3. These products can be obtained from one of Equation 6-10 through 6-13. In the 9 mg sample much more Co metal is formed since there has been the total decomposition of the $LiCoO_2$ product due to the higher pressures of CO_2 (Equation 6-11). The large amount of $CoCO_3$ formed is due to the production of a large amount of CoO initially and its reaction with the generated CO_2 on cooling (Equation 6-12).

The x-ray profile of the 15 mg sample is shown in Figure 6.19. Analysis of the x-ray data shows that large amounts of CoO and $CoCO_3$ are produced and small amounts of Li_2CO_3 and Co metal are also produced. Again these products can be obtained from the above equations and arise for the same reasons as the 9 mg sample. As shown in the previous four x-ray profiles, the solid to solvent mass ratio is important (and throughout this chapter) and thus Table 6.3 presents the mass of solid and solvent (electrolyte) used

for each DSC experiment using different solvents (or electrolytes that react similarly to the solvent).
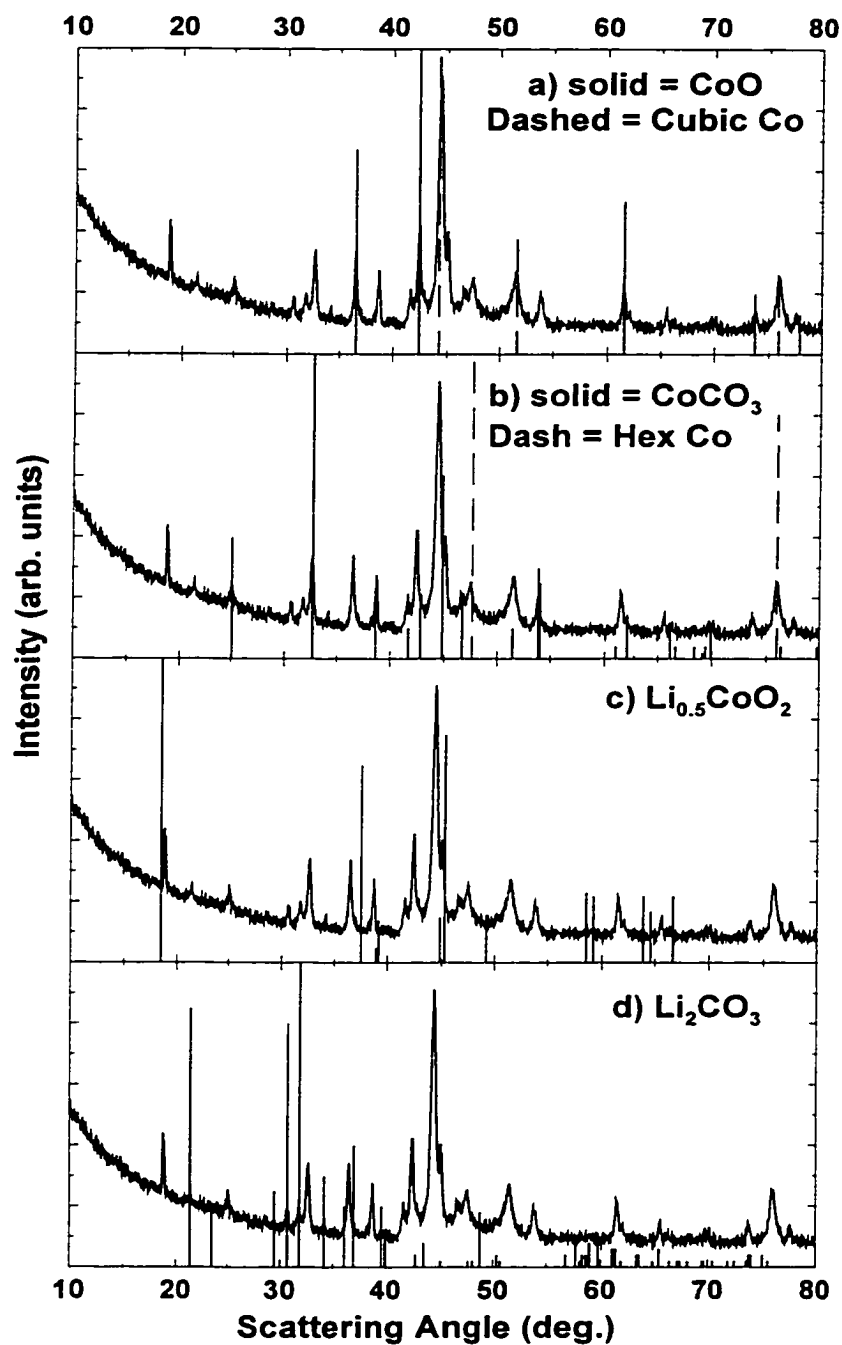
Figure 6.17. X-ray diffraction analysis of the 5 mg sample in Figure 6.12. Each panel contains the 5 mg diffraction profile and the indicated reference peaks.
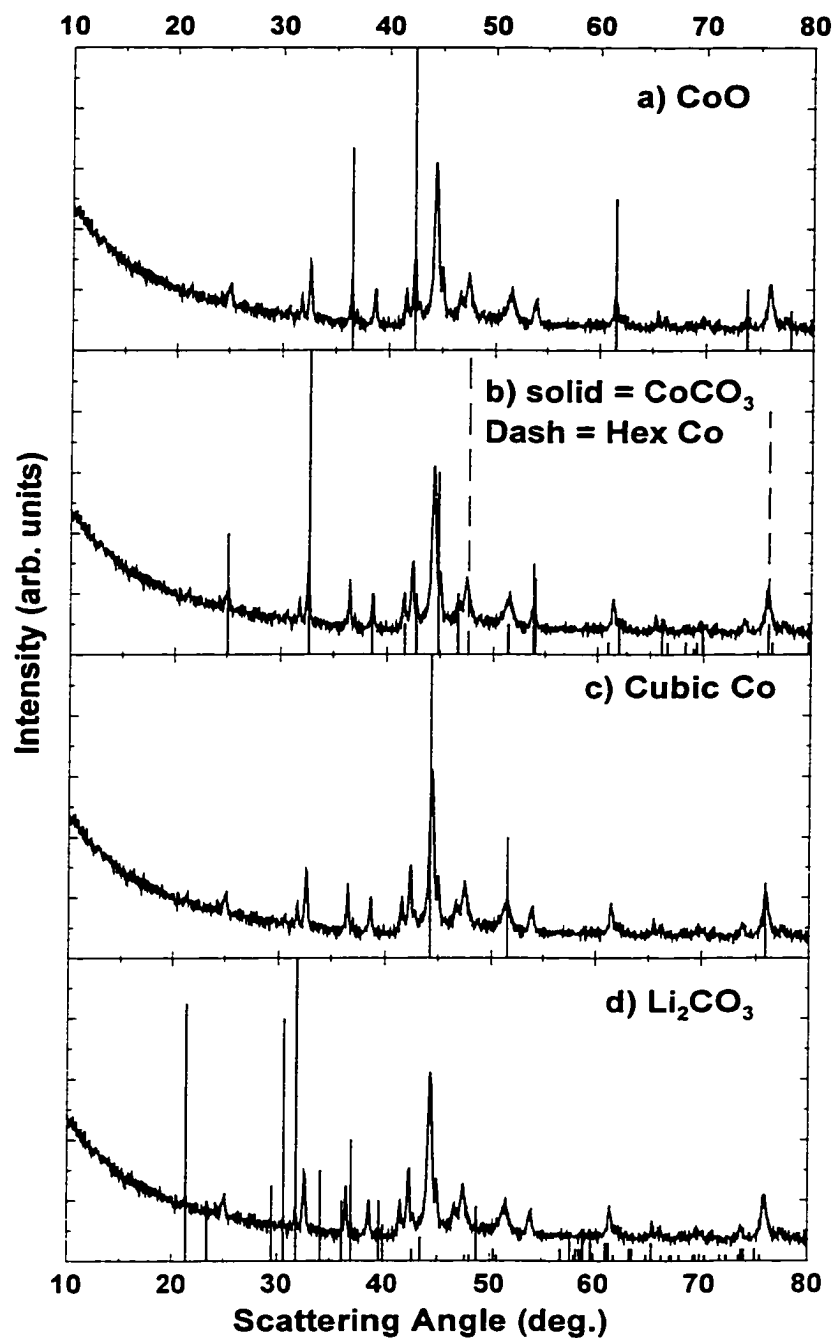
Figure 6.18. X-ray diffraction analysis of the 9 mg sample in Figure 6.12. Each panel contains the 9 mg diffraction profile and the indicated reference peaks.
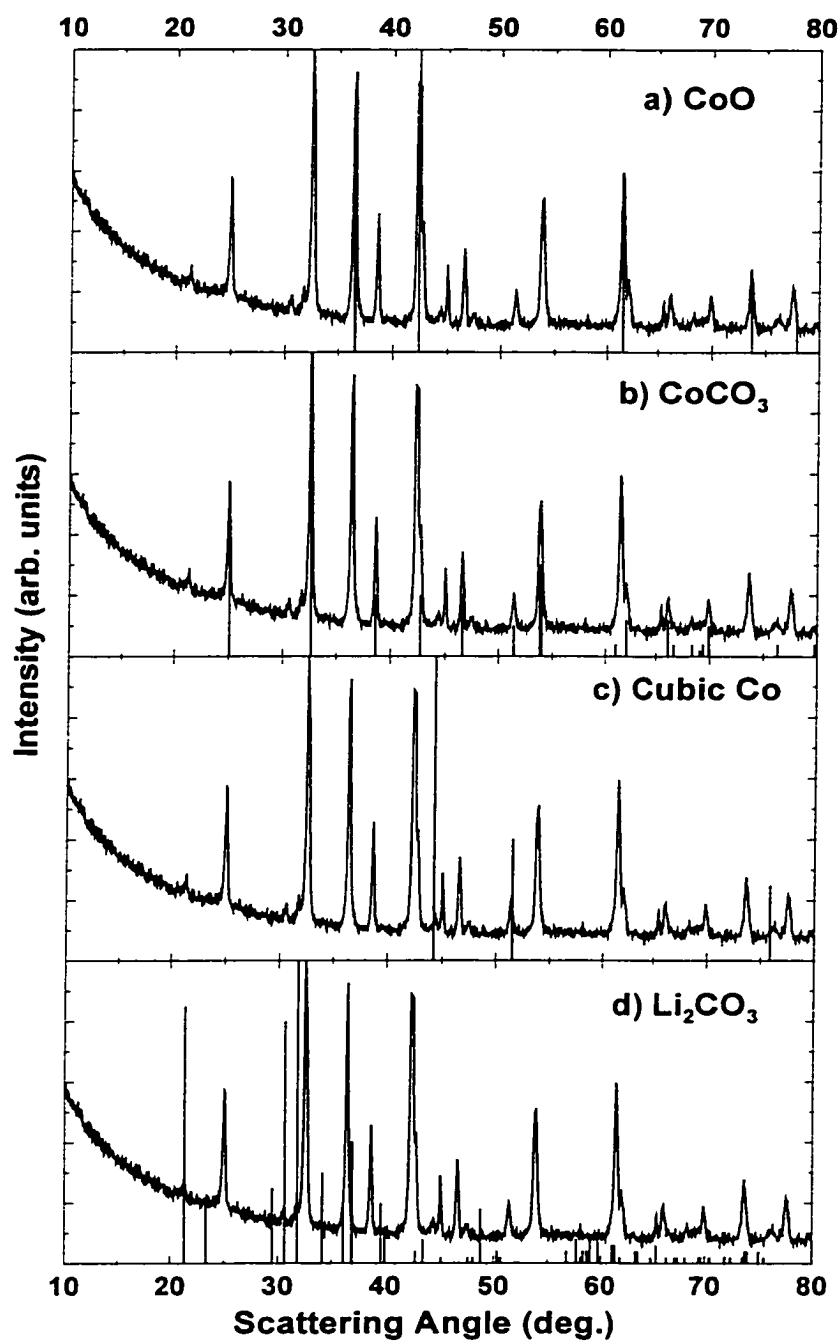
Figure 6.19. X-ray diffraction analysis of the 15 mg sample in Figure 6.12. Each panel contains the 15 mg diffraction profile and the indicated reference peaks.

Table 6.3 Analysis of the mass of $Li_{0.5}CoO_2$ and solvent added to DSC runs of indicated figures

Figure	Scan Rate °C/min	Curve	Mass $Li_{0.5}CoO_2$ (mg)	Mass Electrolyte (mg)
6.11	1	Solid	1	5
		Dash	2	5
	2	Solid	4	4
		Long/ Short dash	7	3
		Dash	3	4
	5	Solid	4	4
		Dash	2	3
		Long/ Short dash	2	3
	10	Solid	1	4
		Dash	6	4
6.26	1	Solid	5	1
		Dash	5	4
	2	Solid	10	5
		Dash	8	3
	5	Solid	7	2
		Dash	4	3
	10	Solid	5	6
		Short Dash	3	4
		Long Dash	7	2

Figure	Scan Rate °C/min	Curve	Mass $Li_{0.5}CoO_2$ (mg)	Mass Electrolyte (mg)
6.28	1	Solid	3	2(4)
		Dash	4	5
	2	Solid	3	1(5)
		Dash	4	5
	5	Solid	1	3
	10	Solid	3	5
		Dash	3	2
6.41	0.5M HQ	Solid	3	5
		Long/ Dash	5	4
		Short/ Dash	2	5
	1M HQ	Solid	3	4
		Dash	4	6
	0.5M BETI	Solid	3	4
		Dash	5	3
	1M BETI	Solid	6	6
		Long/ Dash	6	5
		Short/ Dash	2	5

An important trend in the above x-ray profiles is the development of $CoCO_3$ as the amount of $Li_{0.5}CoO_2$ introduced is increased. In Figure 6.20, the cooling curves of the 3, 5, 13, and 15 mg samples are shown. It is clear that there is increased reactivity with mass which signifies a larger amount of $CoCO_3$ being formed as shown by x-ray studies.
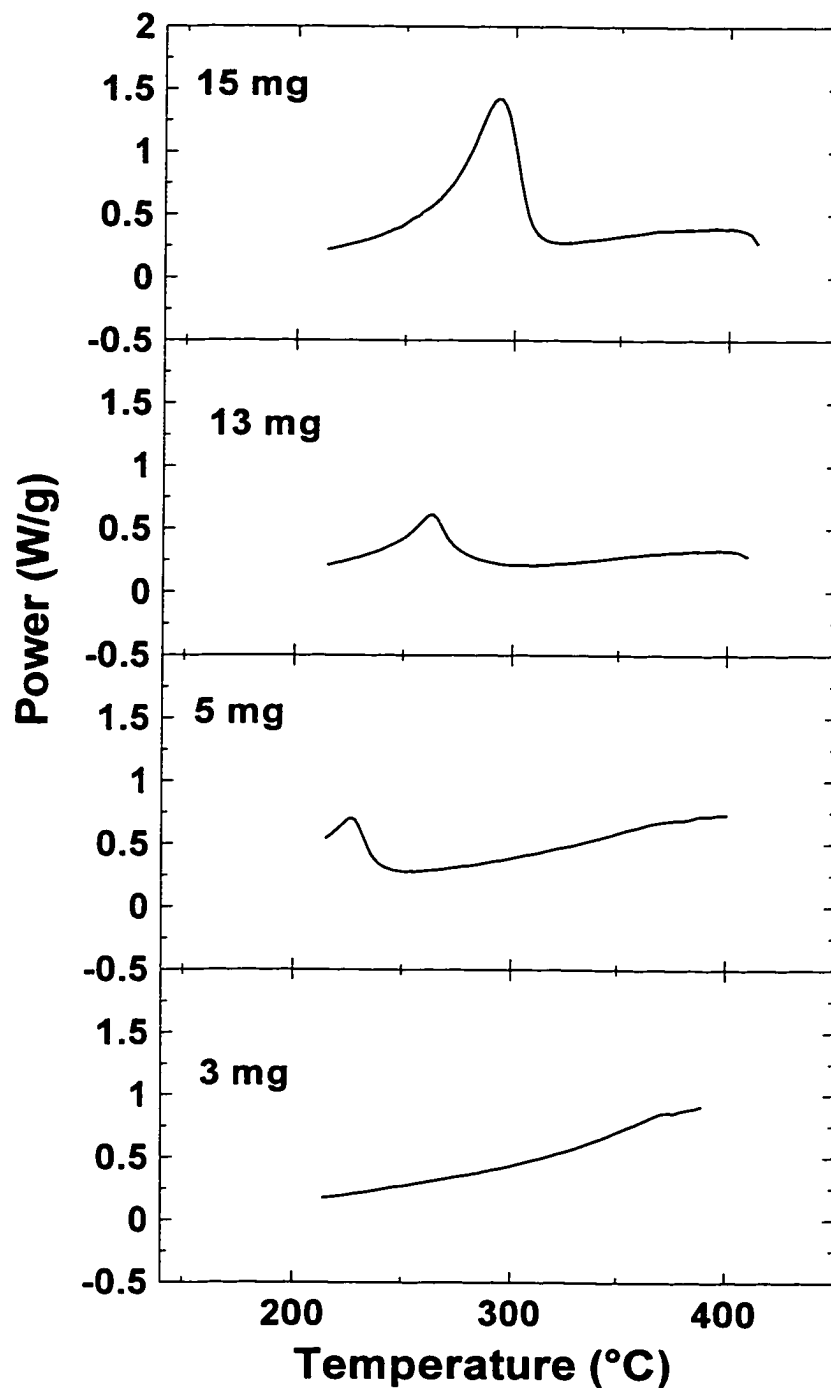
Figure 6.20. Cooling curves (15°C/min) of some of the samples from Figure 6.12.

In addition, an x-ray profile was obtained for the 7 mg sample that leaked during DSC analysis. The profile is shown in Figure 6.21 and shows the production of $LiCoO_2$, CoO and Co_3O_4 according to Equation 6-7, and 6-8. The generated gaseous products could not be contained nor could the solvent and thus there was neither further reduction of the cobalt species nor the generation of carbonates.
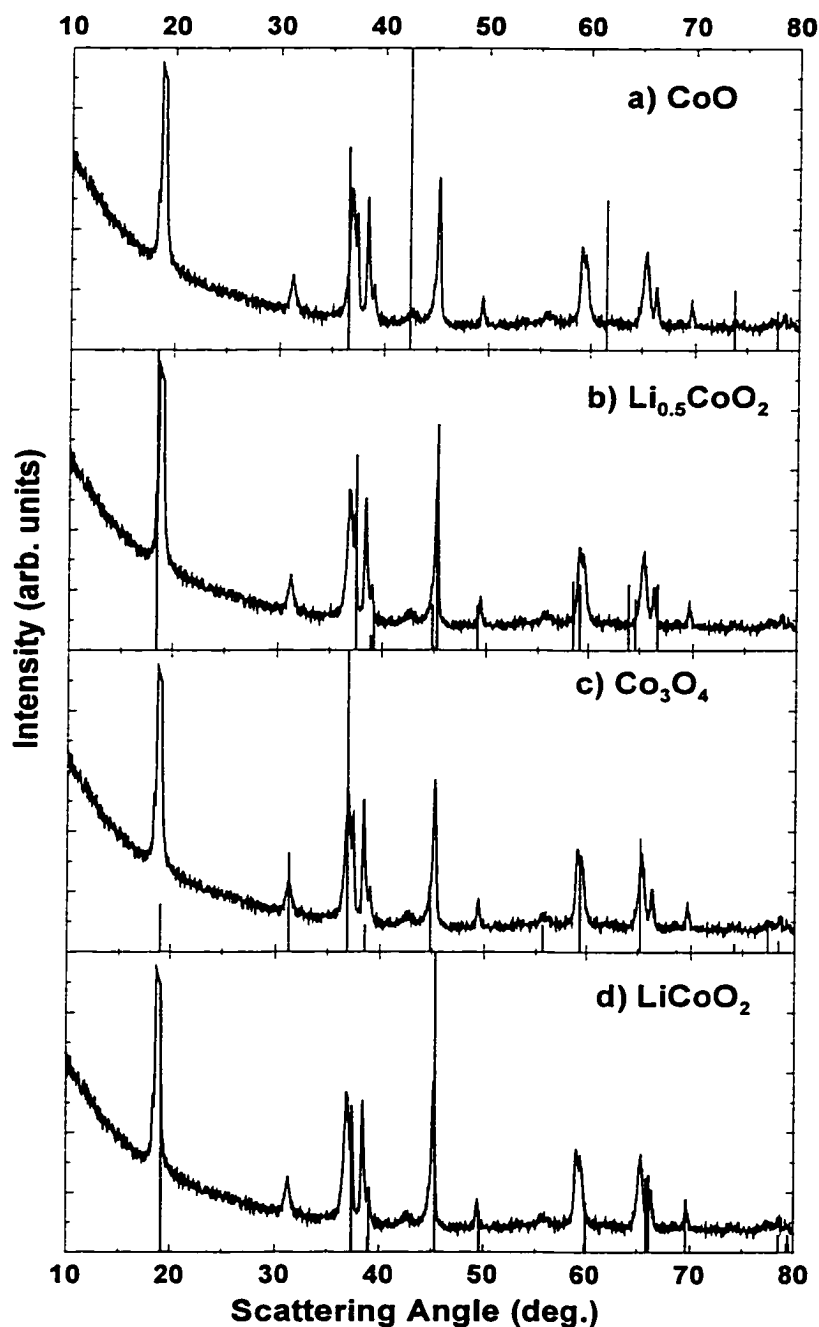
Figure 6.21. X-ray diffraction analysis of the 7 mg sample (leaked) in Figure 6.12. Each panel contains the 7 mg diffraction profile and the indicated reference peaks.

To prove that some of the products in Equation 6-7 to Equation 6-14 are reactive at high temperatures in the EC/DEC (33/67) solvent, pure Co, CoO, $LiCoO_2$, Co_3O_4 and $CoCO_3$ were heated in EC/DEC at 5°C/min to 425°C. The DSC results for these heating experiments are shown in Figure 6.22 and show that they do react exothermically in this solvent at temperatures above 300°C. The dry Co, CoO, $LiCoO_2$ and Co_3O_4 (no solvent present) do not show any reactivity at these temperatures, while $CoCO_3$ decomposes. An x-ray analysis (not shown) of the heating experiments in EC/DEC shows that $CoCO_3$ and Co are formed from CoO (from Equations 6-10 and 6-12) with residual CoO. On heating $LiCoO_2$ in the presence of EC/DEC, Li_2CO_3, CoO, Co, and some of $CoCO_3$ and Co_3O_4 (from Equation 6-7 to Equation 6-13, not 6-9) were formed with some residual $LiCoO_2$ remaining. When heating Co_3O_4 in EC/DEC, CoO was formed with residual Co_3O_4 remaining. Also, heating $CoCO_3$ in EC/DEC resulted in Co and CoO being formed. The cooling curves in Figure 6.22 (shown as short dashed lines) do not show any appreciable reactivity except for the CoO sample. The reactivity seen in the CoO sample is believed to be due to Equation 6-12, where residual CoO reacts with the generated CO_2 to form $CoCO_3$.

6.5 Summary of Reaction of $Li_{0.5}CoO_2$ with EC/DEC (33/67)

In the ARC, where only the low temperature (<260°C) reactions can be analyzed, the electrode decomposes to CoO.

$$Li_{0.5}CoO_2 \xrightarrow{\Delta} 0.5LiCoO_2 + \frac{1}{6}Co_3O_4 + \frac{1}{6}O_2, \qquad (6\text{-}7)$$

$$Co_3O_4 \xrightarrow{\Delta, solv} 3CoO + \frac{1}{2}O_2, \qquad (6\text{-}8)$$

$$\frac{5}{2}O_2 + C_3H_4O_3 \xrightarrow{\Delta} 3CO_2 + 2H_2O. \qquad (6\text{-}9)$$
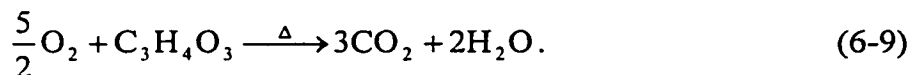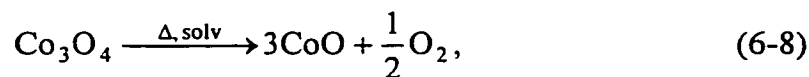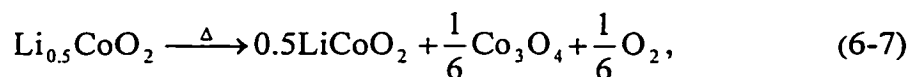
This decomposition is also seen in the DSC and gives rise to the exothermic activity between 200 and 250°C. Upon further heating, in a sealed environment, there is further reduction to cobalt metal (if sufficient solvent is present) and reaction of $LiCoO_2$ with the generated CO_2 to form a number of species including CoO, Co and Li_2CO_3.
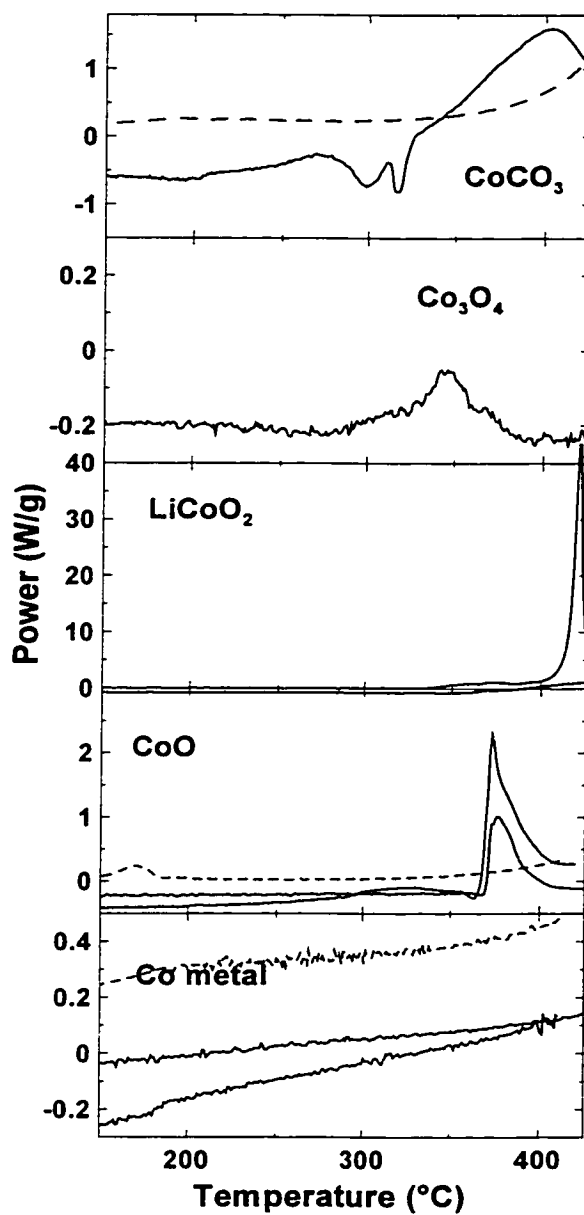
Figure 6.22. DSC of the indicated species in EC/DEC (33/67, vol/vol) at 5°C/min. Cooling curves (15°C/min) are shown as dashed lines.

$$CoO \xrightarrow{\Delta, solv} Co + \frac{1}{2}O_2 \tag{6-10}$$

$$2LiCoO_2 + xCO_2 \xrightarrow{\Delta, solv} Li_2CO_3 + 2Co + \frac{3}{2}O_2 \tag{6-11}$$
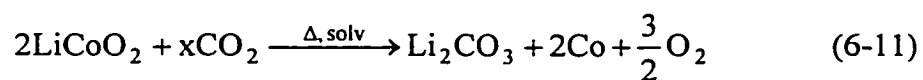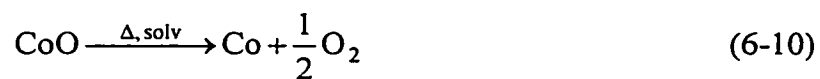
Upon cooling, CoO will react with high pressures of CO_2 to form $CoCO_3$.

$$CoO + CO_2 \longrightarrow CoCO_3 \tag{6-12}$$

An important aspect of the electrode reaction with solvent is the electrode mass to solvent mass ratio. When the mass of electrode is low compared to the mass of solvent a large exothermic reaction occurs above 300°C forming a large amount of Co metal as compared to other species. The amount of carbonate species formed is low since the amount of generated CO_2 is low and most of the CoO has been reduced to Co. When the mass of electrode is larger than the mass of solvent, the remaining solvent does not fully reduce the cobalt compounds to Co metal since a large portion of the fresh solvent is used during the low temperature (<250°C) activity. This lower reducing power causes a reduction in the high temperature activity and thus a large amount of CoO is present in addition to $CoCO_3$ (arising from the reaction of CoO with CO_2 during cooling).

6.6 Reaction of $Li_{0.5}CoO_2$ with Other Solvents

The reaction of $Li_{0.5}CoO_2$ was also investigated in another solvent, EC/PC (50/50, vol/vol,). Figure 6.23 shows the results of ARC experiments on $Li_{0.5}CoO_2$ in the presence of EC/PC (50/50). These profiles are very similar to those of $Li_{0.5}CoO_2$ in EC/DEC (33/67, Figure 6.8) and again a rapid rise in self-heating rate is seen at 130-140°C such that the ARC could no longer track the exotherm properly. An expansion of the ARC sample cell due to the generated gases from the decomposition of the solvent is seen. Figure 6.24 shows reducing the amount of oxidant placed in the sample cell reduces the temperature rise seen in the ARC. Again, the temperature rise versus the inverse heat capacity of the samples in Figure 6.24 was plotted in Figure 6.25. The data are shown in Table 6.4 and have been calculated using Equation 6-3, where a value of 1.3 J/gK is used for the heat capacity of the EC/PC solvent. The slope of the graph is 550 J/g ± 60J/g, which is in good agreement with the heat of reaction determined by the ARC experiment for the EC/DEC samples while the same disagreement between the calculated values (Equation 6-5, 6-6) and experiment occurs.
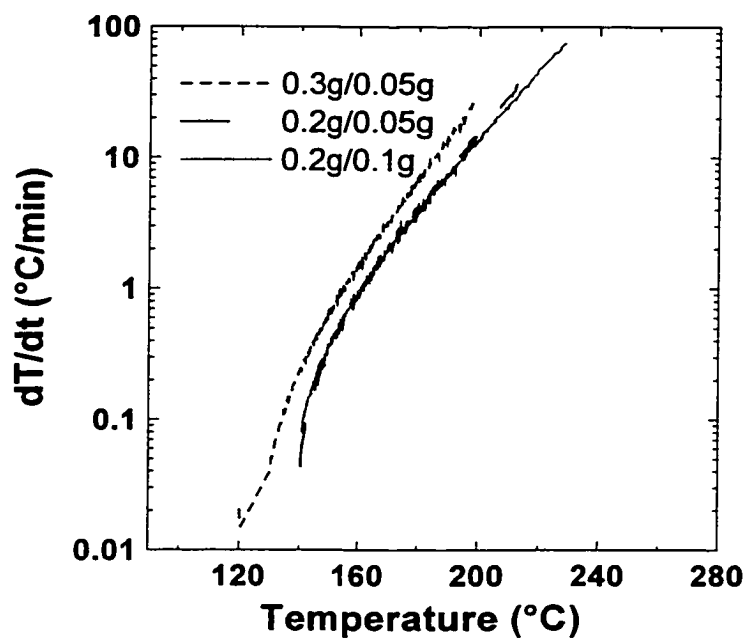
Figure 6.23. ARC profiles of $Li_{0.5}CoO_2$ in the presence of EC/PC (50/50, vol/vol) solvent at the indicated masses.
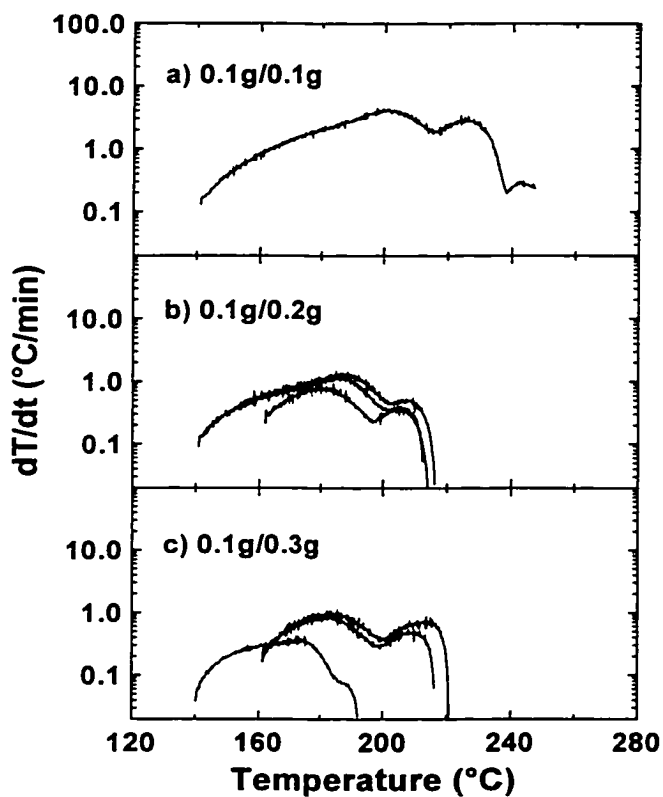
Figure 6.24. Self-heating rate versus temperature of 0.1 g of $Li_{0.5}CoO_2$ in the presence of various amounts of added solvent (EC/PC, 50/50): panel a) 0.1 g solvent; panel b) 0.2 g solvent; panel c) 0.3 g solvent.
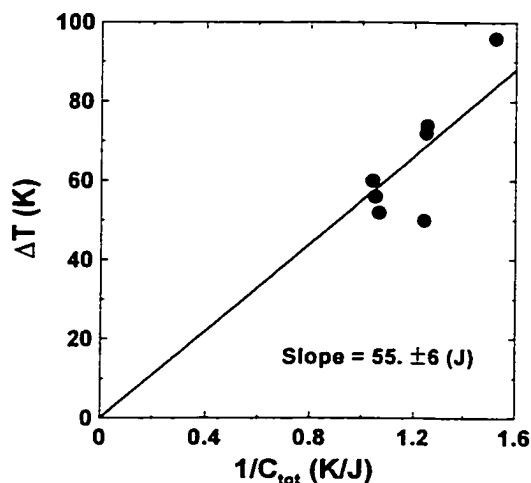
Figure 6.25. Temperature rise, ΔT versus inverse heat capacity $(1/C_{tot})$ of the samples described by the data shown in Figure 6.24. The straight line is the best fit of the equation $\Delta T = h/C_{tot}$.

Table 6-4. Analysis of the results in Figure 6.24.

Trial	Solvent mass (g)	$Li_{0.5}CoO_2$ mass (g)	ΔT (K)	C_{tot} (J/K)
1	0.1005	0.100	96	0.658
2	0.1989	0.101	74	0.799
3	0.2002	0.101	72	0.801
4	0.2060	0.098	50	0.807
5	0.3150	0.099	60	0.963
6	0.3059	0.102	56	0.953
7	0.2989	0.099	52	0.940

Figure 6.26 shows DSC results of 3-10 mg of $Li_{0.5}CoO_2$ in the presence of 4-8 mg of EC/PC (50/50, vol/vol). The results are similar to Figure 6.11, but the initial instability shows two well-resolved exothermic peaks and the high temperature instability occurs near 300°C, some 20 degrees lower than with EC/DEC (33/67, vol/vol). The results indicate that EC/PC (50/50, vol/vol) is a stronger reducing agent than EC/DEC (33/67, vol/vol). Again on cooling the DSC samples, an exothermic event occurs. In addition, a dependence on the electrode to solvent mass is seen (Table 6.3). The results of the heating experiments described in Section 6.4 are shown in Figure 6.27 and confirm the stronger reducing power of the EC/PC solvent solution, since reduction occurs at a lower temperature in EC/PC than in EC/DEC (Figure 6.22). $LiCoO_2$ in EC/PC was fully

reduced to Co metal, $CoCO_3$ and Li_2CO_3 with no residual $LiCoO_2$ remaining, while CoO was reduced to Co and some $CoCO_3$ is formed. Co_3O_4 reacted at high temperature in EC/PC to form CoO, while heating $CoCO_3$ formed CoO and Co metal. The cooling curves in Figure 6.27 (shown as short dashed lines) do not show any appreciable reactivity except for the CoO sample. The reactivity seen in the CoO sample is believed to be due to Equation 6-12, where residual CoO reacts with the generated CO_2 to form $CoCO_3$.
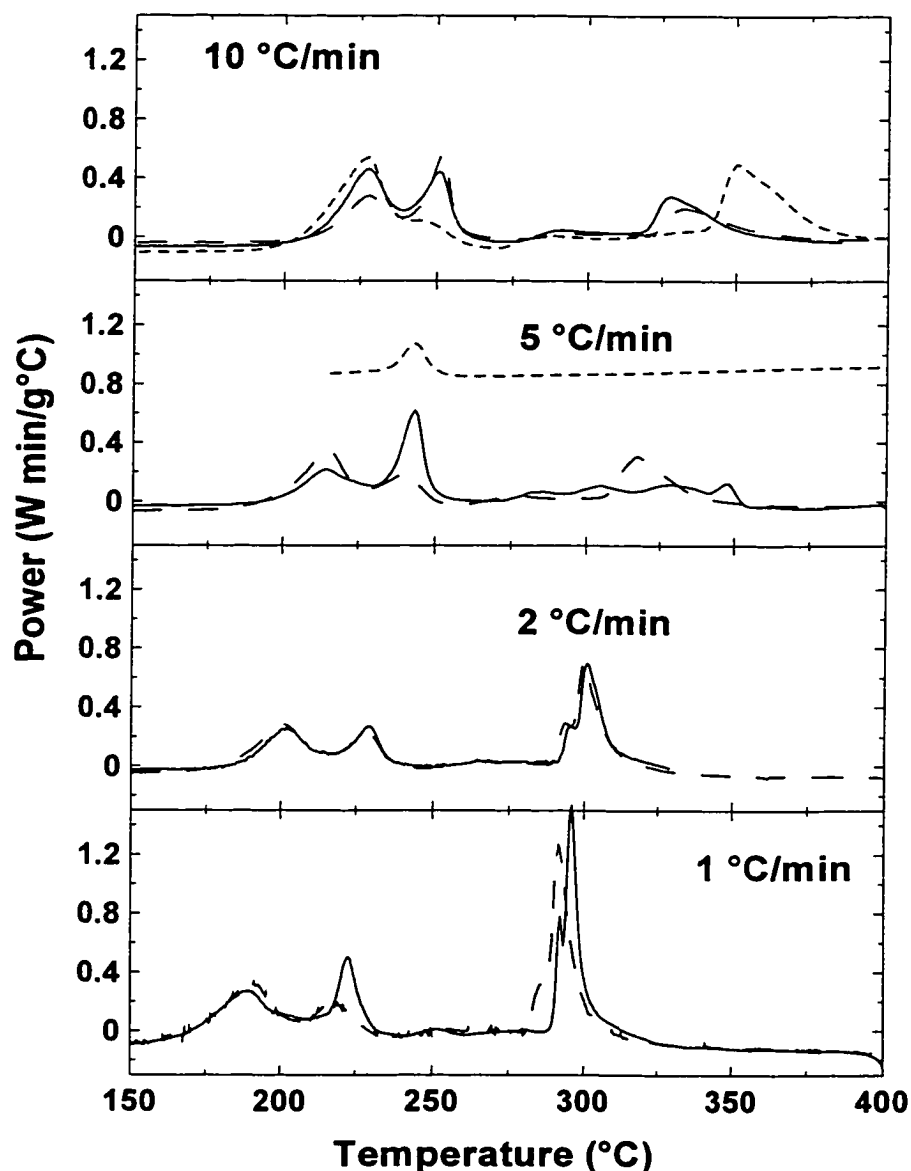
Figure 6.26. DSC profiles of $Li_{0.5}CoO_2$ in the presence of EC/PC (50/50, vol/vol) solvent at indicated heating rate. The dashed curve in the 5°C/min panel represents a typical cooling profile (15°C/min).
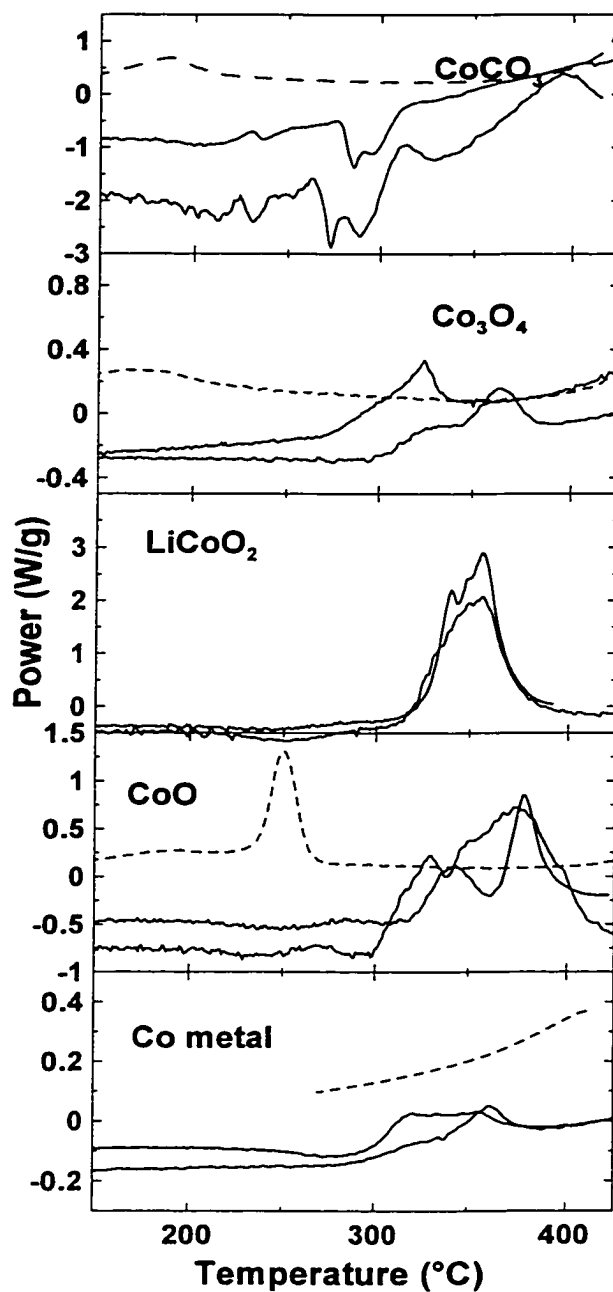
*Figure 6.27. DSC of the indicated species in EC/PC (50/50, vol/vol) at 5°C/min.
Cooling curves (15°C/min) are shown as short dashed lines.*

To date, the solvent systems analysed consisted of a two component organic solvent and thus a single component solvent was analysed to determine if some parts of the decomposition profile could be assigned to one component over another. DSC profiles of $Li_{0.5}CoO_2$ in the presence of pure propylene carbonate (PC) are shown in Figure 6.28. The profiles are very similar to those obtained in EC/DEC and EC/PC and

thus no distinguishing reducing behaviour could be detected for a single pure solvent. Also, the high temperature exothermic behaviour occurs near 300°C, which is lower than the EC/DEC solvent, indicating the stronger reducing power of PC based solvents.
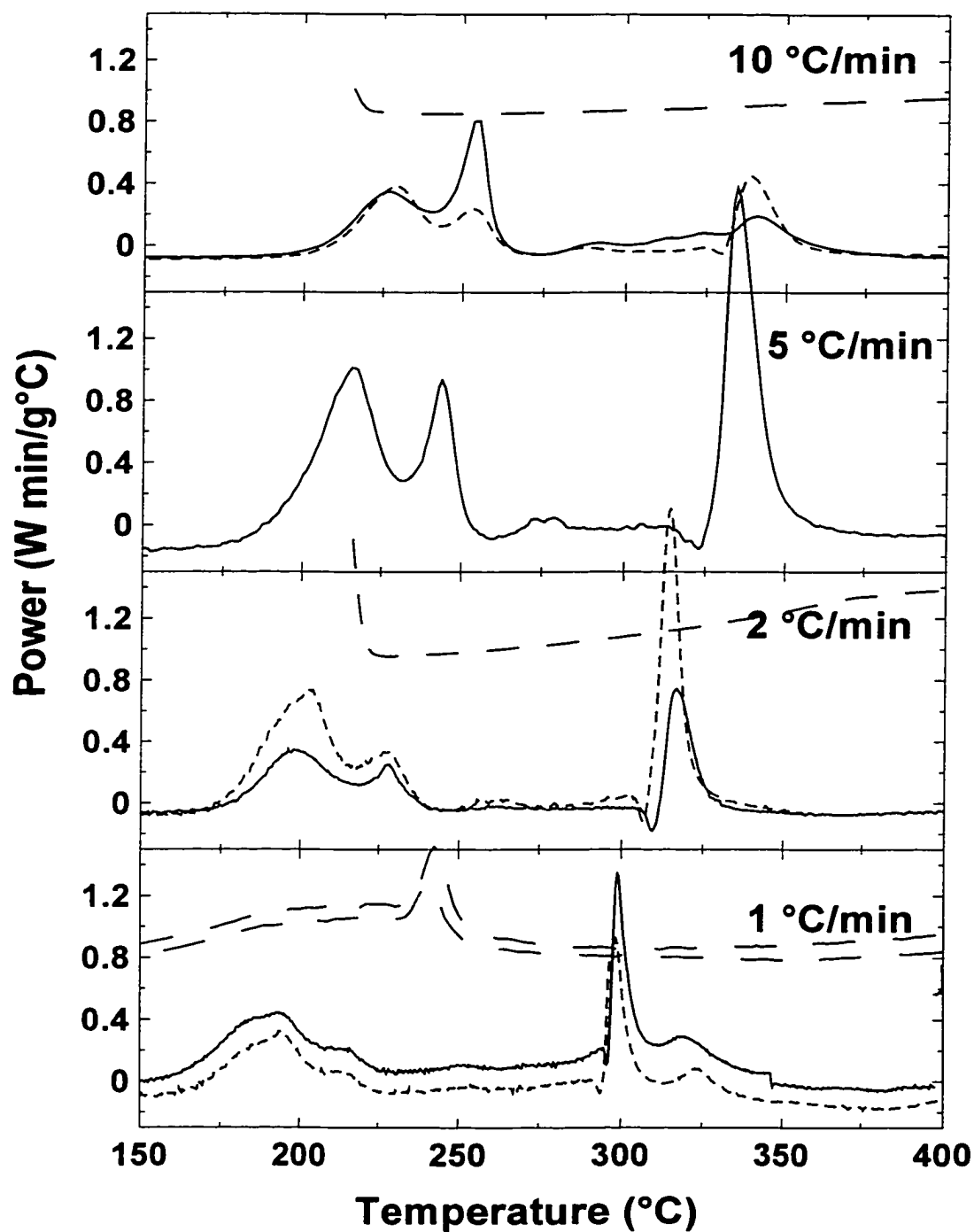
Figure 6.28. DSC profiles of $Li_{0.5}CoO_2$ in the presence of PC solvent at indicated heating rate. Long dashed curves in the panels represent cooling profiles (15°C/min), while short dashed curves are duplicate samples.

6.7 Affect of a LiPF$_6$ Electrolyte

The introduction of the lithium salt in the organic solvent might affect the stability of the electrode and solvent. The self-heating rate of 0.1 g ($\pm$ 5%) of EC/DEC (33/67, vol/vol) electrolyte with various concentrations of LiPF$_6$ is shown in Figure 6.27. The data suggest that at low electrolyte concentration (0-0.5M) there is little to no self-heating of the sample. As the concentration of LiPF$_6$ in EC/DEC (33/67, vol/vol) increases the electrolyte shows stronger self-heating, but the self-heating rates are small and thus the self-heating of the electrolyte should not dramatically affect any self-heating of the solid electrode.
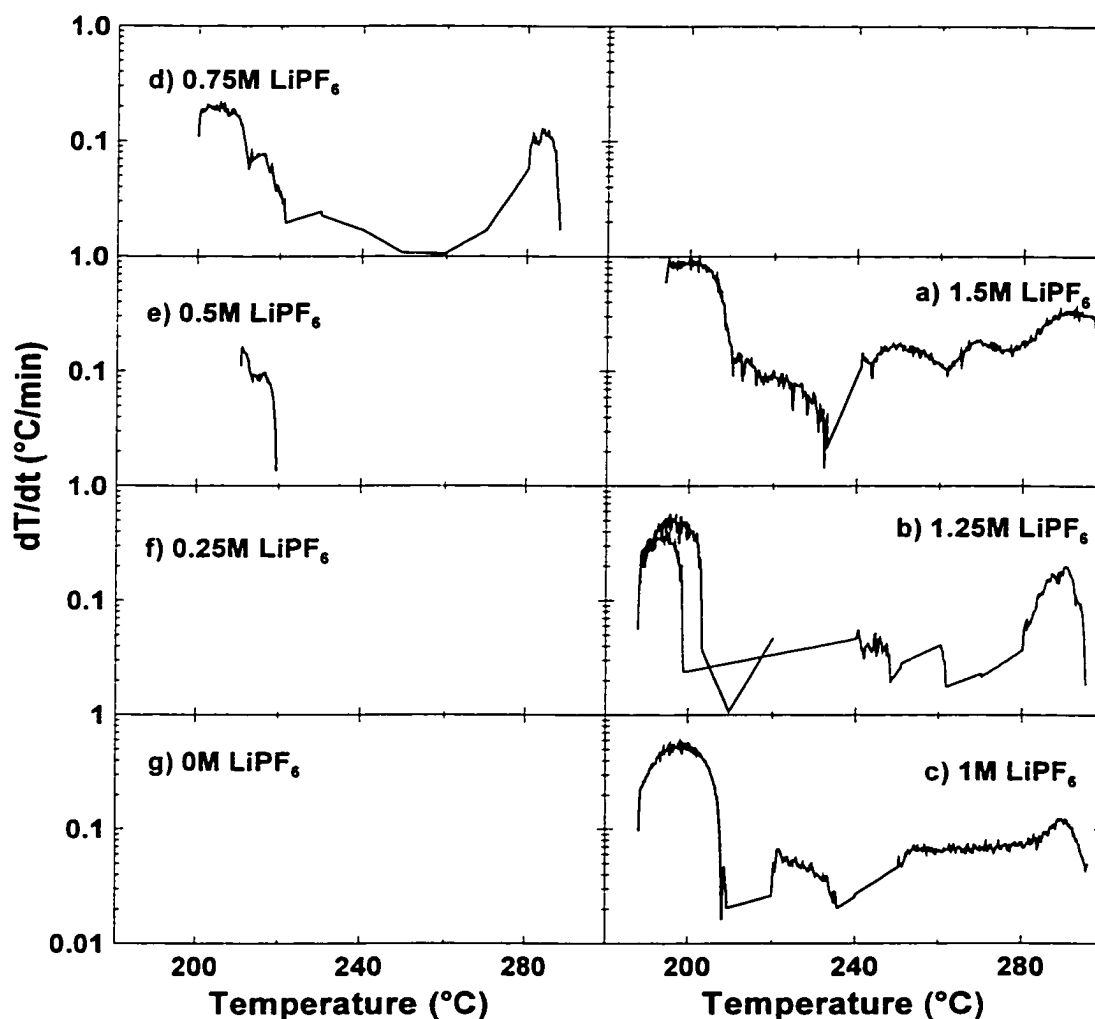
Figure 6.29. Self-heating rate profiles of 0.1 g of LiPF$_6$ in EC/DEC (33/67) at indicated concentration of LiPF$_6$.

An examination of the temperature versus time profiles obtained from the ARC, shown in Figure 6.30, demonstrates an endothermic behaviour before detection of the exotherm. A DSC analysis of the electrolyte was also performed and the results are shown in Figure 6.31. An endothermic behaviour is observed to precede the exothermic behaviour. The results show that as the concentration of $LiPF_6$ increases the reactivity of the electrolyte increases and reaches a near steady state condition above a concentration of about 0.75M. The results in Figures 6.29, 6.30 and 6.31 are discussed further below.
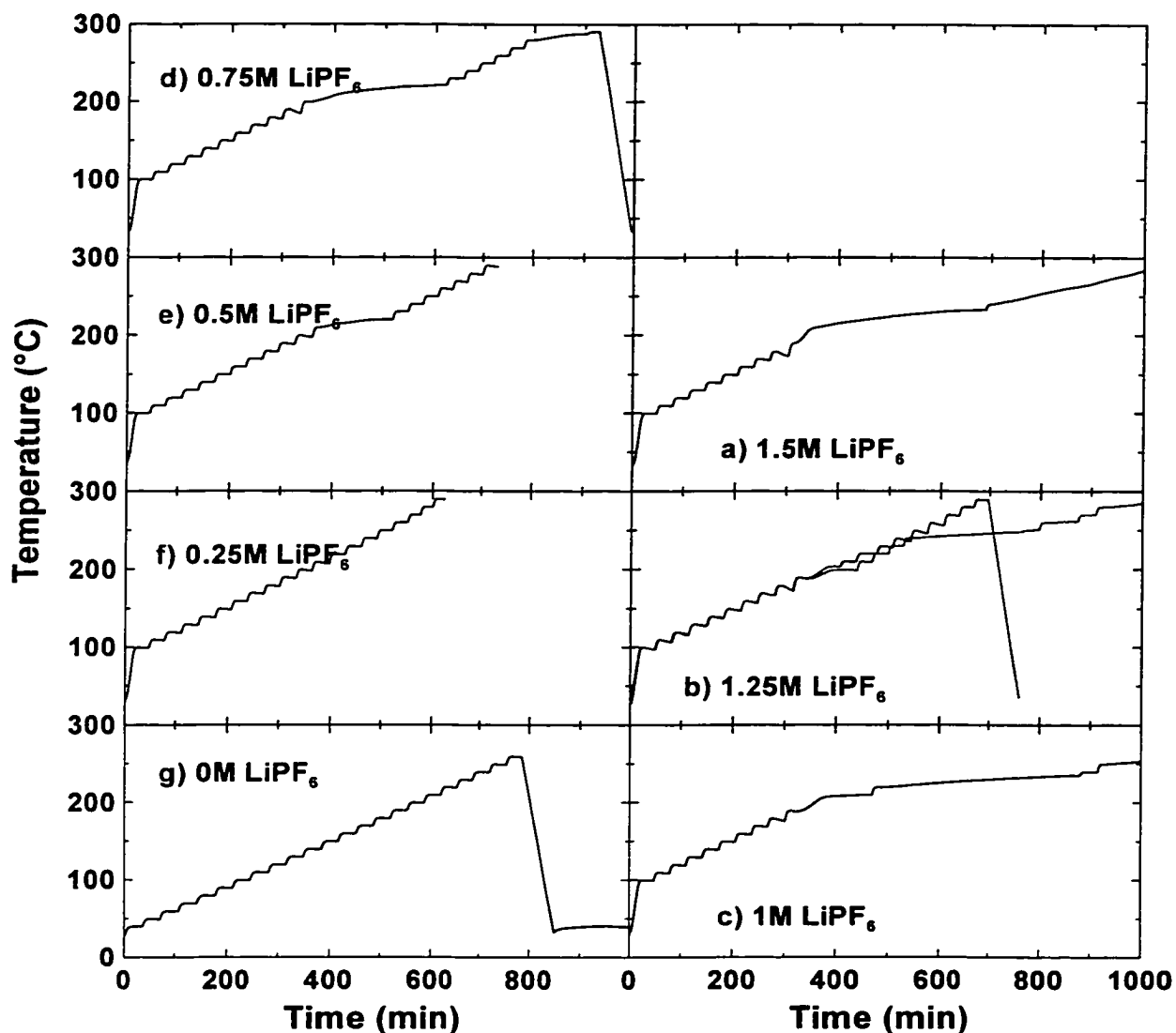
Figure 6.30. Temperature versus time profiles of 0.1 g of $LiPF_6$ in EC/DEC (33/67) at the indicated concentrations of $LiPF_6$.
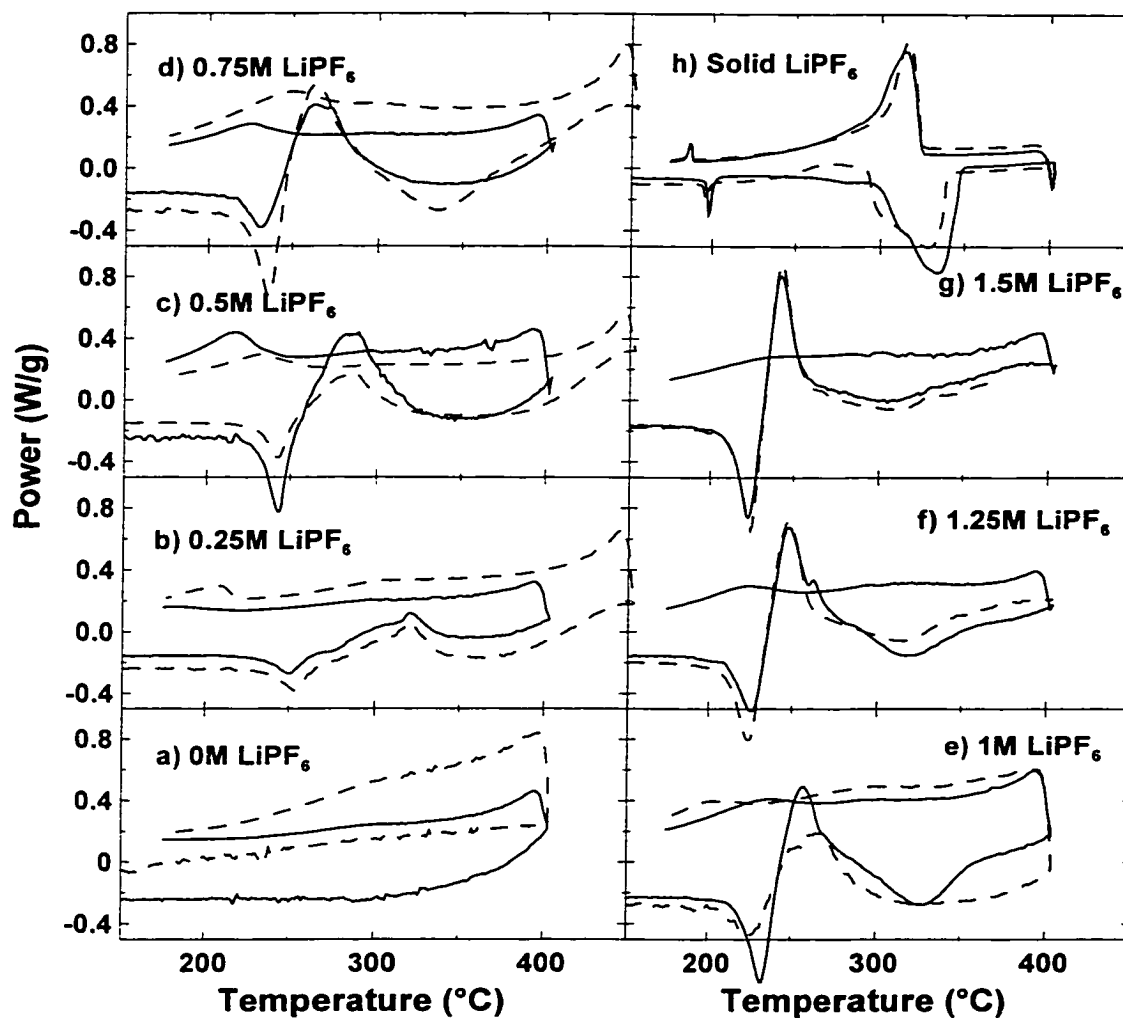
Figure 6.31. DSC of EC/DEC (33/67) with various concentrations of LiPF₆ at 5°C/min (heating and cooling). Duplicate samples are shown as dashed lines.

LiPF₆ is known to be thermally unstable [94], decomposing following:

$$LiPF_{6(s)} \rightleftharpoons LiF_{(s)} + PF_{5(g)}. \qquad (6-14)$$
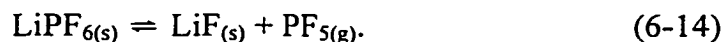
A DSC of solid LiPF₆ (panel h, Figure 6.31) gave a melting point of 200°C and a reversible decomposition peak near 300°C. The welded stainless steel tube allowed for the containment of the decomposition gas and thus the decomposition of solid LiPF₆ according to Equation 6-14 was found to be reversible.

When LiPF₆ was placed in the organic solvent (EC/DEC, 33/67, vol/vol) an irreversible decomposition occurred with both endothermic (230-250°C) and exothermic events (250-320°C).

In the organic solvent the decomposition of $LiPF_6$ by Equation 6-14 also occurs [94] and hence PF_5 will be present in the electrolyte at high temperature. Water, that is present as an impurity in the electrolyte, reacts with the PF_5 that is formed according to [95],

$$PF_5 + H_2O \rightarrow 2HF + PF_3O. \qquad (6\text{-}15)$$
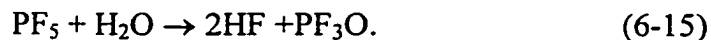
The thermal events near 230°C are likely due to the decomposition and polymerization of the ethylene carbonate solvent by HF. This polymerization leads to polyethylene-oxide-like polymers (Equation 6-16) [96, 97]. The ring-opening polymerization of cyclic carbonates (e.g. EC, PC) has been studied as an alternative synthetic route to obtain polycarbonates by partial elimination of carbon dioxide. This partial elimination results in poly(oxyethylene-co-ethylene carbonate)s and the extent of CO_2 loss depends on the initiator. In $LiPF_6$ electrolytes, the polymerization reaction can be simplistically pictured as following

$$n \quad \underset{\text{[cyclic carbonate structure]}}{\bigcirc} \quad \xrightarrow{\ \text{HF}\ } \quad \left[CH_2\text{-}CH_2\text{-}O \right]_n \ + n\, CO_2 \qquad (6\text{-}16)$$
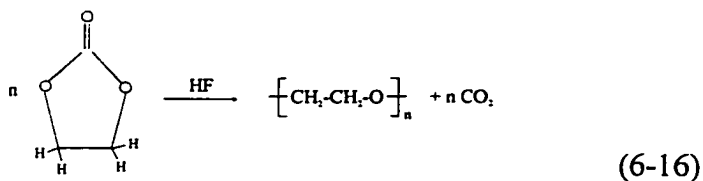
where a full elimination of CO_2 is assumed. It is possible that partial elimination of CO_2 in $LiPF_6$ electrolyte does occur, but the details of this polymeriztion mechanism have not been investigated here. The important result is the observation that a polyethylene-oxide-like polymer is observed with ethylene carbonate.

On heating a 1M $LiPF_6$ EC/DEC (33/67) solution near 120°C, in a sealed glass vial, a yellow/brown solution developed with some clear rubbery precipitate on the side of the container. Heating a vial of 0.5M $LiPF_6$ in EC/DEC (33/67) also produced a yellow/brown solution but the amount of polymer produced was less. A picture of the two vials is shown in Figure 6.32. When the concentration of HF was low (lower molarity electrolyte) the amount of polymer product was lower for nominally identical reaction conditions, thus the HF was either directly involved in the polymerization or the kinetics are dependent on the concentration of HF. In any event, it was clear that more polymers were obtained from the higher concentration of electrolyte.
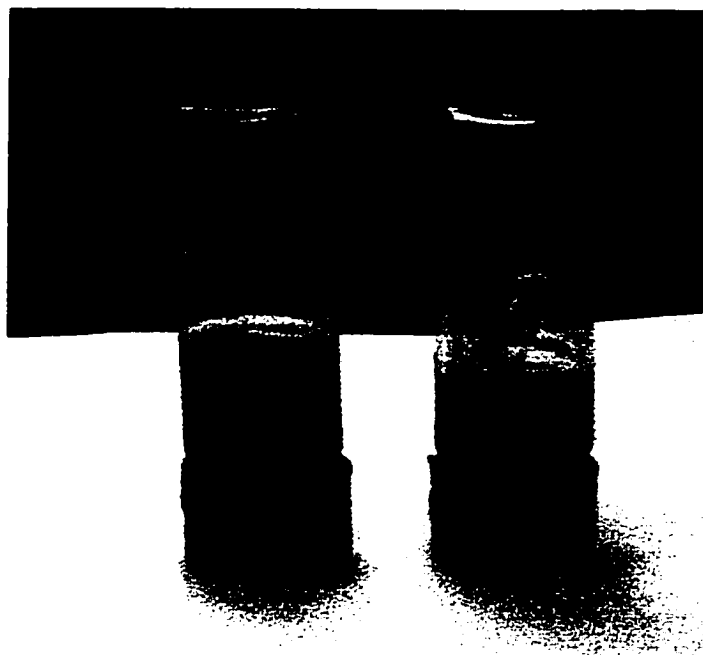
Figure 6.32. Heating experiment on 1M LiPF₆ (left) and 0.5M LiPF₆ (right) in EC/DEC (33/67, vol/vol).

The two different thermodynamic events occurring in the DSC profiles of Figure 6.31 could be due to the multi-component nature of the organic solvent. One-component solvent electrolyte mixtures of 1M LiPF$_6$ were made for DEC, PC, and EC. These electrolytes were then analyzed in the DSC and their results are shown in Figure 6.33. Exothermic peaks at 275°C and 295°C are obtained for EC and PC respectively. A complex decomposition pattern that entails an endothermic process near 225°C, followed by an exothermic process (260°C) and another endothermic process (310°C) is obtained for DEC. A comparison between the results of Figure 6.33 with those of panel e in Figure 6.31 clearly indicate that the reactivity of the 1M LiPF$_6$ EC/DEC electrolyte is due to the combination of the reactivity for both LiPF$_6$ in EC and LiPF$_6$ in DEC electrolyte.

Recently, researchers at University of South Carolina have analysed LiPF$_6$ electrolytes with EC and ethyl-methyl carbonate (EMC) solvents by DSC [98]. Their stainless steel sample cells did not leak. The same trend in reactivity with increasing LiPF$_6$ concentration is seen, except that the steady state conditions for reactivity occurs near 1M LiPF$_6$ concentration in EC/EMC (50/50). They also showed little change in reactivity when the volume ratio of EC to EMC changed. In addition, they analyzed

electrolytes of the individual solvents at different $LiPF_6$ concentrations and an increase in reactivity is seen until the reactivity stabilises near 1M $LiPF_6$ for both solvents.
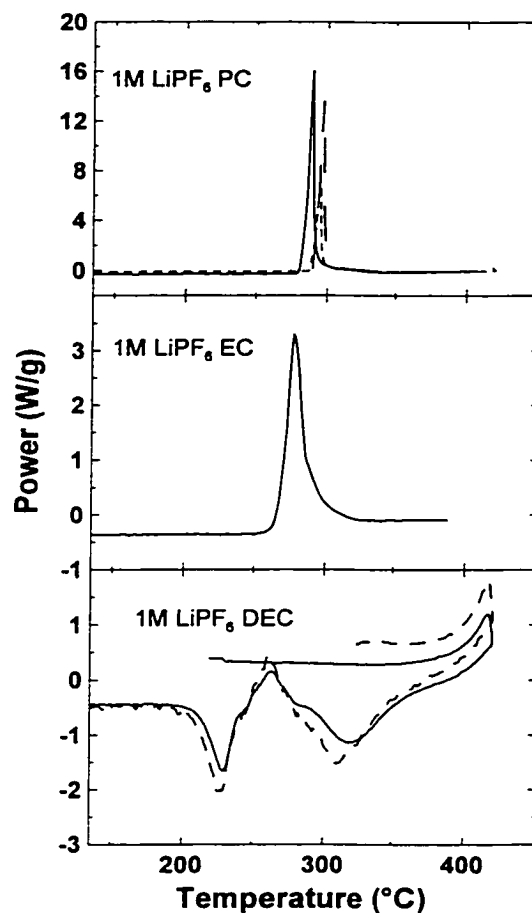
Figure 6.33. DSC of 1M $LiPF_6$ in PC, 1M $LiPF_6$ in EC and 1M $LiPF_6$ in DEC at 5°C/min. Duplicate runs are shown as dashed lines.

Heating experiments were also performed on 1M $LiPF_6$ solutions of EC and DEC in sealed vials. After heating the 1M $LiPF_6$ DEC solution, a white cloudy precipitate formed, while the EC electrolyte showed no reaction (still clear and colourless). The DEC precipitate was not characterized, but was likely a product of polymerization resulting from the water contamination in the solvent. The EC electrolyte was prepared from a pure crystalline solid solvent and thus was expected to contain very little water contamination. When the vial containing 1M $LiPF_6$ in EC was spiked with water and reheated, a large portion of polymer was formed (Equation 6-16) and the solution turned brown. This demonstrates that polymeric species are formed at elevated temperatures

when water impurities are contained within the electrolyte (promotes the production of HF, Equation 6-15). When the vial containing 1M LiPF$_6$ in DEC was spiked with water and reheated, a large amount of white polymer-like precipitate formed and thus the polymer formed in EC/DEC LiPF$_6$ solutions could be due to a combination of the two solvent products.
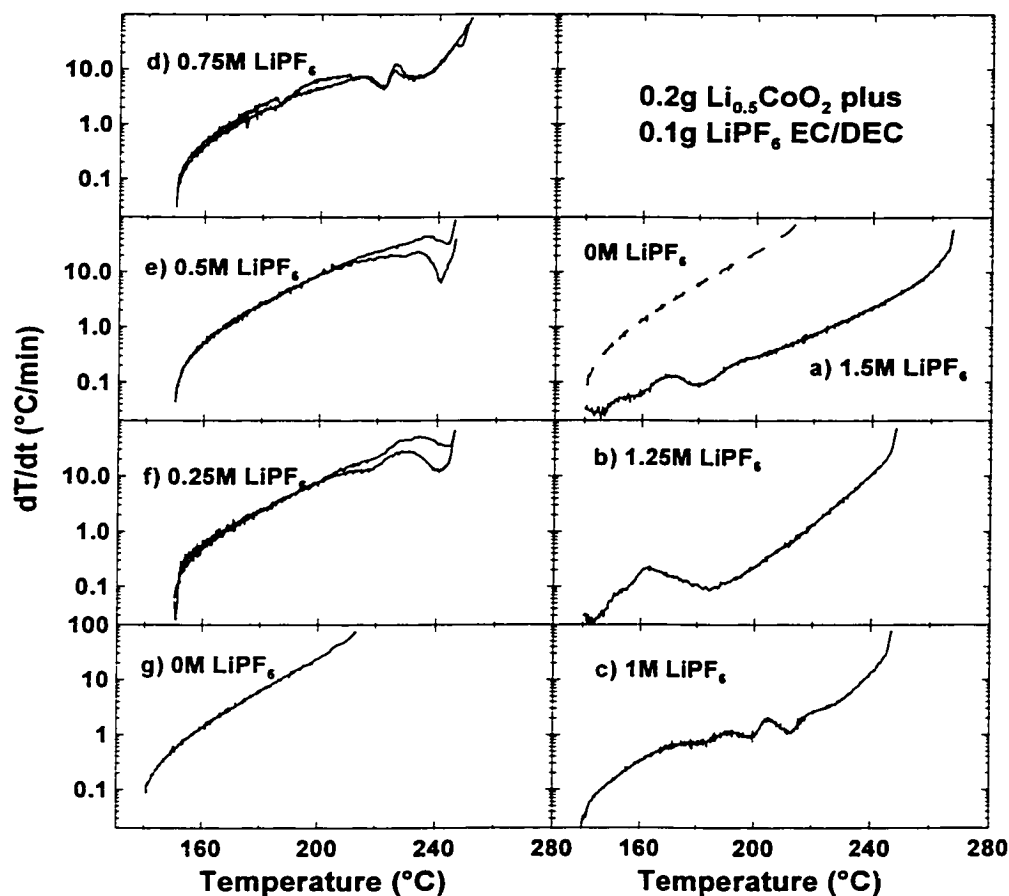
Figure 6.34. Self-heating rate profiles of 0.2 g of Li$_{0.5}$CoO$_2$ in the presence of 0.1 g of LiPF$_6$ in EC/DEC (33/67) with various concentrations of LiPF$_6$. In panel a) the dashed line is that of the 0M LiPF$_6$ sample.

Now that the thermal stability of the electrolyte itself had been studied, the effect of adding the Li$_{0.5}$CoO$_2$ electrode was investigated. Figure 6.34 shows the self-heating rate versus temperature for samples of 0.2 g of Li$_{0.5}$CoO$_2$ in 0.1 g of electrolyte having different concentrations of LiPF$_6$ in EC/DEC 33/67 (vol/vol). For some electrolyte concentrations, the results of several experiments are shown. At low molarities there is a very rapid rise in self-heating rate with temperature. As the molarity increases above

0.5M (panels a-d), there is a strong suppression in the rate of the combustion reaction. Panel a compares the sample with no salt to a sample with 1.5 M electrolyte. The difference in self-heating rates is striking. For some reason the addition of the salt dramatically slows the combustion of the solvent by the oxygen available from the cathode.

DSC profiles for nominally identical masses of $Li_{0.5}CoO_2$ heated in the presence of various concentrations of $LiPF_6$ in EC/DEC (33/67, vol/vol) at 2°C/min are shown in Figure 6.35. It is clear that the decomposition of $Li_{0.5}CoO_2$ is more stable with increasing concentration of $LiPF_6$, confirming the self-heating rate trend in the ARC. The higher temperature accessible with the DSC has allowed the examination of the high temperature (>325°C) exothermic peak. With an increase in the $LiPF_6$ concentration the reactivity at 350°C (0 M sample) is forced to higher temperatures or eliminated.
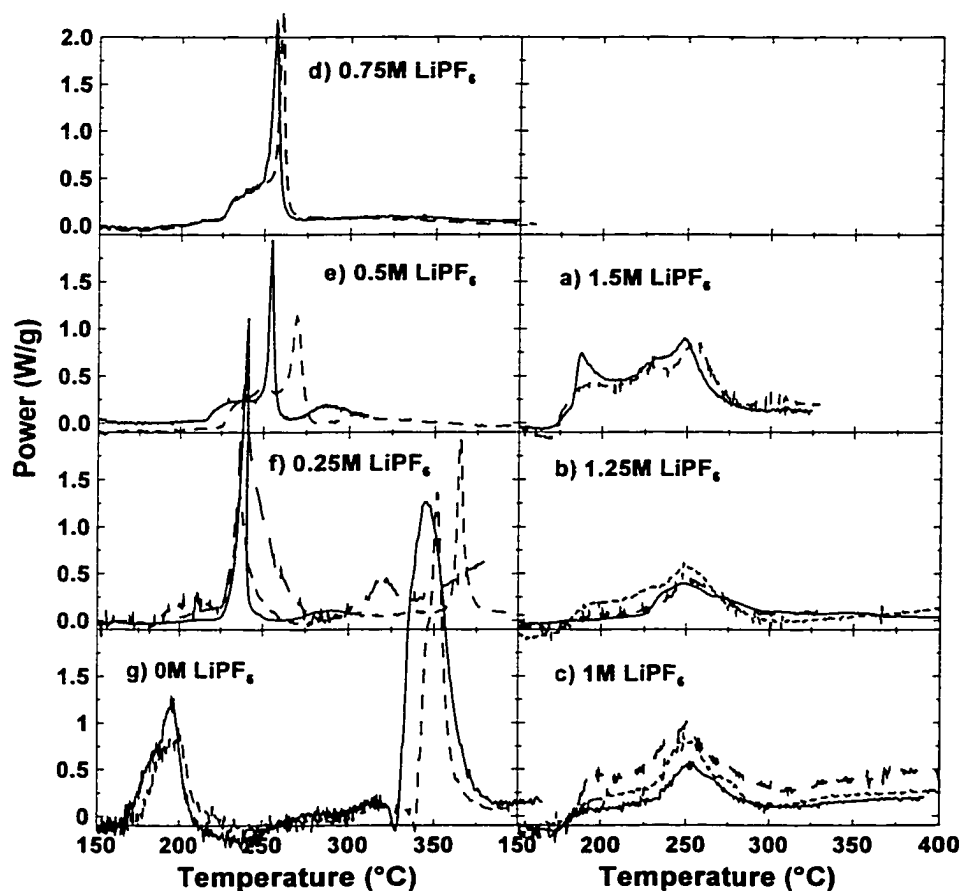
Figure 6.35. DSC profiles of $Li_{0.5}CoO_2$ in the presence of EC/DEC (33/67) at various concentrations of $LiPF_6$ at a temperature scan rate of 2°C/min. Duplicate samples are shown as dashed lines.

Although the role of the $LiPF_6$ salt in the thermal decomposition of the electrode is not completely understood, $LiPF_6$ additions did slow the reaction between $Li_{0.5}CoO_2$ and solvent. It is speculated that this could be due to coating the surface of the electrode particles with salt/solvent decomposition products. I have previously shown how a polymeric species is formed when electrolyte contaminated with water is heated. It should be pointed out that when $Li_{0.5}CoO_2$ decomposes, the oxygen released combusts the solvent (Equation 6-9) and produces water in the combustion and thus water will be present at elevated temperatures. It is likely that this polymer would deposit on the surface of the cathode and impede any self-heating reaction. The results of this study may aid in the design of safer lithium-ion cells. The results in Figures 6.34 and 6.35 suggest that more thermally stable cells, based on a $LiCoO_2$ cathode, could be made using higher concentrations of $LiPF_6$ salt (near 1.5M). Hopefully, the experiments reported here will motivate a commercial cell manufacturer to do a series of safety tests on Li-ion cells as a function of electrolyte molarity.

Figure 6.36 shows the results of heating Co, CoO, Co_3O_4, and $LiCoO_2$ individually in 1M $LiPF_6$ in EC/DEC (33/67). In the presence of Co metal, no change in the DSC profile of the electrolyte alone was obtained, while in the presence of other materials different reactivity occurred. CoO and Co_3O_4 in the presence of 1M $LiPF_6$ showed the formation of $CoCO_3$ and Li_2CO_3, while $LiCoO_2$ showed the formation of many species including Li_xCoO_2, CoO, $CoCO_3$, and Li_2CO_3. These species are believed to be formed following equations previously introduced. Comparing the results of Figure 6.36 with those of Figures 6.22 and 6.27 shows the enhanced reactivity of these species in the electrolyte.

6.8 Summary of $Li_{0.5}CoO_2$ in $LiPF_6$ Electrolyte

When $LiPF_6$ is added to the organic solvent, polymerization of the solvent occurs at high temperature due to the presence of HF impurity.
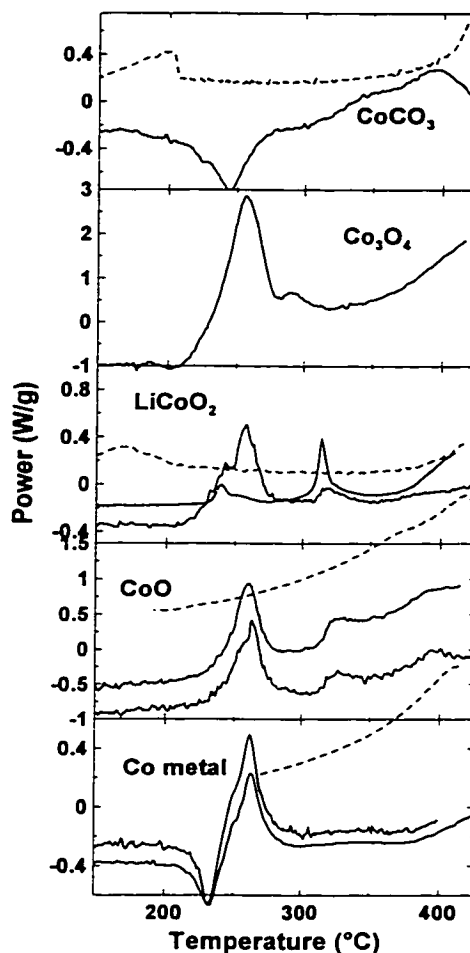
Figure 6.36. DSC of the indicated species in 1M LiPF₆ EC/DEC (33/67, vol/vol) at 5°C/min. Cooling curves are shown as dashed lines.
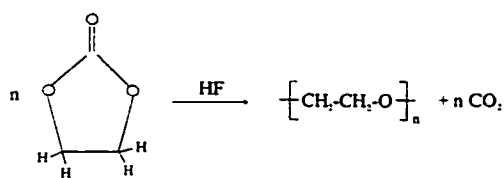
(6.16)

This polymerization leads to the deposition of the product on the surface of the $Li_{0.5}CoO_2$ particles slowing the decomposition of the electrode. As the concentration of $LiPF_6$ in the organic solvent increases, the amount of polymer formed increases and the release of oxygen, as described in Section 6.4, is further hindered. The slower release of oxygen causes the combustion of the solvent in a more controlled manner. This slower combustion causes the temperature to rise less violently and thus the generated heat can

be dissipated more efficiently. Effectively, the presence of the LiPF$_6$ electrolyte salts makes the Li$_{0.5}$CoO$_2$ electrode safer than in the presence of the organic solvent alone.

6.9 Affect of Changing the Electrolyte Salt

Manufacturers and researchers alike are constantly introducing new electrolytes. These electrolytes can have an effect on the thermal stability of the electrode materials. Currently, the 3M Company is promoting the use of lithium sulfonyl imide salts that show good performance, but an analysis of the thermal stability of these lithium sulfonyl imide electrolyte systems is missing. Figure 6.37 shows the DSC profiles of BETI (LiN(SO$_2$CF$_2$CF$_3$)$_2$) and HQ (LiN(SO$_2$CF$_3$)$_2$) salts in solvent (EC/DEC, 33/67, vol/vol) and as solids. The results for the electrolyte solution indicate that there is an irreversible exothermic decomposition of the electrolyte at approximately 320°C. Comparing the results of Figure 6.37 with those of Figure 6.31, a 90 degree increase in the thermal stability of the electrolyte is obtained by replacing LiPF$_6$ with the above lithium sulfonyl imide salts.
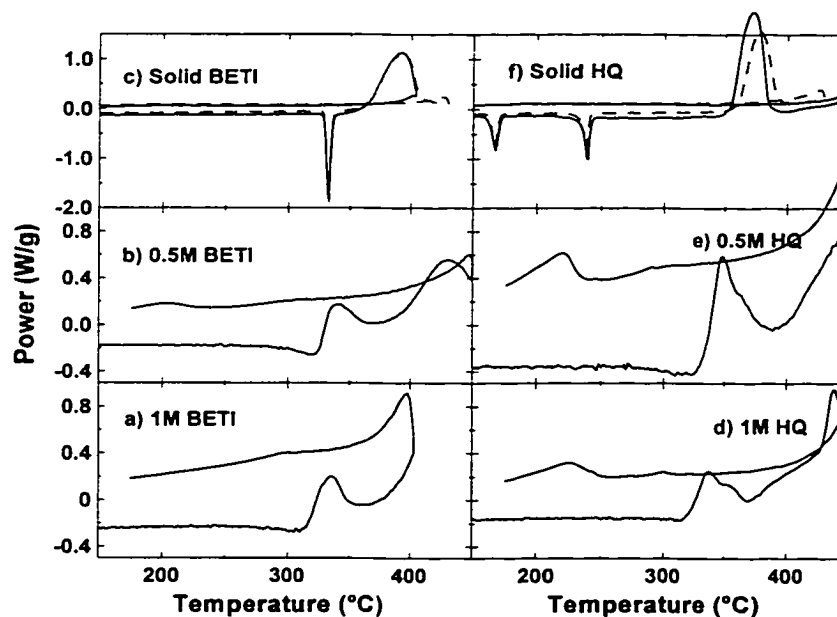
Figure 6.37. DSC profiles of two lithium sulfonyl imide salts in EC/DEC (33/67) at various concentrations or as solids at a temperature scan rate of 5°C/min. Duplicate samples are shown as dashed lines.

In panels c and f of Figure 6.37 the DSC profile of the solid BETI and HQ salt, respectively are analyzed. Solid BETI salt has a sharp endothermic peak near 340°C followed by an exothermic process at 360°C, while solid HQ salt has two sharp endothermic peaks, one at 170°C the other 240°C and an exothermic process also at 360°C. Both salts demonstrate, on cooling, no thermal behaviour. Figure 6.38 gives the results of a DSC experiment where a sample of BETI was heated between 100°C and 340°C twice and then forced to 450°C. Figure 6.38 demonstrates that the endothermic process at 340°C is reversible and has been assigned to the melting point of the BETI salt, while above 360°C the salt undergoes an irreversible thermal decomposition (unlike $LiPF_6$). Figure 6.39 shows a similar experiment for the HQ salt, where the two endotherms and the exotherm are analyzed. The results of Figure 6.39 indicate that the initial endotherm at 170°C is irreversible and signified an impurity in the sample. The impurity in the salt is believed to be water, hydrated on the salt, since the salt is hygroscopic. By contrast, the endotherm at 240°C is reversible and believed to be the melting of the lithium salt, while the exotherm is believed to be the irreversible decomposition of the salt (again unlike $LiPF_6$).
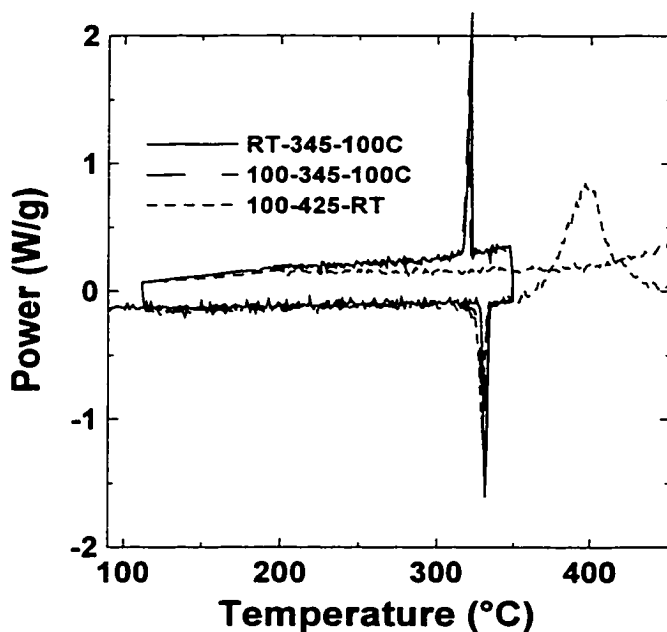
Figure 6.38. DSC of BETI salt, showing reversible melting peak at 340°C followed by decomposition at a temperature scan rate of 2°C/min
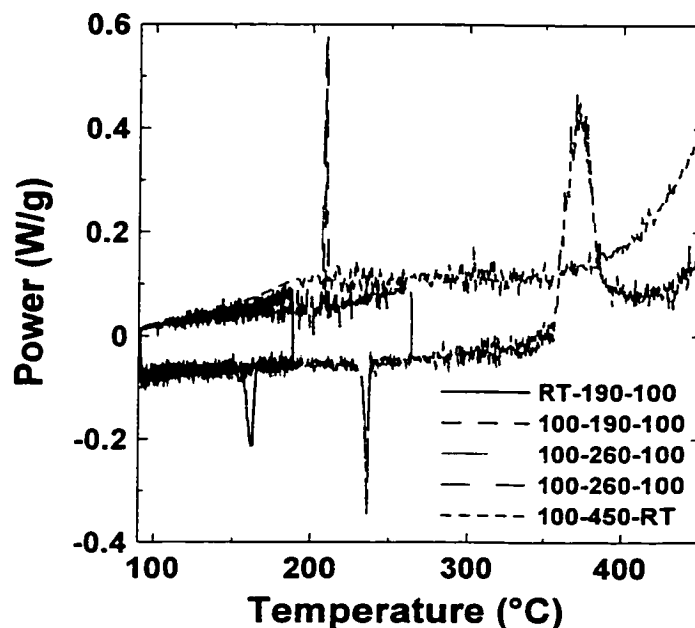
Figure 6.39. DSC of HQ salt, showing irreversible peak at 160°C (water of hydration), reversible peak at 245°C and decomposition peak at 350°C at a temperature scan rate of 2°C/min

Upon heating a 2 ml portion of 1M HQ in EC/DEC (33/67) to about 120°C, no polymeric species had formed under the same conditions as before for LiPF$_6$ and only a change in colour of the clear solution was observed (colourless to pale yellow). When the electrolyte was spiked with water and re-heated again no polymeric species formed. For the polymeric species to form HF is required for initiation. These lithium sulfonyl imide salts are too stable and do not decompose to give any HF and thus show no polymer formation.

The above DSC results indicate that the lithium sulfonyl imide salts demonstrate improved thermal stability as electrolytes over LiPF$_6$. However, improved thermal stability on its own does not guarantee improved thermal stability with Li$_{0.5}$CoO$_2$. The ARC results for 0.2 g of Li$_{0.5}$CoO$_2$ in the presence of the lithium sulfonyl imide electrolytes are shown in Figure 6.40. Figure 6.40 also shows the result for Li$_{0.5}$CoO$_2$ in the presence of the EC/DEC (33/67) solvent, and clearly the two sets of profiles are very similar. The presence of the lithium sulfonyl imide salts did not introduce any increase in the thermal stability of the electrode as compared to the reaction in solvent. LiPF$_6$, as

compared to lithium sulfonyl imide electrolytes, is more thermally unstable as an electrolyte, but demonstrates improved thermal response in the presence of $Li_{0.5}CoO_2$.
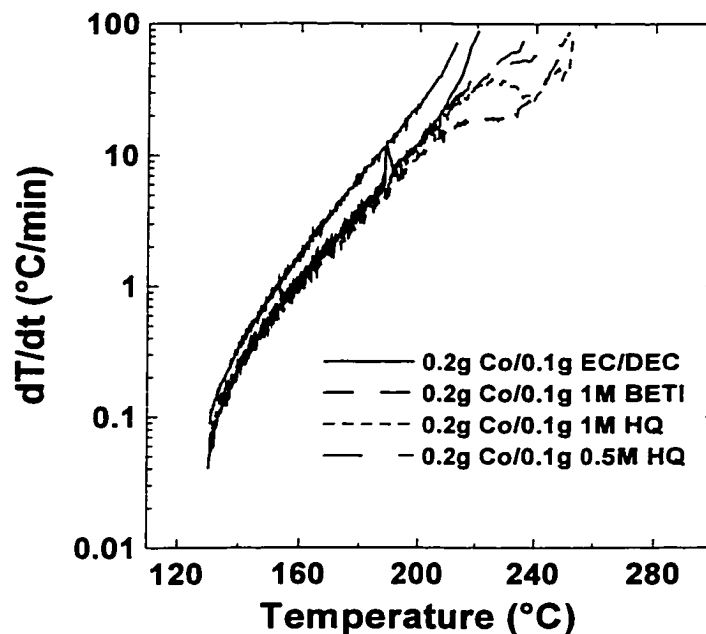
Figure 6.40, Self-heating rate profiles of $Li_{0.5}CoO_2$ in the presence of lithium sulfonyl imide electrolytes at various concentrations in EC/DEC (33/67).

DSC analyses of the $Li_{0.5}CoO_2$ electrode in the presence of the above lithium sulfonyl imide salts are shown in Figure 6.41, in addition one panel shows $Li_{0.5}CoO_2$ in the presence of EC/PC. There are many similarities between the reactivity of $Li_{0.5}CoO_2$ in lithium sulfonyl imide electrolytes and in organic solvents (Figures 6.11, 6.26, 6.28). The first two exothermic processes occur at the same temperature as the previous solvent runs with roughly the same power for each process. These DSC results confirm the ARC results presented above. The position and shape of the high temperature (>250°C) DSC region is the major difference between the samples with solvent as compared to that of the samples with lithium sulfonyl imide electrolytes. In the solvent runs, the sample demonstrates a fairly sharp and large exothermic peak at different temperatures depending on the reducing power of the solvent and the ratio of the mass of the electrode to the solvent mass. In the lithium sulfonyl imide electrolyte samples, the high temperature instability covers a broad range (280-375°C), and is clearly composed of two main peaks (centered about 310 and 350°C). These two peaks could be due to the

decomposition of the electrode, and electrolyte respectively, since the electrode instability in solvent-only runs is near 300°C, while the electrolyte decomposes near 330°C.
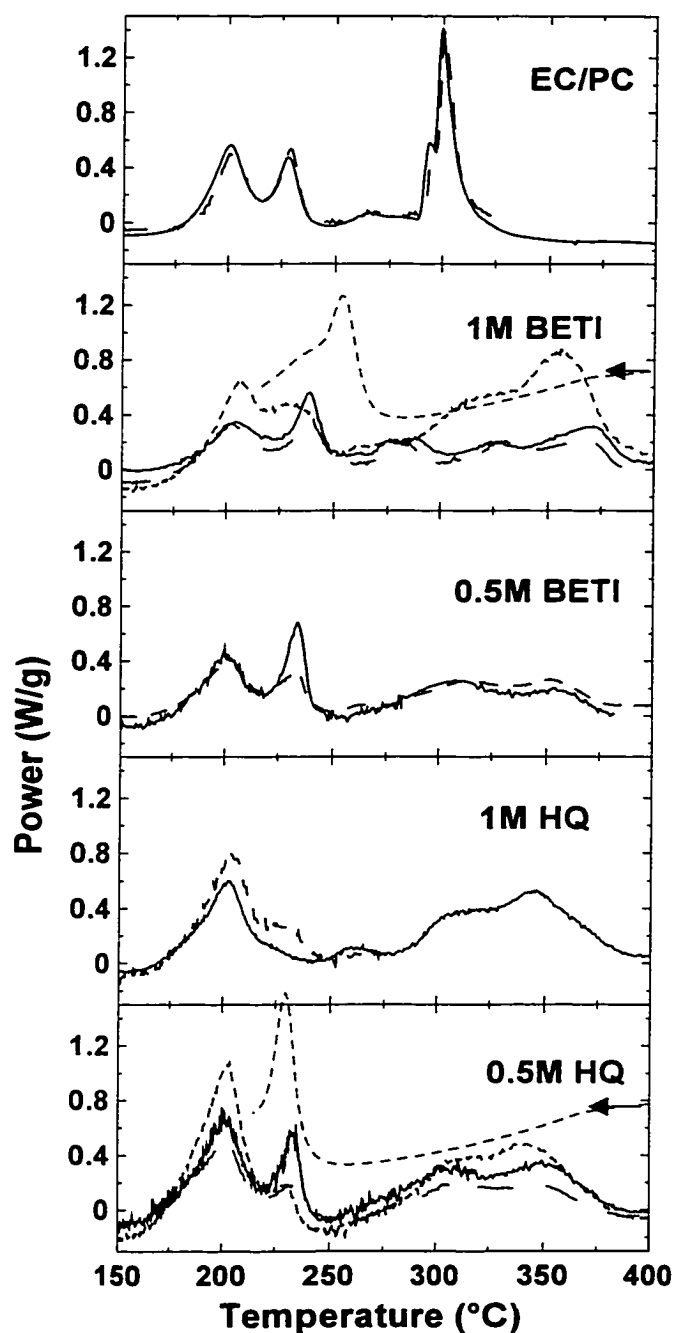
Figure 6.41. DSC of $Li_{0.5}CoO_2$ in the presence of various concentrations of lithium sulfonyl imide salts in EC/DEC (33/67) at 2°C/min. Dashed curves that end at 200°C and have an arrow superimposed are the cooling profiles of a representative sample (15°C/min). $Li_{0.5}CoO_2$ in EC/PC (2°C/min) is shown as comparison.

One common electrolyte salt that has been well-studied is $LiBF_4$ [23]. Figure 6.42 presents the ARC results of $Li_{0.5}CoO_2$ in the presence of $LiBF_4$ EC/DEC (50/50, vol/vol) at various ARC start temperatures (solid lines). The dashed lines in panels d through f are the nominal sample with the $LiPF_6$ electrolyte. In panel a, the dashed line is that of the same nominal $Li_{0.5}CoO_2$ sample in the presence of EC/DEC (33/67) solvent. In the presence of $LiBF_4$, the sample has a detectable self-heating rate at 130°C which is the same temperature as the detectable self-heating for the nominal electrode sample in the presence of EC/DEC. Although the onset of detectable self-heating occurs at the same temperature, the presence of the $LiBF_4$ salt suppresses the self-heating rate at high temperatures. The presence of $LiBF_4$ gives rise to improved stability over the organic solvent EC/DEC.

When the results of the $Li_{0.5}CoO_2$ electrode in the presence of the $LiBF_4$ salt are compared to that of the $LiPF_6$ salt, the $LiPF_6$ salts demonstrates a more depressed (more thermally stable) self-heating rate. These results indicate that the presence of $LiBF_4$ in a cell will give rise to a more rapid decomposition of the $Li_{0.5}CoO_2$ cathode at elevated temperatures. This result combined with those to be presented in Chapter 8 show that $LiBF_4$ should not be chosen as the electrolyte salt if thermally-stable charged lithium-ion cells are desired.

The exposure of a small sealed vial of 1M $LiBF_4$ EC/DEC (50/50) electrolyte to elevated temperatures did not produce any polymeric species. When the electrolyte was spiked with water and reheated, no reaction occurred. This experiment indicates that $LiBF_4$ is more thermally stable than $LiPF_6$ and does not react with the solvent to give polymeric species. These polymeric species improve the thermal stability of the electrode since they coat the electrode particles, hindering the release of oxygen and the subsequent combustion of the solvent. The inability of $LiBF_4$ electrolytes to produce polymers under the same conditions as $LiPF_6$ causes the increased reactivity of this electrode/electrolyte combination, as compared to $LiPF_6$.
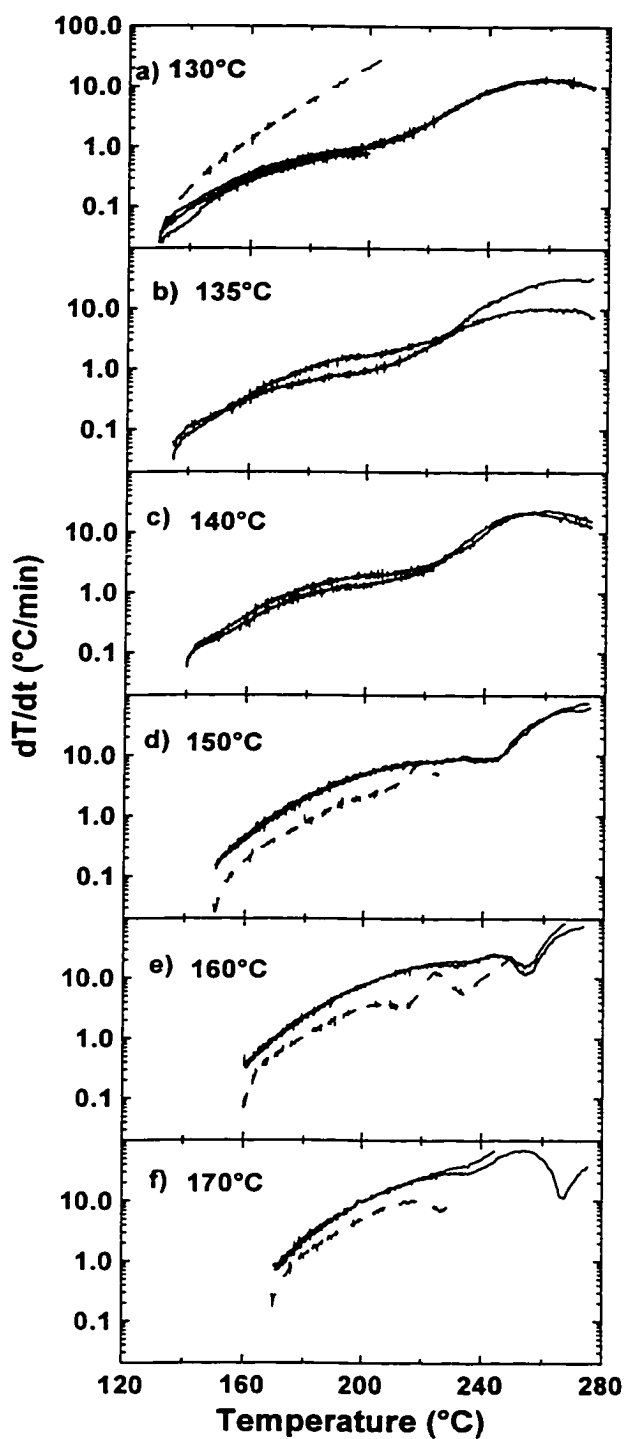
Figure 6.42. Self-heating rate profiles of 0.35 g of $Li_{0.5}CoO_2$ in the presence of 0.35 g of $1M$ $LiBF_4$ EC/DEC (50/50). The dashed line in panel a is that of $Li_{0.5}CoO_2$ in the presence of EC/DEC (33/67) solvent, while in panel d-f the dashed lines represent $Li_{0.5}CoO_2$ in the presence of $1M$ $LiPF_6$ in EC/DEC (33/67).

6.10 Summary of $Li_{0.5}CoO_2$ in Electrolytes of Different Lithium Salts

Electrolytes composed of lithium sulfonyl imide salts, although more thermally stable as electrolyte, provide little additional stability to the decomposition of the $Li_{0.5}CoO_2$ electrode at elevated temperature as compared to in the presence of solvent only. The stability of these electrolytes does not provide a means to produce an initiator for the polymerization of the electrolyte solvent, which can improve thermal characteristics by the deposition of the polymeric product on the surface of the electrode particle and thus hindering the release of oxygen. Heating $LiBF_4$ in EC/DEC did not produce any polymeric product. The $LiBF_4$ electrolyte in the presence of $Li_{0.5}CoO_2$ shows higher reactivity as compared to $LiPF_6$ electrolytes.

Chapter 7

Kinetic Analysis of $Li_{0.5}CoO_2$

7.1 Reaction with 1M $LiPF_6$

A reaction mechanism for the decomposition of a $Li_{0.5}CoO_2$ electrode in the presence and absence of solvent at elevated temperature was determined in Chapter 6. In the presence of $LiPF_6$, an uncharacterised polymeric species forms at elevated temperature and is believed to deposit on the surface of the $Li_{0.5}CoO_2$ particles. This polymeric deposition results in a much more complicated reaction scheme for the decomposition of the electrode. In spite of the incomplete reaction scheme, a reaction model is required to describe the reactions occurring at elevated temperatures between $Li_{0.5}CoO_2$ and electrolyte. This reaction model is needed to predict the outcome of other thermal events. The procedure for determining the kinetic triplet of $Li_{0.5}CoO_2$ in the presence of 1M $LiPF_6$ was described in Section 5.3.
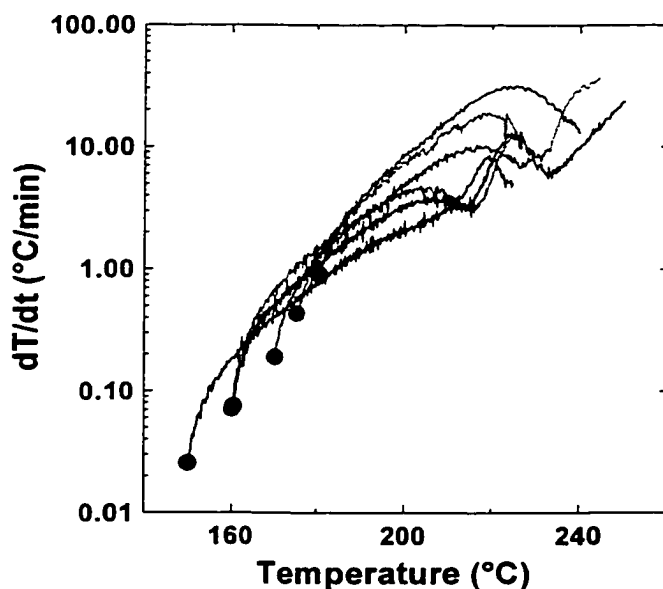
Figure 7.1. Self-heating rate profiles for $Li_{0.5}CoO_2$ charged to 4.2 V. The large circles represent the points to which the ARC samples were quickly heated, for temperatures above 150°C.

112

The ARC results for the self-heating of 0.35 g of $Li_{0.5}CoO_2$ samples charged to 4.2 V in the presence of 0.35 g of 1M $LiPF_6$ are shown in Figure 7.1. The large points in the figure show the start point of each experiment. For the experiment that begins at 150°C, the ARC found the exotherm using the heat-wait-search mode beginning at 100°C. The ARC was forced directly to the start point for the experiments beginning at 160°C and above. In all cases, the self-heating rate increases very rapidly with temperature at the start of the experiment. The self-heating rate continues to increase for about 60°C after the start of the experiment. It then decreases and in many cases a second process appears to start.
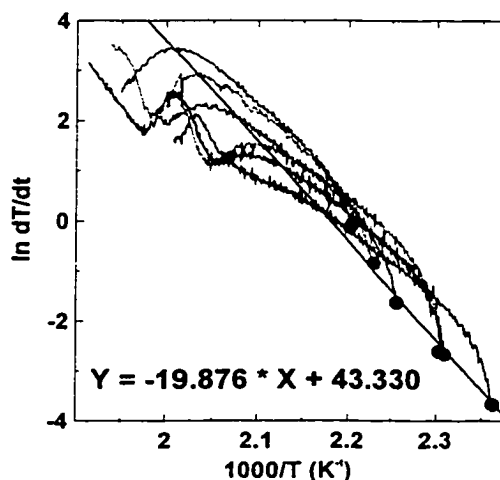
Figure 7.2. Plot of ln dT/dt vs. 1000/T for the reaction of Figure 7.1. The straight solid line was used to estimate the activation energy for the reaction. dT/dt was measured in K/min and the natural logarithm of these values is plotted along the y-axis.

The results of the experiments beginning at different start temperatures were then used to determine the Arrhenius parameters (activation energy (E_a) and frequency factor (γ)) for the reaction of $Li_{0.5}CoO_2$ charged to 4.2 V in electrolyte at elevated temperature with an Arrhenius-type plot (see Figure 7.2). The fitted line shown in Figure 7.2 was used to estimate the kinetic parameters for the reaction. Only the first four starting temperatures were used in the fit in Figure 7.2. This was because the starting self-heating rates for the highest two experiments were on the order of 1 °C/min, which was close to the 5 °C/min heating rate the ARC used to bring the samples to the start point. For these samples there was consumption of some of the reactant before the ARC could begin

collecting data, so the samples were not identical. The activation energy was obtained from the slope of the fitted line while the frequency factor was determined from its y-intercept. The Arrhenius parameters were E_a = 1.7 eV and γ = 6.6 x 10 [18] min^{-1}. Differential scanning calorimetry (DSC) profiles of $Li_{0.5}CoO_2$ charged to 4.2 V at various heating rates are shown in Figure 7.3.
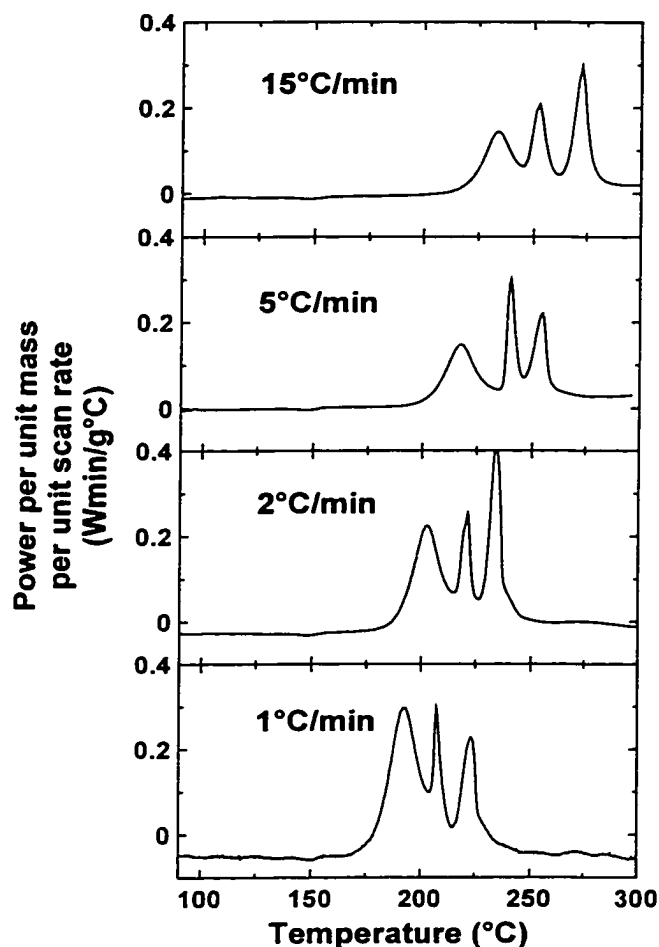
Figure 7.3. DSC experiments on $Li_{0.5}CoO_2$ in electrolyte, charged to 4.2 V, at the heating rate indicated.

Using the Arrhenius parameters determined from Figure 7.2 as initial kinetic values, the experimental data were fit with a mathematical model. The ARC data were fit using Equation 5-6 and the DSC data were fit using Equation 5-12. The reaction model, $f(\alpha)$, was optimized by varying each value of m, n, and p in Equation 5-3. The ARC fitting could only be performed for the first 60 degrees, since this represented the completion of one process while the others could not be fully investigated. The first

reaction process was believed to correspond to the first exothermic peak in the DSC profile.

Comparison of the model predictions to experiment was made by least square analysis. Goodness of fit parameters, χ^2, for the fits to ARC and DSC results are defined here as follows:

$$\chi^2_{ARC} = \frac{1}{N} \sum_{n=1}^{N} \frac{\left[dT/dt_{expt} - dT/dt_{calc} \right]^2}{dT/dt_{expt}}, \qquad (7\text{-}1)$$

$$\chi^2_{DSC} = \frac{10}{N} \sum_{n=1}^{N} \frac{\left[H_{expt} - H_{calc} \right]^2}{H_{expt}}, \qquad (7\text{-}2)$$

and thus

$$\chi^2_{Tot} = \chi^2_{ARC} + \chi^2_{DSC}. \qquad (7\text{-}3)$$

A ten times weighting factor (see above in Equation 7-2) was given to the DSC results because the numerical values of the power per gram per sweep rate were on average about ten times smaller than the self heating rates in the ARC. With this procedure, fit quality to ARC and DSC profiles was given about equal overall weight. Fits were made simultaneously to the results of six experiments: DSC runs at sweep rates of 1, 2, 5 and 15 °C/min and ARC runs starting at 160 and 170°C. The reaction model with the lowest total χ^2 should be indicative of the "true" reaction process for the initial thermal instability of $Li_{0.5}CoO_2$ in electrolyte. The optimization was performed and the values obtained were (see Table 7.1 under All-fit): Ea= 1.28 eV, γ= 1.48×10^{13} min^{-1}, α_0=0.04 (ARC), m=0.26, n= 1.6, p=0.49, and h/C_{tot} = 66.5 K with a total χ^2 of 0.1256.

The difficulty with this method of kinetic analysis is that no physical or experimental support can be postulated for the values of m, n and p. One can obtain remarkably good fits to both DSC (Figure 7.4, panel a All-fit) and ARC (Figure 7.5) results and as such, these kinetic values can accurately predict other thermal events. The DSC profiles shown in Figure 7.4 contain only the first peak of the experimental results for $Li_{0.5}CoO_2$ charged to 4.2 V (Figure 7.3). These plots are presented as normalized curves such that a direct comparison of the peak shapes can be performed to eliminate experimental errors introduced due to the inaccuracy of weighing small amounts (2-7mg) in the glovebox.

Table 7.1. Statistical analysis of the various models in Table 5.1 used to analyze the reaction mechanism of 0.35g $Li_{0.5}CoO_2$ in 0.35 g 1M $LiPF_6$, EC/DEC electrolyte or 0.35 g EC/PC, charged to 4.2V, at elevated temperature.

Model	E_a (eV)	γ ($\times 10^{13}$) (min^{-1})	m	n	p	α	h/C_{tot} (K)	χ^2_{ARC}	χ^2_{DSC}	χ^2_{Tot}
All-fit	1.284	1.48	0.26	1.6	0.49	0.04	66.4	0.0229	0.1027	0.1256
Model 11	1.264	0.508	0	1	0.5	0.03	62.3	0.0523	0.3750	0.4273
Model 12	1.242	0.400	0	1	2/3	0.03	59.3	0.1810	0.1302	0.3112
Model 13	1.262	0.900	0	1	0.75	0.02	58.3	1.9318	0.2267	2.1585
Model 14	1.252	1.075	1	1	0	0.04	58.9	0.8812	0.7955	1.6767
EC/PC	1.18	0.076	0	1	2/3		110			
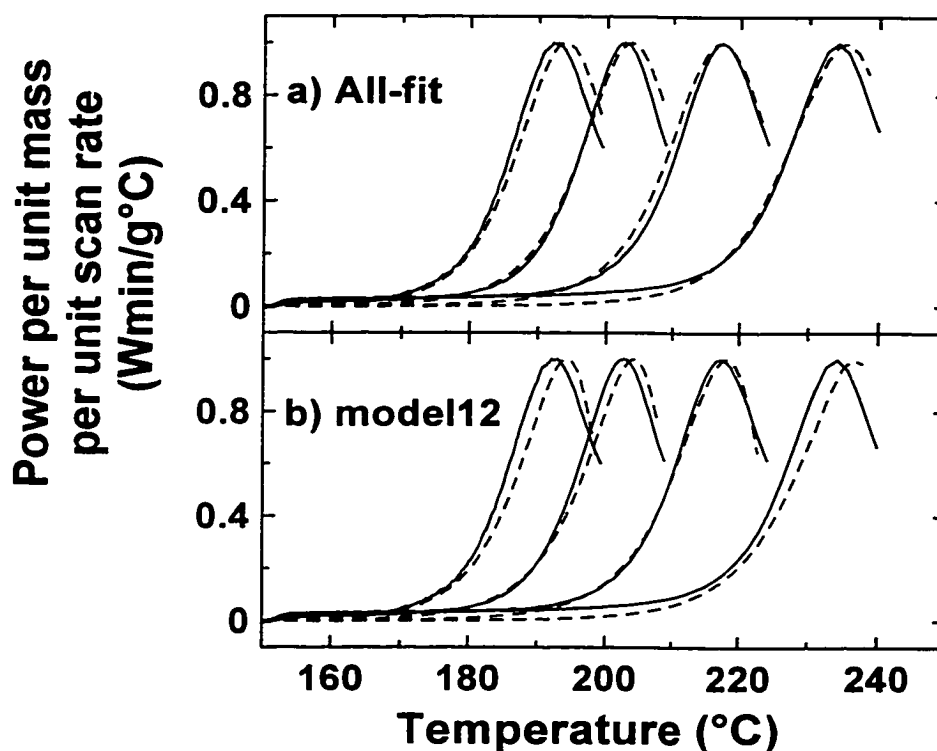
Figure 7.4. DSC comparisons for two models of the first peak of the experimental data (solid) to that of the calculated (dashed) profiles at heating rates of 1, 2, 5, and 15 °C/min. The calculated parameters, with H = 285 J/g, corresponding to each panel are given in Table 7.1 under their respective models.
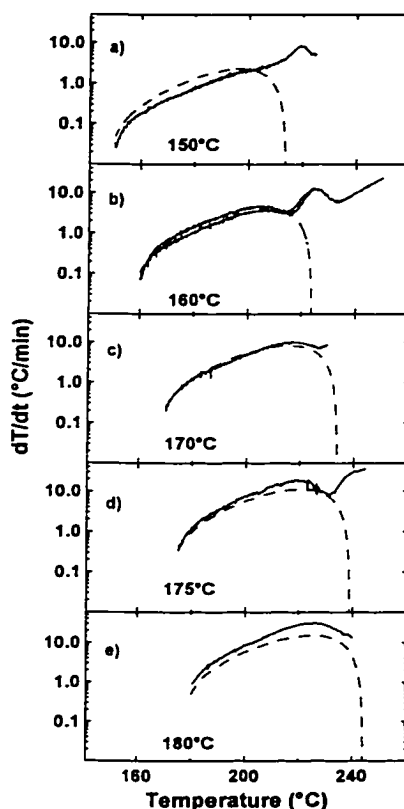
Figure 7.5. ARC experiments (solid) on $Li_{0.5}CoO_2$ in electrolyte compared to the predictions (dashed) of the All-fit model at the start temperature indicated. The parameters are listed in Table 7.1 under All-fit.

An examination of the DSC and ARC profiles for other reaction models in Table 5.1 (Figures 5.2 through 5.6) shows that the Avrami-Erofeev models (model 11 through model 13) and the Prout-Tompkins model (model 14) can give DSC peaks with about the correct halfwidth, and ARC profiles with the correct temperature dependence. Therefore, fitting both the ARC and DSC results using these models was attempted and the results are shown in Table 7.1 under the respective model numbers from Table 5.1. From this set of reaction models, the kinetic triplet for the thermal decomposition of $Li_{0.5}CoO_2$ in electrolyte at elevated temperatures was described most accurately by an Avrami-Erofeev reaction type (#12) with an activation energy of about 1.24 eV, a frequency factor of 4.0×10^{12} min^{-1}, h/C$_{tot}$ = 59.3 K and α_o = 0.03. The calculated ARC (Figure 7.6) and DSC (Figure 7.4, panel b model 12) profiles are shown and compared to the experiment for this choice of kinetic triplet. Good fits were obtained for each experiment and thus

confidence was gained that this kinetic triplet would describe accurately the initial event taking place in the $Li_{0.5}CoO_2$ electrode at 4.2 V in the presence of 1M $LiPF_6$, EC/DEC (33/67) and high temperatures.
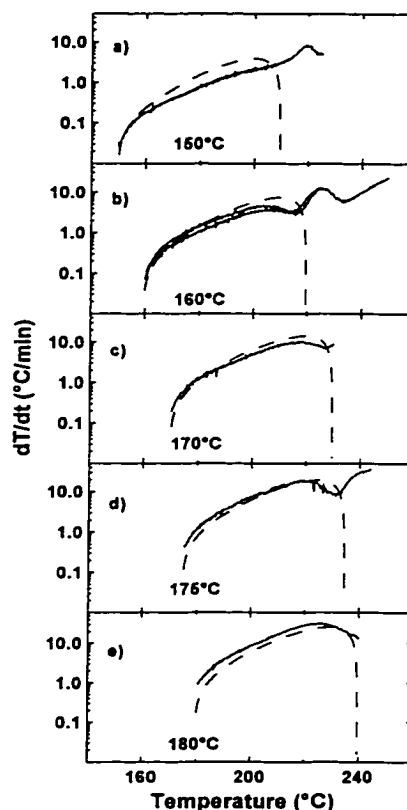
Figure 7.6. ARC experiments (solid) on $Li_{0.5}CoO_2$ in electrolyte compared to the predictions (dashed) of model 12 in Table 5.1 at the start temperature indicated. The parameters are listed in Table 7.1 under model 12.

To further support the proposed Avrami-Erofeev reaction kinetics, for the first reaction process of $Li_{0.5}CoO_2$ in 1M $LiPF_6$ EC/DEC (33/67), a quasi-isothermal DSC run was performed at 193°C. The result of the isothermal run is shown as the solid curve in Figure 7.7. Also indicated in Figure 7.7 as the dashed curve is the result of the calculation for the quasi-isothermal run with the model proposed above. The major difference between the calculated and experimental data are that the reaction model only described the first of three DSC reaction processes. Thus the tail of the experimental isothermal data can not be accurately described with the proposed model, giving rise to the discrepancy between data sets. Including the remaining reaction processes would

produce a more accurate isothermal calculation. In spite of this, the quasi-isothermal experiment supports the proposed Avrami-Erofeev reaction model for the initial instability of $Li_{0.5}CoO_2$ exposed to elevated temperatures in the presence of 1M $LiPF_6$. For comparison, the quasi-isothermal run was predicted using the All-Fit kinetic parameters in Table 7.1 and is shown in Figure 7.8. It is clear that a more accurate description is obtained, but again the tail is not reproduced well and the value of m, n and p have no physical significance.
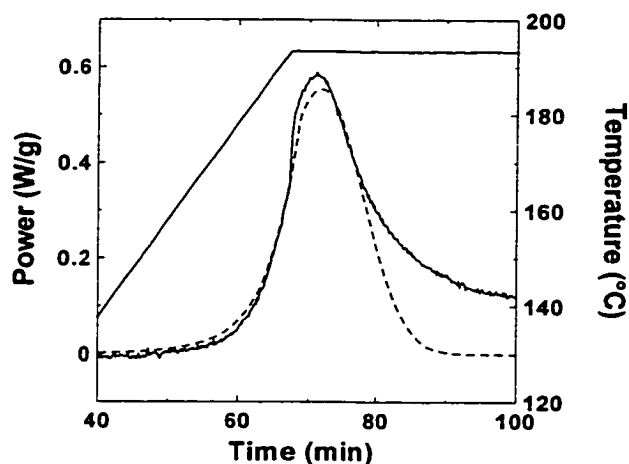
Figure 7.7. Quasi-isothermal DSC experiment on $Li_{0.5}CoO_2$ with 1M $LiPF_6$ at 193°C. Solid curve is the experimental data, while the dashed line is a calculation using the parameters of model 12 in Table 7.1.
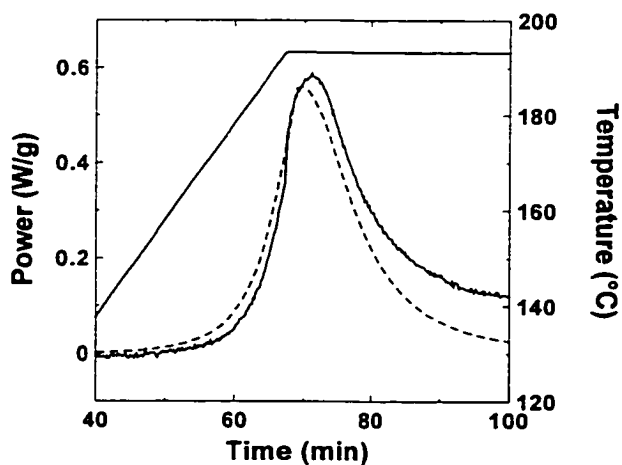
Figure 7.8. Quasi-isothermal DSC experiment on $Li_{0.5}CoO_2$ with 1M $LiPF_6$ at 193°C. Solid curve is the experimental data, while the dashed line is a calculation using the parameters of the All-fit model in Table 7.1.

The Avrami-Erofeev equation has been successfully used in the kinetic analysis of many solid phase decomposition reactions, recrystallisation and phase transformations [70]. The theory of Avrami-Erofeev kinetics is based on the concepts of nucleation and growth. In Avrami-Erofeev reactions the extent of decomposition varies with time in a sigmoid fashion, where the rate increases in the early stages and then falls off at later stages. This behaviour may be interpreted as arising from the production of nuclei (germ nuclei) at various places in the crystal. At the commencement of the transformation there exists a certain number of germ nuclei, followed by the growth of these nuclei (growth nuclei). Decay in the reaction rate is then seen as the growth nuclei overlap, and the area of the interface between reactant and product phases decreases [99]. The correct analysis of the decay period is the important contribution of Avrami-Erofeev kinetics to the study of reactions in the solid state [100]. A derivation of the Avrami-Erofeev equation and a qualitative picture of the reaction mechanism are given in Appendix A.

7.2 Reaction with EC/PC (50/50, vol/vol)

A good understanding has been obtained for the reaction mechanism of $Li_{0.5}CoO_2$ with solvent at elevated temperatures. It is believed that $Li_{0.5}CoO_2$ first decomposes to $LiCoO_2$ and CoO through a Co_3O_4 intermediate, and if the sample is heated to higher temperatures with excess solvent, the production of Co has been identified. The reaction environment for $Li_{0.5}CoO_2$ in solvent is much simpler than in the presence of the electrolyte salt. Modelling the solvent reaction should be simpler. The modelling procedure described in Section 5.3 had to be modified in order to model $Li_{0.5}CoO_2$ in the presence of EC/PC (50/50, vol/vol) since the necessary ARC experiments were not available.

Initially, the heats of reaction for the two DSC peaks between 150 and 280°C in Figure 6.26 were determined. The average value of the heat of reaction for the first peak was 471 ± 130 J/g, while the average value for the second peak was 278 ± 80 J/g. It is interesting to note that the heats of reaction for the peaks are near the 2:1 ratio expected based on Equations 6-7 and 6-8. With the heat of reaction for each peak determined, Arrhenius parameters were required to describe the reaction kinetics. Using the methods

developed by Kissinger [75], the activation energy and frequency factor were determined by plotting the natural logarithm of the ratio of the temperature scan rate (β) over the square of the peak temperature (T_p) versus one over the peak temperature (see Figure 7.9). The slope was related to the activation energy (E_a), while the intercept was related to the frequency factor (γ), since in Kissinger's procedure it is assumed that

$$\ln\left(\frac{\beta}{T_p^{\,2}}\right) = \ln\left(\frac{-R\gamma}{E_a}f(\alpha)\right) - \frac{E_a}{R}\frac{1}{T_p}, \qquad (7\text{-}4)$$

where β is the temperature scan rate and R is the gas constant. An initial value of the frequency factor, γ, was determined by assigning a value of one to the reaction model, $f(\alpha)$.
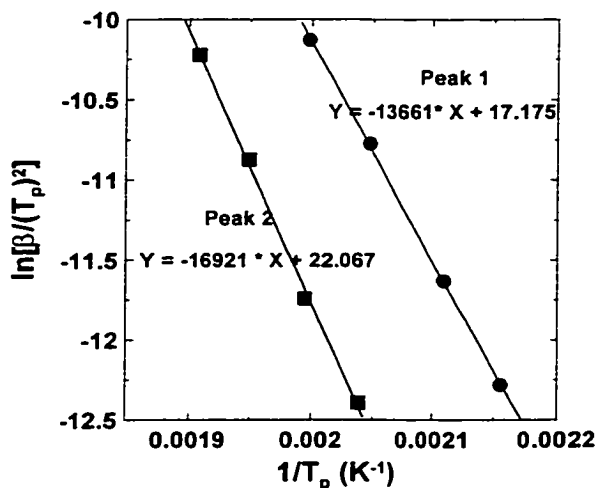
Figure 7.9. Plot required for the determination of activation energy and frequency factor by Kissinger's method. The data were determined from Figure 6.26 ($Li_{0.5}CoO_2$ in EC/PC). β was measured in K/min, T_p in K and the natural logarithm of these values is plotted along the y-axis.

With the activation energy for the events giving rise to the two peaks known and an initial starting value for the frequency factor assumed, an analysis of the possible kinetic triplets was performed to each of four DSC profiles, at different temperature scan rates. The reaction models were limited to those in Table 5.1. The best fit DSC profiles (true kinetic triplets) are shown in Figure 7.10. The kinetic triplet for the first process consisted of an activation energy of 1.18 eV, a frequency factor of 7.6×10^{11} min^{-1}, and an

Avrami-Erofeev reaction model of the type of model 12 in Table 5.1. The second process was also an Avrami-Erofeev reaction, type 12, but an activation energy of 1.46 eV and a frequency factor of 1.4×10^{14} min^{-1} were obtained. The activation energies determined from Kissinger's method were 1.18 and 1.46 eV, for peak 1 and 2 respectively. It is clear from Figure 7.10 that an accurate reproduction of the two processes has been obtained and most importantly the correct shift of the peaks occurred when the temperature scan rate was modified.
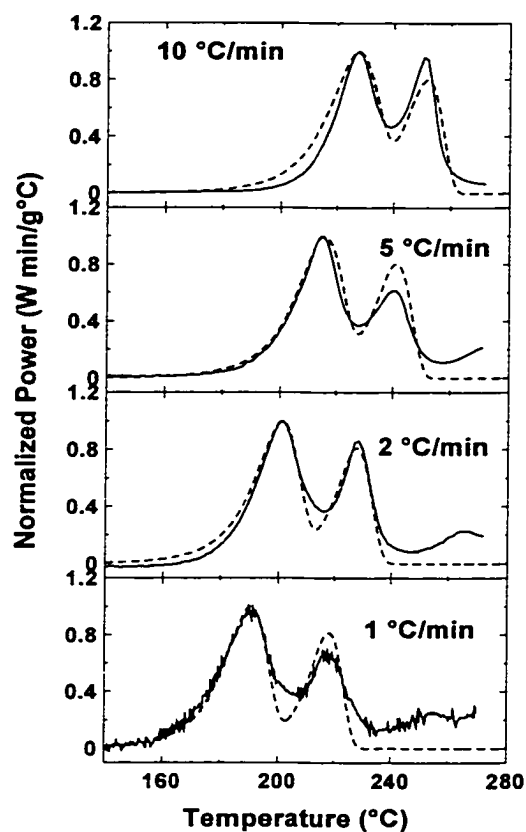
Figure 7.10. DSC profiles of $Li_{0.5}CoO_2$ in the presence of EC/PC (50/50, vol/vol) at the indicated scan rates. The solid curves are the experimental data, while the dashed curves are the calculated profiles using a reaction triplet of: $Ea_1 = 1.18$ eV, $\gamma_1 = 7.6 \times 10^{11}$ min^{-1}, model A-E 12, $Ea_2 = 1.46$ eV, $\gamma_2 = 1.4 \times 10^{14}$ min^{-1}, model A-E 12, and $H_1 = 389$ J/g, $H_2 = 253$ J/g.

To test the reaction triplet obtained above, ARC self-heating rate profiles were calculated for the experimental profiles in Figure 6.23 and 6.24. The same reaction triplet obtained from the DSC was used and the temperature rise for each process was

estimated from the experimental data. The two data sets (experiment and calculated), shown in Figure 7.11, are markedly similar for each of the five sets of samples. This accurate reproduction of ARC profiles supports the proposed reaction triplet and confidence can be assured of their predictions. To predict the ARC profiles, values for the temperature rise of each reaction were measured from Figure 7.11 by eye and are listed as "Experiment" in Table 7.2. These values were adjusted slightly to calculate the ARC profiles and are listed as "Modelled" in Table 7.2. Using the heats of reaction from the DSC experiments, the two temperature rises can be predicted using Equations 6-3 and 6-2. These predicted temperature rises are given in Table 7.2 as "Predicted". Comparisons of the predicted and experimental temperature rises in Table 7.2 are in fair agreement. The temperature rises (predicted, modelled and experimental) for the two reactions are near the expected 2:1 ratio.
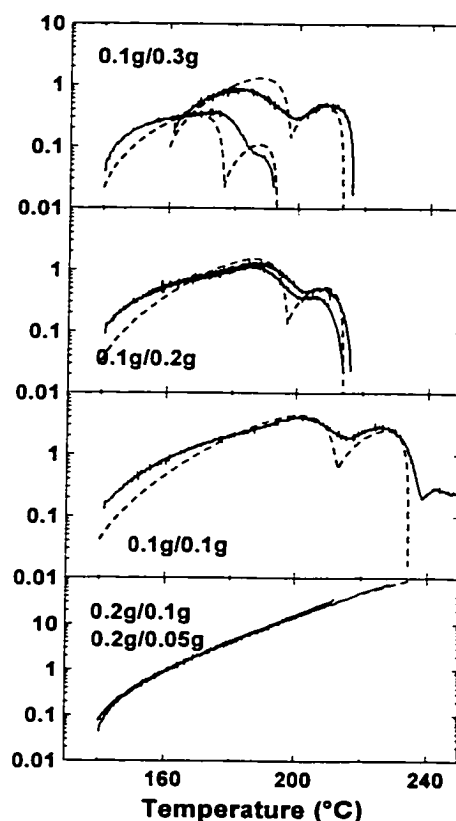
Figure 7.11. ARC self-heating rate profiles of $Li_{0.5}CoO_2$ in the presence of EC/PC (50/50, vol/vol) at the indicated amounts: x g $Li_{0.5}CoO_2$/ x g EC/PC. The solid lines are the data from the experiment, while the dashed lines are the calculated profiles for the model in Figure 7.10.

Table 7.2. Comparison of the calculated and modelled temperature rise of the two reactions that occur in Figure 7.11.

Mass $Li_{0.5}CoO_2$/ Mass EC/PC	Predicted Temp Rise (K)		Modelled Temp Rise (K)		Experiment Temp Rise (K)	
	First Rxn	Second Rxn	First Rxn	Second Rxn	First Rxn	Second Rxn
0.1 g/0.3 g	41	27	38	18	38/43	17/9
0.1 g/0.2 g	49	32	59	19	60	14
0.1 g/0.1 g	59	38	75	24	74	23
0.2 g/0.1 g	103	67	125	44	>88	-
0.2 g/0.05 g	114	74	145	57	>88	-

The reaction is best described using Avrami-Erofeev reaction kinetics, which underlines the importance attached to this expression for the kinetic analysis of solid phase reactions. The same simplistic view of the reaction, described in Appendix A, can be applied to the reaction in EC/PC solvent, except that the kinetics are much faster. Thus the presence of $LiPF_6$ hinders the reaction, likely due to the coating of the reacting particles with decomposition products (polymers) of the thermally unstable electrolyte. By contrast, in pure solvent there is no protective coating formed on the reacting particles and thus an acceleration of the electrode decomposition.

Chapter 8

Anode Investigation

Previous work analysing the thermal stability of lithium-ion cells showed that the reaction between lithium-containing carbon material and electrolyte was detected first, as Li-ion cells were heated [57]. Hence, this reaction plays an important role in determining cell safety. Richard performed the most complete analysis of thermal stability of anode material, but her work centred mainly on one type of anode material, mesocarbon microbeads (MCMB) [57]. Many different types of carbon exist and the major manufacturers of lithium-ion cells use different carbon sources. It was important to understand if the reaction between lithium-containing carbon and electrolyte at high temperatures depended on the carbon type.

8.1 Carbon Structure

For this assessment, six different carbons, differing in morphology (fiber, spheres, flakes), heat-treatment temperature (1200°C – 3000°C) and surface area (0.4 – 9.2 m^2/g) were studied. Three synthetic graphites, KS-75, SFG-44 and SFG-75 (Timcal), a heat-treated MCMB (Osaka gas), a heat-treated carbon fiber (BP-Amoco) and XP-3 petroleum coke (Conoco) were studied. The x-ray diffraction pattern of each sample was measured and their profiles were fitted using the "Structure Refinement Program for Disordered Carbons" to determine the lattice constants and random stacking probability, P [101]. The results are listed in Table 8.1, together with the surface area of each carbon studied and their respective irreversible capacity measurements.

Two natural forms of graphite have been observed and differ in the stacking of their graphene sheets [102]. Graphene sheets are hexagonal arrays of carbon atoms arranged in a honeycomb fashion. In the normal graphite structure, the sheets are stacked in a hexagonal fashion (2H) and the vertical stacking can be represented as ..ABABAB.. where A and B are graphene sheets shifted by 1/3 of a unit cell along the (110) crystal

direction. Less commonly, graphite can be found in a rhombohedral structure (3R) represented as ..ABCABC.. where B is shifted by 1/3 and C by 2/3 of a unit cell with respect to A. In addition, the graphene layers are sometimes situated with random rotations between pairs of layers, giving rise to turbostratic disorder [101, 102]. The hexagonal (2H) structure predominates for natural and synthetic graphite, with turbostratic disorder and 3R intergrowths within the structure [101]. In the "Structure Refinement Program for Disordered Carbons" designed by Shi et al. the probability for turbostratic misalignments between adjacent layers is called the random stacking probability, P [101]. The random stacking probability is an indication of the amount of disorder in the carbon structure and is related to the amount of lithium that can be intercalated into the structure [101].

Table 8.1. Summary of structural parameters of carbons under study.

Carbon	Lattice Constants (Å)		Random Stacking Prob.	Irreversible Capacity (mAh/g)	Surface Area (m^2/g)
	a (± 0.002)	c/2 (± 0.002)	(± 0.02)	(± 10)	(± 0.2)
MCMB	2.457	3.362	.19	50	0.8
SFG-75	2.461	3.358	.04	50	3.5
SFG-44	2.460	3.357	.04	50	4.3
KS-75	2.459	3.355	.10	57	9.2
XP3	2.440	3.445	1.0	50	6.7
Fiber	2.457	3.357	.26	33	0.4

The SFG synthetic graphites had P less than 0.04, which indicated heat treatment to high temperatures (>3000°C) and their structures were almost perfect ABAB.. stacking, while the KS synthetic graphite had P equal to 0.1, indicating a slightly lower

heat treatment temperature [103]. The MCMB and the fiber sample had P equal to 0.19 and 0.26 respectively, indicating lower heat treatment temperatures than the synthetic graphites [103]. The XP-3 sample had P equal to 1, indicating turbostratic misalignments between every pair of adjacent carbon sheets. It was estimated that this sample was heated to near 1200°C [103].

Figure 8.1 shows a SEM image of each of the carbons studied. The SEM images clearly show the differences in morphologies of the various samples; where a sample with a smooth surface resulted in a relatively lower surface area, while a sample composed of many small irregular sized particles resulted in a large surface area. The fiber sample was composed of large cylindrical strands of 200-250 μm in length and 25 μm in diameter. Its low surface area was a direct result of its smooth surface. The MCMB sample was composed of spheres of 25 μm average diameter. The low surface area of this sample was explained by the smooth surface of the spheres. The three synthetic graphites (SFG-75, SFG-44, KS-75) contained irregularly shaped carbon flakes with many crevices which gave rise to a much larger surface area than the fiber or MCMB. The XP3 coke sample was composed of a variety of particle sizes and its uneven structure gave rise to a surface area at the upper end of the samples tested.

8.2 Relationship Between Surface Area and Thermal Stability

All carbon samples were electrochemically reacted with as much lithium as they could hold before the ARC experiments (discharged to 0 V). During the electrochemical lithium intercalation into graphite, a number of side reactions occur due to the reactivity of lithium intercalated graphite in organic solvents (similar to pure lithium, see Figure 2.3). These reactions contribute to the irreversible capacity measured during the first discharge of the battery and produce the SEI [19, 20]. The SEI, once produced to a limiting thickness, suppresses further decomposition of the solvent. Thus, after the first cycle, there is never a direct contact between the carbon electrode and the electrolyte solution.

Fiber

MCMB

XP 3

KS-75

SFG-44

SFG-75
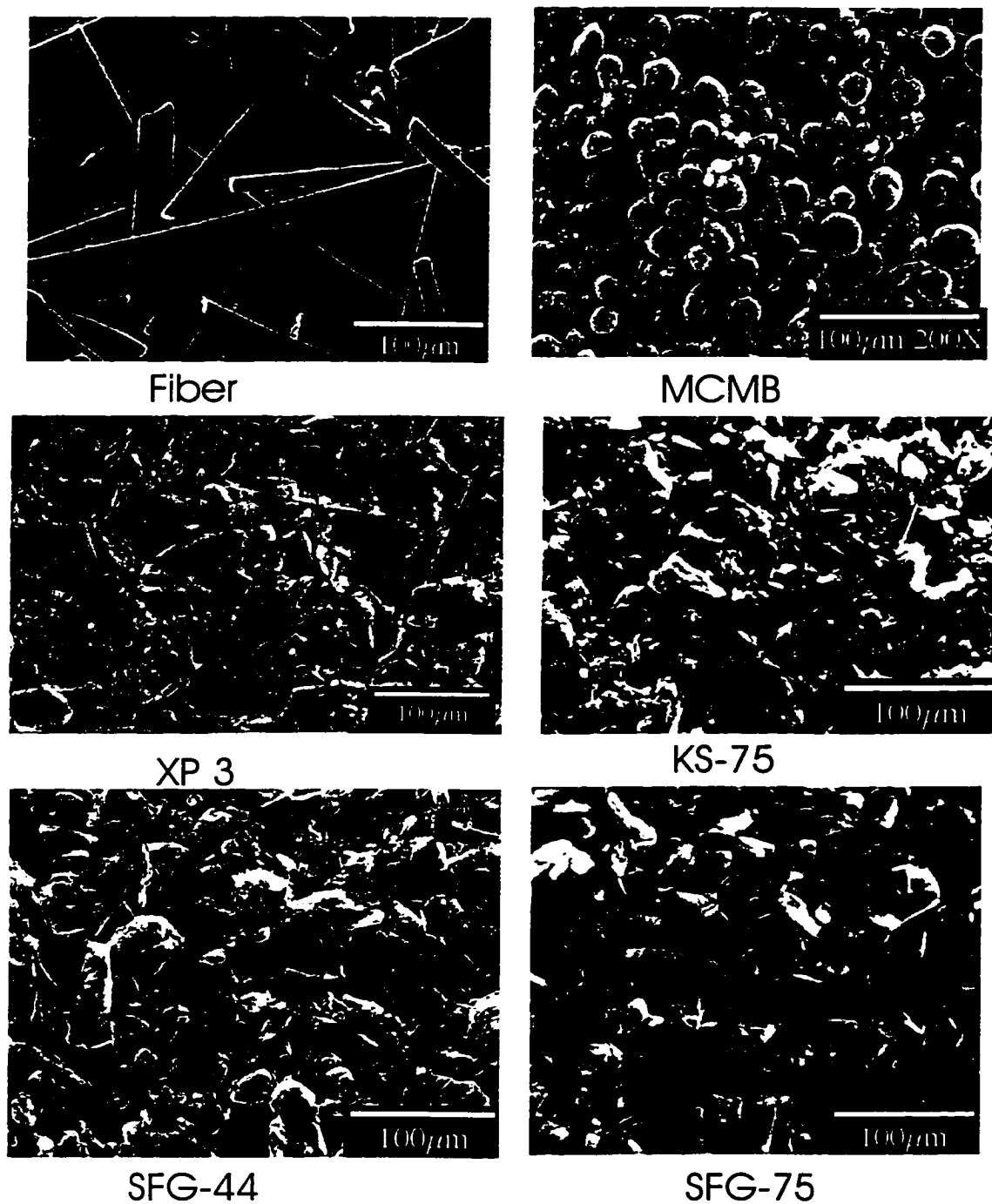
Figure 8.1. Scanning electron micrograph of each of the carbons under study.

It is widely accepted that SEI formation does occur on the carbon anode during the first discharge, but there is no agreement on the structure of this layer. There have been a variety of models proposed by numerous researchers to describe the nature of this

passivating layer. X-ray photoelectron spectroscopy (XPS) was used by Kanamura et al. [104] to conclude that O^{2-} and halides are closest to the carbon surface, while the surface near the electrolyte was composed of partially reduced semi-carbonates. Yang et al. [105] determined by FT-IR that the SEI develops mainly from the reduction of EC to a semi-carbonate $(CH_2OCOOLi)_2$ (see Equation 8-1). Naji et al. [20] have determined the structure of the passive film on a number of carbon materials by transmission electron microscopy. Their analyses have shown that the SEI in an $LiPF_6$ based electrolyte was composed of lithium carbonate and various lithium alkylcarbonate (LiAC) components $(ROCO_2Li)$, in addition to a small amount of lithium halides from the reduction of the electrolyte salt (see Equation 8-1, 8-5). Aurbach et al. have performed an extensive study on the nature on the passivating layer and found that the layers formed on both carbon and lithium show many similarities. They assigned XPS peaks to the lithium-alkyl-carbonate products of solvent reduction [21, 22] on lithium metal. They used FT-IR measurements [23] to determine the nature of the surface film on carbon and found it to be composed of lithium alkylcarbonate(s), lithium carbonate, and species containing P-F and/or P-O bonds using a $LiPF_6$ based electrolyte or B-F/ B-O bonds when utilizing $LiBF_4$ as an electrolyte salt.

Our analysis will be based on an SEI that is composed of LiF, Li_2CO_3, and LiAC. The proposed reactions to form these products are as follows:

Solvent reduction

$$2 \ C_3O_3H_4 + 2 \ e^- + 2 \ Li^+ \rightarrow (CH_2OCOOLi)_2 + C_2H_4 \qquad (8\text{-}1)$$

$$2 \ C_3O_3H_4 + 2 \ e^- + 2 \ Li^+ \rightarrow (CH_2CH_2OCOOLi)_2 \qquad (8\text{-}2)$$

$$C_3O_3H_4 + 2 \ e^- + 2 \ Li^+ \rightarrow Li_2CO_3 + C_2H_4 \qquad (8\text{-}3)$$

Salt reduction

$$LiMF_n + H_2O \rightarrow LiF + 2 \ HF + MOF_{n-3} \qquad (8\text{-}4)$$

$$LiPF_6 + 2 \ Li^+ + 2 \ e^- \rightarrow 3 \ LiF + PF_3 \ , \qquad (8\text{-}5)$$
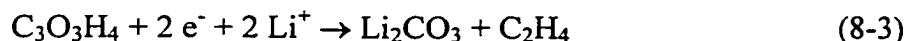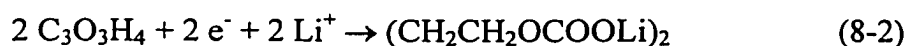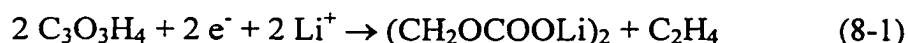
where H_2O was present as an impurity in the electrolyte, $LiMF_n$ was the electrolyte salt and M was typically P, B, or As. The nature of the SEI was an important aspect for the thermal stability of the anode and thus the above description was necessary.

Several ARC experiments were performed on nominally identical samples as described in Section 5.3. Figure 8.2 shows the self-heating rate profiles, at the lowest

onset temperature, of the various lithium-containing carbon samples as a function of temperature. The self-heating reaction(s) in each of the lithium-intercalated carbons begin at 80°C, except for KS-75 (70°C) and for the fiber (90°C). The carbons were grouped into two classes. The first group contained the flaky carbon samples (high surface area) that have the largest self-heating rates and a thermal stability that decreases with increasing surface area. The next group contains the MCMB, fiber and coke carbons, which have similar self-heating profiles, although the coke sample had a much larger surface area. Each self-heating profile contained an initial region of rapid temperature increase, resulting in a peak, followed by a levelling off in the profile (tail). The initial self-heating region was determined by Richard and Dahn to correspond to the decomposition of the metastable components (LiAC) in the solid electrolyte interphase (SEI), while the tail region corresponded to the reaction of intercalated lithium with the electrolyte [68]. In addition, the samples with the lowest initial self-heating rates showed an increase in self-heating rate near 180°C due to the thermal decomposition of the electrolyte [68].
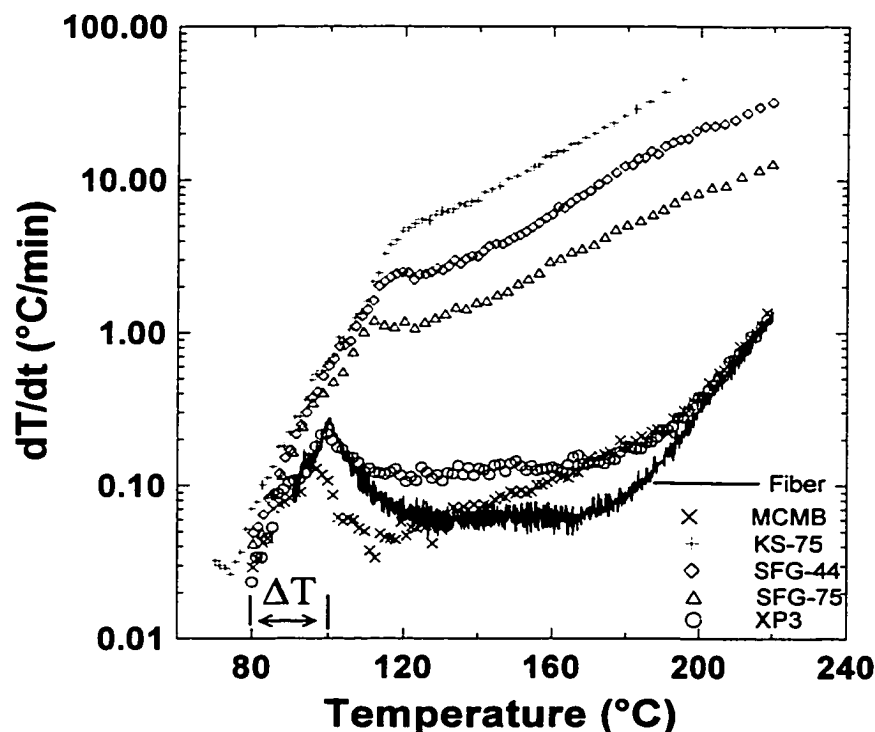
Figure 8.2. Self-heating rate profiles of lithium-intercalated carbons in LiPF₆ EC/DEC (33/67) electrolyte.

Figure 8.2 shows that the self-heating rates for these carbon samples varied by about two orders of magnitude in the tail region. Even if one understands nothing about the reaction mechanisms, it is clear that preparing lithium-ion cells that do not exhibit thermal runaway under abuse conditions with the flaky graphites (KS-75, SFG-75, SFG-44) would be difficult.

In an ARC experiment, the temperature rise, ΔT, associated with the completion of a particular reaction, is proportional to the amount of reactant present. Normally, one would expect the amount of SEI on the carbon to be proportional to its surface area, provided electrolyte molecules could access the same surfaces as the nitrogen molecules used during BET experiments. Therefore, a plot of ΔT (for the reaction process corresponding to the decomposition of the metastable SEI components, i.e. initial peak) versus surface area should yield a straight line. Figure 8.3 shows ΔT, taken from the start of the experiment to the top of the peak (Figure 8.2), versus surface area. Figure 8.3 shows an overall trend of increased ΔT for increasing surface area, except for the XP-coke sample. This "anomalous" behaviour of the coke sample was reproducible, to be shown below.
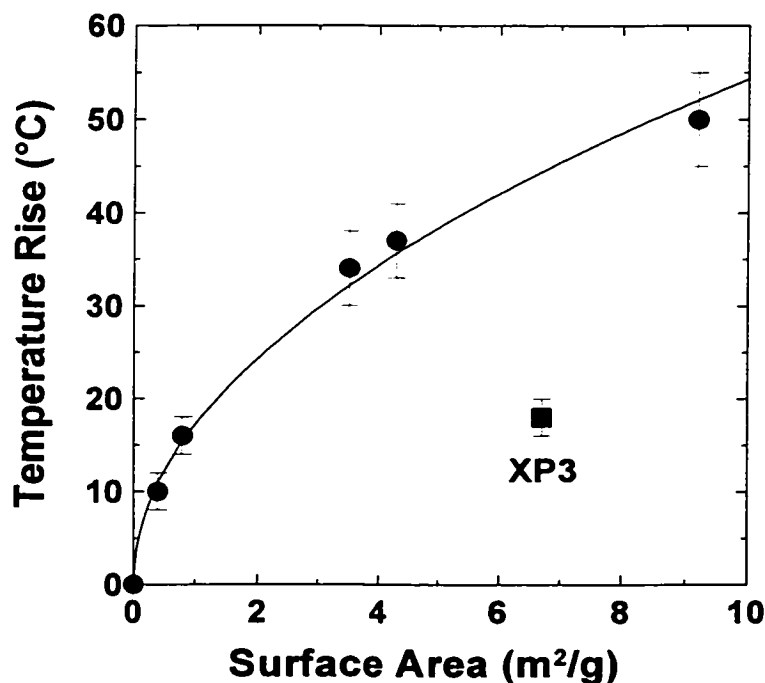
Figure 8.3. Initial temperature rise, ΔT, of the carbons under study as a function of surface area.

Increased surface area should also correlate with increased irreversible capacity of the carbon due to the consumption of more lithium to form the needed SEI to cover the increased surface. Table 8.1 shows that these samples all had similar irreversible capacities. Xing et al. [106] showed that irreversible capacity was not always a good indication of the amount of SEI present on the carbon surface. They found that much of the irreversible capacity was associated with the reduction of surface species on the carbonaceous material. For example, the irreversible capacity for an MCMB carbon that was never exposed to air after heat-treatment was only 8 mAh/g [106], compared to near 30 mAh/g for the same sample in a coated electrode. In addition, BET surface area measurements yield the N_2 – accessible surface. The surface that is accessible to the larger solvent molecules may be substantially different depending on the details of the surface roughness and nanoporosity. Therefore an exact correlation between surface area and irreversible capacity is not always found.

The initial peak in the self-heating profile is believed to be caused by the decomposition of the SEI, but neither the amount of irreversible capacity nor the N_2 surface area can be used to predict accurately the extent of the self-heating reaction(s) in lithium-intercalated carbon materials. On the other hand, increasing the surface area of a particular carbon by grinding was found to increase surface area, increase irreversible capacity and increase the ΔT of the initial peak in the self heating [68].

The coke sample showed a lower self-heating rate than expected, based on its surface area, perhaps due to a difference in surface reaction(s) occurring on the carbon. This is unlikely, as shown below. Alternatively, only a small part of the surfaces accessible to N_2 may be accessible to electrolyte. The low self-heating rate and small ΔT were not due to the intrinsic lower capacity of coke materials for lithium [107] because the initial peak was not dependent on lithium content between the range of LiC_6 and $Li_{0.2}C_6$ [35, 68]. Further experiments are needed to address this "coke anomaly".

All samples analyzed in this work were discharged to zero volts and contained as much lithium intercalated into the carbon lattice as possible. The (002) x-ray diffraction peak of the samples described by Figure 8.2 are shown in Figure 8.4. Comparing the change in the profiles caused by heating MCMB to 220°C in the ARC, Richard and Dahn

[68] showed that about Δx=0.3 Li atoms in Li_xC_6 were consumed. Although in-situ x-ray diffraction experiments are not available for the fiber sample, they are for XP-coke [107] and for flaky graphite [67]. The x-ray patterns are consistent with the consumption of 0.3 Li for all the samples shown in Figures 8.2 and 8.4. The flake graphite samples showed large amounts of the stage 2 lithium-intercalated graphite phase even after long equilibration at 0.0 V. This is thought to be caused by extremely low porosity of the pressed pellets of flaky graphites which limits lithium-ion transport through the electrolyte.
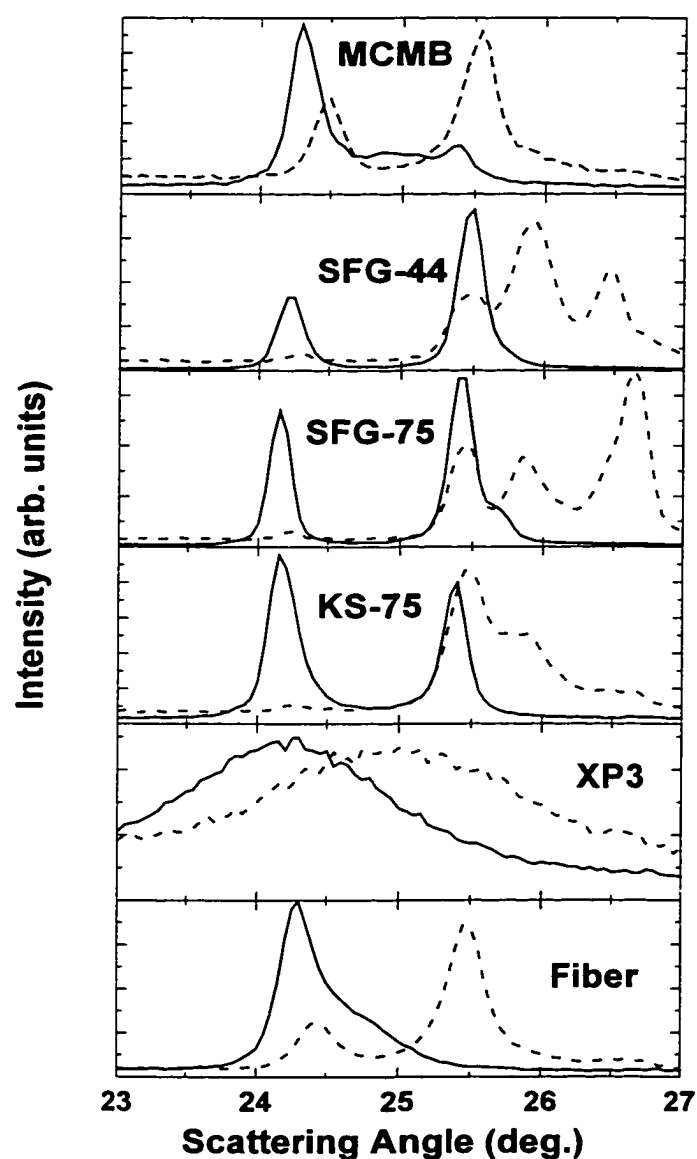
Figure 8.4. X-ray diffraction profiles, collected before (solid lines) and after (dashed lines) ARC experiments for the carbons under study.

The reaction that continued after the peak was previously described to be the reaction of intercalated lithium with electrolyte, slowed by transport through the build up of SEI decomposition products [68]. It is believed and assumed that the SEI formed during room temperature discharge was the same thickness on each of the carbons. Then, after the peak in the self-heating rate, each carbon will have approximately the same layer thickness of decomposed SEI products. The number of intercalated Li atoms that initially pass through this layer per unit time to react with electrolyte should be proportional to the area of contact between the electrolyte and the layer. Thus, the self-heating rate at the beginning of the tail should also be proportional to the surface area of the samples (if the N_2 surface area measures that area accessible to electrolyte). Figure 8.5 shows the initial tail self-heating rates (measured at 120°C from the data in Figure 8.2 for all samples) plotted versus surface area. Figure 8.5 shows the trend for increased self-heating rate in the tail with surface area except for the XP-3 coke sample. This result strongly suggests that the N_2-accessible and electrolyte-accessible surfaces for this sample are inequivalent.
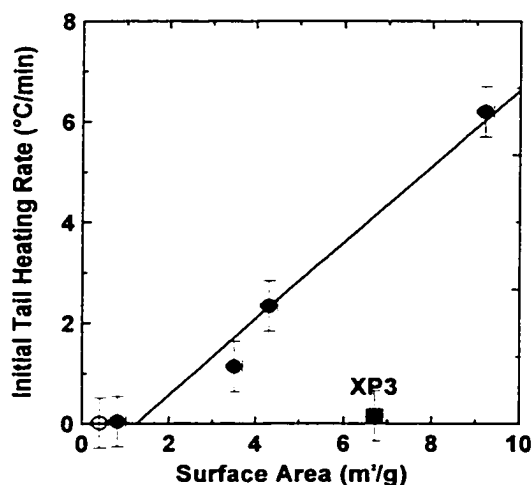
Figure 8.5. Initial self-heating rates of the tail region (at 120°C in Figure 8.2) for each carbon as a function of surface area. Solid circles –80°C start, open circle-90°C start for fiber sample.

8.3 Determination of Arrhenius Constants for Various Carbon Anodes

It has been previously shown that a straight line can fit the initial part of the self-heating rate profile from identical samples heated to different temperatures, where kinetic parameters can be extracted from a typical Arrhenius-type plot. Figure 8.6a shows results for ARC experiments on the XP-3 coke sample that started at 80, 90, 100, 110, 120 and 130°C. The initial data point collected for each experiment is shown as a large circle. Since the sample at the start of each experiment was nominally the same, the differences in self-heating rates are caused only by the reaction kinetics. For simple activated kinetics, a plot of the natural logarithm of the self-heating rate, ln(dT/dt), versus the inverse temperature, (1/T), should yield a straight line. The slope can be used to calculate the activation energy, E_a, and the y-intercept gives the frequency factor, γ, for the decomposition of the SEI layer on the lithium-intercalated carbon.
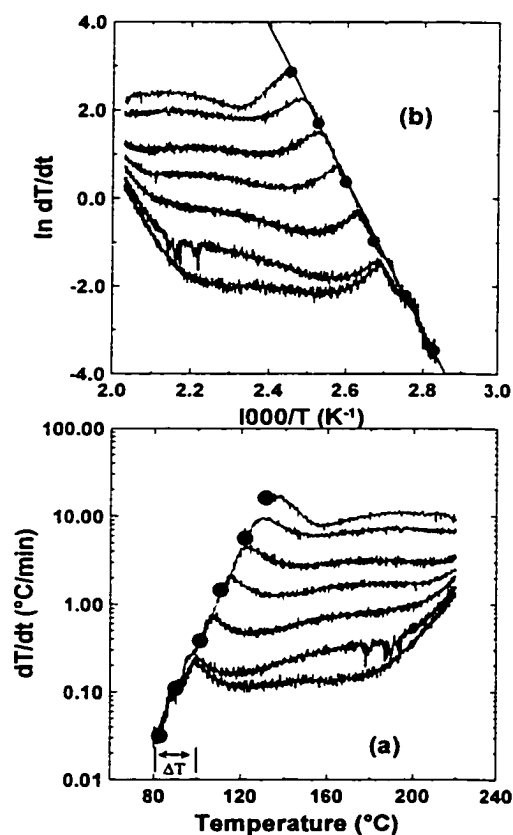
Figure 8.6. a) Self-heating rate profile for lithium intercalated Conoco XP-3 coke in 1M $LiPF_6$ EC/DEC (33/67) for samples initially heated to 40°C, 80°C, 100°C, 110°C, 120°C and 120°C. b) Natural logarithm of the values of dT/dt in a) when measured in K/min as plotted versus 1000/T.

Figure 8.6b shows the results of Figure 8.6a plotted as ln(dT/dt) versus 1000/T. The slope yields an activation energy of 1.48 eV and a frequency factor of 1.8×10^{18} min^{-1} is obtained. The results of the initial starting temperature experiments for the remaining lithium-intercalated carbon samples are shown in Figures 8.7 and 8.8, with the fitted line through the experimental start points shown.
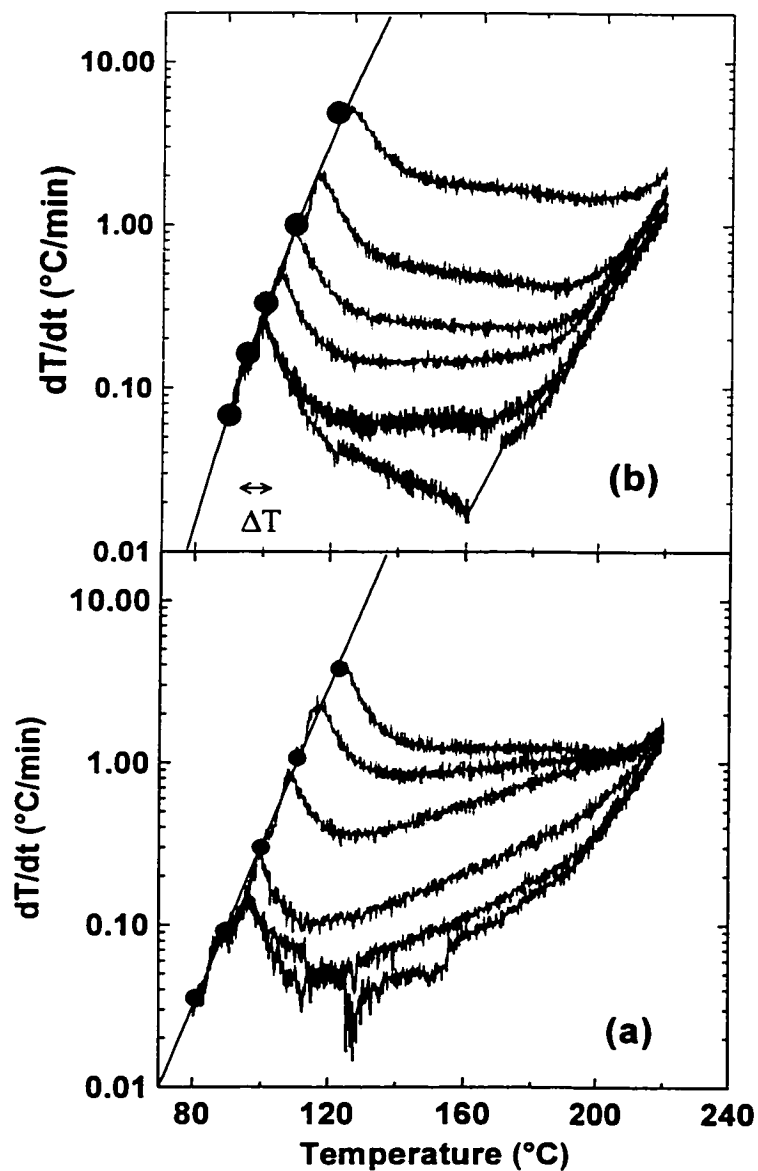
Figure 8.7. Self-heating rate profiles for lithium intercalated a) MCMB and b) fiber graphites in 1M LiPF$_6$ EC/DEC (33/67, vol/vol).
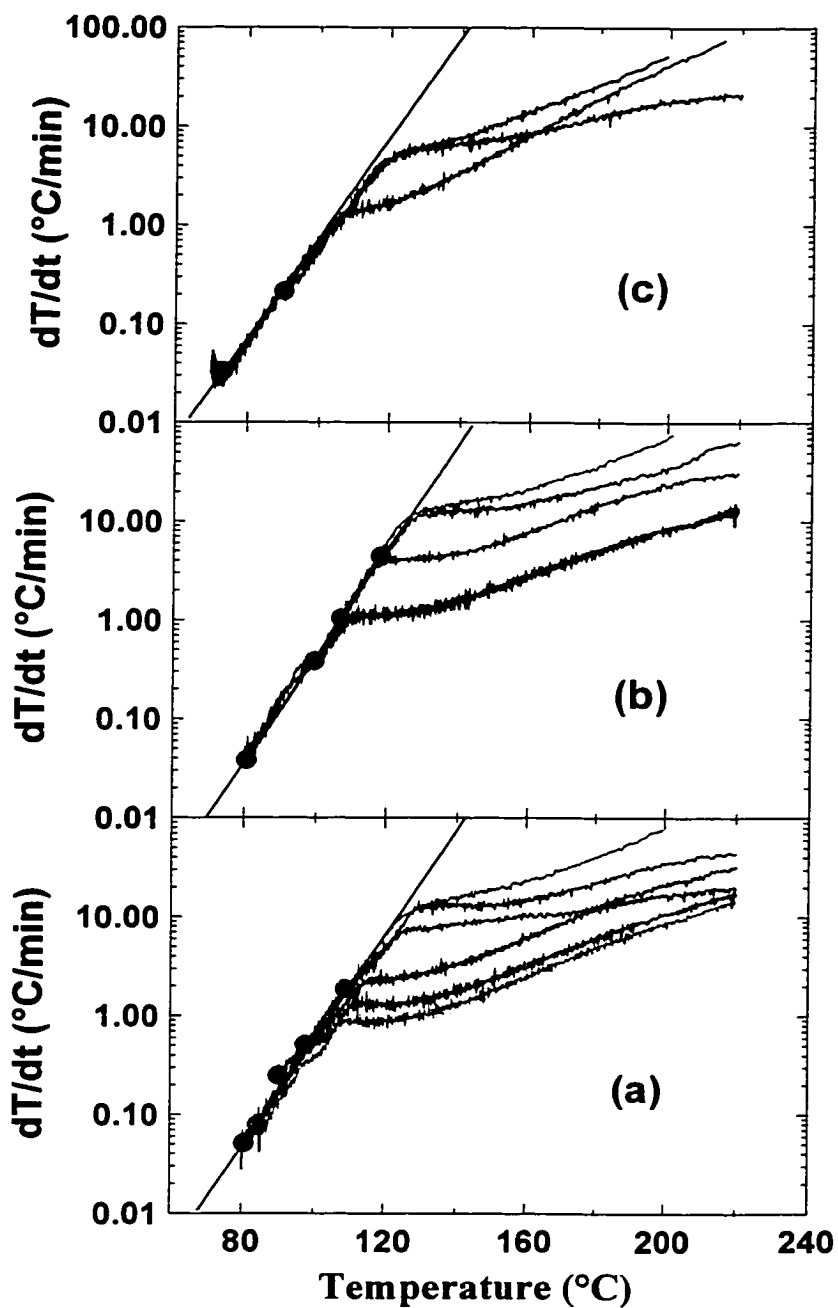
Figure 8.8. Self-heating rate profile for lithium-intercalated a) SFG-44, b) SFG-75, c) KS-75 graphites in 1M LiPF$_6$ EC/DEC (33/67, vol/vol).

The activation energies for the decomposition of the SEI for all the samples (Table 8.2) are very similar and this suggests that the heat generating reactions are the same in each of the samples. The initial self-heating was from the conversion of metastable to stable SEI and thus the nature of the SEI layer determined the activation

energy of the process, not the substance that the layer was deposited on. The activation energy for the XP-3 sample was the same as the others, suggesting again that the apparent anomalies associated with its behavior can be attributed to the inequivalence of the N_2-accessible and electrolyte-accessible surface areas.

Table 8.2. Kinetic parameters for the carbons under study

Carbon	ΔT (°C)	Ea (eV) (± 0.1)	γ (min⁻¹) (± 10%)	Carbon	ΔT (°C)	Ea (eV) (± 0.1)	γ (min⁻¹) (± 10%)
MCMB (LiPF$_6$)	16 ±2	1.4	4.7×10^{16}	XP3	18 ±2	1.5	1.8×10^{18}
SFG-75	34 ±4	1.5	6.4×10^{17}	Fiber	10 ±2	1.5	3.7×10^{18}
SFG-44	37 ±4	1.5	1.6×10^{18}	MCMB (LiBF$_4$)		0.82	4.8×10^{10}
KS-75	50 ±5	1.3	1.8×10^{16}				

8.4 Dependence of the Self-heating Rate Profile on Electrolyte

The nature of the SEI was found to be dependent on the electrolyte solution that was utilized [23, 108]. In the above series of experiments, the electrolyte used was a 1M LiPF$_6$ solution in a 33/67 (vol/vol) mix of EC/DEC and thus the SEI should have the same chemistry for all the carbon samples. Figure 8.9 shows the initial self-heating rate for fresh samples heated directly to the indicated temperatures (these data are all the solid circles in Figures 8.6 to 8.8). At each particular starting temperature, the relative stability of the fresh samples can be compared. At 90°C, for example, the flake graphite materials have the highest initial heating rate followed by the MCMB, coke, and fiber materials and this trend is continued throughout the temperature range.
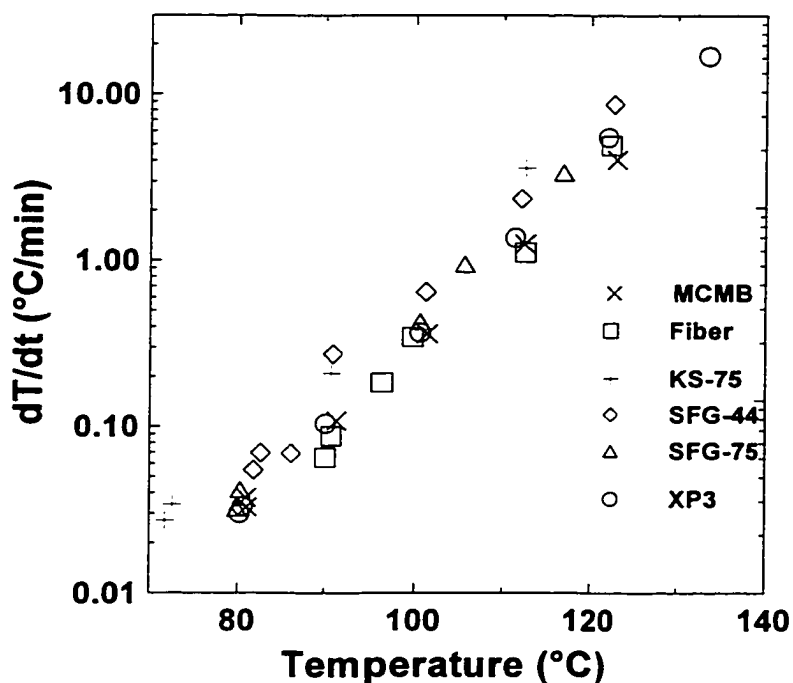
Figure 8.9. Initial self-heating rate of the carbon samples heated directly to the indicated temperatures (these results are the solid circles of Figures 8.6 – 8.8).

According to the description for the self-heating of a lithium-intercalated carbon sample in Section 8.3, if one changes the chemistry of the SEI, the heating profiles should be different. The SEI is dependent on the lithium salt and the solvent used in the electrolyte [108]. Samples of MCMB were intercalated with lithium in 1M LiBF$_4$ dissolved in 50/50 EC/DEC (vol/vol, Mitsubishi Chemicals). The same series of ARC tests were then performed. Figure 8.10 shows all the ARC runs that were started at different temperatures as indicated by the solid dots. The self-heating profiles obtained are very different to those obtained for LiPF$_6$ electrolytes. First, the onset for the exotherm begins at 60°C and second, there is no peak in the profile. Aurbach et al. [23] showed that the SEI formed on carbon in LiBF$_4$-electrolytes did not contain semi-carbonates or other metastable components. The self-heating profiles obtained in LiPF$_6$ shows a peak due to the reaction of metastable components and thus it was not surprising that no peak in the profiles is obtained with LiBF$_4$ as electrolyte salt. The heat generated by the LiBF$_4$ sample must be due to reaction of intercalated lithium with the solvent that occurs at a temperature 20°C lower than in LiPF$_6$. The SEI layer formed on LiBF$_4$ is hypothesised to be not as effective as with LiPF$_6$, thus the diffusion of lithium across the

SEI to react with the solvent at lower temperature is easier, resulting in an earlier onset of self-heating.
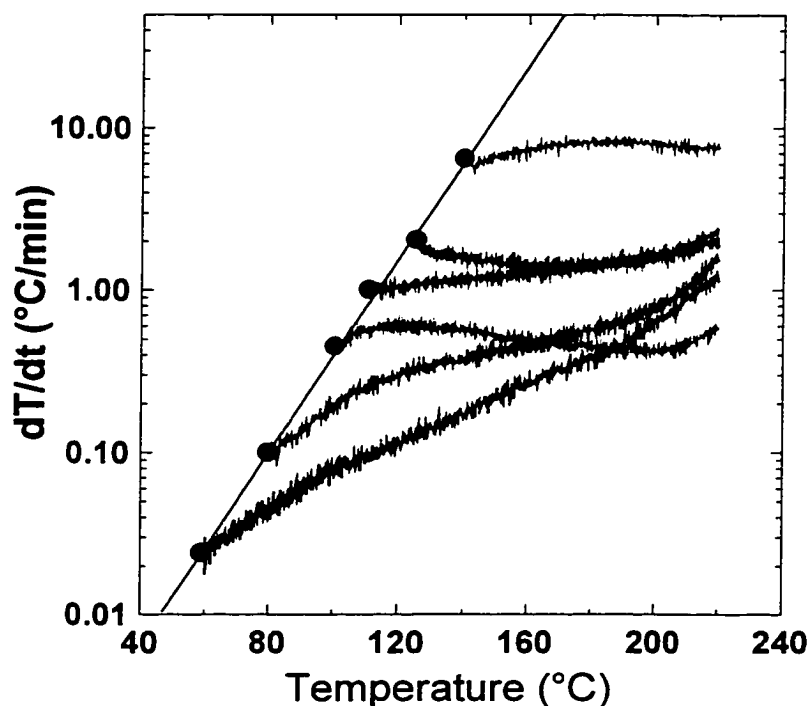
Figure 8.10. Self-heating rate profile for lithium-intercalated MCMB in 1M LiBF₄ EC/DEC (50/50, vol/vol).

The activation energy and frequency factor for the reaction of intercalated lithium with LiBF₄ electrolyte was obtained from the data of Figure 8.10 and is given in Table 8.2. Notice the large difference from that obtained for LiPF₆ electrolytes.

8.5 Characteristics for Improved Thermal Stability in Carbon Anode Materials

The results presented here provide a good indication as to the direction to follow for improved thermal stability in carbon anodes, which will ultimately lead to an increase in cell safety. Taking into account the characteristics required for anode materials, such as capacity, charge retention, and thermal stability, two carbon morphologies, spheres and fibers appear to be better than the others. Furthermore, the fiber had the lowest self-

heating rate in the tail region. The disadvantage of the fiber studied here was its shape, which approximated a miniature "telephone pole". It would be difficult to pack long crossed fibers into dense electrodes. If the fibers could be cut into shorter pieces shaped similar to that of a "soup can", then dense electrodes could be made. This must be performed without substantial increases in surface area. The fibers appear to have the smoothest surfaces of all the samples studied here, and given the control that exists over fiber diameter in the manufacturing process, "soup can" shaped pieces of fiber may ultimately offer the optimum geometry for safety and performance.

BP Amoco Chemicals now manufacture "soup can" shaped carbon fibers under the trade name EnerGraph. The commercialisation of this product was the result of a strong interaction between my research group and BP Amoco. The interaction involved a variety of electrochemical tests and consultations on the necessary requirements for thermally stable charged electrodes as described above.

Chapter 9

Full Thermal Model of Lithium-ion Cells

Manufacturers are constantly looking to improve electrode materials for lithium-ion batteries. When a new material is introduced into a cell, the cell must still meet industry standards regarding the safety of the cell. The safety of these new cells must be re-evaluated for each new material (electrode, electrolyte or additive) introduced into the cell. A mathematical model that describes the heat production within a lithium-ion cell has been developed in the Dahn laboratory [109, 110, 111]. A manufacturer or researcher can use this model to predict the thermal behaviour of a cell with a new electrode material or electrolyte without having to produce an expensive test batch of cells. Although the mathematical model was developed primarily by Tim Hatchard [110], the kinetic triplet that describes the heat produced by the chemical reactions between a unit mass of cathode ($Li_{0.5}CoO_2$) and electrolyte at a given temperature per unit time was taken from my work. In addition, the model presents important results and implications for the safety of lithium-ion cells.

9.1 Description of the Model

The model was developed for the standard 18650 cylindrical shape, which could then be generalized to other shapes and sizes. The cell, 18 mm in diameter and 65 mm in length, was considered as a series of N concentric cylindrical shell rings of equal width. The width, thermal conductivity and temperature difference between the rings determined the heat flow in the cell, while Newton's law of cooling was selected to describe heat flow at the surface. Axial heat flow to and from the cylinder was believed to be minimal and thus ignored throughout the model [110, 111].

Initially, the heat flow within a cylindrical geometry had to be described and with no heat produced within the cylinder the temperature change, ΔT, in each ring during an infinitesimal time interval, Δt, is given by [110, 111]

$$\Delta T_i = \left[\frac{k_T(T_{i+1} - T_i)2\pi r_i}{(r_{i+1} - r_i)} - \frac{k_T(T_i - T_{i-1})2\pi r_{i-1}}{(r_i - r_{i-1})} \right] * \frac{\Delta t}{c_c \rho(\pi r_i^2 - \pi r_{i-1}^2)}, \qquad (9\text{-}1)$$

and

$$\Delta T_N = \left[\frac{k_T(T_N - T_{N-1})2\pi r_{N-1}}{(r_N - r_{N-1})} - (T_w - T_N)h_s 2\pi r_N \right] * \frac{\Delta t}{c_c \rho(\pi r_N^2 - \pi r_{N-1}^2)}. \qquad (9\text{-}2)$$

Equation 9-1 gives the temperature change in the ith ring and Equation 9-2 gives the temperature change in the Nth or outermost ring. The first term in both equations describes the heat flowing into the ring per unit time from the neighbouring inner ring, while the second term describes the heat flowing into the ring per unit time from the neighbouring outer ring. A schematic representing the heat flow to the ith ring as described by Equation 9-1 is shown in Figure 9.1. ΔT_i, is the temperature change of the ith ring and ΔT_N is the temperature change of the outermost ring in the time Δt (s). The outer radius of the ith ring is r_i (cm), k_T is the thermal conductivity of the cylinder material (Wcm^{-1}K^{-1}), Δt is the time step used, c_c is the specific heat capacity of the cylinder material (Jg^{-1}K^{-1}), ρ is the density of the material (gcm^{-3}) and h_s is the surface heat conductivity of the cylinder (Wcm^{-1}K^{-1}).
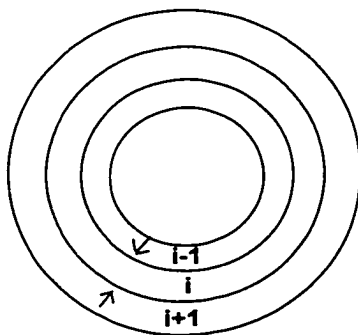
Figure 9.1. Schematic of heat flow into the ith ring according to Equation 9-1.

When a lithium-ion cell is exposed to elevated temperatures, exothermic reactions take place within the cell and contribute to its temperature rise. Thus the above heat flow equations require the addition of a term in their square brackets to describe the power

generated from the reactions of the electrode materials at high temperatures. The necessary power term was [110, 111]

$$P_i \ [\pi(r_i^2 - r_{i-1}^2)] , \qquad (9\text{-}3)$$

where P_i is the power per unit volume produced in the ring and the rest of the equation gives the volume of the ring. It was assumed that the heat produced from the electrode materials could be separated into two contributions, one for the anode the other for the cathode. For the anode, the model developed by Monique Richard [57] was used and the power produced per unit mass of anode, P_a, material was given by,

$$P_a = H_1 \gamma_1 x_f^n \exp\left(\frac{-E_1}{K_B T}\right) + H_2 \gamma_2 x_i \exp\left(\frac{-z}{z_o}\right) \exp\left(\frac{-E_2}{k_B T}\right), \qquad (9\text{-}4)$$

where the two terms are for two separate reactions at the carbon electrode. H_1 and H_2 are the total amounts of heat that can be produced by each reaction per unit mass of reactant (Jg^{-1}), γ_1 and γ_2 are frequency factors and E_1 and E_2 are activation energies for the reactions. The parameters x_f, x_i and z are described in reference [57] but briefly x_f is the amount of lithium-containing metastable species in the solid electrolyte interphase, x_i is the amount of lithium intercalated within the carbon, and z is a dimensionless measure of the SEI thickness [57]. During the course of the modelling, the change in the anode parameters were tracked by the following equations,

$$\Delta x_f = -\gamma_1 x_f^n \exp\left(\frac{-E_1}{k_B T}\right) \Delta t , \qquad (9\text{-}5)$$

$$\Delta x_i = -\gamma_2 x_i \exp\left(\frac{-z}{z_o}\right) \exp\left(\frac{-E_2}{k_B T}\right) \Delta t , \qquad (9\text{-}6)$$

and $$\Delta z = -\gamma_2 x_i \exp\left(\frac{-z}{z_o}\right) \exp\left(\frac{-E_2}{k_B T}\right) \Delta t . \qquad (9\text{-}7)$$

As described in Chapter 5, the power produced for the cobalt electrode (P_c) can be described by,

$$P_c = H\gamma \exp\left(\frac{-E_c}{k_B T}\right) \alpha^m (1-\alpha)^n (-\ln(1-\alpha))^p , \qquad (9\text{-}8)$$

or, $$P_c = H\frac{d\alpha}{dt} . \qquad (9\text{-}9)$$

Here, H is the total heat produced by the reaction per unit mass (J/g), γ is a frequency factor, E_c the activation energy and α is the fractional degree of conversion. The exponents m, n, and p were chosen from the kinetic analysis of ARC and DSC data presented in Chapter 7, where $m = 0$, $n = 1$, $p = 2/3$ (Avrami - Erofeev) were found to fit the experimental data well. The activation energy was taken from Chapter 7 to be 1.24 eV, while the frequency factor was 1.2×10^{13} min^{-1}, which is slightly higher than experimentally determined. This new frequency factor was chosen to take into account the differences in the conditions used in the experiment. Some of the differences that could be identified were that the electrolyte system of the commercial cells was not known, in addition the exact electrode compositions of the commercial cells were also unknown. Also, during the modeling described in Chapter 7, only the first exothermic process was modeled and thus more reactivity was required from the cathode to model this electrode qualitatively.

The thermal model was coded in Fortran and then transposed to a user-friendly Visual C++ application [109, 110, 111]. The user has the ability to adjust numerous parameters and perform calculations for various experimental set-ups, such as full cell thermal response or ARC and DSC of individual electrodes. The versatility of the model is increased by the fact that oven exposure results for prismatic cells are easily handled. The calculations were similar to those above except the prismatic cells were divided into N layers, with heat flow through the edges ignored. The required parameters are the same as before except that the temperature change in each layer was given by,

$$\Delta T_i = \left[\frac{k_T(T_{i+1} - T_i)L \cdot W}{B/N} + \frac{k_T(T_{i-1} - T_i)L \cdot W}{B/N} + P_i(L \cdot W \cdot B/N) \right] * \frac{\Delta t}{c_c \, \rho L \cdot W \cdot B/N}. \quad (9\text{-}10)$$

In Equation 9-10, L and W represent the length and width of the cell, N is the number of layers and B is the cell height or thickness.

9.2 Results and Implications

Figure 9.2 gives the results of a numeric model as compared to the experimental data of a stainless steel cylinder, machined to be the size of an 18650 cell. The cylinder was placed into a 150°C oven and its temperature was monitored with an attached

thermocouple. The results were nearly identical and gave confidence in the simple numeric model proposed in Section 9.1. The full experimental details of the oven, heating regime and thermocouple set up are given in detail in refernce 110 and 111.
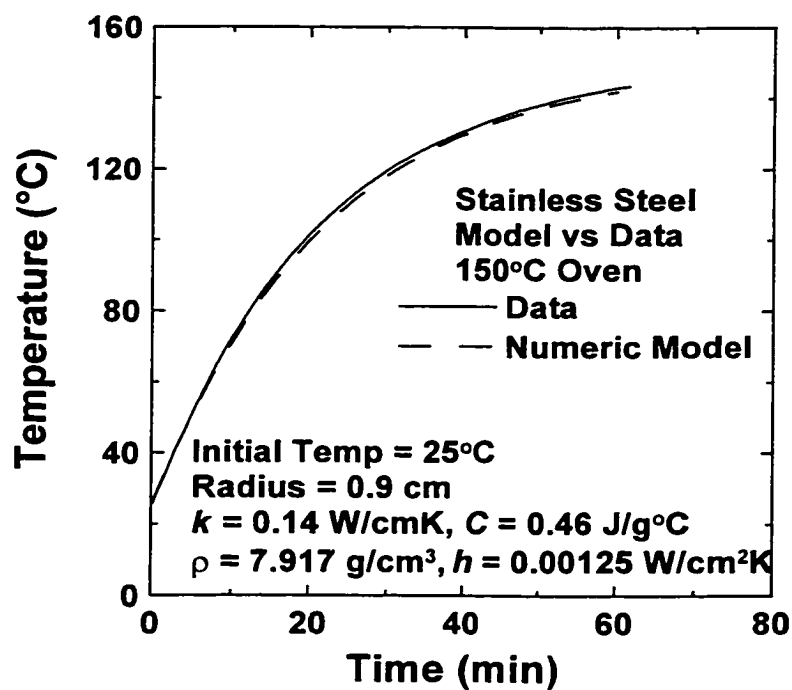
Figure 9.2. A comparison of model predictions to actual data for a solid stainless steel cylinder. Solid curve-oven data, dashed- model prediction

The results of various oven exposure tests are shown in Figure 9.3 and compared to the model predictions. These tests were performed on E-One/Moli Energy 18650 MCMB/LiCoO₂ cells charged to 4.2 V. The cells, after being charged, were quickly inserted into a heated oven and the temperature of the cell was monitored by an attached thermocouple. The results of the mathematical model were obtained using the parameters listed in Table 9.1 at the desired oven temperature. The results of the model compared qualitatively well for the initial cell warm-up and the amount/ duration of over-shoot in oven temperature.. More important is the fact that the model could accurately predict whether or not the cell proceeded into thermal runaway.
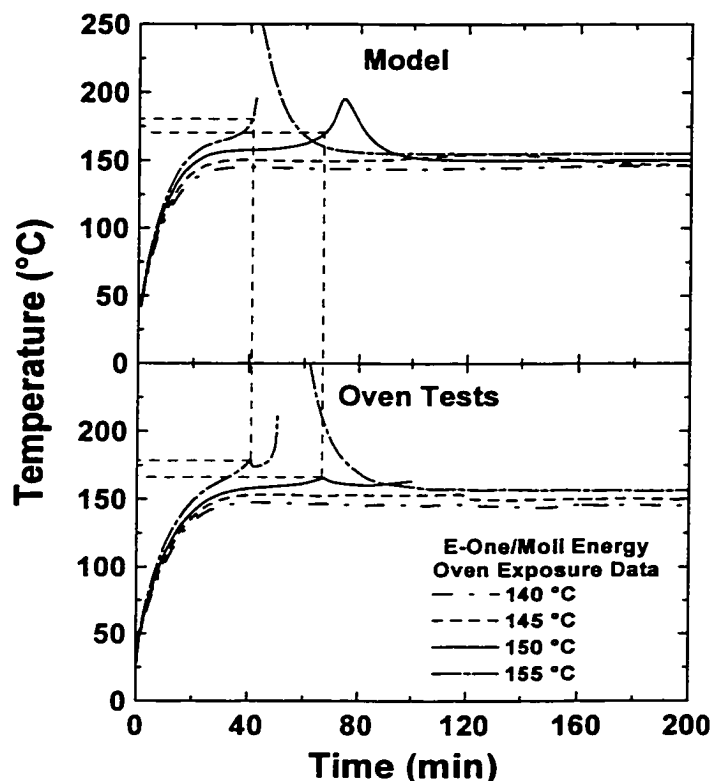
Figure 9.3. A comparison of oven exposure test results to model predictions. Top panel-model predictions, bottom panel- oven results for 18650 E-One/Moli Energy cells charged to 4.2V.

The deviations seen between the model predictions and experimental data are easily explained. The exact time of thermal runaway was not accurately reproduced due to the presence of the safety vent on the commercial cells. As described in Section 3.1, the opening of the pressure vent allows for the cooling of the cell due to the rapid release of gaseous decomposition products. The opening of the pressure vent was difficult to model. In spite of this, it was clear that if the cells did not contain a safety vent, the point of thermal runaway would have been very accurately modeled. In addition the model predicted a maximum temperature for the cells that entered thermal runaway near 250°C, while the actual cells reached temperatures exceeding 700°C (in the span of seconds!). This difference was due to the fact that only the first exothermic process in the decomposition of $Li_{0.5}CoO_2$ was modeled. A more accurate reproduction of the high temperature behavior would have been obtained if the complete reaction kinetics of the $Li_{0.5}CoO_2$ electrode were known.

Table 9.1. Standard model parameters used to describe E-One/Moli Energy LiCoO₂/graphite chemistry.

Parameter	Value
Cathode frequency factor, γ	1.2×10^{13} (min^{-1})
Cathode activation energy, E_a	1.24 (eV)
Cathode α_o	0.03 (unitless)
Cathode m	0 (exponent)
Cathode n	1 (exponent)
Cathode p	2/3 (exponent)
Cathode H	314 (Jg^{-1})
Anode SEI frequency factor, A_1	1×10^{17} (min^{-1})
Anode intercalated lithium frequency factor, A_2	1.5×10^{15} (min^{-1})
Anode SEI activation energy, E_1	1.4 (eV)
Anode intercalated lithium activation energy, E_2	1.4 (eV)
Anode x_{fo}	0.15 (dimensionless)
Anode x_{io}	0.75 (dimensionless)
Anode z_o	0.033 (dimensionless)
Anode n	1 (exponent)
Anode SEI H	257 (Jg^{-1})
Anode intercalated lithium H	1714 (Jg^{-1})
Carbon mass	
(Cylindrical, 18650)	6 (g)
(Thin prismatic, 3.5 x 6.2 x 0.36 cm)	1.7 (g)
(Thick prismatic, 3.5 x 6.2 x 0.36 cm)	7.2 (g)
LiCoO₂ mass	
(Cylindrical, 18650)	12 (g)
(Thin Prismatic, 3.5 x 6.2 x 0.36 cm)	4.1 (g)
(Thick Prismatic, 3.5 x 6.2 x 0.36 cm)	17 (g)
Start temperature	28 (°C)
Average cell specific heat	0.83 (Jg^{-1}K^{-1})
Average jelly roll radial thermal conductivity	0.034 (Wcm^{-1}K^{-1})
Average jelly roll density (cylindrical)	2.58 (gcm^{-3})
Average density (prismatic)	1.70 (gcm^{-3})
Can density	7.917 (gcm^{-3})
Can specific heat	0.46 (Jg^{-1}K^{-1})
Surface emissivity (matches that of E-one/Moli label (8))	0.80 (dimensionless)
Can thermal conductivity	0.14 (Wcm^{-1}K^{-1})
Length (cylindrical, 18650)	6.5 (cm)
Length (prismatic)	6.2 (cm)
Radius (cylindrical)	0.9 (cm)
Width (prismatic)	3.5 (cm)
Thickness (prismatic)	Thin 0.36 (cm) Thick 1.5 (cm)

The mathematical model can separate the contributions of the individual electrodes to determine where and when each electrode reacts with electrolyte at elevated temperature. A clear picture can now be obtained of what occurs and when it occurs inside a cell during an oven exposure test. The individual contributions to the temperature rise in a lithium-ion cell placed in a heated oven are shown in Figure 9.4. Initially, at a temperature near 100°C, the metastable components of the solid electrolyte interphase (SEI) at the anode (as tracked by x_f) decompose. This rapid decomposition increases the temperature of the cell, such that the reaction of the intercalated lithium at the anode (as tracked by x_i) begins. This reaction produces enough heat to overshoot the set temperature of the oven and initiate the reaction at the cathode (as tracked by α). Here α increases as the cathode/electrolyte reaction proceeds, while x_f and x_i decreases as the anode reaction proceeds. The reaction of the intercalated lithium at the anode and the cathode reaction continue to heat the cell until about 175°C where the rapid reaction at the cathode causes the completion of the anode reaction and the cell to enter thermal runaway.
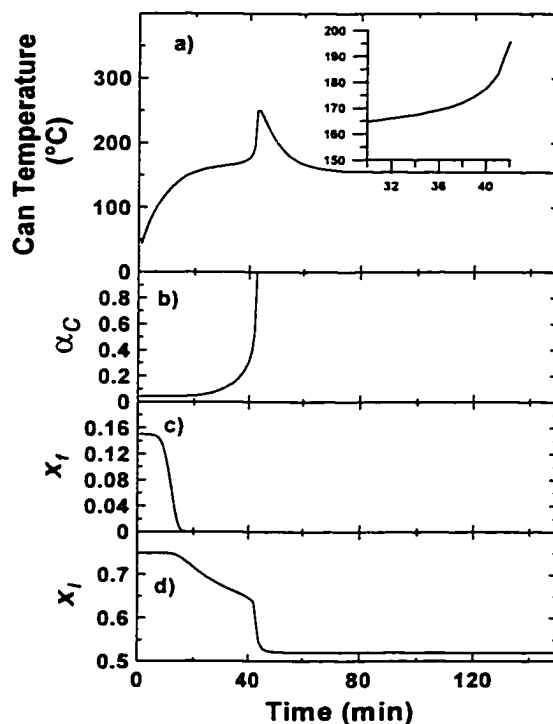
Figure 9.4. Tracking the changes in parameters during an oven exposure test: panel a) surface temperature of the cell, b) fractional degree of conversion for the cathode, c) decomposition of the SEI, d) reaction of intercalated lithium at the anode.

The power of this mathematical model is in its ability to predict the response for a change in reaction conditions. When the size of a cell is increased, the ability to dissipate any generated heat decreases due to the decrease in the surface area to volume ratio of the cell. This model can calculate the effect of a cell size increase without fabricating these larger cells as shown in Figure 9.5. Manufacturers can now test the effect of an increase to the cell radius, and thus capacity, on the results of an oven exposure safety test.
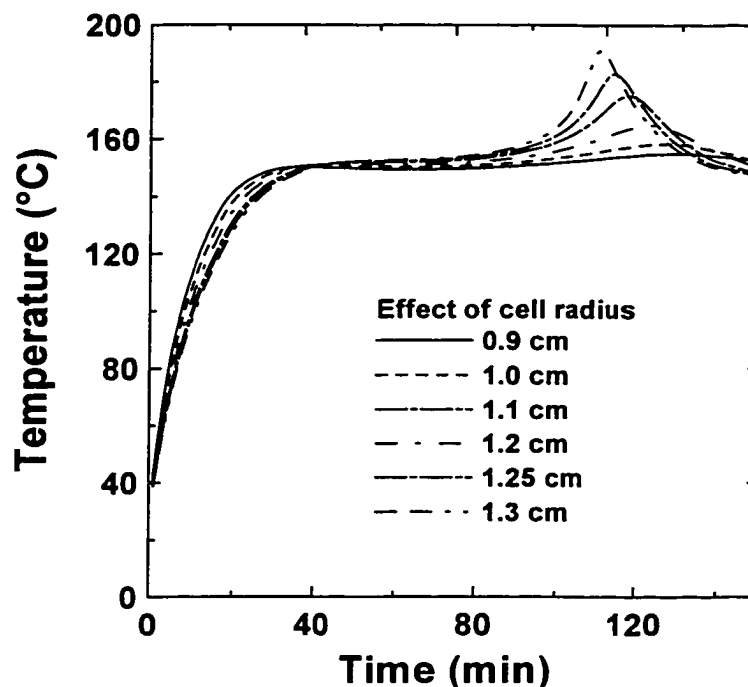
Figure 9.5. The effect of increasing the cell radius on oven exposure tests for LiCoO₂/MCMB chemistry (E-One/Moli Energy).

The model allows for the prediction of prismatic type cells, and predictions for two different thicknesses of cells at two different temperatures are shown in Figure 9.6. All parameters (in Table 9.1) were as before except the thickness, and the amount of electrode material was scaled for prismatic lithium-ion cells. Both cells have little overshoot of the oven temperature at 140°C, while at 160°C the thinner cell was much safer, overshooting the set temperature by only 10 degrees. By contrast, the thicker cell at 160°C could not dissipate the internally generated heat fast enough and goes to thermal runaway.
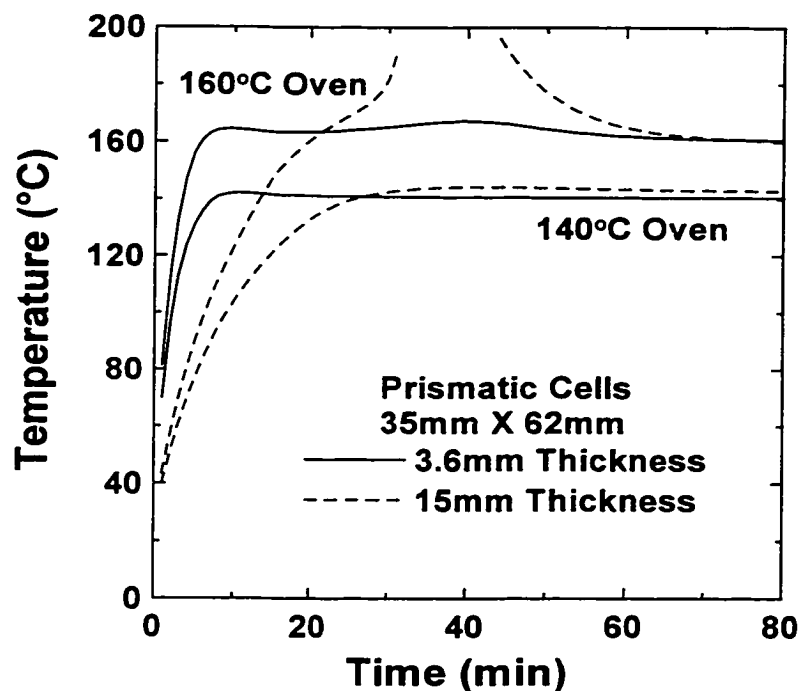
Figure 9.6. A comparison of oven exposure tests predictions for LiCoO₂/MCMB prismatic cells (4.2V) of two thicknesses, solid curve- 3.6 mm thick cell, dashed curves- 15 mm thick cell.

In addition to these predictions the model can predict the result of changing a variety of parameters, such as an increase in the surface heat conductivity (by changing the label of the cell [112]). Electrode developers can investigate and predict the result of new electrode materials without actually producing test batches of these cells. In addition, new electrolytes or additives can be tested in the same way. Reducing the need for full scale lithium-ion test batches will come as significant savings to electrode developers and manufacturers alike.

Chapter 10

Other Cathode Materials

10.1 LiMn₂O₄ Reaction Mechanism

As stated in Chapter 2, $LiCoO_2$ is the most widely used cathode material for lithium-ion batteries. Manufacturers and researchers alike are constantly trying to introduce new electrode materials on the basis of improved lithium capacity or safety. Currently, two manufacturers are using $LiMn_2O_4$ as cathode material due to the improved safety characteristics of this material that could allow for the introduction of larger sized electrochemical cells. In this section, I will present the results of ARC experiments on $LiMn_2O_4$, charged to 4.2 V.

The rinsing procedure described in Section 4.2.2 was used on $LiMn_2O_4$, charged to 4.2V, to obtain information about the reactions that occur during exposure to elevated temperature. Figure 10.1 shows the x-ray diffraction profiles of the $Li_xMn_2O_4$ sample charged to 4.2V (gives the near λ-MnO_2 structure [113]) before the rinsing procedure and the same sample after DMC rinsing. The peaks in the profile due to the sample holder and those from λ-MnO_2 are indicated. The diffraction patterns are identical to the eye and thus the bulk structure of the electrode is maintained during the rinsing procedure.
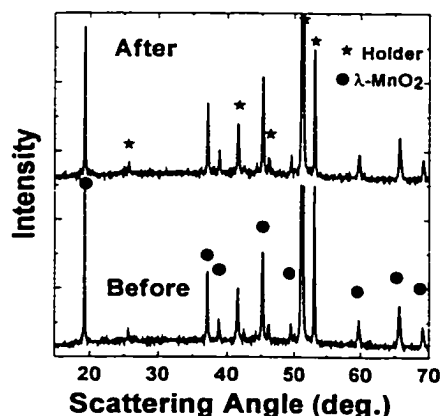
Figure 10.1. X-ray diffraction profiles of $Li_xMn_2O_4$ charged to 4.2 V before and after the DMC rinsing procedure. Indicated peaks are due to the sample holder.

To determine the effect that the DMC rinsing procedure had on the thermal response of the electrode, a 0.2 g portion of the rinsed electrode had 0.1 g of 1M LiPF$_6$ in EC/DEC added to it. The self-heating rate profile is shown as the solid curve in Figure 10.2, and is compared to an fresh electrode with the same amount of added electrolyte (the dashed curve in Figure 10.2). The profiles are very similar and the small differences can be attributed to the fact that the fresh electrode was not dry before the excess electrolyte was added and thus it contains more than 0.1 g of electrolyte [48]. The x-ray diffraction and the ARC results in Figures 10.1 and 10.2, respectively, demonstrate that the DMC rinsing procedure can be used to remove the electrolyte from the surface of the electrode without changing the bulk structure or the thermal response.
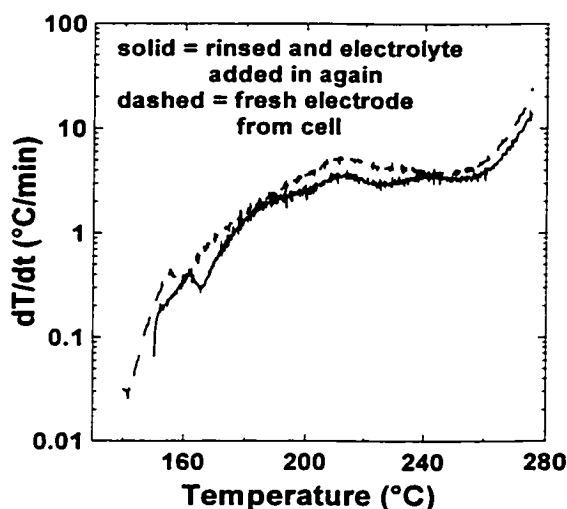
Figure 10.2. Self-heating rate of 0.2 g Li$_x$Mn$_2$O$_4$ charged to 4.2 V in the presence of 0.1 g of 1M LiPF$_6$ in EC/DEC. The dashed line is that of the fresh electrode while the solid line is that of the rinsed electrode.

The thermal stability of the dry charged electrode with no additional solvent or electrolyte present was then examined. The self-heating profiles of two 0.2 g samples of the rinsed and dried electrode are shown in Figure 10.3. The experiment demonstrates that the detectable (SHR >0.02°C/min) exothermic event for the dried electrode begins at 160°C and the whole experiment occurs at a fairly low self-heating rate (< 1°C/min). There seem to be two processes occurring during the ARC experiment and thus for one sample (A), the ARC experiment was terminated at 240°C, where the first decomposition

process was believed to be finished. At the termination of both experiments (A and B), the ARC samples were taken into an argon filled glovebox and the sample tube was opened. The electrode sample was then retrieved and an x-ray diffraction analysis was performed on each sample. The x-ray diffraction profiles are shown in Figure 10.4, together with literature results [113]. The literature profiles show a clear conversion of the λ-MnO_2 structure to the β-MnO_2 structure as samples are heated to 350°C. The x-ray profiles obtained from the ARC experiment are also shown in Figure 10.4, but these were obtained with less counting time (thus more noise) and with a different sample holder (thus some peaks due to sample holder- as indicated). A comparison between the x-ray profiles demonstrates that initially the electrode sample charged to 4.2 V has the λ-MnO_2 structure and upon exposure to elevated temperatures converts to the β-MnO_2 structure. The sample that was exposed to higher temperatures (B) had a more complete conversion to the β-MnO_2 structure. Thus, dry samples of $Li_xMn_2O_4$ charged to 4.2 V transform from the λ-MnO_2 structure to the β-MnO_2 structure with the release of heat starting near 160°C. This agrees with the results of DSC experiments presented in reference [113].
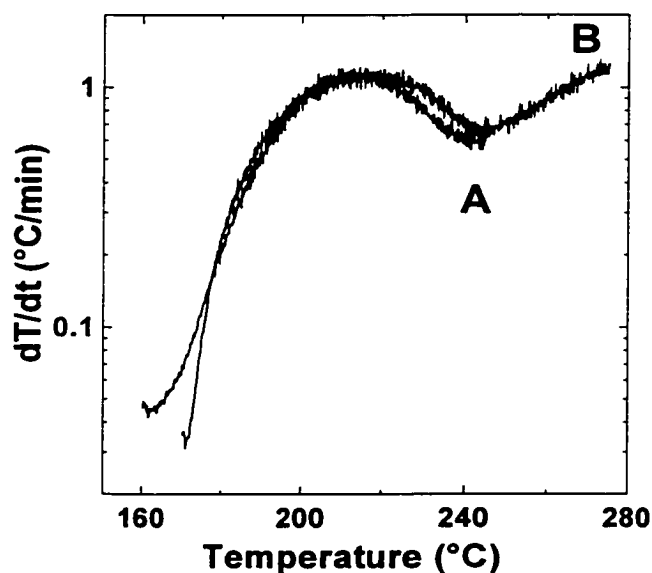
Figure 10.3. Self-heating rate of 0.2 g of $Li_xMn_2O_4$ charged to 4.2 V (dry). Sample A was terminated at 250°C, while sample B was terminated at 275°C.
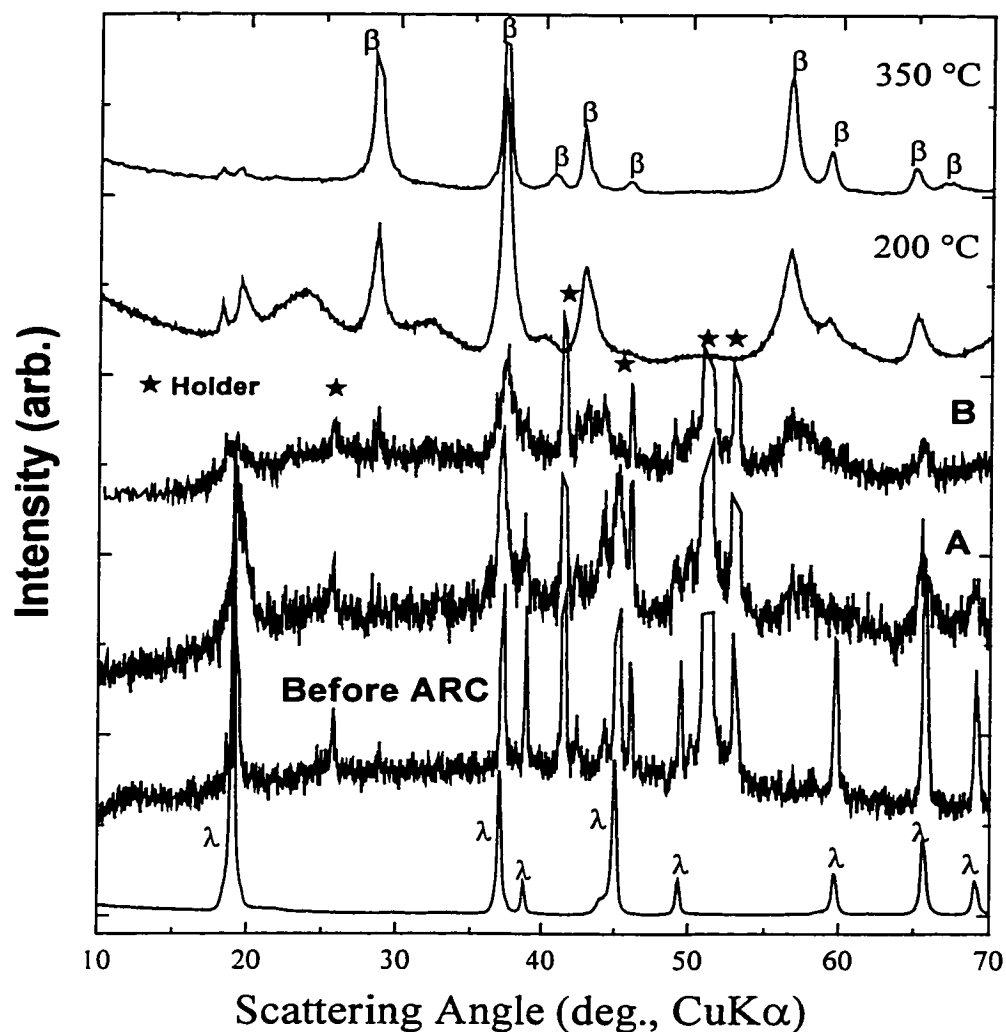
Figure 10.4. Comparison of the x-ray diffraction profiles of Li$_x$Mn$_2$O$_4$ (4.2 V) after rinsing, before the ARC experiment, and of the two samples from the experiments described by Figure 10.3. The results are compared to literature results of λ-MnO$_2$ heated to different temperatures [113].

Figure 10.5 compares the self-heating rate of the dry electrode powder (dashed line) to that of the same powder with a small portion of added EC/DEC solvent (solid line). The initial self-heating temperature is the same as that of the λ to β transition (160 – 170°C) for the sample with no added solvent. The sample with the added solvent demonstrates further self-heating at higher temperatures resulting in a rapid rise in self-heating rate. This is believed to be due to the combustion of the solvent.
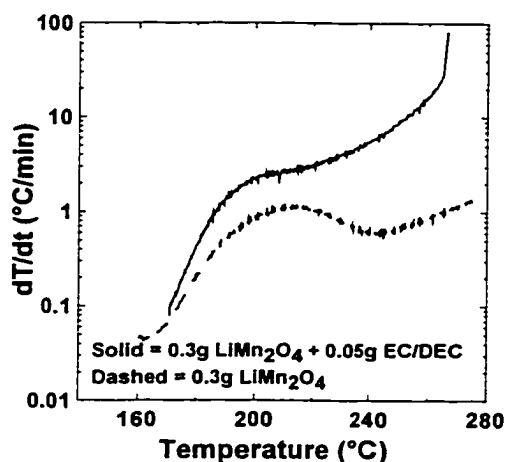
Figure 10.5. Solid Line - Self-heating rate (SHR) profile of 0.3 g of the rinsed $Li_xMn_2O_4$ electrode charged to 4.2 V in the presence of 0.05 g of EC/DEC. The dashed line shows the SHR profile of the rinsed electrode with no additional solvent or electrolyte added.

Figure 10.6 shows the x-ray diffraction profile of the sample containing the added solvent shown in Figure 10.5 after the termination of the ARC experiment. The x-ray analysis shows that the sample has been reduced primarily to MnO, with small amounts of Mn_2O_3 and $MnCO_3$ present. This is believed to be due to combustion of the solvent that releases CO_2, H_2O and possibly other products if the combustion was not complete. After the ARC experiment a severe expansion of the ARC tube due to the generated pressure was noted.
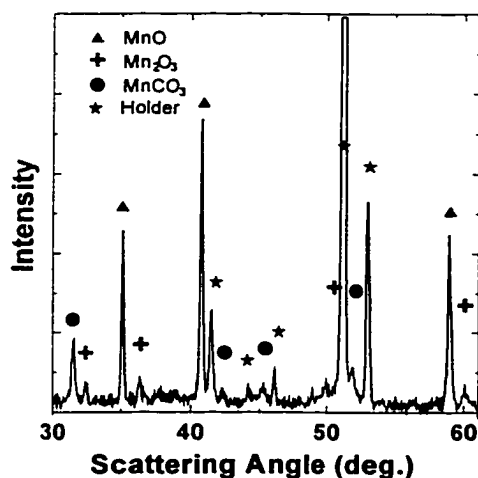
Figure 10.6. X-ray diffraction profile of $Li_xMn_2O_4$ with added solvent after the termination of the ARC experiment. The indicated peaks are due to the sample holder and from the standard reference compounds MnO, Mn_2O_3, and $MnCO_3$.

It is believed that the $Li_xMn_2O_4$ electrode is oxidizing the solvent causing its combustion. Thus if the amount of the electrode material (oxidizer) placed into the ARC sample tube is limited then the temperature rise as seen in the ARC experiment would be reduced. The temperature rise due to the solid state transformation would be lower (since a smaller amount of solid is present) and when the solid was depleted of available oxygen, the solvent oxidation would finish. A detailed discussion of the decrease in adiabatic temperature rise was given in Chapter 6. Figure 10.7 shows the decomposition of 0.1 g of the charged/rinsed electrode in the presence of 0.1 g of the solvent mixture (solid curve). In addition, Figure 10.7 also shows the self-heating rate profile of a 0.1 g sample of the dried electrode (dashed curve, showing only the λ to β transition). There is a large difference between the two results. For the wet sample, the solid state transformation, previously described, begins at 180°C and continues for about 10 degrees after which the solvent combustion occurs (beginning near 200°C) which produces a rapid rise in the self-heating rate and a temperature rise of nearly 80°C. On the other hand, the dry sample did not show a second exotherm, because there was no solvent present to oxidize.
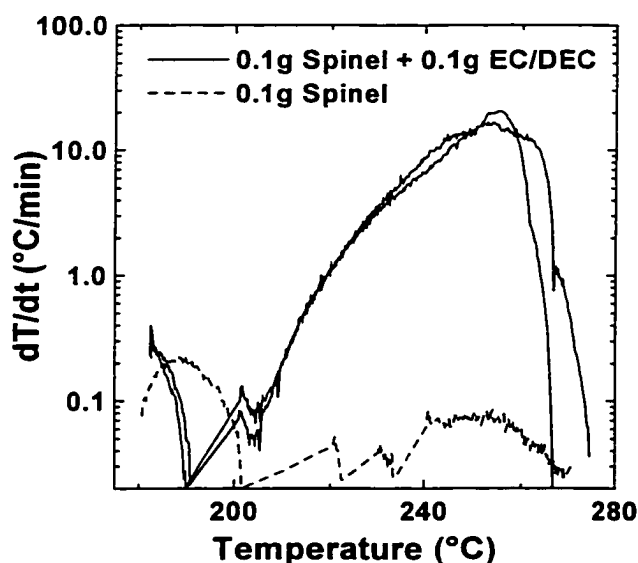
Figure 10.7. Solid - self-heating rate profile of 0.1 g of rinsed $Li_xMn_2O_4$ electrode charged to 4.2V in the presence of 0.1 g of EC/DEC. Dashed - 0.1 g of the rinsed $LiMn_2O_4$ with no additional electrolyte or solvent added to the sample tube.

The temperature rise seen during the experiment can be tested if a model for the decomposition can be derived. Assume that the cathode decomposes in the presence of solvent (say EC) according to

$$Mn_2O_4 + 2/5 \; C_3H_4O_3 \rightarrow 2MnO + 6/5 \; CO_2 + 4/5 \; H_2O. \qquad 10\text{-}1$$
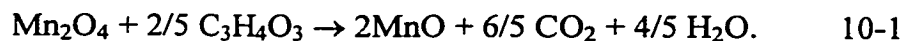
Equation 10-1 shows that one mole of the delithiated spinel material will release two moles of oxygen atoms. Assuming the heats of combustion are 2715 kJ/mol and 1161.4 kJ/mol for DEC and EC respectively [92, 93], then the heat generated when 0.1 g of the sample reacts with 0.1 g of solvent is 263 J. The temperature rise predicted for the exotherm as measured in the ARC was determined by dividing the heat generated by the heat capacity of the sample plus sample holder (total = 0.8 J/K), giving a temperature rise of 330°C. The experiment showed a temperature rise of only about 80°C. The calculated and experimental results are in disagreement. Some possible reasons for the disagreement are listed. First, it was assumed that the portion of the solvent that reacts is completely combusted to CO_2 and H_2O, without proof. Second, we have assumed all the solid is converted to MnO, which is not correct from x-ray studies. Equation 10-1 is similar to what has been proposed, in Section 6.3, for the decomposition mechanism of $Li_{0.5}CoO_2$ in solvent during an ARC experiment to 280°C.

Figure 10.8 shows a number of self-heating rate profiles of 0.2 g of $Li_xMn_2O_4$ charged to 4.2 V reacting in the presence of 0.1 g of electrolyte with various concentrations of $LiPF_6$ in EC/DEC. It is clear that as the concentration of $LiPF_6$ increases, the onset temperature of exothermic activity (greater than 0.02°C/min) decreases. Thus, the thermal stability of the electrode decreases as the concentration of $LiPF_6$ increases. A salt-initiated process occurs at the start of the instability, whose activity increases as the concentration of $LiPF_6$ increases.

This process is not understood and is **opposite to the effect observed with $Li_{0.5}CoO_2$ described in part chapter 6**. Apparently, $Li_{0.5}CoO_2$ and $Li_xMn_2O_4$ have fundamental differences in the way they react with solvent in the presence of salt in the solvent mixture. As shown in Chapter 6, a polymeric species is formed when the electrolyte ($LiPF_6$ in EC/DEC, containing HF impurity) is heated. It was proposed that

the polymer then coats the $Li_{0.5}CoO_2$ particles depressing self-heating reactions. In $Li_xMn_2O_4$ electrodes, the HF impurity at elevated temperatures has also been shown in the literature to cause the dissolution of the manganese [114, 115]. These competing HF reactions with spinel electrodes may explain the differences between the two electrodes with respect to the behaviour at high temperatures in electrolytes at varying concentrations. As the concentration of $LiPF_6$ increases, the amount of HF increases and this should increase the dissolution of Mn into the heated electrolyte. It is speculated that this may keep the surface of the particles clean of any polymeric product and allow the solvent oxidation to proceed more rapidly than in the absence of salt.
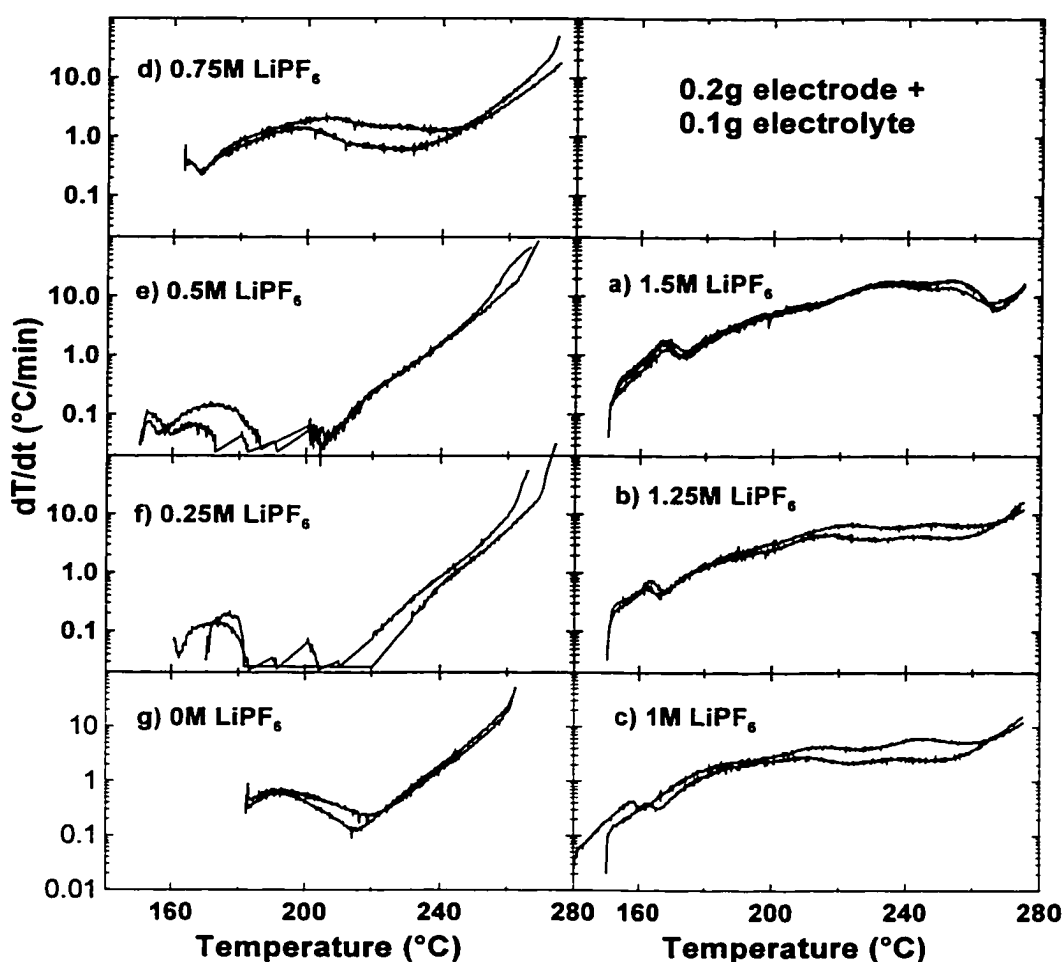
Figure 10.8. Self-heating rate profiles of 0.2 g of rinsed $Li_xMn_2O_4$ electrode charged to 4.2 V in the presence of 0.1 g of $LiPF_6$ in EC/DEC electrolyte at the indicated concentrations. The results of duplicate experiments are shown for each concentration.

The thermal stability of $Li_xMn_2O_4$ in electrolyte decreases as the concentration of $LiPF_6$ increases. Therefore, in full Li-ion cells there must be an optimum concentration window for the thermal stability of the electrode and the conductivity of the electrolyte. Figure 10.8e (0.5 M $LiPF_6$), for example, shows that there is very little self-heating of the cathode powder until the solvent oxidation occurs at about 210°C. The solvent oxidation can not be controlled in these samples and thus all profiles showed self-heating above 240°C. A salt concentration near 0.5 M should still give electrolytes that are conductive enough for many applications. Thus, it is believed that the concentration of $LiPF_6$ in $LiMn_2O_4$ cells should be optimized near 0.5 M for applications that require increased thermal stability (larger sized cells-EV, electric bicycles).

10.2 DSC Comparisons

A qualitative DSC comparison of the most common and new possible cathode materials for lithium-ion batteries was performed. This DSC analysis was performed on electrode materials prepared following the procedure described in Section 4.1.1. After assembly of the electrochemical cell in 1M $LiPF_6$ EC/DEC (33/67, vol/vol), it was charged to the desired voltage. When the cell obtained the desired voltage, the charging current stopped for 30 minutes and then continued to charge the cell, at 80% of the previous current, until the desired voltage was reached anew. This cycling regime was continued twelve times such that the cell stabilized near the desired voltage. After the charging cycle, the cell was removed and DSC sample cells were prepared in welded stainless steel tubes. Upon cell disassembly the sample was removed from the aluminium foil and then transferred to the sample tube. The tube was sealed with no additional electrolyte or solvent added. The samples were analyzed in the DSC at a temperature scan rate of 2°C/min.

Figure 10.9 shows the DSC results of $LiCoO_2$ charged to various voltages. The top panel of Figure 10.9 shows the charging regime of the electrochemical cell. The specific capacity of the cell, from the top panel, is listed in the DSC panels under the corresponding voltage of the cell. The two curves in each of the DSC panels indicate

different samples from two different cells charged to the indicated voltage. This graph serves as the template for further comparisons, since LiCoO2 is the most widely used cathode material in commercial lithium-ion cells. The y-axis of all the DSC plots has been limited to 1.5 W/g. If the power to a sample exceeds 1.5 W/g dramatically, its profile has been cut and the peak power has been indicated with an arrow near the peak.

Figure 10.9. DSC profiles of LiCoO2 charged to indicated voltages (bottom panels). Duplicate scans are from a nominally identical sample. Top panel- charge characteristics of LiCoO2.

Figure 10.9 shows that as LiCoO₂ is charged to higher voltages the electrode becomes more thermally unstable. It is the goal of all manufacturers to optimize electrochemical properties (cycling characteristics, structural stability, capacity), thermal stability and cost and thus this thermal stability comparison will be useful. In addition, the surface area of this material is very low (0.1 m²/g).

Figure 10.10. DSC profiles of LiNiO₂ charged to indicated voltages (solid lines, bottom panels). Duplicate scans are from a nominally identical sample, while dashed lines are from the LiCoO₂ sample at the indicated voltage. Top panel- charge characteristics of LiNiO₂.

Electrodes prepared from $LiNiO_2$ have long been known to be thermally unstable [51], but its favourable electrochemical properties and cost have ensured its continued study and possible use. The DSC profiles of $LiNiO_2$, charged to various voltages in 1M $LiPF_6$ EC/DEC (33/67) are shown in Figure 10.10. The results for $LiCoO_2$ are shown as the dashed lines for comparison and the $LiCoO_2$ capacity is shown under its respective profile. $LiNiO_2$ demonstrated much more thermal instability than $LiCoO_2$, it liberated more heat and the onset of thermal instability usually occurred at a lower temperature than $LiCoO_2$. The surface area of $LiNiO_2$ is also low (0.7 m^2/g). In particular, when $LiNiO_2$ was charged to a voltage of 4.4 V or higher the sample exhibited a very exothermic DSC peak. It is clear that $LiNiO_2$ electrochemical cells charged to 4.4V or higher will be extremely unstable and require special attention in order to eliminate the exposure of $LiNiO_2$ cells to these voltages. Although $LiNiO_2$ gives an increase in capacity compared to $LiCoO_2$, the sacrifice in the thermal stability of the electrode is large and hinders the possibility of using $LiNiO_2$ in commercial applications.

To improve the thermal stability of $LiNiO_2$, commercial suppliers have replaced a small portion of the Ni by Co, to give $LiNi_{0.8}Co_{0.2}O_2$ [116]. This material shows good electrochemical characteristics but the thermal stability, as seen in Figure 10.11, is not appealing. The maximum evolved power and onset temperature for $LiNi_{0.8}Co_{0.2}O_2$ is lower and higher respectively than $LiNiO_2$, but the reactivity is enhanced over $LiCoO_2$. The evolved power, even at 4.0 V, is likely too much to construct a thermally stable cell with this electrode. The surface area of $LiNi_{0.8}Co_{0.2}O_2$ is very similar to $LiCoO_2$ (0.3 m^2/g).

Currently, $LiMn_2O_4$ has been commercialized as a cathode for lithium-ion batteries due to its improved thermal stability. The DSC profiles of $LiMn_2O_4$ at various voltages are shown in Figure 10.12. Clearly, $LiMn_2O_4$ demonstrates improved thermal stability over $LiCoO_2$, although its surface area is larger (0.6 m^2/g). It is interesting to note that the DSC profiles of $LiMn_2O_4$ charged to 4.2, 4.4, and 4.6 V are very similar. This is due to the fact that very little lithium remains in the structure at these voltages and thus they are almost identical. This is shown in the capacity graph as the top panel of Figure 10.12, where very little lithium is removed between 4.2 and 4.6V. Although $LiMn_2O_4$ at 4.2, 4.4, and 4.6 V has an initial thermal instability near 220°C, it releases
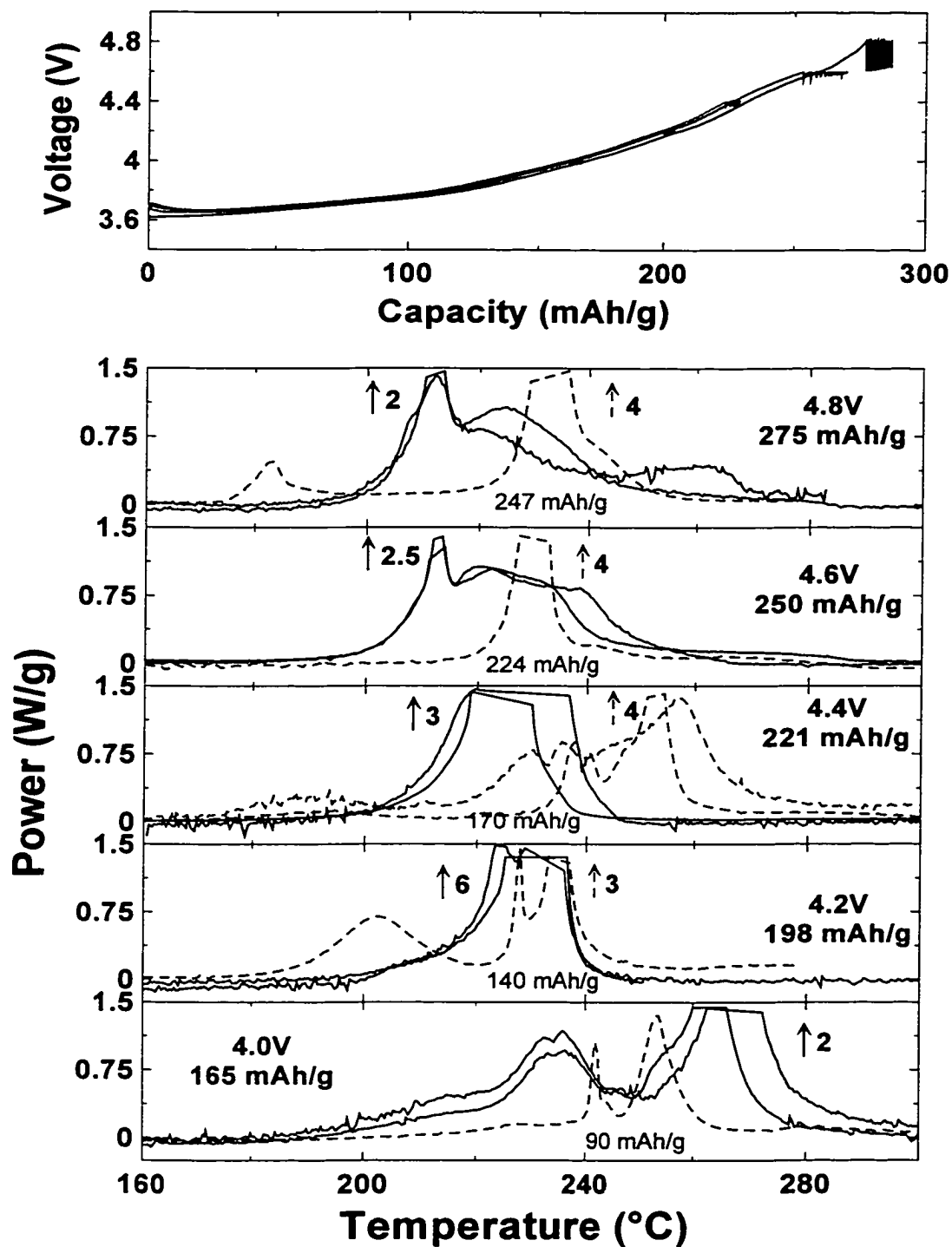
Figure 10.11. DSC profiles of LiNi₀.₈Co₀.₂O₂ charged to indicated voltages (solid lines, bottom panels). Duplicate scans are from a nominally identical sample, while dashed lines are from the LiCoO₂ sample at the indicated voltage. Top panel- charge characteristics of LiNi₀.₈Co₀.₂O₂.
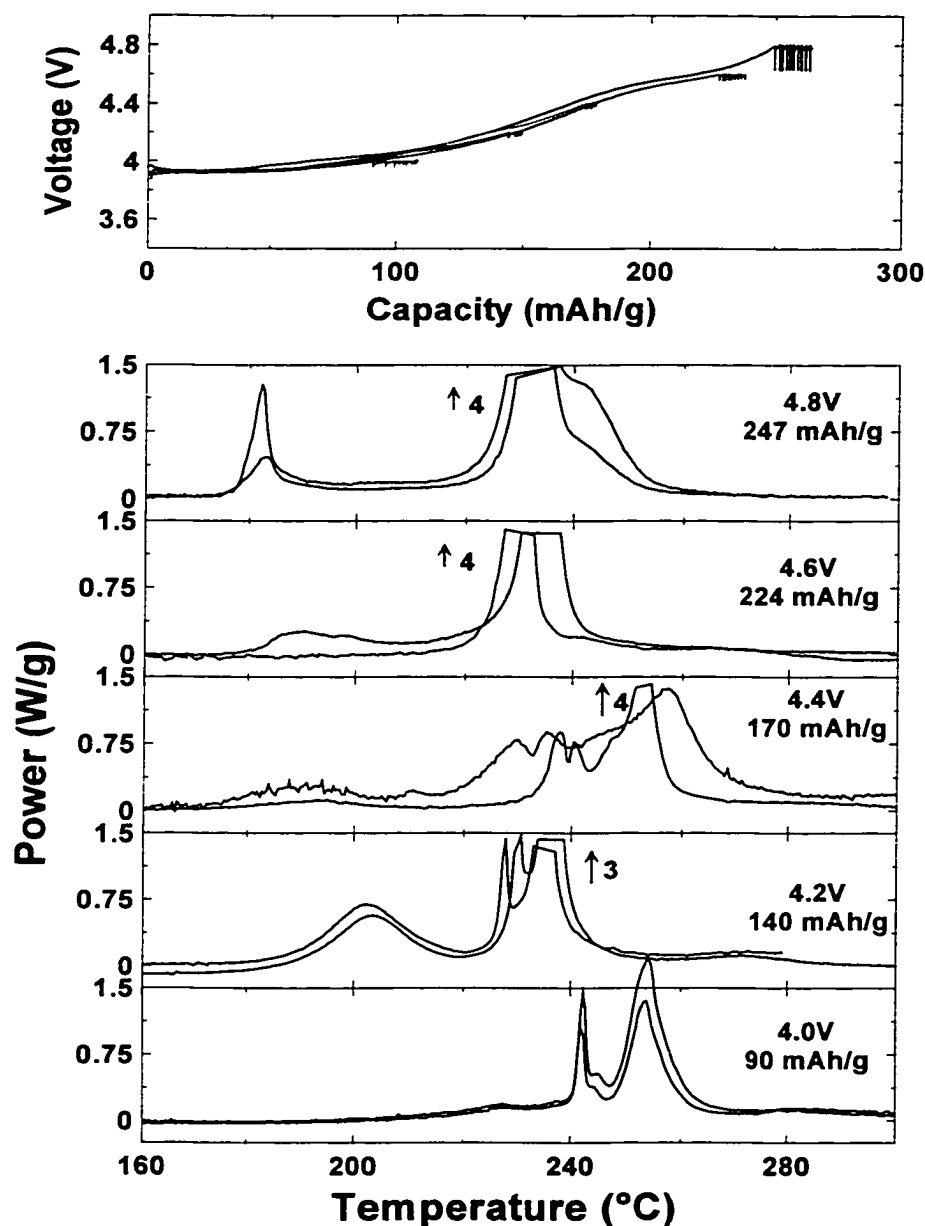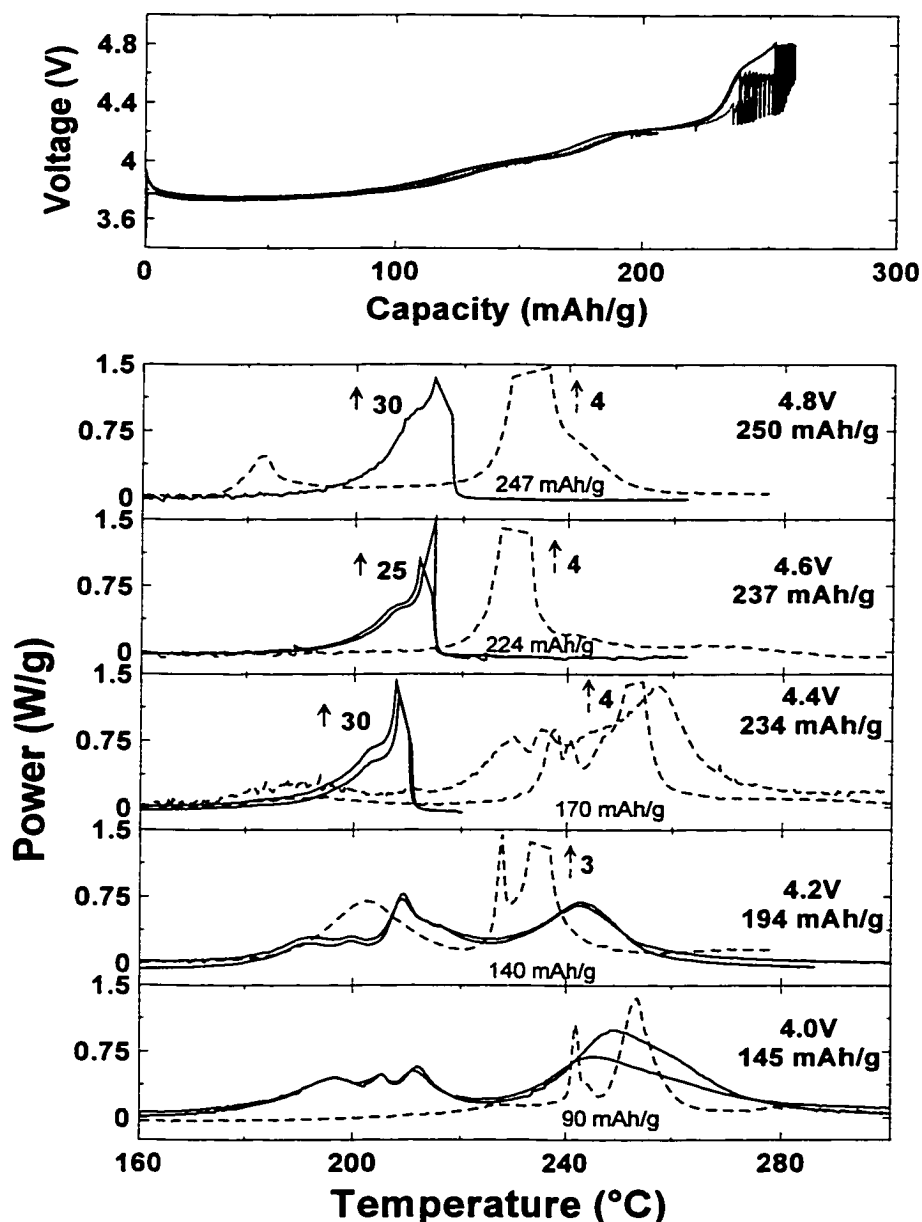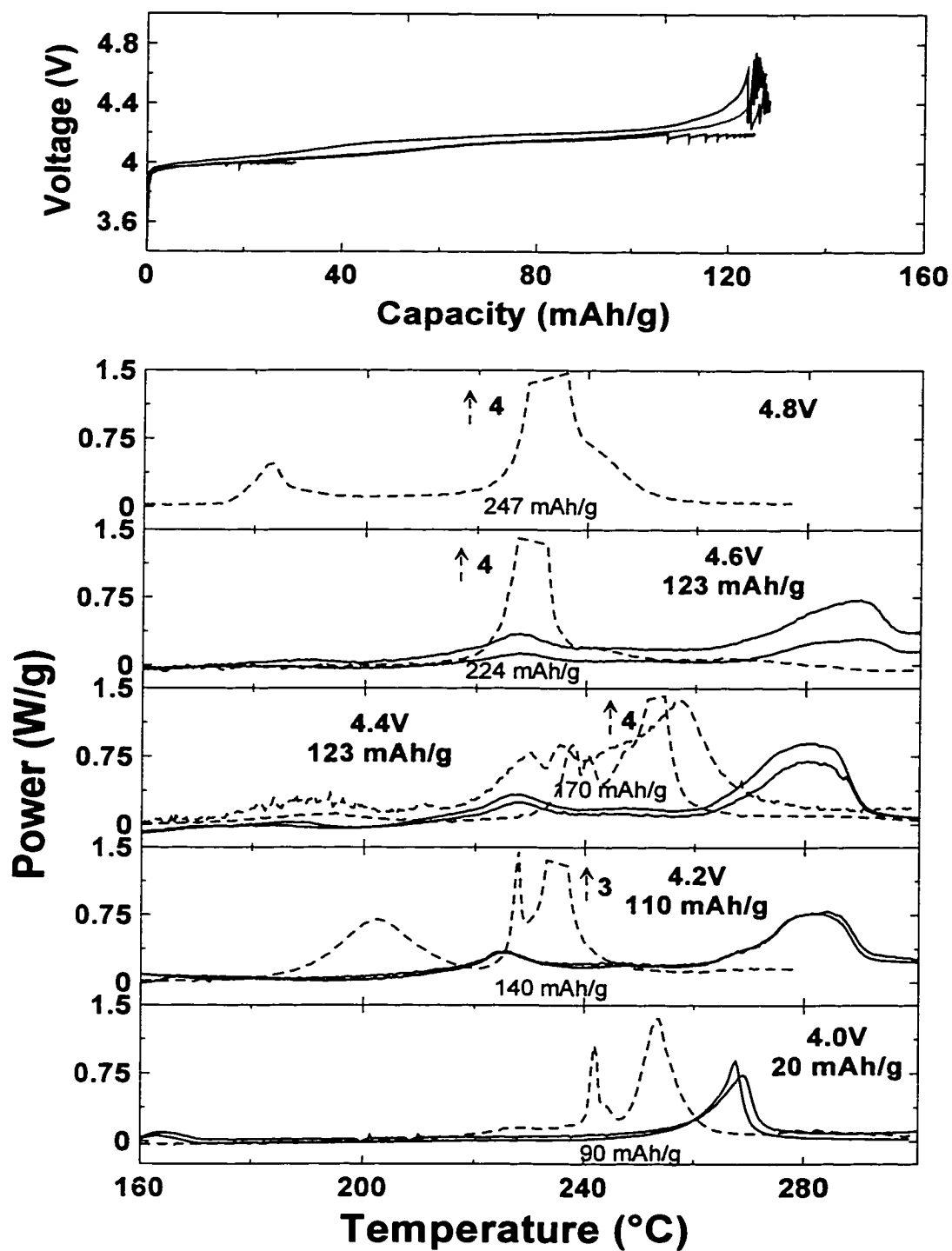
Figure 10.12. DSC profiles of LiMn₂O₄ charged to indicated voltages (solid lines, bottom panels). Duplicate scans are from a nominally identical sample, while dashed lines are from the LiCoO₂ sample at the indicated voltage. Top panel- charge characteristics of LiMn₂O₄.

little heat. It's main reactivity is near 280°C, some 30 - 40° higher than $LiCoO_2$. One of the shortcomings of $LiMn_2O_4$ as electrode material is that it has a lower capacity than most proposed commercial electrodes. It is interesting to note that $LiMn_2O_4$ charged to 4.0V, with only 20 mAh/g of capacity has its only instability at 265°C, but when charged to higher voltages the main instability was centred at 280°C. At higher voltages there was an initial instability near 230°C, which was absent from the electrode at 4.0V.

Recently, researchers at FMC Corporation have introduced a new cathode material which they describe as offering improved capacity and safety characteristics. The active electrode is similar to $LiNi_{0.8}Co_{0.2}O_2$, but with addition of Ti and Mg in a small amount to give $LiNi_{0.7}Co_{0.2}Ti_{0.05}Mg_{0.05}O_2$ [117]. Figure 10.13 shows the comparison of this material with that of $LiCoO_2$ at various voltages. Although the FMC material offers more capacity than $LiCoO_2$, the heat released at the various voltages is higher and its surface area is larger (0.8 m^2/g). Clearly, there was only a gain in the capacity of the electrode while no significant increase in the safety properties of the electrode was seen. In addition, using Ti and Mg would likely increase the cost of the bulk electrode powder.

The materials chosen thus far show no safety advantage over commercial $LiCoO_2$, except for $LiMn_2O_4$ whose low capacity has limited its widespread introduction to the commercial market. Truly, there must be other safer bulk electrodes. Recently, in Dr. Jeff Dahn's laboratory, researchers have developed a new class of cathode materials based on the "correct" oxidation state of a number of metals [118, 119, 120]. These materials are based on Co, Mn, and Ni. These materials offer high lithium capacity and superior safety performance. The cycling regime and DSC profiles of one of these compounds ($Li[Ni_{3/8}Co_{1/4}Mn_{3/8}]O_2$), as compared to $LiCoO_2$, is shown in Figure 10.14. The figure shows that the main exothermic reaction for this new material up to 4.2 V is above 280°C, some 40-60° higher than $LiCoO_2$. At 4.6 V, the new material has two well-resolved DSC peaks, whose total power is large, but due to the peak splitting may not pose serious consequences in safety tests. The electrode at 4.8 V has a similar reactivity as $LiCoO_2$. Clearly, there can be improvements to capacity and an understanding of safety characteristics by synthesizing new materials in a controlled manner. It is

interesting to note that this material is more thermally stable than $LiCoO_2$ although its surface area is much larger (5.9 m^2/g).
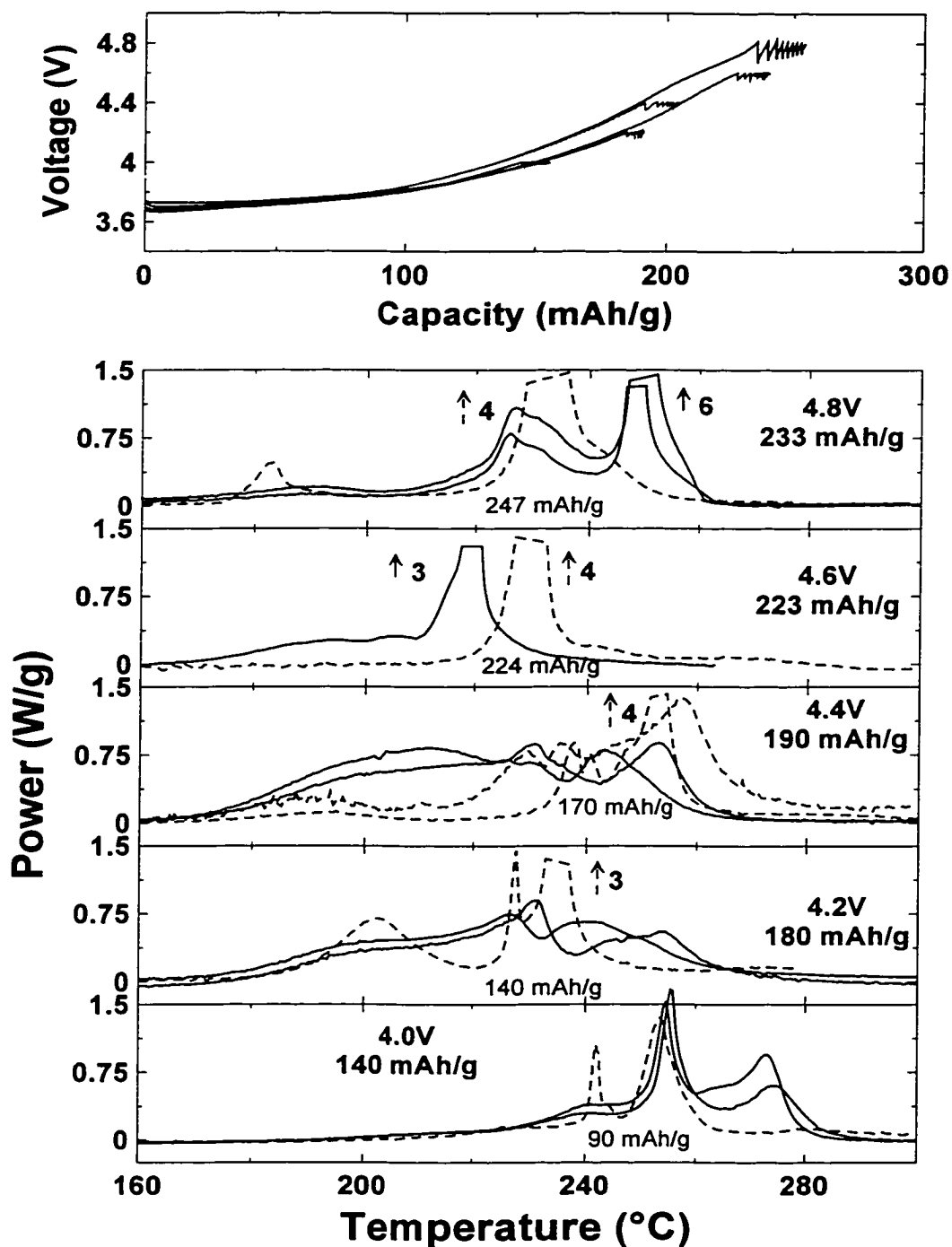
Figure 10.13. DSC profiles of $LiNi_{0.7}Co_{0.2}Ti_{0.05}Mg_{0.05}O_2$ charged to indicated voltages (solid lines, bottom panels). Duplicate scans are from a nominally identical sample, while dashed lines are from the $LiCoO_2$ sample at the indicated voltage. Top panel- charge characteristics of $LiNi_{0.7}Co_{0.2}Ti_{0.05}Mg_{0.05}O_2$.
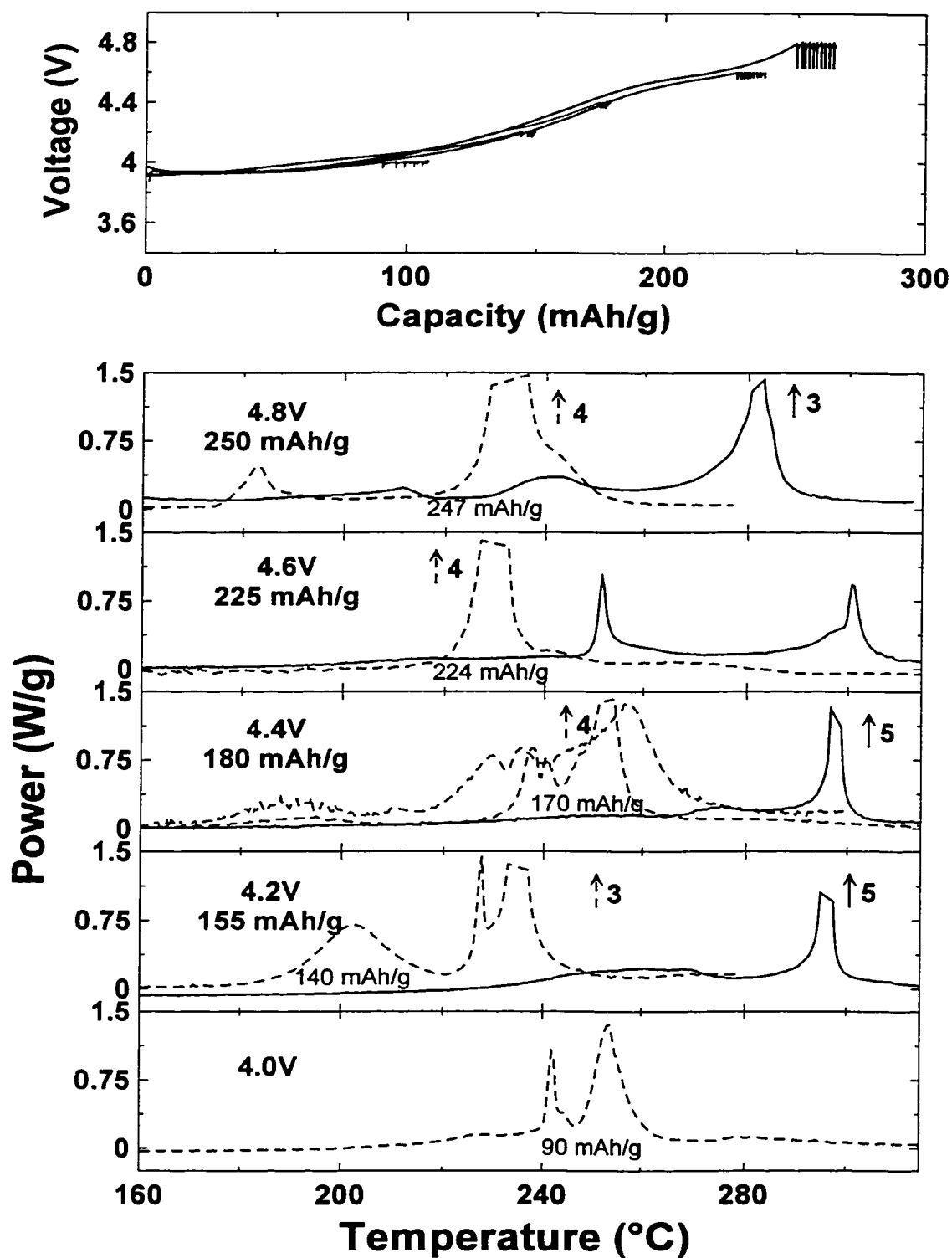
Figure 10.14. DSC profiles of Li[Ni₃/₈Co₁/₄Mn₃/₈]O₂ charged to indicated voltages (solid lines, bottom panels). Duplicate scans are from a nominally identical sample, while dashed lines are from the LiCoO₂ sample at the indicated voltage. Top panel- charge characteristics of Li[Ni₃/₈Co₁/₄Mn₃/₈]O₂..

Recently, LiFePO₄ has been suggested as an electrode material for lithium-ion batteries [121, 122]. Although its theoretical capacity is rather low (169 mAh/g), preparative methods have been developed such that nearly all the lithium (160 mAh/g) in the structure can be extracted and re-inserted without loss. In addition, the de-lithiated structure shows fairly low reactivity, even with a large surface area (15.2 m²/g). A DSC comparison of Li_xFePO_4 charged to 3.8V (no lithium remaining in structure) to $LiCoO_2$ near the same lithium capacity (4.4V) is shown in Figure 10.15. The exothermic activity of LiFePO₄ (3.8V) is much depressed as compared to $LiCoO_2$, although the main exothermic activity occurs at the same temperature. The large decrease in the power evolved from the charged electrode material attracts the attention of manufacturers trying to introduce larger cells. The disadvantage of LiFePO₄ is that its capacity is limited to 169 mAh/g, its operating voltage is lower (3.5 V) and high surface area. Replacing the cathode of commercially available cells with LiFePO₄ will not increase the capacity of the cell significantly as compared to a cathode of $LiCoO_2$. There is also speculation about the rate of charge and discharge this electrode can provide to obtain the full lithium capacity of the electrode.
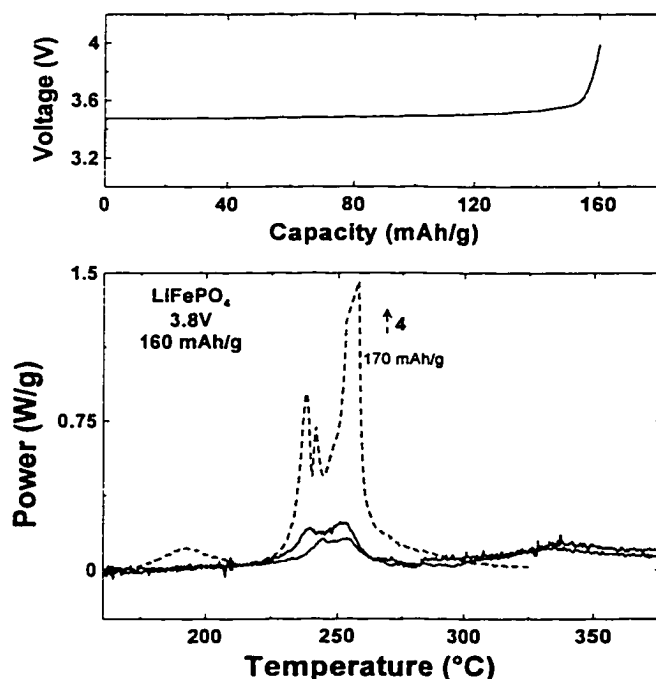
Figure 10.15. DSC profiles of LiFePO₄ charged to 3.8 V (solid line). Duplicate scans are from a nominally identical sample, while dashed lines are from the $LiCoO_2$ sample at the indicated capacity. Top panel- charge characteristics of LiFePO₄.

Table 10.1 presents a review of the electrodes analysed by DSC in this section. The table contains a column for each of capacity (mAh/g), onset temperature (°C), peak temperature (°C), peak power (W/g), and total evolved heat (J/g). Tables such as these are required in order to choose the correct electrode for a specific application.

Table 10.1. Analysis of DSC profiles from Figure 10.9 to 10.15 and surface area of dry electrode material.

Mat.	4.0 V					4.2 V				
	Cap (mAh/g)	T_o (°C)	T_p (°C)	P_p (W/g)	H_{tot} (J/g)	Cap (mAh/g)	T_o (°C)	T_p (°C)	P_p (W/g)	H_{tot} (J/g)
$LiCoO_2$	90	219	254	1.8	760	140	190	236	3.4	990
$LiNiO_2$	145	174	247	0.8	1300	194	181	209	0.8	1200
$LiNi_{0.8}Co_{0.2}O_2$	165	193	267	2.5	1400	198	194	234	5.7	1300
$LiMn_2O_4$	20	254	267	0.8	310	110	216	281	0.8	890
FMC	140	236	255	1.6	720	180	180	231	0.9	1200
$Li[Ni_{3/8}Co_{1/4}Mn_{3/8}]O_2$						158	245	295	5.2	310

Mat.	4.4 V					4.6 V				
$LiCoO_2$	170	181	256	3.8	1100	224	180	231	4.0	760
$LiNiO_2$	234	182	209	30.5	1300	237	184	214	23.9	1600
$LiNi_{0.8}Co_{0.2}O_2$	221	197	228	3.1	1600	250	193	213	2.5	1200
$LiMn_2O_4$	123	209	280	0.8	860	123	207	289	0.7	990
FMC	190	175	220	0.9	1600	223	169	231	3.1	1200
$Li[Ni_{3/8}Co_{1/4}Mn_{3/8}]O_2$	185	270	297	4.3	290	219	252 (1) / 300 (2)		1.0 / 1.0	400
$LiFePO_4$	160 (3.8V)	221	252	0.3	520	Surface Area (m²/g)				15.2

Mat.	4.8 V					Surface Area (m²/g)
$LiCoO_2$	247	175	232	3.5	1700	0.1
$LiNiO_2$	250	187	216	31.2	1200	0.7
$LiNi_{0.8}Co_{0.2}O_2$	275	192	212	2.0	1200	0.3
$LiMn_2O_4$	-	-	-	-	-	0.6
FMC	233	173	250	5.8	1600	0.8
$Li[Ni_{3/8}Co_{1/4}Mn_{3/8}]O_2$	246	230	282	2.8	660	5.9

Chapter 11

Conclusions and Further Work

11.1 Conclusions

When this thesis began, thermal stability (safety) of lithium-ion batteries were not a topic of open discussion [123]. Manufacturers were aware of the problems associated with exposing these electrochemical cells to elevated temperatures, but preferred to address issues concerning other aspects, such as capacity and rate capability. Currently, the thermal stability of lithium-ion cells is attracting much more attention [124]. The increased attention is due to a number of factors including; the increased market share of lithium-ion cells, production of large lithium-ion cells (EV applications), and the stability of new higher capacity electrode materials. The work performed during the course of this thesis has, I believe, increased the knowledge on the stability of electrode materials at elevated temperatures.

I have developed an experimental method that allows accelerating rate calorimetry (ARC) and differential scanning calorimetry (DSC) studies of the reaction between charged cathode powders and solvents or electrolytes of arbitrary molarities. $Li_{0.5}CoO_2$ was determined to react with organic solvents through a combustion process, where the presence of solvent reduces $Li_{0.5}CoO_2$ to $LiCoO_2$, Co_3O_4 and CoO. Upon heating to higher temperatures CoO is further reduced to Co metal. In the presence of electrolyte salt, there is a dramatic inhibiting effect that is believed to be due to a polymeric coating of the electrode particles by the decomposition products of the electrolyte.

A detailed study of $LiMn_2O_4$ revealed a different reaction mechanism where the delithiated structure (λ-MnO_2) transforms to the β-MnO_2 structure with the release of heat followed by solvent oxidation and reduction of the solid to MnO. Again a much more complicated decomposition mechanism occurs in the presence of $LiPF_6$ salt. The

addition of electrolyte salt (LiPF$_6$) tends to make samples of LiMn$_2$O$_4$, charged to 4.2 V, more reactive at low temperatures, while the opposite was true for Li$_{0.5}$CoO$_2$ in electrolyte. This suggests that strategies to improve the thermal stability of cells by changing the salt concentration are different for the two electrodes. For Li$_{0.5}$CoO$_2$, higher salt concentrations, near 1.5 M, are preferred, while for LiMn$_2$O$_4$, charged to 4.2 V, salt concentrations near 0.5 M are preferred.

It was also determined that changing the electrolyte salt has a dramatic effect on the self-heating rate and DSC profiles of a Li$_{0.5}$CoO$_2$ sample. In addition, the presence of a more thermally stable electrolyte does not necessarily produce a more thermally stable electrode.

In the beginning the goal of this thesis was to enhance the understanding of the thermal stability of anode materials. Previous ARC studies were limited to one type of carbon, MCMB, and here I showed the similarities of the reactions(s) occurring at elevated temperatures between five lithium-containing graphite materials and 1M LiPF$_6$ in EC/DEC (33/67). The mechanism previously proposed was confirmed in my study of lithium-containing carbon materials. This study has proposed that a graphitic fiber, shaped like miniature "soup cans", would be the ideal carbon anode material for lithium-ion batteries in terms of safety and performance.

An accurate DSC analysis of some of the most commonly studied cathode materials for lithium-ion batteries was performed. The results of this DSC study confirm the understanding about the stability of these electrodes presented in the literature. In addition, a new electrode synthesized in Jeff Dahn laboratory has been examined and showed much-improved thermal characteristics over LiCoO$_2$, while matching its capacity for lithium. These new electrode materials offer the hope of high-capacity thermally stable electrodes.

Avrami-Erofeev reaction kinetics were used in Chapter 7 to describe the decomposition kinetics of Li$_{0.5}$CoO$_2$ at elevated temperature in the presence of 1M LiPF$_6$ EC/DEC and EC/PC. A qualitative model for the decomposition was developed that justifies the use of an Avrami-Erofeev kinetic description for the decomposition. This kinetic description is a likely decomposition mechanism for other layered cathode materials for lithium-ion batteries. An interesting result is the fact that the kinetic model

did not change when a description of the reaction in solvent was performed. This suggests that the polymer has an inhibiting effect on the reaction kinetics, but the decomposition model remains the same.

Many researchers are using DSC, while others use ARC, to study the thermal stability of electrode materials and here I have shown the advantage of using a combination of both techniques to determine reliable kinetic triplets for the reactions under study. Once reliable kinetic triplets have been determined and tested against a variety of experiments, accurate predictions of the outcome of other thermal events can be achieved. In this case, an accurate model of oven exposure tests for lithium-ion cells was developed using kinetic triplets of the electrodes and simple principles of heat flow. Models, such as these, have many uses for electrode developers and accurate reproduction of results can save a company large amounts of time and resources in deciding to pursue a particular electrode, electrolyte or cell development. The techniques developed here can also be transferred to other technologies where thermal stability problems exist, such as reactor design.

11.2 Further Work

This project has a number of avenues that are available for investigation. Each avenue is another thesis unto itself and thus I will briefly describe some of the most important aspects I believe need to be addressed in this project. On the anode side of the cell, a more detailed reaction mechanism is required for the thermal stability of lithium intercalated carbon materials in electrolyte. The rinsing procedure developed for cathode materials should be applied to the anode and hopefully this will allow for a more detailed mechanistic understanding of the reactions occurring at the carbon anode at elevated temperatures. In addition, "Hard" carbons have not been analyzed for thermal stability in any study and should be examined [125]. "Hard" carbons are not commercialised widely, but offer an increase in lithium capacity due to the incorporation of lithium into the nanoscopic pores of the carbon structure. Presently, there is a lot of research on using thin metallic films as the anode material for lithium-ion batteries [126]. These thin metallic films alloy with lithium and potentially offer large increases to the capacity of

the anode. It would be interesting to see how these large increases (~ up to five times) in capacity affect the thermal stability of the anode.

On the cathode side, a necessary analysis from the results of this thesis is the change in surface passivation during heating of the electrode as the concentration of $LiPF_6$ increases in the electrolyte. A detailed analysis of the polymer formed at each molarity, may offer insight as to why there is a change in thermal stability with electrolyte concentration. In addition, this thesis has analyzed a number of cathode materials, but when a new cathode material is developed there is no way to determine if this material will be safe or not. It would beneficial to have a more detailed understanding as to why some materials are safe and others are not.

Currently, my laboratory is synthesizing many types of new cathode materials based on Co, Mn, and Ni ions. The synthetic methods of these new materials allow for the substitution of ions in a controlled way to give, for example, $Li[Ni_xCo_{1-2x}Mn_x]O_2$ type structures. Performing a DSC analysis on each of the charged electrodes in electrolyte as the value of x varies will enhance the understanding of why some materials (Mn) are more thermally stable than others (Ni). The analysis of these experiments will aid in proposing necessary traits for improved thermal stability of cathode material. A theoretical examination of oxygen loss from electrodes in the presence of electrolyte would also be beneficial in understanding why some materials are more thermally stable.

In this study a detailed analysis of $LiCoO_2$ charged to one voltage (4.2 V) was performed. Although this is the most common charge voltage for Li-ion cells, with a $LiCoO_2$ cathode, a more detailed analysis is required on the performance of electrode materials at different states of charge. During the process of my study, a few $LiCoO_2$ samples with increased surface area (by mechanical alloying the sample in Table 4.1) were analyzed (not shown in thesis) and gave striking results. Upon detection of self-heating the ARC sample proceeded rapidly to thermal runaway and all samples exploded in the ARC. This initial examination shows a large dependence for the safety of the electrode on the surface area of the sample. This surface area dependence needs to be addressed. It would be interesting to relate the kinetic parameters obtained in Chapter 7 to surface area. This relationship to kinetic parameters would be very beneficial to electrode developers. The surface area of a new sample of a previously thermally studied

electrode could be added into the full thermal model described in Chapter 9 and the resulting thermal stability of the electrode and/or cell would be known. Also some of the most stable electrodes analyzed in Chapter 10 have the largest surface area. If their surface areas could be reduced would their safety increase?

There have been reports of coating electrode materials to enhance safety and a stability study of these coated electrode materials could be performed [127]. For example, the coating $LiCoO_2$ with aluminium oxide has been discussed [127].

Commercial lithium-ion cells operate for nearly 1000 charge/discharge cycles without serious degradation of cell performance. In this study, the electrodes only underwent a few charge/discharge cycles. It is important to test if the stability remains the same after 100, 300, 500 or 1000 cycles.

One part of a lithium-ion cell that plays a large role in the overall thermal stability of the cell is the electrolyte. My analysis with $Li_{0.5}CoO_2$ showed that when the electrolyte was changed to one based on a lithium sulfonyl imide salt, a much more thermally unstable electrode developed. Thus new electrolyte systems (salts and/or solvents) need to be analyzed [128, 129]. An interesting new solvent has been developed consisting solely of an anion and a cation [130]. These ionic liquids are said to have high ionic conductivity and thermal stability. It would be useful to analyze the thermal stability of this type of solvent in relation to charged lithium-ion electrodes. In addition, there have been numerous reports of additives placed in the electrolyte for improve performance and these should be tested [55]. Some of these additives improve the performance of the cells under thermal abuse scenarios [50] or improper charging of the cell [131]. Other additives may improve loss in cell capacity as the cell partakes in a large number of charge/discharge cycles [132]. Additives to the electrolyte known as flame retardants have been used to hinder the combustion of the solvent [133]. These additives are used to improve a specific aspect of cell performance, but any change to the electrolyte may affect the thermal stability of the electrode and should be analyzed. Water was also found to have a large effect on the performance of the electrolyte and a more detailed analysis of its role at high temperature is required.

There are numerous manufacturers of commercial lithium-ion cells and with the methods I have developed here, it would be interesting to compare the chemistry of

individual commercial cells. Thus, commercial cells could be obtained and charged to a specific voltage after which ARC and DSC samples could be made using their active components. In this fashion an accurate comparison of the reactivity of the active components of commercial cells could be made.

Lithium-ion polymer cells are beginning to see more widespread use and thermal analysis of this technology is limited and would benefit from a well designed thermal analysis program.

Appendix A.1

Qualitative Picture of Reaction Model

Consider a spherical particle of $Li_{0.5}CoO_2$, surrounded by electrolyte.
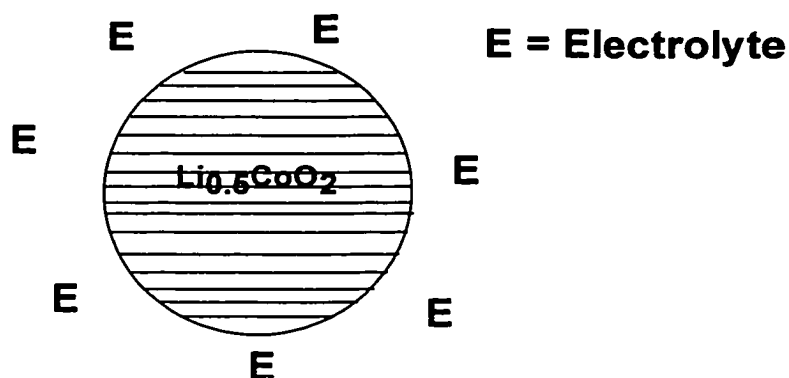
Figure A.1. A particle of $Li_{0.5}CoO_2$ at room temperature surrounded by electrolyte (E).

When the temperature increases, random nucleation, initiated at the edges and surface cracks in the particle, occurs. Nuclei of Co_3O_4 and CoO form with the release of oxygen and the formation of $LiCoO_2$ particles.
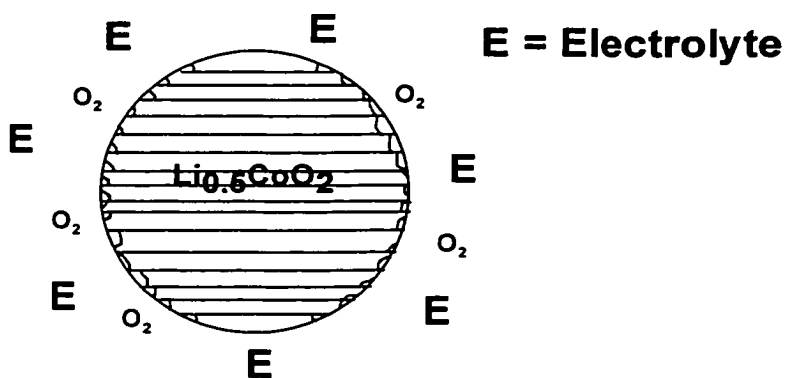
Figure A.2. The particle in Figure A.1 at elevated temperatures, with the release of oxygen (O_2) and the formation of Co_3O_4, CoO and $LiCoO_2$.

The oxygen released combusts the solvent and causes the temperature of the surrounding environment to rise. The $LiCoO_2$ particles continue to grow (form more CoO, Co_3O_4) in a two-dimensional fashion along the planes in the $Li_{0.5}CoO_2$ particle.

This continued growth releases more oxygen (combust more electrolyte), raises the temperature further and forms more $LiCoO_2$.
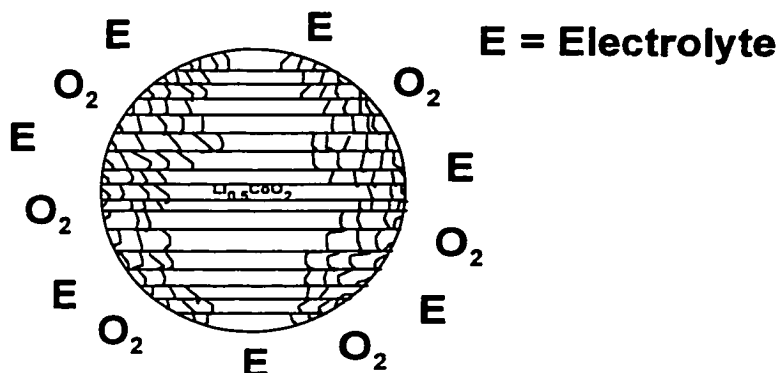
Figure A.3. The particle in Figure A.2 at higher temperatures than in Figure A.2.

In the presence of solvent the above reactions occur rapidly, since the combustion products of the solvent (CO_2, H_2O, etc..) are easily removed. By contrast, in the presence of $LiPF_6$ electrolyte the decomposition of the electrolyte salt occurs as well. It is well known that $LiPF_6$ electrolytes (based on carbonates) are not stable at these temperatures and thus their decomposition products (polymeric species) deposit on the surface and in the cracks of the particle slowing down the release of oxygen, thus the temperature rise and the decomposition reaction. With higher concentration of electrolyte salt, more decomposition products are deposited slowing down the reaction even further. When a stable electrolyte is used (lithium triflate salts) similar decomposition kinetics occurs as the solvent reaction, since no decomposition of the electrolyte occurs until higher temperatures.

Appendix A.2

Derivation of the Avrami-Erofeev Kinetic Equation [70]

If q_i^K is the probability of an elementary event in which the ith molecule does not react in the Kth time interval when

$$0 = t_0 < t_1 < t_2 < ...t_{K-1} < t_K < ...t_n = t \qquad (A-1)$$

then the probability of a complex event Q_i, that the ith molecule does not react in any of the time intervals in Equation A-1 is

$$Q_i = \prod_{K=1}^{K=n} q_i^K . \qquad (A-2)$$

If P_i is the probability that the ith molecule reacts by time t and p_i^K is the probability that the ith molecule reacts in the Kth time interval then

$$P_i = 1 - Q_i \qquad \text{and} \qquad p_i^K = 1 - q_i^K . \qquad (A-3)$$

Taking logarithms and summing to the limit $n = \infty$

$$\ln(1 - P_i) = \lim_{n \to \infty} \sum_{K=1}^{K=n} \ln(1 - p_i^K) = -\int_0^t P_i dt . \qquad (A-4)$$

Summing over all the possible values of i and normalizing for the N molecules of the component under consideration present at $t = 0$ gives

$$\frac{1}{N} \sum_{i=1}^{N} \ln(1 - P_i) = -\frac{1}{N} \sum_{i=1}^{i=N} \int_0^t P_i dt . \qquad (A-5)$$

Since values of P_i for various molecules of the same component may differ by only infinitely small amounts for finite time intervals, then

$$\ln\left(1 - \frac{1}{N} \sum_{i=1}^{i=N} P_i\right) = -\int_0^t \left(\frac{1}{N} \sum_{i=1}^{i=N} P_i\right) dt . \qquad (A-6)$$

Here $i = N$ and

$$\left(\frac{1}{N}\sum_{i=1}^{i=N}P_i\right) = P,\qquad\qquad\text{(A-7)}$$

where P is the mean probability that an individual molecule will react by the time $t(P)$, and

$$\left(\frac{1}{N}\sum_{i=1}^{i=N}P_i\right)dt = pdt\qquad\qquad\text{(A-8)}$$

is the mean probability that an individual molecule will react in the time interval between t and $t + dt(p\ dt)$. Thus, Equation A-6 is now

$$P = 1 - \exp\left(-\int_0^t pdt\right).\qquad\qquad\text{(A-9)}$$

When N is large, P may be identified as the fractional degree of conversion, α; thus Equation A-9 becomes

$$\alpha = 1 - \exp\left(-\int_0^t pdt\right).\qquad\qquad\text{(A-10)}$$

The volume of a product in a reaction at time t is given by

$$V(t) = \int_0^t V(t,\tau)\left(\frac{dN}{dt}\right)_{t=\tau}d\tau,\qquad\qquad\text{(A-11)}$$

where the (dN/dt) term describes the law of nucleation and the law of growth is related to the volume a nucleus occupies at a time τ. In solid state reactions, the rate of nucleation may be given by either of the expressions $dN/dt = $ const. or $dN/dt = t^\sigma$ const, where σ is a shape factor. Consider a spherical particle, see Figure A.4, for both nucleation expressions, the probability an individual molecule will react between t and dt is pdt and is proportional to the total volume of the spherical layers in the particle at the instant t at the peripheral of the nuclei which originated at time τ.

$$V(t) \propto pdt\qquad\qquad\text{(A-12)}$$

The radii of the spheres at the inner and outer boundaries of these layers are

$$r = k_r(t-\tau),\qquad\qquad\text{(A-13)}$$

and,

$$r + dr = k_r(t + dt - \tau).\qquad\qquad\text{(A-14)}$$
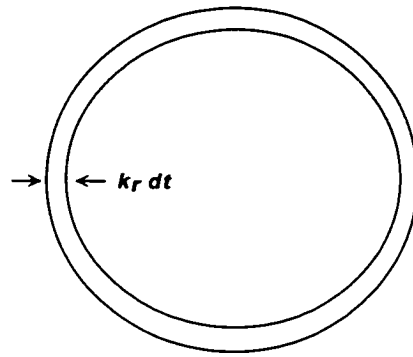
$$V_{ring} = 4\pi(kr(t\text{-}\tau))^2 k_r \, dt$$

$$V_{ring} \propto SA \times Thickness$$

Figure A.4. Spherical particle for the development of the Avrami-Erofeev kinetic equation.

Figure A.4 depicts the growth of the particle, where the volume of the spherical layer between the inner and outer ring is proportional to the surface area of the ring and the thickness of the spherical ring. Thus from Equation A-11 through Equation A-14,

$$pdt = dt \int_0^t 4\pi k_r^3 (t - \tau)^2 \frac{dN}{dt} d\tau . \qquad (A\text{-}15)$$

Substituting Equation A-15 into A-9 and solving gives

$$\alpha = 1 - \exp(-Kt^4) \qquad (dN/dt = \text{const}) \qquad (A\text{-}16)$$

and,

$$\alpha = 1 - \exp(-Kt^{\sigma+4}) \qquad (dN/dt = t^\sigma \text{ const}) \qquad (A\text{-}17)$$

$Li_{0.5}CoO_2$ is a layered structure and as presented in Section A.1, it is conceivable that the growth of the nuclei will be along the planes of the structure. This growth mechanism will be different from the spherical model presented above. The growth will be along the planes giving rise to a cylindrical geometry. The surface area of the sphere in the expression for volume (Equation A-11) is now replaced by the circumference of the sphere and the length of the cylinder is taken into the value of K. This alters Equation A-15 to

$$pdt = dt \int_0^t 2\pi k_r^2 (t - \tau) \ \frac{dN}{dt} d\tau , \qquad (A\text{-}18)$$

which yields,

$$\alpha = 1 - \exp(-Kt^3). \qquad (A-19)$$

Taking into account these geometric possibilities leads to the generalized Avrami-Erofeev equation,

$$\alpha = 1 - \exp(-Kt^n), \qquad (A-20)$$

where n is an integer to describe the decomposition mechanism. The Avrami-Erofeev equation can be written in a general form of,

$$[-\ln(1-\alpha)]^{1/n} = K(t - t_o), \qquad (A-21)$$

from which the differentiated form is

$$\frac{d\alpha}{dt} = nK^{1/n}[-\ln(1-\alpha)^{1-1/n}](1-\alpha), \qquad (A-22)$$

similar to what is presented in Table 5.1. In this thesis, a value of n = 3 was used in Equation A-20 to A-22, which leads to a value of -1 for σ in Equation A-17. Avrami-Erofeev reaction kinetics were described in Chapter 5 to follow the equation,

$$\frac{d\alpha}{dt} = k[-\ln(1-\alpha)^p](1-\alpha), \qquad (A-23)$$

where a value of 0.5, 2/3, 0.75 can be chosen for p. In the kinetic analysis of Chapter 7, model 12 of Table 5.1 was found to best describe the kinetics of $Li_{0.5}CoO_2$. In model 12 a value for p of 2/3 (n = 3) is used. The $nK^{1/n}$ term in Equation A-22, has been absorbed into the value k in Equation A-23.

Bibliography

1. D. Sperling, *Scientific American*, **195**, 54 (1996).

2. H. Takeshita, presentation at *Power 2000*, San Francisco, October 2000.

3. M. Broussely; J.P. Planchat; G. Rigobert; D. Virey; G. Sarre, *J. Power Sources*, **68**, 8 (1997).

4. S. Tobishima; K. Takei; Y. Sakurai; J. Yamaki, *J. Power Sources*, **90**, 188 (2000).

5. I. Buchmann, *Batteries in a Portable World*, 2nd Ed., Cadex Electronics Inc, Richmond, BC, 2001, pp 1-8.

6. D. Linden, *Handbook of Batteries*, 2nd Ed., McGraw Hill, Toronto, 1995, chp 36.

7. M.S. Whittingham, *Prog. Solid State Chem.*, **12**, 41 (1978).

8. J.R. Dahn, A.K. Sleigh, H. Shi, B.M. Way, W.J. Weydanz, J.N. Reimers, Q. Zhong, U. von Sacken, in *Lithium Batteries: New Materials, Developments, and Perspectives*, Elsevier, Amsterdam, 1994, pp 1-47.

9. M. Armand, *Solid State Ionics*, **69**, 309 (1994).

10. M.M. Thackeray, in: J.O. Besenhard (Ed.), *Handbook of Battery Materials*, Wiley-VCH, Weinheim, 1999, pp. 293.

11. M.S. Whittingham, in: M. Wakihara, O. Yamamoto (Ed.), *Lithium Ion Batteries*, Wiley-VCH, Weinham, 1998, pp. 46.

12. M. Armand, in *Materials for Advanced Batteries*, Plenum, New York, 1980.

13. A.N. Dey, B.P. Sullivan, *J. Electrochem. Soc.*, **117**, 222 (1970).

14. J.O. Besenhard, H.P. Fritz, *J. Electroanal. Chem.*, **53**, 329 (1974).

15. K.C. Lim, A.M. Lackner, P.O. Braatz, W.H.Smith, J.D. Margerum, H.S. Lim, in *Batteries for Portable Applications and Electric Vehicles*, Electrochemical Society, Pennington, NJ, 1997, pp 470-479.

16. T. Zheng, J.N. Reimers, J.R. Dahn, *Phys. Rev. B.*, **51**, 734 (1995).

17. T. Zheng, J.R. Dahn, *Phys. Rev. B.*, **53**, 3061 (1996).

18. E. Peled, *J. Electrochem. Soc.*, **126**, 2047 (1979).

19. D. Aurbach, Y. Ein-Eli, O. Chusid, Y. Carmeli, M. Babai, H. Yamin, *J. Electrochem. Soc.*, **141**, 603 (1994).

20. A. Naji, J. Ghanbaja, B. Humbert, P. Willmann, D. Billaud, *Journal of Power Sources*, **63**, 33 (1996).

21. D. Aurbach, Y. Gofer, B. Ben-Zion, P. Aped, *Journal of Electroanalytical Chemistry*, **339**, 451 (1992).

22. D. Aurbach, I. Weissman, A. Schechter, H. Cohen, *Langmuir*, **12**, 3991, (1996).

23. D. Aurbach, Y. Ein-Eli, B. Markovsky, A. Zaban, S. Luski, Y. Carmeli, H. Yamin, *J. Electrochem. Soc.*, **142**, 2882 (1995).

24. R. Fong, U. von Sacken, J.R. Dahn, *J. Electrochem. Soc.*, **137**, 2009 (1990).

25. T. Ohzuku, Y. Iwakoshi, K. Sawai, *J. Electrochem. Soc.*, **140**, 2490 (1993).

26. D.P. Wilkinson, J.R. Dahn, *US Patent Application 5 130 211* (1993).

27. D. Guyomard, J.M. Tarascon, *J. Electrochem. Soc.*, **140**, 3071 (1993).

28. D. Guyomard, J.M. Tarascon, *US Patent Application 5 192 629* (1993).

29. B. Simon, J.P. Boeuve, M. Broussely, *J. Power Sources*, **43-44**, 65 (1993).

30. C.W. Lee, R. Venkatachalapathy, J. Prakash, *Electochem. and Solid-State Lett*, **3**, 63 (2000).

31. T. Nagaura and K. Tozawa, *Prog. Batteries Solar Cells*, **9**, 209 (1990).

32. K. Mizushima, P.C. Jones, P.J. Wiseman, J. B. Goodenough, *Mater. Res. Bull.*, **15**, 783 (1980).

33. C. Delmas, *Mater. Sci. Eng.*, **B3**, 97 (1989).

34. Y. Gao, M.V. Yakovleva, W.B. Ebner, *Electrochem and Solid-State Lett.*, **1**, 117 (1998).

35. U. von Sacken, E. Nodwell, A. Sundher, J. R. Dahn, *Journal of Power Sources*, **54**, 240 (1995).

36. M. Winter, J.O. Besenhard, M.E. Spahr, P. Novak, *Adv. Mat.*, **10**, 725 (1998).

37. SONY, Product information sheet June 2001
    http://www.sony.co.jp/Products/en/BAT/ION

38. B.A. Johnson, R.E. White, *J. Power Sources*, **70**, 48 (1998).

39. Underwriters Laboratory Inc., document **1642**, *Standard for Lithium Batteries, 3rd Ed.*, ISBN 1-55989-829-1 (1995).

40. UN document ST/SG/AC.10/11: *Transport of Dangerous Goods- Lithium Batteries*, International Air Transport Association (1998).

41. IEC document 21A/217/(committee draft), "*Secondary Cells and Batteries containing alkaline or other non-acid electrolytes, Secondary Lithium cell and batteries for portable application, Part 1- Secondary Lithium cells*", Secretary: W.J. Woidt, Germany (1997).

42. P. Biensan, B. Simon, J.P. Peres, A. deGuibert, M. Broussely, J.M. Bodet, F. Perton, *J. Power Sources*, **81-82**, 906 (1999).

43. J. Matthews, *ZDNetAsia* "'Alien' substance caused Dell notebook battery to ignite", October 20,2000.

44. J.G. Spooner, *ZDNetNews* "Compaq recalls 55,000 notebook batteries", October 27, 2000.

45. M. Kanellos, *CnetNews* "Dell to mount massive notebook battery recall", May 3, 2001.

46. H. Maleki, G. Deng, A. Anani, J. Howard, *J. Electrochem. Soc.*, **146**, 3224 (1999).

47. S. Tobishima, *Key Engineering Materials*, **181-182**, 135 (2000).

48. D.D. MacNeil, T.D. Hatchard, J.R. Dahn, *J. Electrochem. Soc.*, **148**, A663 (2001).

49. Texas Instruments, Product Information Sheet 3LP Header Information Nov. 1998.

50. H. Mao, Canadian Patent Application no. **CA2156800**, (1995). H. Mao and U. von Sacken, Canadian Patent Application no. **CA2163187**, (1995). H. Mao and D. Wainwright, Canadian Patent Application no. **CA2205683**, (1997).

51. J.R. Dahn, E.W. Fuller, M. Obrovac, U. von Sacken, *Solid State Ionics*, **69**, 265 (1994).

52. Z. Zhang, D. Fouchard, J.R. Rea, *Journal of Power Sources*, **70**, 16 (1998).

53. J.R. Dahn, Z. Lu, "Improved Cathode Composition for Lithium-ion Batteries", U.S. Patent filed June 2001.

54. T. Nakano, Y. Ota, Japanese Patent Application JP 11329495 A2, November 30 1999.

55. J. Cho, G. Kim, *Electrochem. and Solid-State Lett.*, 2, 253 (1999).

56. A. Du Pasquier, F. Disma, T. Bowmer, A.S. Gozdz, G. Amatucci, and J-M. Tarascon, *J.Electrochem. Soc.*, 145, 472 (1998).

57. M.N. Richard, *Accelerating Rate Calorimetry Study on the Fundamentals of Lithium-Ion Safety*. PhD Thesis, Dalhousie University (1998).

58. C.N. Schmutz, J.M. Tarascon, A.S. Godz, P.C. Warren, F.K. Shokoohi, in *Rechargeable Lithium and Lithium-Ion Batteries* (Eds. S. Megahed, B.M. Barnett, L. Xie), Electrochemical Society, Pennington, NJ, 1995, pp. 400.

59. D.L. Townsend, J.C. Tou, *Thermochimica Acta*, 37, 1 (1980).

60. J.C. Tou, L.F. Whiting, *Thermochimica Acta*, 48, 21 (1981).

61. P.W. Atkins, *Physical Chemistry*, 5th Ed., Freeman, New York (1994).

62. G. Hohne, W. Hemminger, H.J. Flammersheim, *Differential Scanning Calorimeter, An Introduction for Practitioners*. Springer-Verlag, Berlin, 1996.

63. A.C. Davis, *A Study of Sequentially Sputtered Mo-Sn Thin Films*. MSc. Thesis, Dalhousie University (2000).

64. P.A. Tipler, *Physics For Scientists and Engineers*, Worth Publishers, New York, NY, 3rd edn., 1991, pp. 525-526.

65. R.C. Weast *CRC Handbook of Chemistry and Physics*, CRC Press, Boca Raton Florida, 70th edn., 1989, pp. D-186-D187.

66. J. Sempere, R. Nomen, R. Serra, and F. Gallice, J. Thermal Anal. and Cal., 58, 215 (1999).

67. J. R. Dahn, *Phys. Rev. B*, 44, 9170 (1991).

68. M.N. Richard and J.R. Dahn, *J. Electrochem. Soc.*, 146, 2078 (1999).

69. J.N. Reimers, J.R. Dahn, *J. Electrochem. Soc.*, 141, 2091 (1992).

70. W.E. Brown, D. Dollimore, A.K. Galwey, *Comprehensive Chemical Kinetics*, **22**, 91 (1980).

71. C. Popescu, E. Segal, E. *Int. J. Chem. Kinetics*, **30**, 313 (1998).

72. S. Vyazovkin, C.A. Wight, *J. Phys. Chem. A*, **101**, 8279 (1997).

73. S. Vyazovkin, *Int. J. Chem. Kinetics*, **28**, 95 (1996).

74. T. Ozawa, *Bull. Chem. Soc. Jpn.*, **38**, 1881 (1965).

75. H.E. Kissinger, *Anal. Chem*, **29**, 1702 (1957).

76. J.C. Oxley, J.L. Smith, E. Rogers, W. Ye, A.A. Aradi, and T.J. Henly, *Energy and Fuels*, **14**, 1252 (2000).

77. J.H. Raley, F.F. Rust, and W.E. Vaugham *J. Am. Chem. Soc.*, **70**, 88 (1948).

78. K. Matsuyama, Y. Higuchi, *Bull. Chem. Chem. Soc. Jpn.* **12**, 2296 (1985).

79. H. Yasutake *J. Ind. Exp. Soc.* **52**, 350 (1991).

80. K. Wrabetz, J. Wong, Z. Fresenius *Anal. Chem.* **329**, 487 (1987).

81. J.C.M. Torfs, D. Leen, A.J. Dorrepaal, and J.C. Heijens, *Anal. Chem.*, **56**, 2863 (1984).

82. E. Gimzewski, G. Audley *Thermochimica Acta*, **214**, 129 (1993).

83. J. F. Griffiths, M. F. Gilligan, P. Gray *Combust. Flame* **24**, 11 (1975).

84. H. S. Kesling, F. J. Liotta, M. Nandi *SAE Tech. Pap. Ser.* 1994 941017.

85. D.D. MacNeil, and J.R. Dahn, *J. Phys. Chem. A.*, **105**, 4430 (2001).

86. J. Sempere, R. Nomen, R. Serra, *J. Thermal Anal and Cal.*, **56**, 843 (1999).

87. U. Biader Ceipidor, E. Brizzi, R. Bucci, A.D. Magri, *Thermochimica Acta*, **247**, 347 (1994).

88. D.D. MacNeil, L. Christensen, J. Landucci, J.M. Paulsen, and J.R. Dahn, *J. Electrochem.Soc.,*, **147**, 970 (2000).

89. I.A. Vasilev, *Thermodynamic Properties of Oxygen-Containing Organic Compounds*, Khimiya, Leningrad (1984).

90. N.A. de Kolossowsky, and W.W. Udowenko, *Compt. Rend.*, **197**, 519 (1933).

91. W.D. Johnston, R.R. Heikes and D. Sestrich, *J. Phys. Chem. Solids* **7**, 1 (1958).

92. L. Vogdanis, B. Martens, H. Uchtmann, F. Hensel, W. Heitz, *Makromol. Chem.*, **191**, 456 (1990).

93. M. Mansson, *J. Chem. Thermodyn.*, **4**, 865 (1972).

94. D. Aurbach, *J. Power Sources*, **89**, 206 (2000).

95. D. Aurbach, A. Zaban, Y. Ein-Eli, I. Weissman, O. Chusid, B. Markovsky, M. Levi, E. Levi, A. Schechter, E. Granot, *J. Power Sources*, **68**, 91 (1997).

96. S. Sloop, J. Kerr, K. Kinoshita, *Paper 105* to be presented at 200th meeting of the Electrochemical Society, San Fransico, CA (2001).

97. L. Vogdanis, B. Martens, H. Uchtmann, F. Hensel, W. Heitz, *Makromol. Chem*, **191**, 465 (1990).

98. G. Botte, R.L. White, Z. Zhang, submitted to *J. Power Sources*, **97-98**, 570 (2001).

99. K.J. Laidler, *Chemical Kinetics*, 3rd Ed., McGraw-Hill, Toronto, 1965, pp. 318.

100. F.C Tompkins, *The International Encyclopedia of Physical Chemistry and Chemical Physics*, **21**, 34 (1966).

101. H. Shi, J. N. Reimers, J. R. Dahn, *J. Appl. Cryst.*, **26**, 827 (1993).

102. H. Jagodzinski, *Acta Crystallogr*, **2**, 298 (1949).

103. T. Zheng, *The Physics and Chemistry of High Capacity Carbonaceous Materials for Lithium-ion Batteries*, Ph. D. thesis, Simon Fraser University (1996).

104. K. Kanamura, H. Tamura, S. Shiraishi, Z-I, Takehara, *Journal of Electroanalytical Chemistry*, **394**, 49 (1995).

105. C.R. Yang, Y.Y. Wang, C.C. Wan, *Journal of Power Sources*, **72**, 66 (1998).

106. W. Xing, J. R. Dahn, *J. Electrochem. Soc.*, **144**, 1195 (1997).

107. J.R Dahn, R. Fong, M.J. Spoon, *Phys. Rev. B*, **42**, 6424 (1990).

108. D. Aurbach, A. Zaban, A. Schechter, Y. Ein-Eli, E. Zinigrad, B. Markovsky, *J. Electrochem. Soc.*, **142**, 2873 (1995).

109.   J.R. Dahn, D.D. MacNeil, T.D. Hatchard, "Method and apparatus for characterizing high-energy electrochemical cells using power functions obtained from calorimetry", U.S. Patent Application 55139USA6A, filed December 29 1999.

110.   T.D. Hatchard, *A Thermal Model for Lithium-ion Batteries in Oven Exposure Tests*. MSc Thesis, Dalhousie University (2001).

111.   T. D. Hatchard, D.D. MacNeil, A. Basu, J.R. Dahn, *J. Electrochem. Soc.*, **148**, A755 (2001).

112.   J.R. Dahn, T.D. Hatchard, D.D. MacNeil "Batteries with emissive surfaces", U.S. Patent Application 55138USA19, filed December 28 1999.

113.   O. Schilling, and J.R. Dahn, *J.Electrochem. Soc.* **1998**, *145*, 569.

114.   A. Du Pasquier, A. Blyr, P. Courjal, D. Larcher, G. Amatucci, B. Gerand, and J-M. Tarascon, *J. Electrochem. Soc.*, **146**, 428 (1999).

115.   A. Du Pasquier, A. Blyr, A. Cressent, C. Lenain, G. Amatucci, J.M. Tarascon, *J. Power Sources*, **81-82**, 54 (1999).

116.   C. Delmas, I. Saadoune, A. Rougier, *J. Power Sources*, **43-44**, 595 (1993).

117.   Y. Gao, Private Communications (2000).

118.   Z. Lu, D.D. MacNeil, J.R. Dahn, accepted to *Elect. Solid-State Letts.* (2001).

119.   Z. Lu, D.D. MacNeil, J.R. Dahn, accepted to *Elect. Solid-State Letts.* (2001).

120.   Z. Lu, and J.R. Dahn, submitted to *J. Electrochem. Soc.* (2001).

121.   A.K. Padhi, K.S. Nanjundaswamy, J.B. Goodenough, *J. Electrochem. Soc.*, **144**, 1188 (1997).

122.   A. Yamada, S.C. Chung, K. Hinokuma, *J. Electrochem. Soc.*, **148**, A224 (2001).

123.   For example see the Proceedings of the 192nd Meeting of the Electrochemical Society, Paris, Sept 1997.

124.   For example see the Proceedings of the 200th Meeting of the Electrochemical Society, San Francisco, Sept 2001.

125.   E. Buiel, J.R. Dahn, *Electrochimica Acta*, **45**, 121 (2000).

126.   J.R. Dahn et al., *Papers 256, 257, and 258* to be presented at 200th meeting of the Electrochemical Society, San Fransico, CA (2001).

127.   S. Yoon, H. Kim, S. Oh, *J. Power Sources*, **94**, 68 (2001).

128.   Y. Choquette, G. Brisard, M. Parent, D. Brouillette, G. Perron, J. E. Desnoyers, M. Armand, D. Gravel, N. Sloughi, *J. Electrochem. Soc.*, **145**, 3500 (1998).

129.   Z.X. Shu, R.S. McMillan, J.J. Murray, I. J. Davidson, *J. Electrochem. Soc.*, **143**, 2230 (1996).

130.   J. Cada, T.D.J. Dunstan, D.M. Ryan, V. Katovic, *ECS Meeting Abstracs*, MA 99-2, 2252 (1999).

131.   M. Adachi, "Non-aqueous electrolyte secondary cell having shuttle agent" US Patent Application 5763119, filed April 1996.

132.   Y. Wang, M. Zhang, U. von Sacken, B. Way, "Additives for improving cycle life of non-aqueous rechargeable lithium batteries" US Patent Application 6045948, filed March 1998.

133.   H. Sugita, H. Yamamoto, "Lithium ion secondary cell solvent" US Patent Application 6040091, filed June 1998.